Modélisation par éléments finis des phénomènes thermomécaniques et de macroségrégation dans les procédés de solidification

Weitao Liu

To cite this version:

Weitao Liu. Modélisation par éléments finis des phénomènes thermomécaniques et de macroségrégation dans les procédés de solidification. Sciences de l'ingénieur [physics]. École Nationale Supérieure des Mines de Paris, 2005. Français. NNT : 2005ENMP1283 . pastel-00001339

HAL Id: pastel-00001339
https://pastel.hal.science/pastel-00001339

Submitted on 22 Aug 2005

ECOLE DES MINES
DE PARIS

Ecole Doctorale 364 : Sciences Fondamentales et Appliquées

N° attribué par la bibliothèque
|__|__|__|__|__|__|__|__|__|__|

T H E S E

pour obtenir le grade de
Docteur de l'Ecole des Mines de Paris
Spécialité «Mécanique Numérique»

présentée et soutenue publiquement par

Weitao LIU

Soutenue le 9 Juin 2005

FINITE ELEMENT MODELLING OF MACROSEGREGATION AND THERMOMECHANICAL PHENOMENA IN SOLIDIFICATION PROCESSES

Directeur de thèse: Michel BELLET
Co-Directeur de thèse: Hervé COMBEAU

Jury

M.	Yves FAUTRELLE	Président
M.	Eric ARQUIS	Rapporteur
M.	Dominique GOBIN	Rapporteur
Mme	Joëlle DEMURGER	Examinatrice
M.	Hervé COMBEAU	Directeur de thèse
M.	Michel BELLET	Directeur de thèse

Acknowledgments

I would like to thank the director of CEMEF, Jean Loup Chenot for the invitation, providing me with the opportunity to study in Ecole des Mines de Paris. I would like to thank the CEMEF laboratory of Ecole des Mines de Paris and the LSG2M laboratory of Ecole des Mines de Nancy.

I would like to thank my directors, Dr. Michel Bellet and Professor Hervé Combeau, for their guidance, support, and inspiration through my study at CEMEF and LSG2M laboratories.

I am sincerely grateful to Professor Eric Arquis and Professor Dominique Gobin for the report on this dissertation, and I am also sincerely grateful to Mme Joëlle Demurger and Professor Yves Fautrelle for the examination of this dissertation.

I would like to thank the members of our research group: Alban Heinrich, Steven Le Corre, Victor D. Fachinotti, Sylvain Gouttebroze, Boubeker Rabia, Ludovic Thuinet for the discussion on thermal mechanics and solidification. I am also grateful to Cyril Gruau for his help during the implementation of mesh adaptation.

This work has been supported by the French Ministry of Industry, the French Technical Center of Casting Industries (CTIF) and the following companies: Arcelor, Ascometal, Fonderie Atlantique Industrie, Aubert et Duval Alliages, Erasteel, Industeel Creusot and Research PSA. Their financial support is gratefully acknowledged.

Contents

Chapter 1

General introduction

Introduction générale – Résumé en français

Ce chapitre est une introduction générale au présent travail. Les principaux phénomènes physiques à la base de la formation des macroségrégations lors de la solidification des alliages métalliques sont présentés. A l'échelle microscopique, il s'agit de la microségrégation résultant du rejet de solutés dans la phase liquide et de la diffusion dans la phase solide. A l'échelle macroscopique, les espèces chimiques ainsi rejetées sont transportées dans la pièce sous l'effet des mouvements de convection dans la phase liquide. Ces mouvements de convection sont causés par les gradients de masse volumique, eux-mêmes générés par les gradients de température et de concentration en solutés. C'est cette convection thermo-solutale qui donne naissance aux macroségrégations, hétérogénéités de concentration à l'échelle de la pièce ou du lingot de fonderie, qui vont affecter diverses propriétés (mécaniques, chimiques…) en service ou lors de transformations ultérieures.

D'autre part, le retrait à la solidification, présenté par la grande majorité des alliages métalliques, est un autre phénomène essentiel. Le retrait induit à la fois des écoulements dans la phase liquide et des déformations de la phase solide. Le défaut de retassure primaire ainsi que la formation de lames d'air à l'interface pièce-moule sont une conséquence directe du retrait. Outre ce retrait, les phénomènes de dilatation thermique participent aussi à la génération de contraintes et de distorsions, pouvant dégénérer en ruptures, et qu'il est donc nécessaire de modéliser pour optimiser les procédés de coulée.

En conséquence, les objectifs de ce travail sont définis : proposer une modélisation des phénomènes de macroségrégation et des phénomènes thermomécaniques (contraintes–déformations) dans le cadre d'une approche bidimensionnelle par éléments finis. Ce travail se situe dans une certaine continuité au sein des laboratoires LSG2M (logiciel de volumes finis SOLID) et Cemef (logiciels d'éléments finis R2SOL et THERCAST).

Chapter 1

General introduction

1.1 Background

Solidification occurs in many metal forming processes, ranging from conventional processes like foundry, welding, ingot casting etc. to the latest technologies like crystal growth or laser processing.

The essential feature in the solidification of a metallic alloy is the liquid-solid phase change associated with the release of latent heat and the solute redistribution. The solutes are often redistributed non-uniformly in the fully solidified casting, giving birth to what is usually called segregation. Segregation occurring on a microscopic scale (i.e., between and within dendritic arms) is known as microsegregation. While segregation occurring on a macroscopic scale (i.e., in a range from several millimeters to centimeters or even meters) is called macrosegregation. Microsegregation can be controlled or reduced by a high temperature treatment (homogenization). However, macrosegregation occurring on the macroscopic dimensions of the casting cannot be eliminated by homogenization.

Taking into account shape, location or concentration, several types of macrosegregation can be observed in an ingot or a casting as described in more detail further, such as “centerline segregation”, “A-segregation”, “V-segregation”, and “freckles” (Beckermann [2001]). Macrosegregation is important, because it affects (like microsegregation) the mechanical properties of casting products. In some cases, macrosegregation can be very important. An impressing example consists of the freckles appearing in the directional solidified Ni-base superalloys of aeroengine turbine blades (Frueh et al. [2002]). In metal processing, metallurgists always attempt to overcome the centreline macrosegregation in continuous casting steel slabs and direct chill aluminum castings (aluminum DC castings), centreline macrosegregation in slabs decreases the quality of the final products. The macrosegregation in the ingots can be a source of problems in further processing such as rolling, forging and heat treatment. For these reasons, researchers have struggled with macrosegregation for decades.

In the literature, experimental and theoretical studies on solidification phenomena have been carried out by a lot of researchers. The mechanisms of different types of macrosegregation are well identified. It results from the relative movement of the liquid and solid phases. Movement of liquid can be induced by the solidification shrinkage, the thermal-solutal buoyancy force and possibly by external forces, such as magnetic forces.

In addition, solidification shrinkage as a result of liquid-solid phase change and thermal contraction is another important feature in the solidification of castings. The solidification shrinkage induces the liquid movement and the solid deformation. Many solidification phenomena are related to shrinkage. For instance, the descent of liquid level associated with feeding flow leads to the so called “shrinkage pipe”. Shrinkage pipes appear in the upper portion of risers, taking the shape of an inverted cone. The prediction of pipe formation is important in large castings and ingots. The numerical analysis is characterized by the computation of the liquid free surface. Thermal contraction in the solid can induce the distortions, cracks and residual stresses in castings and molds. Thermal mechanical analysis of solidification process is then essential to predict defects and control the quality of castings.

In France, the project OSC (Optimisation des Systèmes de Coulée), which aims at the numerical modeling of casting processes, has been supported by the French Ministry of Industry, the French Technical Center of Casting Industries (CTIF) and the following companies: Arcelor-Irsid, Ascometal, Fonderie Atlantique Industrie, Aubert et Duval Alliages, Erasteel, Industeel and PSA. Under the frame of OSC project, my Ph.D. work is dedicated to modeling macrosegregations and deformations during the solidification of castings.

From the point of view of scientific research, the solidification processing of castings involves the following phenomena: heat transfer with phase change, redistribution of solutes in liquid and solid phases; thermal-solutal convection in liquid and mushy zones, fluid flow driven by solidification shrinkage; transport of solute; and thermal stresses and deformations in solidifying castings and molds. The complicated transport phenomena result in defects such as shrinkage, macrosegregation, distortions and cracks. Hence, the numerical simulation on the formation of defects is a very challenging field.

We will review and discuss the basic solidification phenomena in the following text.

1.2 Solidification phenomena

1.2.1 Solidification and structure

A pure metal solidifies at a constant temperature T_f, the melting temperature. The material is in the liquid state above T_f, and it becomes solid below T_f. However, an alloy solidifies in a range of temperature. The solid and the liquid coexist in a range of temperature between liquidus and solidus. Redistribution of solutes in the solid and liquid phases occurs in the solidification of alloys, which distinguishes alloys from pure metals.

During the solidification of a pure metal with a positive temperature gradient, the general solid-liquid interface is parallel to the temperature isotherm; the interface morphology is planar. The interface becomes unstable under a negative temperature gradient: the dendrite, like a tree, is formed in the supercooled liquid pool.

An alloy can be solidified with a planar interface only if the ratio of the heat flux at solid-liquid interface to the velocity of moving front is sufficiently large. With the ratio decreasing, the interface becomes unstable, and cellular and dendritic interfaces can be observed. The constitutional supercooling associated with the redistribution of solutes and thermal condition is responsible for the instability of interface and the structure morphology.

Generally, a cast alloy freezes with a dendritic interface. The region, which is composed of dendritic solid and interdendritic liquid, is known as the mushy zone. The typical structure, which is composed of the chill zone, the columnar zone and the equiaxed zone, obtained in a steel ingot is shown in Figure 1-1.

- Chill zone. The zone consists of fine equiaxed grains. The mould wall provides with plenty of sites for nucleation, and the crystals grow in the supercooled liquid due to the mould chilling. This leads to the formation of a fine equiaxed zone in the skin.
- Columnar zone. Just ahead of the chill zone, the gradient of temperature in the liquid is rather steeper. Thus, the fine equiaxed grains in the chill zone can not develop toward the center of the ingot. The dendrites grow perpendicular to the mold wall, resulting in the columnar structure. This structure can be extended to the center of an ingot if the cooling condition is well controlled.
- Equiaxed zone. Generally many small grains suspend in the liquid at the center of ingot. These small grains can originate from the fragment of dendrites growing in the columnar zone. The movement of liquid is important during the pouring and during solidification. The dendrites can be broken by the flow, and fragments can be brought into the liquid center. These fragments can remelt or survive and grow to form the equiaxed grains.

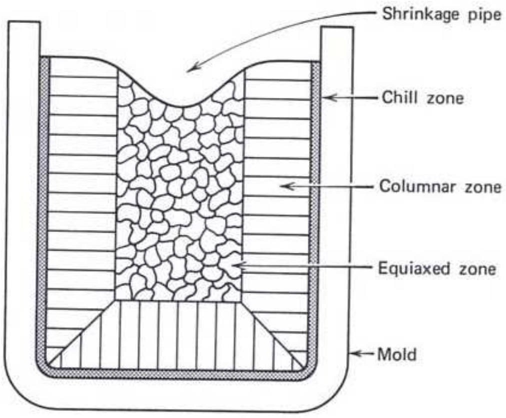

Figure 1-1 Schematic of the structure in a steel ingot, Verhoeven [1975]

1.2.2 Shrinkage

Shrinkage results from the density difference between liquid and solid. On the macro scale, shrinkage defects can be classified into the porosity and the pipe. The porosity consists of dispersal vacuities or holes in metal. The causes of porosity are the insufficient feeding in the mushy zone and the evolution of the absorbed gas in liquid. The interdendritic feeding flow is responsible for the porosity. Three important factors that affect the feeding flow are: 1) the freezing range of the metallic alloy, which affects the grain structure; 2) the cooling rate, which also affects the grain structure; 3) the thermal gradient, generally the feeding liquid moves along the direction of the thermal gradient. Porosities often appear in the hot spots where the liquid pools are isolated and the thermal gradient is low. While the pipe results from the cumulated effects of local shrinkage. It results from the descent of liquid level, associated with the progress of the solidification. The prediction of pipe formation is of importance especially in the case of ingots or large parts.

1.2.3 Macrosegregation

Segregation refers to non-uniformity of chemical composition. It can be classified into macro- and micro- segregation. Microsegregation results from the solute enrichment in the interdendritic liquid during solidification. While macrosegregation results from the local microsegregation and the relative movement of liquid and, possibly, solid phases. Macrosegregation that occurs in alloy castings or ingots ranges in scale from several millimeters to centimeters or even meters. Positive (negative) segregation refers to the composition above (below) the nominal composition. The non-uniform distribution of chemical composition can significantly affect the mechanical properties of castings, and therefore its numerical modeling is important from the industrial point of view.

The classical map of segregation in a steel ingot is shown in Figure 1-2. Negative segregation known as the sedimentary equiaxed cone appears in the bottom of ingot. Fragments of dendrites with poor solute content, which have been solidified in the early stage, settle down to the bottom, resulting in the negative segregation cone. Positive segregation (hot-top segregation) appears near the centerline, and particularly at the top of the ingot. The positive segregation arises from the thermal and solutal convection and shrinkage-driven interdendritic fluid flow during the final stages of solidification. The so-called A-segregation appearing in the columnar zone is also called freckles or segregated channels. These regions are highly enriched in solutes. When the velocity of the solidification front is lower than that of solutal convection in the same direction, the channels occur (Mehrabian *et al.*[1970]). The V-segregation in the center arises from the equiaxed grains settling, the deformation of connected solid skeleton and the solidification shrinkage.

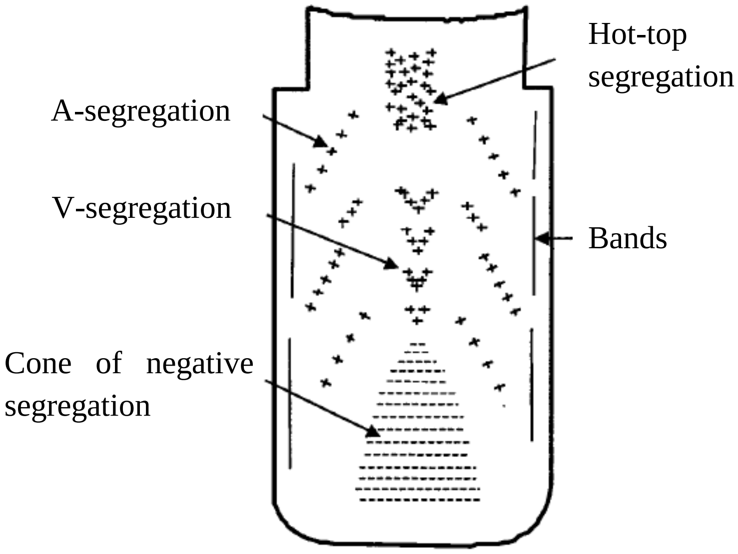

Figure 1-2 Schematic of the macrosegregation pattern in a steel ingot, Flemings [1974]

1.2.4 Liquid movement /and solid deformation

In ingot casting, strong turbulent fluid flow occurs during mould filling, and it vanishes after a short period. During the cooling and solidification of the ingot, fluid flow is principally driven by the density gradient in the liquid. This density gradient arises, first of all, from temperature gradient in the liquid, leading to thermal convection. As a consequence of solidification, solutes are rejected into the interdendritic liquid, and a non-uniform concentration is set up in the liquid. These gradients of solutes also contribute to the density gradient, leading to the solutal convection. The thermo-solutal convection is important in the solidification of ingots. The convection is responsible for the formation of macrosegregation. Furthermore, it influences the temperature distribution, the advancement of solidification front, the local solidification rate and therefore the structure.

There are other (additional) causes of liquid movement. The solidification shrinkage and the contraction of the liquid and solid can induce the feeding flow, which influences the formation of porosity, shrinkage and macrosegregation. Forced fluid flow can also arise from the electromagnetic or centrifugal forces.

The fluid flow can separate dendrites from solidifying dendrites; and bring these small crystals (the nuclei) to the center of bulk liquid. The nuclei grow in the region where the melt is undercooled. Later, when the grains have grown to a sufficient size, they settle down to the bottom, resulting in the sedimentary equiaxed zone with negative macrosegregation (Flemings [1974]).

Once the liquid has been solidified, the deformation occurs as a result of thermal contraction, boundary constraint (contact with the mold) and pressure exerted by the non-solidified liquid metal. The contraction of solidifying shell and the expansion of mold cause a gap between mold and casting, which affects the heat transfer and consequently the solidification processing. On the other hand, the mechanical behavior of the solidifying metal depends upon the local temperature, the grain structure and the deformation path.

As we can see from what precedes, solidification processing involves several complex physical phenomena. The interactions between many aspects that occur during solidification can be shown in Figure 1-3: main solidification phenomena occurring on microscopic scale are illustrated as a core; surrounding around the core, macroscopic scale transport phenomena are presented. It should be noted that these macro and microscopic phenomena are intimately coupled. For example, the macroscopic convection flow affects the temperature and the solute distributions; consequently it influences the grain growth (on microscopic scale). On the other hand, the grain growth changes the temperature and the concentration in the interdendritic liquid, which affect the macroscopic fluid flow. On the macroscopic scale, the fluid flow associated with transport of energy and solute affects the deformation in the solid, and *vice versa*.

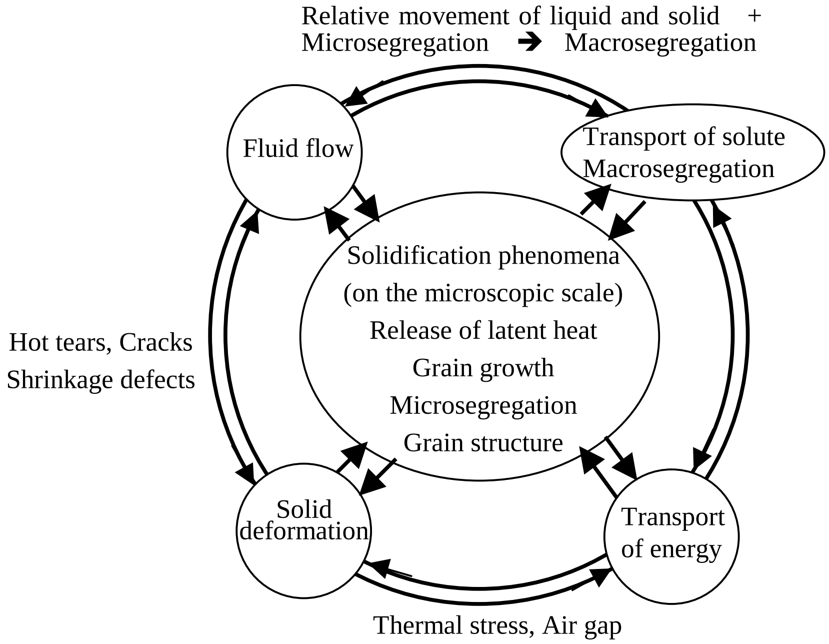

Figure 1-3 Interactions between macro and microscopic phenomena in the solidification of castings

Researchers have developed numerical models for several decades to reveal such phenomena. Great progresses have been achieved: models coupling heat, mass, momentum and solute transfer have been developed to predict shrinkage defects and macrosegregation. Thermomechanical models have been used to predict stresses and deformations in castings. In the following paragraph, the related previous work at CEMEF laboratory will be presented, as it is the basis for my Ph.D. work.

1.3 Related previous work

Developing history of R2SOL

CEMEF laboratory, in collaboration with LSG2M laboratory of Ecole des Mines de Nancy, has developed the 2-dimensional finite element code R2SOL for the two-dimensional numerical simulation of solidification processes. R2SOL has the following characteristics:

- Resolution of Navier-Stokes equations.
- Arbitrary Lagrangian-Eulerian (ALE) formulation.
- Thermal resolution in enthalpy formulation for the liquid-solid phase change.
- Resolution of the transport equations for the alloying elements.
- Coupling resolution of momentum, energy and mass conservation equations by a spatial averaging approach, in order to model the thermo-solutal convection and predict the macro-segregation. The mechanical behavior of metal is Newtonian in the liquid zone, and the Darcy term is added in the mushy zone. The solid phase is assumed to be rigid and stationary.

The first two points were developed by Laurence Gaston [1997] in her Ph.D. work on the simulation of mold filling, leading to the software R2. A velocity-pressure P2+/P1 formulation was used in R2 to solve the Navier-Stokes equations, and mesh updating was carried out by an ALE method to describe the free surface. Combining some procedures in the finite volume code SOLID developed at Ecole des Mines de Nancy, Laurence Gaston [1999], in her postdoctoral period, implemented the last 3 points in R2 to simulate the solidification processes, leading to the new software called R2SOL.

Following those developments, the P1+/P1 formulation, using linear triangles for 2-dimensional plane problems, instead of the quadratic P2+/P1 formulation, was implemented in R2SOL by Alban Heinrich [2003] in his Ph.D. work on the two-dimensional thermomechanical simulation of the steel continuous casting.

At the beginning of my thesis, in September 2001, the P1+/P1 mechanical solver was limited to Navier-Stokes equations.

The main objectives of my work to develop the new version of R2SOL were then defined as follows: 1) calculation of macrosegregation; 2) calculation of stresses and deformations in the solid phase, coupling with the natural convection in liquid phase. The related previous work of CEMEF laboratory and remained problems are presented in the following paragraphs.

Calculation of segregation

Like in the previous work of Laurence Gaston, we also assume that the solid phase is fixed and rigid (both in the mushy zone and in the solid zone). The movement of liquid is driven by the thermal-solutal convection. As shown in Figure 1-4, the behavior of the liquid metal is Newtonian.

Fluid flow in the mushy zone obeys the Darcy's law. A set of averaged conservation equations is used to describe the transport phenomena. The previous work provides a good basis for the new development. However, additional developments are needed to solve the remained problems and extend the computational capacity:

- the convergence rate of the resolution of the energy equation is relatively low; the energy solver needs to be improved.
- in the numerical solution, thermal shock (temperature oscillation) often appears near the boundary. The problem remains to be solved.
- assuming that solutes diffuse infinitely both in the solid and liquid phases, lever rule as a microsegregation model is used to predict macrosegregation. Scheil model (solutes diffuse infinitely in the liquid phase, but do not diffuse in the solid phase) is to be implemented in the new version of R2SOL.
- prediction of macrosegregation by the old version of R2SOL is limited to small pieces; additional developments are needed to compute macrosegregation in large industrial ingots.
- treatment of Darcy's and inertia terms in the momentum equation is not as good. In some cases, the resolution of velocity field is incorrect. Computations of these terms need to be improved.
- implementation of mesh adaptation to improve the numerical results.
- extending the Navier-Stokes solver from the plane case to the axisymmetric case.

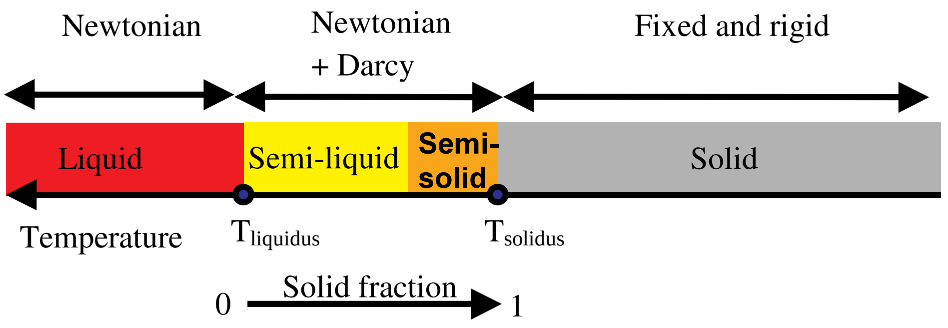

Figure 1-4 Schematic of the material behavior in R2SOLfor macrosegregation modeling

Calculation of fluid flow and solid deformation

For coupling resolution of deformation in the solid and convection in liquid, CEMEF laboratory has developed a 3-dimensional FEM software called THERCAST® (Jaouen [1998]). Considering continuum medium as illustrated in Figure 1-5, the different behaviors of the metal are clearly distinguished by the critical temperature T_C, being thermo-viscoplastic (THVP) above T_C and thermo-elastoviscoplastic (THEVP) under T_C. The Lagrangian scheme is used to compute the deformation in solid regions, the computational grid is allowed to move with the material: this is essential to treat the air gap between mold and casting. An arbitrary Lagrangian-Eulerian scheme is used to compute the thermal convection in liquid pool and mushy zone, taking into account the liquid contraction and the solidification shrinkage. This prevents the mesh from degenerating and allows tracking the free surface. The unilateral contact condition is applied to the boundary between mold and casting. The heat transfer coefficient is determined by the size of air gap between mould and casting.

The same strategy as mentioned above is adopted in my work for 2-dimensional problems. Some subroutines in THERCAST® to treat THEVP and THVP models can be used in R2SOL. However, we need to do the following work:

- extension of the material behavior from Newtonian to elastic-viscoplastic.
- adaptations to the different coordinate systems (from 3D to 2D), particularly for the axisymmetric case.

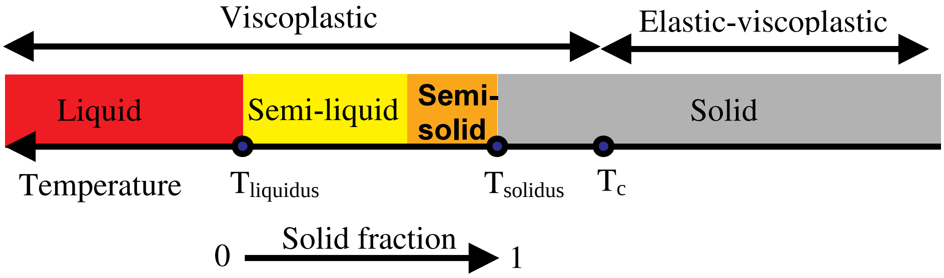

Figure 1-5 Schematic of the material behavior for stress-strain analysis

It should be noted that the mushy metal is considered as a single continuum in the computation of deformation. That is to say, the liquid and solid in the mushy zone move together with the same velocity. While in the macrosegregation model the mushy metal is considered as a two-phase medium, in which we assume that the solid is fixed and rigid, while the movement of the liquid is taken into account.

1.4 Objectives and outline

1.4.1 Objectives

In the framework of the project OSC (Optimisation des Systèmes de Coulée), the main objectives of my Ph.D. work are as follows:

- Computation of macrosegregation;
- Mesh adaptation;
- Computation of stress and deformation in the solidified zones.

It has been presented that many phenomena can affect macrosegregation. We have limited our study to macrosegregation associated with thermo-solutal convection, as it has been stated that macrosegregation results essentially from microsegregation and the relative movement between solid and liquid phases. Firstly, natural convection occurs on the macro scale, transporting heat and solutes through the whole casting. Secondly, latent heat release and solute rejection occur at the micro scale, in the interdendritic space. It is impossible to solve the conservation equations at the microscopic scale due to the complex morphology of grains and the computational cost. An averaging approach is adopted following the previous works of Beckermann and Viskanta [1988]. The basic idea of the approach is to average the microscopic equations over a representative elementary volume. This element is defined such that its size is small enough to capture the global transport of energy, mass, concentration and momentum, but large enough to smooth out the details of microscopic phenomena as the interdendritic fluid flow, latent heat release and solute redistribution. A set of averaged governing equations is established and applied to predict macrosegregation.

Fluid flow in the mushy zone close to the liquidus and in the liquid just ahead of the liquidus is important in the formation of macrosegregation. Deeper in the mushy zone, close to the solidus, dendrites are very compact, so that the permeability is very low and the velocity is nearly equal to zero. Dramatic change of permeability occurs in the mushy zone close to the liquidus, resulting in great variation of velocity field. This may lead to a boundary layer of velocity near the solidification front. Therefore, in order to accurately capture the macrosegregation, finer meshes should be applied in the region near the liquidus. Similarly, it is necessary to use fine mesh to capture pencil-like freckles. As suggested in the pioneer work of Kämpfer [2002] for instance, mesh adaptation seems to be an efficient numerical tool in this field. The automatic determination of the objective mesh size is not an easy task and no reliable error estimators have been evidenced so far for the complicated coupled solidification problems. For simplicity, we have decided to pilot the remeshing procedure in order to get fine layers of elements within the mushy zone and ahead of the liquidus. The adaptive mesh is created by using a mesh generator “MTC” developed at CEMEF (Coupez [1991]).

The similar strategy as THERCAST® is adopted to model the fluid flow and the deformation in solid. As has been stated in the previous section, only thermal convection in the liquid pool is considered and solutal convection is not taken into account. The present work has consisted in implementing the THEVP and THVP models in the 2 dimensional code R2SOL, especially for the axisymmetric problem. This part of work has been done in collaboration with another Ph.D. student, Alban Heinrich.

To summarize, there are two models in the scope of present study. The first model is used to predict macrosegregation during dendritic columnar solidification of casting alloys. We assume that the solid phase is fixed and non-deformable (both in mushy zone and solid zone). The behavior of liquid metal is Newtonian. The liquid movement in the mushy zone follows the Darcy’s law. Not taking into account the solid deformation and solidification shrinkage, the computational domain is fixed. Hence, a Eulerian formulation can be used, associated with a mesh refinement strategy.

The second model is used to simulate shrinkage pipe, air gap and solid deformation. Here, the mushy metal is considered as a continuum, without any relative movement between the solid and liquid phases. Unlike the first model, the configuration of casting changes as a result of solidification shrinkage and deformation in solid. Therefore, ALE formulation is used. The art of numerical simulation is different from that of first model. The different models and their computational capacity are summarized in the Table 1- 1.

Table 1- 1 models considered in the present study

	Mushy zone	Liquid movement induced by	Solid deformation	Prediction
Model I	Two phases	Thermal solutal convection	No	Macrosegregation
Model II	Single continuum	Thermal convection Solidification shrinkage	Yes	Pipe shrinkage Stresses and strains in solid (including air gaps)

1.4.2 Outline

The bibliographic review is presented in chapter 2. In this chapter, firstly, we review the pioneering work on macrosegregation of Flemings in the 1960s. Then, the modern numerical models on macrosegregation are presented. Finally, we present models coupling fluid flow and deformation in solid, which focus on the prediction of shrinkage pipe.

Regarding the objectives of my work, the thesis is decomposed into two parts. The first part is the computation of macrosegregation with mesh adaptation. The second part is the computation of deformation in solid.

The first part consists of chapters 3-5. Chapter 3 is devoted to the numerical approach to prediction of macrosegregation. The algorithm for the mesh adaptation is presented in chapter 4.

Numerical results of macrosegregation are presented and discussed in chapter 5. The computation of a benchmark test has been carried out. The influence of mesh size and time step on the numerical results has been investigated. Finally, macrosegregation in an industry ingot has been predicted by R2SOL. The results obtained by R2SOL are compared with other numerical models.

Coupling resolution of fluid flow and deformation in solid is presented in chapter 6. The behavior of metal is extended from Newtonian to elastoviscoplastic. Special attention is given to the computation of tangent rheological modules in the axisymmetric case. The validation of thermal elastoviscoplastic model has been done by some simple tests. The computational results of a benchmark test are shown, as well as an application to an industrial ingot.

Chapter 2

Bibliographic review

Revue bibliographique – Résumé en français

Concernant la macroségrégation, les premières analyses dues à Flemings sont passées en revue. Dans ces travaux, le phénomène est analysé analytiquement et expérimentalement. Un premier modèle numérique est proposé, en prenant en compte l'écoulement liquide interdendritique et le transport de soluté dans la zone pâteuse. Ceci permet une première compréhension de la macroségrégation.

La revue est ensuite focalisée sur les modèles de prise de moyenne spatiale, qui sont comparés aux modèles issus de la théorie des mélanges. Ces deux méthodes simples d'homogénéisation sont en effet une manière de traiter le changement d'échelle existant entre micro et macroségrégation. Les concepts de base de la prise de moyenne sont alors présentés. Le principe consiste à moyenner les équations de conservation établies à l'échelle microscopique (masse, quantité de mouvement, énergie, espèces chimiques) sur un volume élémentaire représentatif (v.e.r.) de la zone pâteuse (liquide-solide).

Dans l'étude des phénomènes de macroségrégation, la representation de l'écoulement de liquide dans la région proche de la surface isotherme à la température de liquidus s'avère capitale, car on y trouve des gradients de vitesse importants, dûs aux variations importantes de la perméabilité. Par conséquent, dans le but d'améliorer la précision des calculs, certains auteurs, tels Kämpfer et Rappaz ont mis en œuvre des méthodes de raffinement dynamique des grilles de calcul qui sont présentées.

Concernant l'aspect thermomécanique (distorsions et contraintes), différents modèles de prédiction des retassures primaires sont analysés dans la section 2.2. On note en particulier que dans la plupart des cas, le total des pertes de volume correspondant au retrait à la solidification et à la dilatation thermique est affecté à la formation de la retassure primaire. A l'évidence, cette analyse est pour le moins contestable, puisqu'elle néglige complètement le volume correspondant à la formation des lames d'air entre pièce et moule. Dans la continuité des certains travaux menés préalablement au laboratoire, l'objectif est donc de tenir compte de cette complexité au moyen d'une analyse thermomécanique plus fine.

Chapter 2

Bibliographic review

2.1 Macrosegregation models

Around 1967, M.C. Flemings and coworkers published a series of papers (Flemings *et al.* [1967, 1968A, and 1968B]). They examined analytically and experimentally macrosegregation, which results from interdendritic fluid flow. Considering the fluid flow in the mushy zone, they established the first model of macrosegregation called Local Solute Redistribution Equation, leading to a comprehensive understanding of the formation of macrosegregation. Since then, numerical models coupling fluid flow in the mushy and in the bulk liquid have been developed to predict macrosegregation.

Following history of macrosegregation models, firstly, we present the basic theory and the model of Flemings in section 2.1.1. Secondly, we focus on the models coupling fluid flow in the mushy zone and in the bulk liquid in sections 2.1.2. The present work on macrosegregation is based on these models. In section 2.1.3, we review numerical models with mesh adaptation.

2.1.1 Flemings’ macrosegregation model

Before reviewing Flemings’ macrosegregation model, we briefly present the basic theory for microsegregation that has been stated in the textbook "Solidification processing" of Flemings [1974].

Microsegregation

Solute enrichment in the interdendritic liquid during solidification results in microsegregation. As shown in Figure 2-1, redistribution of solute in the dendrite and in the interdendritic liquid can be described by the two simple models: 1) instantaneous diffusion of solute in the solid and liquid phases (lever rule); 2) non-diffusion in the solid and instantaneous diffusion in the liquid (Scheil model).

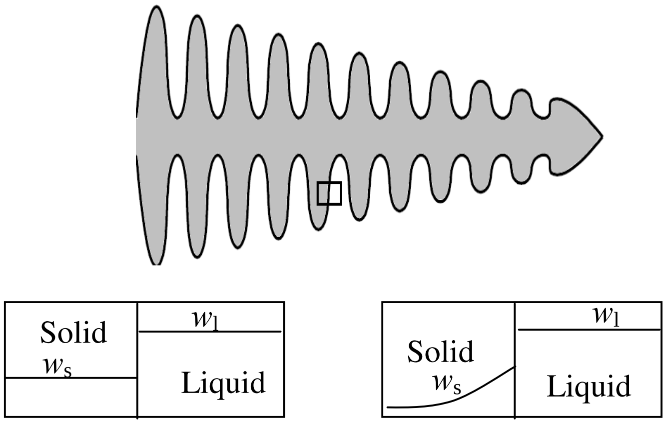

a) lever   b) Scheil model

Figure 2-1 Basic microsegregation models

For a binary alloy with a partition coefficient *k*, solidified in a closed one-dimensional space, the lever rule and Scheil models can be expressed by the following equations (2-1) and (2-2) respectively:

$$w_0 = w_l\left[1 - f_s(1-k)\right] \tag{2-1}$$

$$w_0 = (1.0 - f_s)\, w_l + \int_0^{f_s} k w_l \, df_s$$

$$or \quad \frac{df_l}{dw_l} = -\frac{1}{1-k}\,\frac{f_l}{w_l} \tag{2-2}$$

where w_0 is the initial mass concentration; w_l is the mass concentration in the liquid phase; f_s, f_l are the mass fractions of solid and liquid respectively.

In addition, if we assume that the solid density ρ_s and the liquid density ρ_l are constant and equal, that is:

$$\rho_l = \rho_s = \rho = \text{constant} \tag{2-3}$$

this implies that the mass fraction is equal to the volume fraction. Thus, we will use the terms *solid fraction* and *liquid fraction*, and, unless specified, we will not distinguish anymore between mass and volume fractions.

Local solute redistribution equation

By performing mass and solute balances over a representative elementary volume characteristic of the macroscopic scale shown in Figure 2-2, Flemings *et al*. derived equation (2-4), called “local solute redistribution equation” (LSRE). The solute enters and leaves the elementary volume only because of the transport by the liquid flow, and diffusion is neglected at the macroscopic scale.

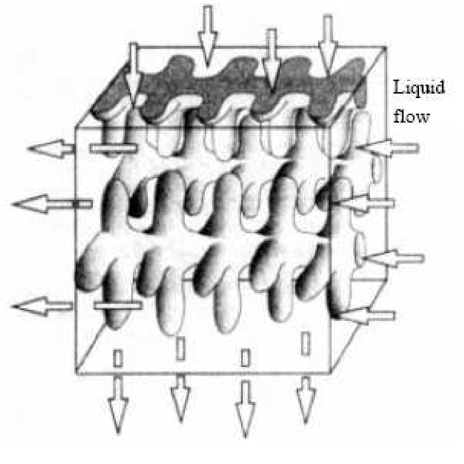

Figure 2-2 Schematic of interdendritic liquid flow through a fixed dendritic solid network

$$\frac{\partial f_l}{\partial w_l} = -\left(\frac{1-\beta}{1-k}\right)\left[1 + \frac{\mathbf{v}\cdot\nabla T}{\dot{T}}\right]\frac{f_l}{w_l} \tag{2-4}$$

where $\beta = \frac{\rho_s - \rho_l}{\rho_s}$ is the solidification shrinkage; $\mathbf{v}$ is the intrinsic averaged liquid velocity; ∇T is the temperature gradient; $\dot{T}$ is the rate of temperature change, $\dot{T} = \frac{\partial T}{\partial t}$.

The LSRE model demonstrates how interdendritic liquid flow is responsible for macrosegregation. The physical significance of equation (2-4) can be understood by the following remarks:

1. When there is no solidification shrinkage and no relative movement of the liquid, β and $\mathbf{v}$ both vanish in equation (2-4), the equation reduces to the Scheil equation (2-2), implying no macrosegregation.
2. Equation (2-4) reduces to the Scheil equation when the liquid velocity is just that required to feed solidification shrinkage. For simplicity, considering steady unidirectional solidification, the velocity of moving isotherm can be expressed as $\frac{-\dot{T}}{\nabla T}$. Applying the mass conservation equation, we have $\frac{\mathbf{v}\nabla T}{\dot{T}} = \frac{\beta}{1-\beta}$. Hence, equation (2-4) becomes the Scheil equation.
3. If the flow velocity in the direction of increasing temperature is so large that the term in the square brackets in equation (2-4) becomes negative, local melting occurs, leading to the formation of segregation channel. The details of discussion on flow instability can be found in the literature (Mehrabian *et al.* [1970]).

Mehrabian *et al.* [1970] proposed that the interdendritic fluid flow driven by solidification contraction could be calculated by Darcy's law. Taking into account the gravity force on fluid, the equation for calculating $\mathbf{v}$ is given by:

$$\mathbf{v} = \frac{-\mathrm{K}}{\mu f_l}(\nabla p - \rho_l \mathbf{g}) \tag{2-5}$$

where, μ is the viscosity; K is the permeability; ∇p is the pressure gradient; $\mathbf{g}$ is the gravity vector.

Mehrabian *et al.* [1970] applied the LSRE equation (2-4) and Darcy's equation (2-5) to horizontal, unidirectional, steady-state solidification ingots with aluminum-copper alloys. Numerical results showed that the parameter $\frac{\mathbf{v} \cdot \nabla T}{\dot{T}}$ has a marked effect on segregation. Furthermore, "A" and "V" segregations in commercial ingots were interpreted by the LSRE model.

Kou *et al.* [1978] applied the LSRE model to predict the macrosegregation in rotated ingots with Sn-Pb alloys. The centrifugal force was considered as an additional term in equation (2-5). The macrosegregation predicted by the calculation agreed well to the experimental results.

In the previous works of Mehrabian and Kou, the temperature field in the mushy zone was either assumed or measured to serve as an input to the analysis of fluid flow. Fujii *et al.* [1979] extended the LSRE model to macrosegregation in multicomponent low-alloy steel. For the first time, the momentum (Darcy's) equation and energy equation were coupled and solved simultaneously.

2.1.2 Coupling fluid flow in the mushy and bulk liquid zones

2.1.2.1 The first multi-domain model

The first macrosegregation model coupling the flow in the mushy zone and in the bulk liquid was reported by Ridder *et al*. [1981]. The steady axi-symmetric solidification problem was considered, such a case being encountered in different casting processes, e.g. vacuum arc refining, electroslag remelting and continuous casting. The computational domain was decomposed in two regions: the mushy zone and the pure liquid zone. The interdendritic fluid flow driven by solidification shrinkage was calculated by solving Darcy's and LSRE equations. Temperature-induced natural convection in the bulk liquid was calculated by solving the stream function. An iterative procedure involving the resolution of the two sets of equations was performed as follows:

1) calculating the pressure, velocity and fraction of liquid in the mushy zone;
2) calculating the natural convection in the bulk liquid;
3) repeating procedures 1) and 2) to get consistent solutions in the mushy zone and in the bulk liquid zone. Coupling computation in the two domains was performed by applying the boundary condition to the liquidus isotherm. The pressure at the liquidus isotherm obtained in the step 2) was used as a boundary condition to compute the fluid flow in the mushy zone. While the velocity at the liquidus isotherm obtained in the step 1) was used as a boundary condition to compute the natural convection in the bulk liquid. When the pressure at the liquidus isotherm had stabilized, the concentration distribution in the mushy zone was obtained finally.

The model of Ridder was validated by solidification tests with Sn-Pb alloys. The temperature profiles, the sizes and shapes of mushy zone were controlled and measured in the experiments. Experimental data were used for initial values and boundary conditions in the numerical resolution. Good agreement between experiment and simulation was obtained.

Remarks

Two distinct equations, discretized by a differential method, were used to compute the velocities in the mushy and bulk liquid zones. The interface between the mushy zone and the bulk liquid zone was determined by the liquidus isotherm. In the case of steady solidification, the liquidus isotherm is fixed, and it does not evolve with time. So that it is not necessary to track the interface in the numerical resolution; and a fixed and conforming mesh can be used. The conforming mesh means that the nodes at the boundary of two regions coincide.

In Ridder's work, the concentration in the bulk liquid was assumed to be homogeneous, and solutal convection was neglected.

The multi-domain model of Ridder is not suitable for the non-steady case, for which the liquidus isotherm moves during the solidification. It is indeed difficult to track the phase interface and generate a conforming mesh dynamically.

2.1.2.2 Continuum models based on mixed theory

In order to overcome the difficulty of the multi-domain approach, single-domain continuum or volume-averaged models have been proposed by several researchers. These models consist of a single set of equations, which can be applied to the solid, mushy and liquid regions. Therefore, the equations can be solved on a single and fixed grid. The phase interfaces are implicitly defined by the enthalpy and the solute concentration fields.

The first single-domain continuum models were developed in the eighties (Bennon and Incropera [1987A], Voller and Prakash [1987], Voller *et al.* [1989]). Such models were developed from volume averaging techniques based on classical mixture theory. In these models, the mushy zone was viewed as a solid-liquid mixture with macroscopic properties, and individual phase conservation equations were summed to form a set of mixture conservation equations.

Bennon and Incropera [1987B] applied their continuum models to the solidification of a binary NH_4-H_2O alloy. “A” segregations, for the first time, were predicted by a numerical approach. Single domain models were demonstrated to be efficient tools for simulating solidification processes.

However, there were some misunderstandings in the development and application of the early continuum models. For instant, in the case of dendritic solidification, the net interaction between liquid and solid phases was postulated to exist, and the net force was computed by the Darcy’s law. The net interaction as internal force in the system was not clearly understood. Voller *et al.* [1989] identified the mushy fluid models, and indicated that the net force existed in the case of columnar dendritic solidification, while the force vanished for the flow of amorphous materials (e.g. waxes, the equiaxed zone).

Later, Prescott *et al.* [1991] clarified the mixture continuum models. They introduced Newton’s third law, and reconsidered the interaction between liquid and solid phases. Assuming that the solid phase was non-deformable and fixed, Prescott *et al.* demonstrated that the momentum equation based on the mixture theory was equivalent to the equation that was deduced from the averaging approach. Although the equivalent equation has been obtained by the mixture continuum and volume-averaged models, the continuum model has a shortcoming of weak linkage between micro and macro phenomena.

2.1.2.3 Volume averaged models

Beckermann and Viskanta [1988] proposed a volume-averaged model, to predict the double-diffusive convection during dendritic solidification of a binary alloy. The macroscopic conservation equations were rigorously derived from microscopic (exact) equations. The derivation procedure was presented more systematically by Ganesan and Poirier [1990]. More recently, Bousquet-Melou *et al.* [2002] proposed a non-homogeneous dendritic solidification model, in which all the terms arising from the averaging process (micro- and macro-contributions to momentum transport due to phase change and geometry) were estimated and compared on the basis of the characteristic length scale associated with the dendritic structure.

As volume averaged models deal clearly with the relationship between microscopic and macroscopic parameters, a volume averaged approach to predict macrosegregation has been adopted in the present work. For completeness we briefly remind the basic conceptions of the averaging technique, and then give an example, the mass conservation, to show the derivation procedure to average the conservation equation. The general volume averaging technique can be found in the literature (Gray [1975], Hassanizadeh and Gray [1979], Gray [1983]).

Consider a representative elementary volume ΔV as shown in Figure 2-3, we have the following definitions and theorems.

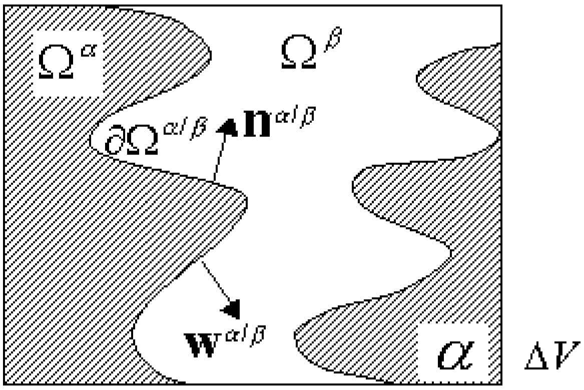

Figure 2-3 Volume used to average the conservation equation

Definition 2.1.1 *Phase indicator function* χ_α. The phase indicator function χ_α is a function of space *x* and time *t*, being equal to 1 in phase α and zero elsewhere:

$$\chi_\alpha(x,t)=\begin{cases}1 & \text{if } x\in\Omega^{\alpha}\\ 0 & \text{if } x\notin\Omega^{\alpha}\end{cases} \tag{2-6}$$

Definition 2.1.2 *Volume fraction of phase* α. It is defined as:

$$g_\alpha=\frac{1}{\Delta V}\int_{\Delta V}\chi_\alpha(x,t)\,dv=\frac{\Delta V_\alpha}{\Delta V} \tag{2-7}$$

where ΔV_α is the portion of ΔV that is occupied by the α phase. In addition, for the two phases α and β system, we have:

$$g_\alpha+g_\beta=1 \tag{2-8}$$

Definition 2.1.3 *Volume-averaged quantity* $\langle\psi_\alpha\rangle$. The volume-averaged quantity of a variable ψ (scalar, vector or tensor) in phase α is defined as:

$$\langle\psi_\alpha\rangle=\frac{1}{\Delta V}\int_{\Delta V}\psi(x,t)\chi_\alpha(x,t)\,dv \tag{2-9}$$

If ψ is the velocity of the interdendritic liquid, its volume average is also called superficial velocity.

Definition 2.1.4 *Intrinsic volume-averaged quantity* $\langle\psi_\alpha\rangle^{\alpha}$. With respect to the phase α it is defined as:

$$\langle\psi_\alpha\rangle^{\alpha}=\frac{1}{\Delta V_\alpha}\int_{\Delta V}\psi(x,t)\chi_\alpha(x,t)\,dv=\frac{\Delta V}{\Delta V_\alpha}\langle\psi_\alpha\rangle=\frac{\langle\psi_\alpha\rangle}{g_\alpha} \tag{2-10}$$

The relation between the average value and the intrinsic average value of ψ is as follows:

$$\langle\psi_\alpha\rangle=\langle\psi_\alpha\rangle^{\alpha}g_\alpha \tag{2-11}$$

Theorem 2.1.1 *Temporal derivative of* ψ. The relationship between the average of the time derivative and the time derivative of the average is given by:

$$\left\langle \frac{\partial \psi_\alpha}{\partial t} \right\rangle = \frac{\partial \langle \psi_\alpha \rangle}{\partial t} - \frac{1}{\Delta V} \int_{\partial\Omega^{\alpha/\beta}} \psi_\alpha \mathbf{w}^{\alpha/\beta} \cdot \mathbf{n}^{\alpha/\beta} dA \tag{2-12}$$

where A_α is the interfacial area between the phase α with other phases, $\mathbf{n}$ is the outward unit normal of the infinitesimal element of area dA, and $\mathbf{w}$ is the velocity of the microscopic interface.

Theorem 2.1.2 *Spatial derivative of* ψ. The relationship between the average of the spatial derivative and the spatial derivative of the average is given by:

$$\langle \nabla \psi_\alpha \rangle = \nabla \langle \psi_\alpha \rangle + \frac{1}{\Delta V} \int_{\partial\Omega^{\alpha/\beta}} \psi_\alpha \mathbf{n}^{\alpha/\beta} dA \tag{2-13}$$

Now let us deduce the macroscopic mass conservation equation for the solidification system by using the definitions and the theorems. Consider the following microscopic mass conservation equation (2-14) for the liquid phase:

$$\frac{\partial \rho_l}{\partial t} + \nabla \cdot (\rho_l \mathbf{v}_l) = 0 \tag{2-14}$$

where $\mathbf{v}_l$ is the microscopic velocity of the liquid. Multiplying by $\chi_l / \Delta V$ and integrate over ΔV yields:

$$\frac{1}{\Delta V} \int_{\Delta V} \frac{\partial \rho_l}{\partial t} \chi_l dv + \frac{1}{\Delta V} \int_{\Delta V} \nabla \cdot (\rho_l \mathbf{v}_l) \chi_l dv = 0 \tag{2-15}$$

Applying Theorem 2.1.1 to the first term in equation (2-15) and Theorem 2.1.2 to the second term, leads to:

$$\frac{\partial \langle \rho_l \rangle}{\partial t} + \nabla \cdot \langle \rho_l \mathbf{v}_l \rangle = \Gamma_l \tag{2-16}$$

$$\text{with } \Gamma_l = -\frac{1}{\Delta V} \int_{A_l} \rho_l (\mathbf{v}_l - \mathbf{w}^{l/s}) \cdot \mathbf{n}^{l/s} dA \tag{2-17}$$

Similarly, we can deduce the macroscopic mass conservation equation for the solid phase, and obtain:

$$\frac{\partial \langle \rho_s \rangle}{\partial t} + \nabla \cdot \langle \rho_s \mathbf{v}_s \rangle = \Gamma_s \tag{2-18}$$

$$\text{with } \Gamma_s = -\frac{1}{\Delta V} \int_{A_s} \rho_s (\mathbf{v}_s - \mathbf{w}^{s/l}) \cdot \mathbf{n}^{s/l} dA \tag{2-19}$$

In the equations (2-16)-(2-19), the terms Γ_k ($k = l, s$, solid and liquid respectively) represent the interfacial transfer associated with phase change (solidification or melting). Note that in the case of a two-phase solidification system, we have $\partial\Omega^{s/l} = \partial\Omega^{l/s}$, $\mathbf{w}^{s/l} = \mathbf{w}^{l/s}$, $\mathbf{n}^{s/l} = -\mathbf{n}^{l/s}$ and mass gained by the solid equals to the mass lost by the liquid, consequently, $\Gamma_s = -\Gamma_l$. Adding equations (2-16) and (2-18), we get:

$$\frac{\partial\left[\langle\rho_l\rangle+\langle\rho_s\rangle\right]}{\partial t}+\nabla\cdot\left[\langle\rho_l\mathbf{v}_l\rangle+\langle\rho_s\mathbf{v}_s\rangle\right]=0 \qquad (2\text{-}20)$$

We define the average density $\langle\rho\rangle$ and the average momentum $\langle\rho\mathbf{v}\rangle$ for the liquid and solid mixture as follows:

$$\langle\rho\rangle=\langle\rho_l\rangle+\langle\rho_s\rangle \qquad (2\text{-}21)$$

$$\langle\rho\mathbf{v}\rangle=\langle\rho_l\mathbf{v}_l\rangle+\langle\rho_s\mathbf{v}_s\rangle \qquad (2\text{-}22)$$

Then, equation (2-20) can be written as:

$$\frac{\partial\langle\rho\rangle}{\partial t}+\nabla\cdot\langle\rho\mathbf{v}\rangle=0 \qquad (2\text{-}23)$$

In the case of stationary solid phase, and if the densities of the solid and liquid are equal and constant. Equation (2-20) can be written as:

$$\nabla\cdot\langle\mathbf{v}_l\rangle=0 \qquad (2\text{-}24)$$

In the same way one can deduce the macroscopic conservation equations of momentum, energy and solute, these equations will be presented in the next chapters.

Continuum or volume averaged models provide useful tools to simulate the macroscopic transport phenomena during solidification. These models have been applied to prediction of macrosegregation in steel ingots (Vannier [1995], Gu and Beckermann [1999]); however, the numerical predictions show only quantitative agreement with experimental results. In particular, the fact that equiaxed solidification and grain transport has been neglected explains that such models fail in the prediction of negative macrosegregation in the bottom of large ingot.

Recently, considerable progresses have been made to account for nucleation, grain growth, the movement of both liquid and solid phases and coupling microsegregation. Combeau *et al.*[1998] and Beckermann [2000] have summarized these models.

2.1.3 Modeling of solidification with mesh adaptation

As it has been discussed, macrosegregation arises from micro and macroscopic solidification and transport phenomena. Using the volume averaged model, one can predict fluid flow and associated transport phenomena at the scale of a casting system. However, computation on a coarse mesh yields low accurate prediction. For example, generally the mesh size used for ingots is of the order of centimeter. It is then impossible to capture the fluid flow in the segregated channels. The width of A-segregated channels can be at a scale of about one millimeter (Combeau *et al*. [1998]). In order to increase the computational accuracy, the mesh adaptation is needed.

Based on the averaged model, Kämpfer [2002] has proposed an adaptive domain decomposition method to predict macrosegregation. The overall computational domain is discretized using a coarse mesh, on which the energy conservation equation is solved. According to the temperature and solid fraction obtained, the mushy, solid and liquid zones are determined. The critical zone for macrosegregation is the narrow region near the liquidus, where the velocity of liquid and the concentration gradient are quite different from zero, as shown in Figure 2-4 (a) and (b). The critical zone is discretized using a much finer mesh as shown in Figure 2-4 (c). Then, the fluid flow and solute transport equations are solved on the different meshes. An iterative procedure is performed to couple the resolutions on the two meshes and match the boundary condition, as shown in Figure 2-4 (c) and (d).

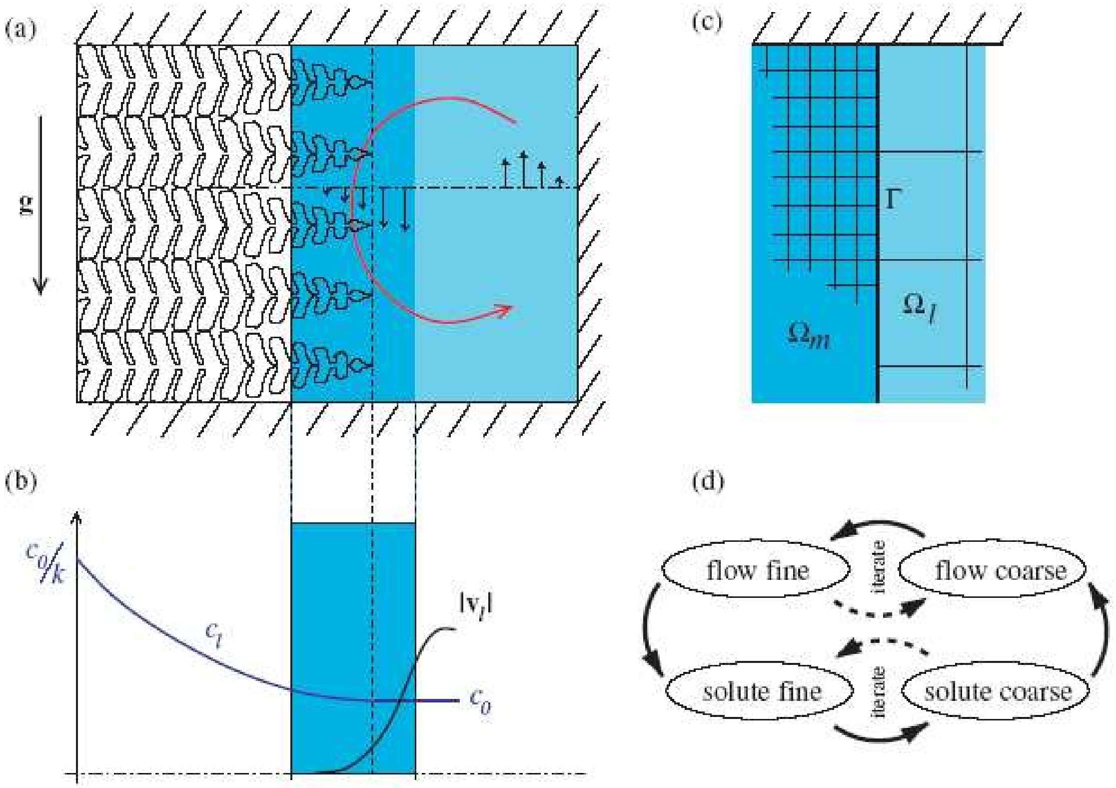

Figure 2-4 The critical regions during columnar solidification processes with respect to buoyancy driven flow and the associated solute profile in the liquid, from Kämpfer [2002]. (a) distinguished zones of solid, mushy and liquid; (b) profiles of liquid concentration and velocity of liquid; (c) a coarse mesh in the domain of bulk liquid Ω_l, and a much finer mesh in the critical region Ω_m; (d) iterative procedures

In Kämpfer [2002] work, the energy equation is solved only on the coarse mesh. The reason is that the thermal diffusion is sufficiently large and the temperature field is quite smooth, so that the resolution on the coarse mesh can be considered to be a good approximation. The energy and solute equations are solved by the streamline upwinding Petrov-Galerkin (SUPG) approach, while the momentum equation is solved by the Galerkin least squares (GLS) approach.

The refinement of the mesh is achieved by subdividing the coarse parent element (the level of mesh refining is controlled by the user) as shown in Figure 2-4 (c). This results in non-conforming meshes in the two regions. A special mortar method is used to match the boundary conditions at the interface between the two regions. This method assures the continuity of the field and its normal derivative through the iterative procedure.

The efficiency of this domain decomposition method has been validated. Figure 2-5 shows the velocity field and the map of macrosegregation, predicting the formation of freckles. We can see that a freckle is captured on the finer mesh.

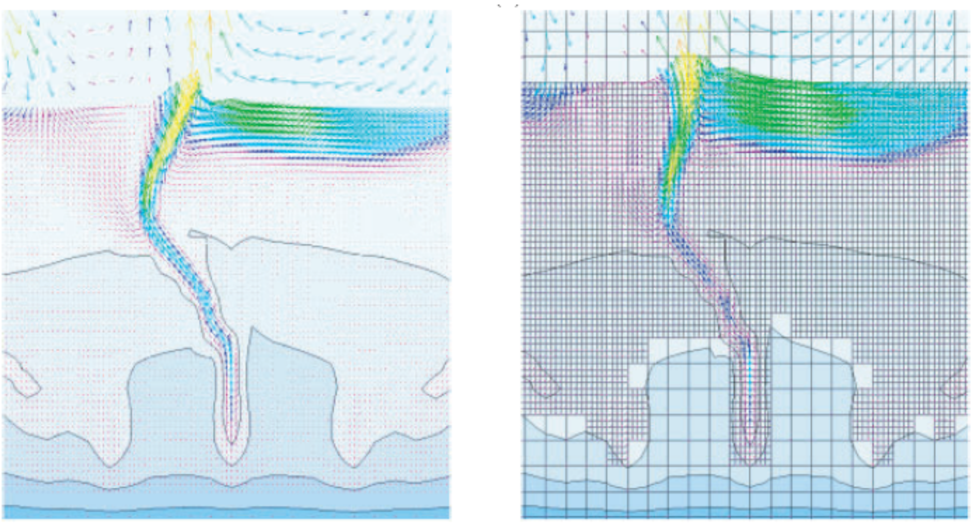

Figure 2-5 Prediction of freckles in unidirectional solidification with mesh adaptation, Kämpfer [2002]

Mencinger [2004] has proposed another mesh adaptation method for the melting process of pure metal with the natural convection. The single-domain model is used which does not require the tracking of the solidification front. In order to enhance the precision, an adaptive structured grid is adopted. The grid density is controlled by a user-defined function. For instance, the function can depend on the normal of the gradient of enthalpy or the step-function with the 'step' at the mold walls. Fine grids near the solidification front and the boundary of cavity are obtained by solving the user-defined function with partial differential equations (Laplace operator). However, the method appears to be limited to structured mesh. The melting process is modeled by solving enthalpy and momentum equations on the structured adaptive mesh. Figure 2- 6 shows an example of the adaptive mesh.

Remarks

Although the averaged single-domain model can simulate the macroscopic solidification using a fixed mesh, the adaptive mesh is also needed to improve the numerical results. Following Kämpfer's work, we have proposed a method for computing macrosegregation with mesh adaptation. Unlike Kämpfer's work, an adapted single conforming mesh is generated, without boundary between the fine and coarse regions. Resolutions for averaged conservation equations of energy, solute and momentum are carried out on the whole domain and the iterative procedure to couple fields in the mushy zone and bulk liquid zone is not needed. Concurrently, the use of unstructured adapted meshes makes the method more general than the one developed by Mencinger.

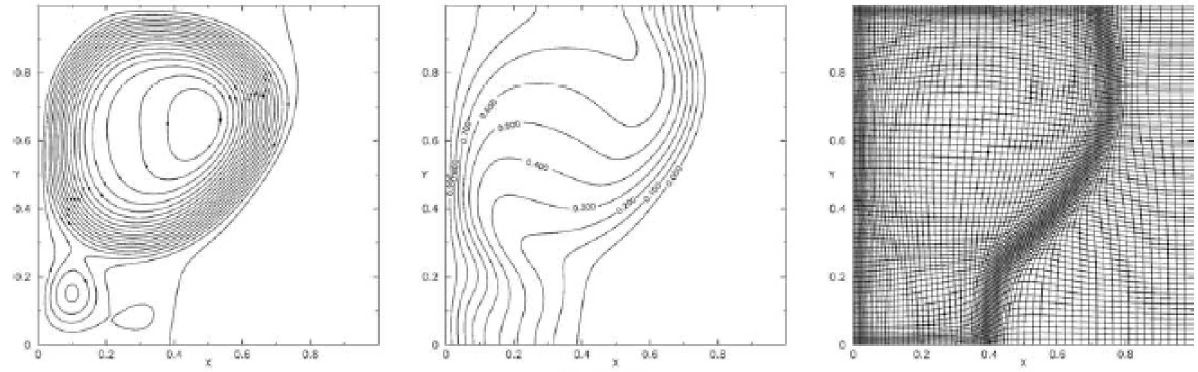

Figure 2- 6 An example of mesh adaptation, Mencinger [2004]: streamlines, temperature field and grid

2.2 Solid deformation and pipe formation

Pipe shrinkage results from the volume change of solidification, as well as contraction in the liquid and solid phases. Risers are designed to compensate the volume contractions. Modeling of pipe is important for ingots and large castings, because in these cases one should pay attention to the size and shape of risers. In order to predict the pipe, we need to consider the fluid flow with free surface. In addition, thermal contraction and dilation induce the deformations in the solidifying casting and the mold, and consequently affect the heat exchange at the interface. Heat transfer with fluid flow and thermal mechanics are actually coupled. Numerical simulation of such a complicated problem is characterized by the arts to treat the free surface of liquid and deformation in solid.

Hereunder, we review models of pipe formation. Firstly, the general methods to treat free surface in the fluid mechanical models are presented. Secondly, an approach to the coupled resolution of fluid flow and deformation in solid is introduced.

2.2.1 Fluid mechanical models

Roch *et al*. [1991] proposed a simple method to compute the free surface in the solidification of an ingot. As shown in Figure 2-7, the feeding is considered as perfect: at each time increment, the incremental shrinkage volume is assigned to the pipe formation and the liquid feeding cannot be interrupted by an excessive pressure drop arising from a too low permeability of the mushy zone. The volume change ΔV at each time step can be calculated as follows:

$$\Delta V = \int_{t1}^{t2} (\Delta \varepsilon^{tr} \dot{g}_s dt + 3\alpha(T(t))\dot{T})dt \qquad (2\text{-}25)$$

where $\Delta \varepsilon^{tr}$ is the ratio of volume variation due to solidification, $\dot{g}_s$ the change rate of solid volume fraction, $\alpha(T(t))$ the coefficient of the linear thermal expansion depended on the temperature, $\dot{T}$ the temperature rate.

Then, the descent level of liquid is determined by equation (2-26).

$$\Delta h = \frac{\Delta V}{S} \tag{2-26}$$

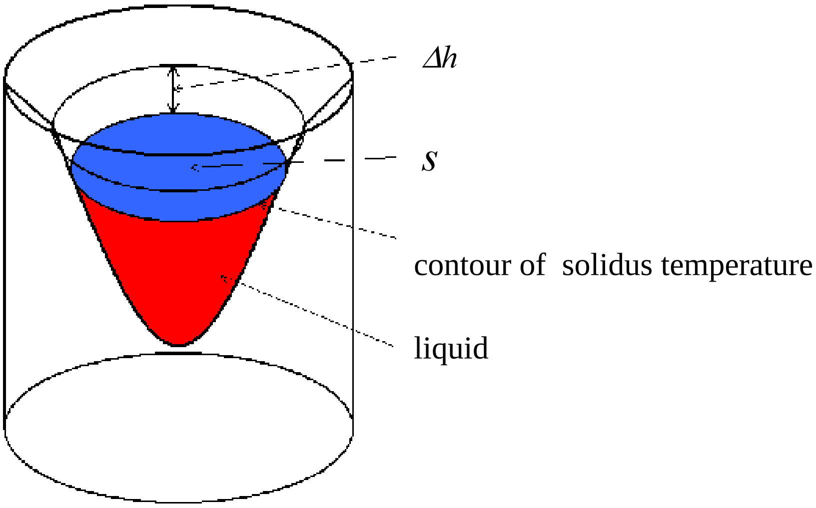

Figure 2-7 Schematic of the pipe

This approach is easy to carry out and effective. But if there are two or more risers in the casting system, how to assign the incremental shrinkage volume ΔV to the different risers? This would need specific additional rules to be calculated. Another problem is that the sum of local volume contraction is entirely assigned to pipe growth, which is not true. Solid contraction occurring in the solidified zone contributes to the air gap between the casting and mold, but not to the pipe.

Chiang and Tsai [1992A,1992B] firstly used the continuum mixture model to simulate shrinkage-induced fluid flow and natural convection in alloy solidification. A rectangular cavity with a riser located on the top is considered. The cavity is cooled at the bottom surface, while all of the other surfaces are adiabatic. The solidification process is modeled on a fix and regular grid. The free surface at the top of riser is assumed to be flat due to thermal condition, and the movement is one-dimensional. In fact, this model is not able to predict the shape of pipe shrinkage because of special treatment of free surface.

Kim and Ro [1993] reported an approach to model the solidification of pure metal ingots. The general conservation equations of heat, mass and momentum are solved. The coordinate transformation ($x=x(\eta,\xi,t)$ and $y=y(\eta,\xi,t)$) is used to handle the moving domains of liquid and solid. The downward velocity of the free surface is determined from the mass conservation over the liquid phase. However, the method can not be used for alloy ingots.

Based on the classical mixture theory, Barkhudarov *et al.*[1993] used a single set of conservation equations to model the fluid flow during solidification. The VOF algorithm is used to treat the free surface problem. In VOF algorithm, a function F is equal to zero in the void regions and to unity in the regions occupied by the fluid. The governing equation for the VOF is:

$$\frac{dF}{dt} = \frac{\partial F}{\partial t} + (\nabla F)\cdot\vec{V} = 0 \tag{2-27}$$

in order to take into account solidification shrinkage, a source term S_s is added into the equation (2-27), and the equation is expressed as:

$$\frac{\partial F}{\partial t}+(\nabla F)\cdot\vec{V}=-S_{sl} \tag{2-28}$$

$$S_{sl}=\frac{1}{V_0}\frac{\Delta M_{sl}}{\Delta t}(\frac{1}{\rho_l}-\frac{1}{\rho_s}) \tag{2-29}$$

where V_0 is the total cell volume open to the fluid, ΔM_{sl} is the liquid mass solidified in the cell over time Δt, ρ_s and ρ_l are the densities of the liquid and solid phases respectively.

The solidification process of an aluminum sand casting has been modeled. Figure 2-8 shows the shrinkage cavity forming at the top of casting. We can see the fluid flow induced by the shrinkage and the pipe formation.

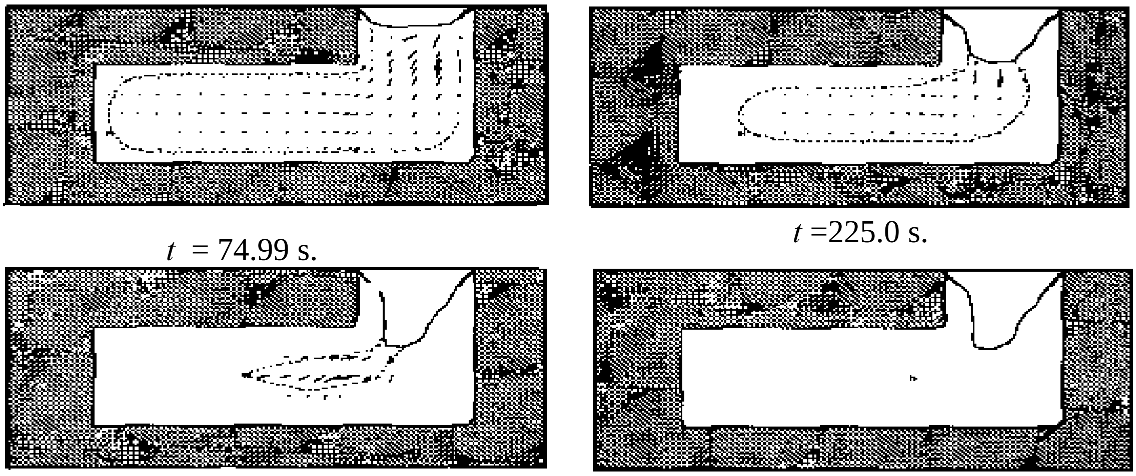

t = 74.99 s.

t =225.0 s.

t =350.0 s.

t = 400.0 s.

Figure 2-8 Results of the shrinkage formation.The dashed line constitutes the solidification front and short straight-lines represent the feeding velocities, Barkhudarov *et al.* [1993]

Ehlen *et al.* [2000] adopted a similar approach to treat the free surface as Barkhudarov *et al.* [1993]. A set of averaged conservation equations is used to predict the pipe formation and macrosegregation. A cylinder Al7wt%Si ingot (H=107mm, R=40mm) has been cast in the cast iron chill mold to validate the model. Figure 2-9(a) and (b) show the distribution of computed temperature and solid fraction after 30 s and 80s respectively. The free surface has been fully developed at 80s, the calculated shape is in good agreement with the experimental result as shown in Figure 2-9(c).

Considering the shrinkage induced fluid flow, Ehlen *et al.* [2000] has predicted the inverse segregation. In the condition of dendritic growth, a high solute concentration exists in the interdendritic liquid. This liquid is drawn toward the dendrite stalks on the cooling face by solidification shrinkage, leading to high solute concentration at the outer region of the casting. This is known as inverse segregation, which is opposite to normal solute concentration distribution: low concentration at the outer region and high concentration at the center.

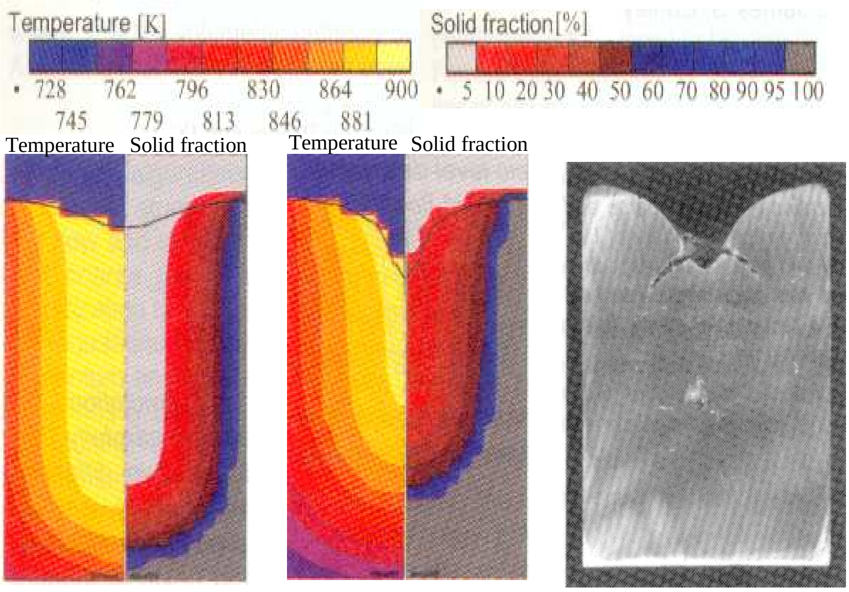

(a) time =30 s (b) time = 80 s (c) experiment

Figure 2-9 Results of the shrinkage cavity formation, Ehlen *et al*. [2000]

Naterer [1997] proposed a control-volume based finite-element method to simulate the solidification shrinkage. The continuum mixture model is used. The governing equations are discretized linear quadrilateral elements. The free surface is handled by the adapted mesh through coordinate transformation, avoiding the classical problem of numerical diffusion in VOF algorithm.

2.2.2 A thermal mechanical model

For predicting the pipe formation, the models based on fluid flow as mentioned above do not consider the air gap associated with the solid deformation. Bellet *et al.* [2004] have developed a thermal mechanical model to predict pipe formation, coupling fluid flow and deformation in solid. The main idea has been presented in section 1.4, and the model has been implemented in the code THERCAST®. By comparing with other methods, this approach has the advantage of taking into account the deformation of the whole casting.

The unilateral contact condition is applied to the boundary between mold and casting. The contact is treated by the penalty method. This allows calculating the gap between mold and casting. The ALE scheme is used to compute the fluid flow in liquid pool and mushy zone, this allows tracking the free surface.

The thermal mechanical model has been applied to simulate solidification process of a large part. The part is characteristic by its size (2.5×7.0×1.0 m), weight (125 tons) and chemical composition (close to pure iron). Using symmetry conditions, only half of the casting has been calculated. The average mesh size of the part is approximately 0.10 m. The pipe shapes computed at 2 h, 28 h and 55 h are shown in Figure 2- 10 as well as the distribution of liquid fraction. The final shapes between calculation and measurement show a reasonable agreement.

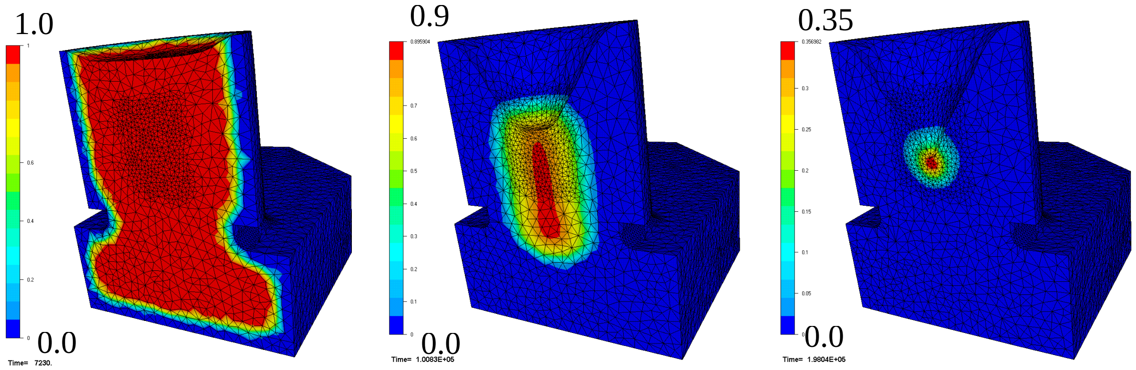

time = 2 h time = 28 h time = 55 h

Figure 2- 10 Evolution of pipe shrinkage, with liquid fraction distribution

To summarise, the thermal mechanical approach to the prediction of pipe formation is very encouraging:

- modelling of the fluid flow driven by difference of density and solidification shrinkage in liquid and mushy zones, and the deformation of solidifying part simultaneously;
- the influence of the part deformation on the pipe formation has been taken into account.
- Proper tracking of the free surface.

It is one of our tasks to implement such model in R2SOL.

Chapter 3

Modeling of macrosegregation

Modélisation de la macroségrégation – Résumé en français

Ce chapitre constitue une des contributions principales et est consacré à la présentation du modèle développé. Les hypothèses adoptées ainsi que les principales équations sont tout d'abord exposées. Les différentes stratégies de résolution sont ensuite discutées : couplage faible ou fort lors de la résolution incrémentale des différentes équations, résolution en système fermé ou ouvert de la conservation des solutés, ce dernier point étant en continuité par rapport aux travaux de Vannier et Combeau dans le logiciel de volumes finis SOLID.

Dans le cadre de l'approche fortement couplée en système ouvert, le modèle de microségrégation considéré est la règle des leviers, en système ouvert, et la formation d'un eutectique est prise en compte. Des itérations sont alors effectuées à chaque incrément de temps, de manière à résoudre de manière consistante les différentes équations de conservation et à satisfaire le modèle de microségrégation.

En approche non couplée, la solidification est considérée localement en système fermé, c'est-à-dire que la relation entre fraction de liquide et température est fixée en fonction de la concentration locale en début de solidification. Dans ce cadre, le modèle de Scheil peut également être utilisé, en plus des leviers. Les détails des modèles numériques et les stratégies de résolution sont présentées en section 3.1 et 3.2. La résolution des équations des modèles de microségrégation est exposée en section 3.4.

Pour la résolution du problème thermique, les méthodes SUPG et d'« upwind » nodal ont été implantées dans le logiciel R2SOL. Par ailleurs, cette résolution a été rendue plus robuste d'une part par la programmation d'une méthode de recherche linéaire, facilitant la convergence de la méthode de Newton-Raphson, et d'autre part par l'utilisation de la méthode dite « cond-split » préalablement développée au Cemef. Le solveur thermique est présenté à la section 3.3. La resolution du transport de soluté utilise la même formulation SUPG et est détaillée en section 3.5.

En ce qui concerne la résolution du problème de mécanique des fluides (section 3.6), le solveur pré-existant utilisant des éléments P1+/P1 a été étendu aux écoulements axisymétriques, ce qui a nécessité des développements particuliers pour les termes d'inertie et de perméabilité. Une formulation P1/P1 stabilisée par moindres carrés a également été utilisée et est présentée.

La section 3.7 est consacrée aux différents tests ayant servi à la validation de ces différentes formulations.

Chapter 3

Modeling of macrosegregation

The present chapter is dedicated to the modeling of macrosegregation in columnar dendritic solidification. Firstly, in section 3.1 we present the hypotheses and averaged conservation equations for energy, solute, mass and momentum. The resolution strategy and computational organization in the two-dimensional finite element code R2SOL are introduced in section 3.2.

Then, we focus on the resolution of energy, solute and momentum equations in sections 3.3 to 3.6. Followed, the validation tests will be presented in section 3.7.

For clarity, we omit the averaging notation $\langle\cdot\rangle$ that has been used in section 2.1.2.3. For example, we note simply **V** for the average velocity in liquid instead of $\langle \mathbf{v}_l \rangle$.

3.1 Governing equations

3.1.1 Hypotheses

The analysis of fluid flow, temperature and solute distribution for the solidification system is based on the following hypotheses:

- The liquid flow is laminar, Newtonian, with a constant viscosity μ, and the solid phase is fixed and non deformable. The mixture is saturated, *i.e.*, $g_s+g_l=1$, with g_s denoting the volumic solid fraction and g_l the liquid one.
- The analysis is restricted to a binary alloy.
- The mushy region is modeled as an isotropic porous medium whose permeability K is defined by the Carman-Kozeny formula as follows:

$$\mathrm{K} = \lambda_2{}^2 g_l{}^3 (1-g_l)^{-2}/180 \tag{3-1}$$

  where λ_2 is the secondary dendrite arm spacing.

- The solid and liquid densities are equal and constant, $\rho_l=\rho_s=\rho_0$, except in the buoyancy term of the momentum equation where density depends on the temperature T and the solute mass concentration in liquid w_l according to the following linear approximation:

$$\rho=\rho_0(1-\beta_T(T-T_{ref})-\beta_w(w_l-w_{ref})) \tag{3-2}$$

  where: $\beta_T=-\dfrac{1}{\rho}\left(\dfrac{\partial\rho}{\partial T}\right)_p$ is the thermal expansion coefficient;

  $\beta_w=-\dfrac{1}{\rho}\left(\dfrac{\partial\rho}{\partial w_l}\right)_p$ is the solutal expansion coefficient;

T_{ref} and w_{ref} are the reference temperature and reference mass concentration respectively, at which the liquid density takes its value ρ_0.

- Thermodynamic equilibrium exists at the liquid-solid interface, *i.e.*, at the interface we have:

$$T^* = T_s = T_l \tag{3-3}$$

$$\text{and} \quad w_s^* = k w_l^* \tag{3-4}$$

where T_s and T_l are the temperatures for the solid and liquid, respectively. w_s and w_l are the mass concentrations for the solid and liquid respectively. The superscript * indicates the interface value.

Moreover, within an elementary representative volume, we assume that the temperature is homogeneous, *i.e.*, $T = T_s = T_l$, because the thermal diffusion is sufficiently large.

- Furthermore, in order to simplify the treatment of the phase diagram of the binary alloy system, the liquidus and solidus are approximated by straight lines. For example, Figure 3-1 shows the equilibrium phase diagram for the Pb-Sn system. In the mushy state for the hypo-eutectic part of the diagram (that is a weight percentage of Sn less than 61.9%), we have the following relations:

$$T = T_f + m w_l^* \tag{3-5}$$

$$\frac{w_s^*}{w_l^*} = k = \text{constant} \tag{3-6}$$

where T_f is the melt temperature of pure Pb; *k* partition coefficient (<1); *m* liquidus slope (<0);

Above 61.9% Sn, similar relations can be written with T_f melt temperature of pure tin and w the weight percentage of lead.

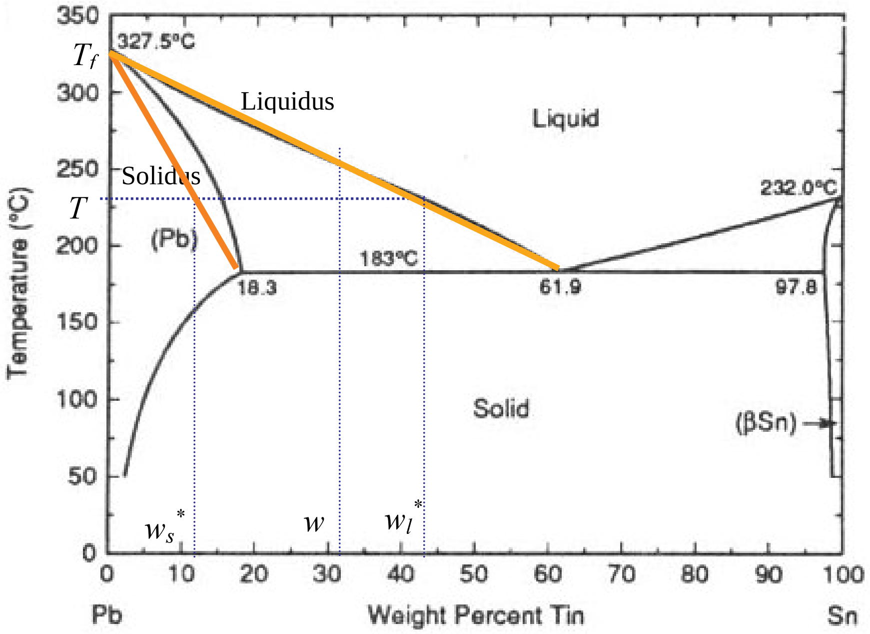

Figure 3-1 The equilibrium phase diagram for the Pb-Sn alloy

3.1.2 Conservation equations

- **Mass conservation**

Assuming that the solid and liquid densities are equal and constant, the mass conservation equation gives:

$$\nabla \cdot \mathbf{V} = 0 \tag{3-7}$$

where $\mathbf{V}$ is the average liquid velocity (the solid is fixed). For the details of derivation procedure one can refer to section 2.1.2.3.

- **Momentum conservation**

Following the work of Ganesan and Poirier [1990], with the hypotheses stated in section 3.1.1, one can deduce the averaged momentum conservation equation for the liquid phase as follows:

$$\rho_0 \frac{\partial \mathbf{V}}{\partial t} + \frac{\rho_0}{g_l} \nabla \cdot (\mathbf{V} \times \mathbf{V}) = \nabla \cdot (\mu \nabla \mathbf{V}) - g_l \nabla p + g_l \rho\, \mathbf{g} - \frac{\mu}{\mathrm{K}} g_l \mathbf{V} \tag{3-8}$$

where p is the intrinsic pressure in liquid and $\mathbf{g}$ the gravity vector.

The permeability K tends towards infinity in the pure liquid region, and then equation (3-8) is reduced to the Navier-Stokes equation. In the region where the liquid fraction is lower, the permeability tends to zero and the last term in equation becomes dominant, while inertia and rheological terms vanish, yielding the Darcy's relation (2-5).

- **Solute conservation**

Redistribution of solute at the macroscopic scale is governed by the equation:

$$\frac{\partial w}{\partial t} + \mathbf{V} \cdot \nabla w_l - \nabla \cdot (\varepsilon \nabla w_l) = 0 \tag{3-9}$$

where ε is a diffusion coefficient: $\varepsilon = D_l g_l$, where D_l denotes the diffusion coefficient in the liquid phase. Usually the diffusion term is negligible, and one can take an arbitrarily small value ε for the numerical stability.

- **Energy conservation**

The energy equation can be written in an enthalpy form as follows:

$$\rho_0 \left(\frac{\partial H}{\partial t} + \nabla H_l \cdot \mathbf{V} \right) - \nabla \cdot (\lambda \nabla T) = 0 \tag{3-10}$$

where λ is the average thermal conductivity; H is the volume averaged specific enthalpy; H_l is the volume averaged specific enthalpy in the liquid phase.

Assuming that the specific heat for the solid is equal to the one for the liquid, being c_p, and denoting L the latent heat of fusion per unit of mass, we have the following relations:

The volume averaged specific enthalpy of the solid H_s:

$$H_s = \int_{T_0}^{T} c_p d\tau \tag{3-11}$$

The volume averaged enthalpy of the liquid H_l:

$$H_l = \int_{T_0}^{T} c_p d\tau + L \tag{3-12}$$

The volume averaged enthalpy H for the mushy metal:

$$H = g_l H_l + (1 - g_l) H_s = \int_{T_0}^{T} c_p \, d\tau + g_l L \tag{3-13}$$

In the case of a given constant specific heat c_p and taking the reference temperature $T_0 = 0$, the definitions of the volume averaged enthalpies of the solid, liquid and mushy metal can be rewritten as follows:

$$H_s = c_p T \qquad \text{for the solid} \tag{3-14}$$

$$H_l = c_p T + L \qquad \text{for the liquid} \tag{3-15}$$

$$H = c_p T + g_l L \qquad \text{for the mushy metal} \tag{3-16}$$

With these assumption, the energy equation can be rewritten as:

$$\rho_0 \left(\frac{\partial H}{\partial t} + c_p \nabla T \cdot \mathbf{V} \right) - \nabla \cdot (\lambda \nabla T) = 0 \tag{3-17}$$

3.2 Resolution strategy

3.2.1 Coupling the equations

Before detailing the resolution for the conservation equations of energy, solute, and momentum, we briefly present the resolution strategy. This strategy is the same as that used in the finite volume code SOLID (Vannier [1995]).

There are two unknown variables in the energy equation (3-17). The average enthalpy H is chosen as the primary unknown. In order to eliminate the temperature T, T is considered as a function of H, and is computed by the approximation of the first order of Taylor's expansion:

$$T = T^* + (\frac{\partial T}{\partial H})^* (H - H^*) \tag{3-18}$$

In the liquid and solid states, we have $\frac{\partial T}{\partial H} = \frac{1}{c_p}$. In the mushy state, $\frac{\partial T}{\partial H}$ is determined by the local thermal equilibrium for the mushy metal accounting for the latent heat release. Since the latent heat release depends on the microsegregation models, heat release during solidification makes the energy equation highly non-linear. Therefore, a Newton-Raphson method is used to solve for the primary unknown H. When a converged solution for H is obtained, the temperature T and the liquid fraction g_l can be deduced from the relations (3-5), (3-13) and the local microsegregation model, for instance the lever rule model. This will be explained in section 3.4.

In the solute transport equation (3-9), there are also two unknown variables, the average mass concentration w, and average mass concentration in liquid w_l. To solve the solute transport equation one can choose either w or w_l as the primary unknown. The relationship between w and w_l is also depending on the microsegregation model.

The mixed velocity-pressure P1+/P1 formulation is used to solve the weak form of the momentum equation (3-8) together with a weak form of the mass conservation equation (3-7). In the momentum equation, the temperature T and average solute mass concentration in liquid w_l appear in the buoyancy term. The permeability K appearing in the Darcy term is a function of the liquid fraction g_l. T, w_l and g_l rely on the resolution of heat and solute equations. On the other hand, the liquid movement affects the heat and solute transport. Thus, the resolution of momentum, energy and solute equations are coupled.

The general organization of the computational resolution is illustrated in Figure 3-2. In each time step, energy, solute and momentum equations are solved in this order. Two approaches, named *no-coupling* and *full-coupling*, have been implemented in R2SOL.

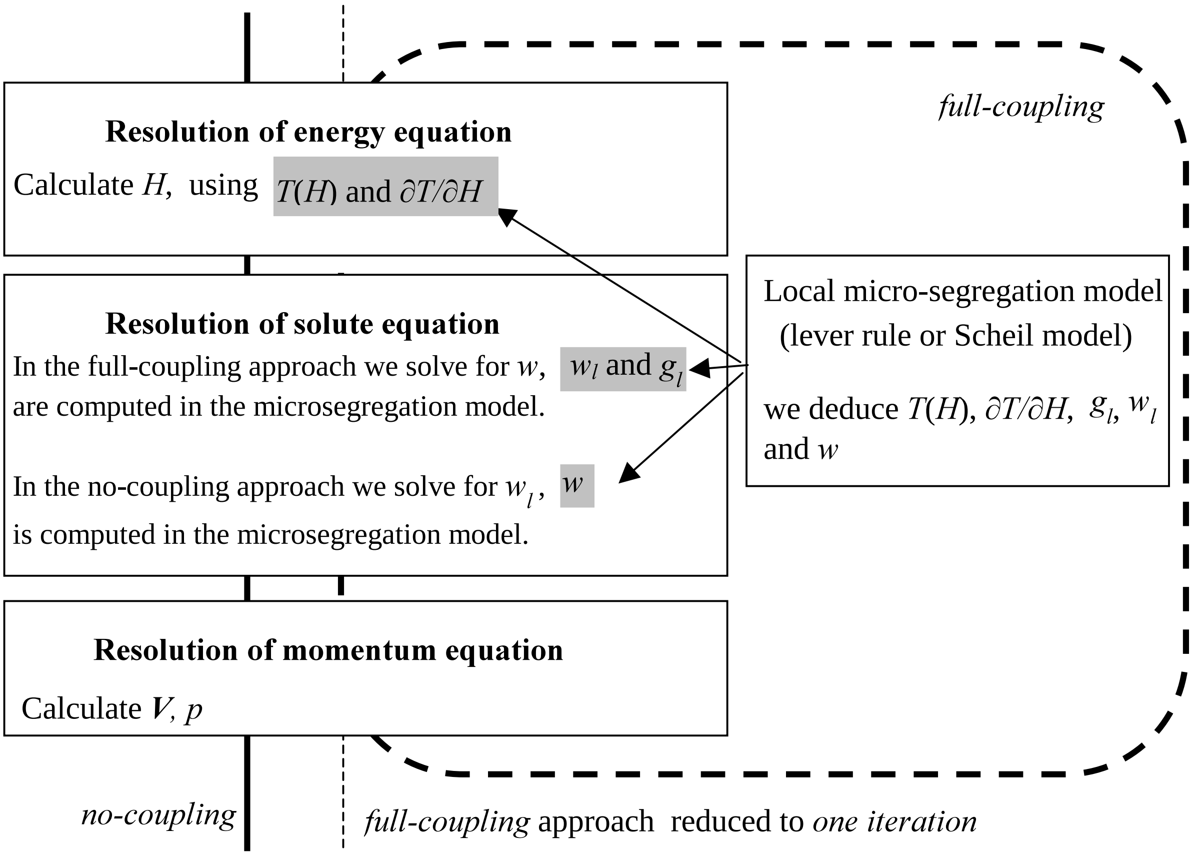

Figure 3-2 Resolution strategies to predict macrosegregation

In the *no-coupling* approach, we locally fix the solidification path in the resolution of energy equation. *i.e*., the liquidus temperature and solidus temperature are locally fixed according to: 1) the initial nominal concentration; 2) the local solute concentration just before solidification, which allows to take into account the solute enrichment in the liquid pool. The details will be presented in section 3.3. In the *no-coupling* approach, within each time step we solve the equations of energy, solute and momentum, without any iteration to get consistent fields of temperature, solute concentration and velocity. Actually, as the solidification path is locally fixed in the mushy zone, the resolution of solute transport equation is not coupled with the resolution of energy equation. The solidification in the mushy zone is treated as a closed system. After solving the energy equation we get the new fields of liquid fraction g_l and temperature T. Those new values are used in the resolution of the solute equation.

In the full-*coupling* approach, the solidification of a binary alloy in the whole casting is considered using an open approach. After resolution of energy and solute equations, we have a consistent set of variables: the enthalpy H, the temperature T, the liquid fraction g_l, and the average concentration w, which satisfy the local thermal equilibrium with the lever rule. Iterations can be performed within each time increment to give converged consistent resolutions that satisfy the three governing equations. This type of resolution is called *fully coupled resolution*. Since the computational cost of the *fully coupled resolution* may be expensive, one can solve the three governing equations with only one iteration in each time step (*full-coupling*, reduced to *one iteration*).

3.2.2 The finite element solver

In convection dominated problems, it is well known that spurious oscillations may appear in the finite element resolution of the advection-diffusion equations, when they are discretized by the standard Galerkin method (Rappaz *et al*. [2002]). In order to overcome this numerical difficulty, an explicit nodal upwind method has been used so far to treat advection terms in R2SOL (Gaston [1999]). This method consists of computing the upstream trajectory of the material particles. Following the previous work, the nodal upwind method has been used in the present work, and some improvements in the solvers for the energy and momentum equations will be detailed in the sections 3.3 and 3.6 respectively.

Alternately, the Streamline-Upwind/Petrov-Galerkin (SUPG) method introduced by Hughes and Brooks [1979] can be considered as a successful stabilization technique to prevent oscillations in the convection dominated problems. The first step to develop the streamline upwind methods has been achieved by introducing some artificial diffusion in the streamline direction, using a modified test function for the advection term only. The modified test function gives more weight to the upwind nodes. This leads to the so-called SU (streamline upwind) method. Then, the stabilized test functions have been applied to all terms of the weak form, not only the advection term. This leads to the consistent formulation of the finite element method, named SUPG. Thereby, the SUPG method is often used for the advection-diffusion problems. A good review of the SUPG stabilization approaches can be found in Fries *et al*. [2004].

In the resolution of momentum equations, besides the advection problem, instability arises from the selection of interpolation functions for velocity and pressure (Rappaz *et al*. [2002]). Historically, these problems have been solved using the P1+/P1 formulation in R2SOL, which will be presented in section 3.6.

For the incompressible Navier-Stokes equations, the SUPG and PSPG (Pressure-Stabilizing/Petrov-Galerkin) stabilized methods have been proposed by Tezduyar *et al*. ([1992], Tezduyar and Osawa [2000]. Comparing the treatment of incompressibility constraint in the mixed P1+/P1 formulation, PSPG scheme is an alternative stabilized method. The stabilization is guaranteed by the additional term which consists of a perturbation $\tau \mathbf{V} \cdot \nabla N$ multiplied with the residual of the momentum equation, τ being the stabilization parameter, and N being the interpolation function for the pressure. It should be mentioned that in the PSPG formulation one can use an equal-order interpolation function for the velocity and pressure fields.

More recently as a first attempt, we have implemented the SUPG formulation for the energy equation and, in collaboration with Victor Fachinotti and Michel Bellet, the SUPG-PSPG formulation for the momentum equations. The new development has been used to simulate the formation of macrosegregation. The new method will be presented after the old one.

3.3 Resolution of the energy equation

The thermal analysis of the solidification process of a casting is performed using the energy conservation equation (3-10) with the following boundary and initial conditions:

$$T = T_{imp} \qquad \text{on} \quad \partial\Omega_{\mathrm{T}} \tag{3-19}$$

$$-\lambda \nabla T \cdot \mathbf{n} = \phi_{imp} \qquad \text{on} \quad \partial\Omega_{\mathrm{q}} \tag{3-20}$$

$$-\lambda \nabla T \cdot \mathbf{n} = h(T - T_{ext}) \qquad \text{on} \quad \partial\Omega_{\mathrm{c}} \tag{3-21}$$

$$T = T_{\mathrm{init}} \qquad \text{at} \quad t = 0 \tag{3-22}$$

Where: $\partial\Omega_{\mathrm{T}}$ is the boundary of the domain Ω occupied by the casting on which the temperature T_{imp} is imposed;

$\partial\Omega_{\mathrm{q}}$ is the boundary on which the outward heat flux ϕ_{imp} is imposed;

$\partial\Omega_{\mathrm{c}}$ is the boundary on which the heat exchange is defined by the heat exchange coefficient h with the external temperature T_{ext};

T_{init} is the initial temperature.

A nodal upwind and a SUPG method are used. Firstly, we present the nodal upwind method following Gaston's work [1999]. Then, the new solver based on the SUPG method is detailed. Further, we present improvements resulting from our personal contribution regarding convergence and treatment of thermal shocks.

3.3.1 Resolution with the nodal upwind method

3.3.1.1 Time discretization

The enthalpy of the liquid phase, is a function of time and space. Its derivative, following the liquid particles at the average velocity **V**, can be expressed as:

$$\frac{d_{<l>}H}{dt} = \frac{\partial H_l}{\partial t} + \nabla H_l \cdot \mathbf{V} \tag{3-23}$$

Then, the energy equation (3-10) can be rewritten as:

$$\rho_0\left(\frac{\partial H}{\partial t}+\frac{d_{<l>}H}{dt}-\frac{\partial H_l}{\partial t}\right)-\nabla\cdot(\lambda\nabla T)=0 \tag{3-24}$$

Let $H_l^{t-\Delta t}$ be the liquid enthalpy at point *x*, but at the previous time step; $\tilde{H}_l^{t-\Delta t}$ the liquid enthalpy at time $t-\Delta t$ of the particle which, at time *t*, is at the same position *x*. The total and partial derivatives of the liquid enthalpy are approximated by the following implicit finite difference expressions:

$$\frac{d_{<l>}H}{dt}\approx\frac{1}{\Delta t}(H_l^t-\tilde{H}_l^{t-\Delta t}) \tag{3-25}$$

$$\frac{\partial H_l}{\partial t}\approx\frac{1}{\Delta t}(H_l^t-H_l^{t-\Delta t}) \tag{3-26}$$

For simplicity, the superscript 0 is used instead of $t-\Delta t$ for any quantity, and the superscript t is omitted for the quantity at time t. Substituting equations (3-25) and (3-26) into equation (3-24), one can write the energy equation in semi-discretized form:

$$\rho_0\left(\frac{H-H^0}{\Delta t}+\frac{H_l^0-\tilde{H}_l^0}{\Delta t}\right)-\nabla\cdot(\lambda\nabla T)=0 \tag{3-27}$$

Remark

The particle value of a scalar quantity at time $t-\Delta t$ is computed by an upwind transport approach that will be discussed in the section 6.2.4.

3.3.1.2 Spatial discretization

The computational domain is decomposed into triangle elements. The P1 linear interpolation functions N are used. The standard Galerkin method is applied to equation (3-27), leading to:

$$R(H,T)=[\mathbf{M}]\{H\}+[\mathbf{K}]\{T\}-[\mathbf{M}]\{H^0\}-[\mathbf{M}]\,\{\tilde{H}_l^0-H_l^0\}-\{F\}=0 \tag{3-28}$$

with:

$$[\mathbf{M}]_{ij}=\frac{\rho_0}{\Delta t}\int_\Omega N_iN_j\,d\Omega \tag{3-29}$$

$$[\mathbf{K}]_{ij}=\int_\Omega\lambda\nabla N_i\cdot\nabla N_j\,d\Omega+\int_{\partial\Omega_c}hN_iN_j\,d\Gamma \tag{3-30}$$

$$\{F\}_i=\int_{\partial\Omega_q}-\phi_{imp}N_i\,d\Gamma+\int_{\partial\Omega_c}hT_{ext}N_i\,d\Gamma \tag{3-31}$$

The enthalpy H is chosen as the primary unknown; the temperature T is treated as the first order Taylor's expansion (3-18). The discretized equation (3-28) then becomes:

$$\left([\mathbf{M}]+[\mathbf{K}][\frac{\partial\mathbf{T}}{\partial\mathbf{H}}]^*\right)\{H\}=[\mathbf{M}]\{H^0\}-[\mathbf{K}]\left(\{T^*\}-[\frac{\partial\mathbf{T}}{\partial\mathbf{H}}]^*\{H^*\}\right)+[\mathbf{M}]\,\{\tilde{H}_l^0-H_l^0\}+\{F\} \tag{3-32}$$

Where T^* and H^* are intermediate temperature and averaged enthalpy respectively in the Newton-Raphson iterations. $\left[\frac{\partial \mathbf{T}}{\partial \mathbf{H}}\right]^*$ is a diagonal matrix computed by the intermediate value of H^*.

In the old version of R2SOL, the diagonal terms in $\left[\frac{\partial \mathbf{T}}{\partial \mathbf{H}}\right]^*$ are averaged using the values of three nodes in the triangle element. The enthalpy H is obtained directly by solving equation (3-32) through an iterative procedure.

Now, we have re-written the equation (3-32) in the standard form of Newton-Raphson, denoting *n* the iteration number:

$$[\frac{\partial \mathbf{R}}{\partial \mathbf{H}}]^{(n)}\{\delta H\} = -\mathbf{R}(H^{(n)}, T^{(n)}) \tag{3-33}$$

$$\begin{aligned}\left([\mathbf{M}] + [\mathbf{K}][\frac{\partial \mathbf{T}}{\partial \mathbf{H}}]^{(n)}\right)\{\delta H\} &= [\mathbf{M}]\{H^0 - H^{(n)}\} - [\mathbf{K}]\{T^{(n)}\} + [\mathbf{M}]\ \{\tilde{H}_l^0 - H_l^0\} + \{F\} \\ &= -R(H^{(n)}, T^{(n)})\end{aligned} \tag{3-34}$$

This time, the variation in enthalpy δH is calculated in each iteration, and then the enthalpy and the temperature are updated as follows:

$$H^{(n+1)} = H^{(n)} + \eta\, \delta H \quad \text{with} \quad 0 < \eta \leq 1 \tag{3-35}$$

$$T^{(n+1)} = T(H^{(n+1)}) \tag{3-36}$$

where η is a coefficient determined by a linear search method (Saleeb *et al.* [1998]), which will be presented in section 3.3.3.

Remarks:

- The energy equation is highly non-linear due to the solidification. Although the convergence rate of Newton-Raphson method is quadratic, the resolution becomes difficult when the trial solution is far from the solution. The linear search method is then used to control the increment of enthalpy and to improve convergence.
- The matrix $[\frac{\partial \mathbf{T}}{\partial \mathbf{H}}]$ is diagonal. The values of the diagonal terms are not identical due to the solidification. Thus, the stiffness matrix in equation (3-33) is non-symmetric. In the previous version of R2SOL, the average value of $\frac{\partial T}{\partial H}$ in each triangle element was used to generate a symmetric stiffness matrix, $\left[\frac{\partial \mathbf{T}}{\partial \mathbf{H}}\right] = \left(\frac{\partial T}{\partial H}\right)^e \mathbf{I}$. But this strategy may lead to non-convergence. In this work, we preferred to form the non-symmetric stiffness matrix. The PETSC (Portable Extensible Toolkit for Scientific Computation) solver, instead of the old linear equation solver in R2SOL, has also been implemented to solve the non-symmetric equation (3-33). The details of PETSC solver can be found in the web site (PETSC [2003]).

- As we know, the value of $\frac{\partial T}{\partial H}$ is zero when eutectic transformation occurs. In the old version of R2SOL and in SOLID, $\frac{\partial T}{\partial H}$ takes a small value, e.g. $\frac{\partial T}{\partial H}=\frac{1}{10c_p}$, during the eutectic transformation. Now we prefer to take the true value, $\frac{\partial T}{\partial H}=0$, in the case of eutectic transformation, the convergence resolution is achieved easily.

3.3.2 Resolution with the SUPG method

In the context of the finite element method, the general weak form of the energy equation (3-17) can be expressed as follows:

$$\forall\varphi \quad \int_\Omega \varphi\left[\rho_0\left(\frac{\partial H}{\partial t}+c_p\nabla T\cdot\mathbf{V}\right)-\nabla\cdot(\lambda\nabla T)\right]\mathrm{d}\Omega=0 \tag{3-37}$$

where φ is the test function.

In the classical Galerkin method (Szabó and Babuška [1991], Rappaz *et al.* [2002]), the test function is selected identical to the interpolation function of the solution approximation, *i.e.*, $\varphi=N$. For the convection-dominated problem, the Galerkin method suffers from spurious oscillations and may not be used in practice. Therefore, the SUPG test function is used, *i.e.*,$\varphi=\tilde{N}=N+\tau\mathbf{V}\cdot\nabla N$, where τ is the stabilization parameter and will be detailed soon in the following text. The weak form of energy equation can be then expressed by:

$$\forall N \quad \int_\Omega \tilde{N}\left[\rho_0\left(\frac{\partial H}{\partial t}+c_p\nabla T\cdot\mathbf{V}\right)-\nabla\cdot(\lambda\nabla T)\right]\mathrm{d}\Omega=0 \tag{3-38}$$

Equation (3-38) can be expanded as follows:

$$\forall N \quad \int_\Omega \tilde{N}\,\rho_0\frac{\partial H}{\partial t}\,d\Omega+\int_\Omega \tilde{N}\,\rho_0 c_p\nabla T\cdot\mathbf{V}d\Omega-\int_\Omega N\,\nabla\cdot(\lambda\nabla T)\,d\Omega-\int_\Omega \tau\mathbf{V}\cdot\nabla N\,\nabla\cdot(\lambda\nabla T)\,d\Omega=0 \tag{3-39}$$

Applying the Green's theorem to the third term in equation (3-39) and using the boundary conditions (3-20) and (3-21), one obtains:

$$\begin{aligned}\forall N \quad &\int_\Omega \tilde{N}\,\rho_0\frac{\partial H}{\partial t}\,d\Omega+\int_\Omega \tilde{N}\,\rho_0 c_p\nabla T\cdot\mathbf{V}d\Omega+\int_\Omega\lambda\nabla T\cdot\nabla N\,d\Omega\\ &+\int_{\partial\Omega_q} N\,\phi_{imp}d\Gamma+\int_{\partial\Omega_c} N\,h(T-T_{ext})\,d\Gamma-\int_\Omega \tau\mathbf{V}\cdot\nabla N\left[\nabla\cdot(\lambda\nabla T)\right]d\Omega=0\end{aligned} \tag{3-40}$$

Re-arranging the terms in equation (3-40), yields:

$$\begin{aligned}\forall N \quad &\int_\Omega N\,\rho_0\frac{\partial H}{\partial t}\,d\Omega+\int_\Omega N\,\rho_0 c_p\nabla T\cdot\mathbf{V}d\Omega+\int_\Omega\lambda\nabla T\cdot\nabla N\,d\Omega\\ &+\int_{\partial\Omega_q} N\,\phi_{imp}d\Gamma+\int_{\partial\Omega_c} N\,h(T-T_{ext})\,d\Gamma\\ &+\int_\Omega \tau\mathbf{V}\cdot\nabla N\left[\rho_0\frac{\partial H}{\partial t}+\rho_0 c_p\nabla T\cdot\mathbf{V}-\nabla\cdot(\lambda\nabla T)\right]d\Omega=0\end{aligned} \tag{3-41}$$

Following Tezduyar and Osawa [2000], the last integration in equation (3-41) presents the stabilization term which consists of a perturbation $\tau \mathbf{V}\cdot\nabla N$ multiplied by the residual of energy equation. Later, this stabilized strategy will be used again in the SUPG-PSPG formulation for the momentum equations. In the case of linear elements, the stabilized diffusion term vanishes, leading to:

$$\begin{aligned}\forall N \quad & \int_{\Omega} N\,\rho_0 \frac{\partial H}{\partial t}\,d\Omega + \int_{\Omega} N\,\rho_0 c_p \nabla T\cdot\mathbf{V}d\Omega + \int_{\Omega}\lambda\nabla T\cdot\nabla N\,d\Omega \\ & + \int_{\partial\Omega_q} N\,\phi_{imp}d\Gamma + \int_{\partial\Omega_c} N\,h(T - T_{ext})\,d\Gamma \\ & + \int_{\Omega}\tau\mathbf{V}\cdot\nabla N\left[\rho_0\frac{\partial H}{\partial t} + \rho_0 c_p\nabla T\cdot\mathbf{V}\right]d\Omega = 0\end{aligned} \tag{3-42}$$

In order to discretize equation (3-42), now we apply the implicit scheme to the time derivative term. Integrating each term over the computational domain, we then have:

$$R(H,T) = \left[\mathbf{M}_{\text{sup}g}\right]\{H\} + \left[\mathbf{A}_{\text{sup}g}\right]\{T\} + [\mathbf{K}]\{T\} - \left[\mathbf{M}_{\text{sup}g}\right]\{H^0\} - \{F\} = 0 \tag{3-43}$$

with:

$$\begin{aligned}[\mathbf{M}_{\text{sup}g}]_{ij} &= \int_{\Omega}\frac{\rho_0}{\Delta t}(N_i + \tau\mathbf{V}\cdot\nabla N_i)N_j\,d\Omega \\ [\mathbf{A}_{\text{sup}g}]_{ij} &= \int_{\Omega}\rho_0 c_p\,(N_i + \tau\mathbf{V}\cdot\nabla N_i)\nabla N_j\cdot\mathbf{V}d\Omega \\ [\mathbf{K}]_{ij} &= \int_{\Omega}\lambda\nabla N_i\cdot\nabla N_j\,d\Omega + \int_{\partial\Omega_c} hN_iN_j\,d\Gamma \\ \{F\}_i &= \int_{\partial\Omega_q} -\phi_{imp}N_i\,d\Gamma + \int_{\partial\Omega_c} hT_{ext}N_i\,d\Gamma\end{aligned}$$

$\{H^0\}$is the vector of nodal enthalpies at previous time step. The stabilized SUPG test function is defined by (Hughes and Brooks [1979], Zienkiewicz and Taylor [1989]):

$$\varphi_i = \tilde{N}_i = N_i + \frac{\theta\,h}{2}\left(\frac{V_k}{\|\mathbf{V}\|}\right)_{\text{e}}\frac{\partial N_i}{\partial x_k} \tag{3-44}$$

where $\left(\dfrac{V_k}{\|\mathbf{V}\|}\right)_e$ denotes the unit velocity vector, estimated at the center of the element. θ is an upwind parameter, which can be optimized as a function of the mesh Peclet number Pe_h (Zienkiewicz and Taylor [1989]):

$$\theta = \coth\frac{Pe_h}{2} - \frac{2}{Pe_h} \tag{3-45}$$

The mesh Peclet number is defined as: $Pe_h = \dfrac{\|\mathbf{V}\|\cdot h}{\alpha}$. h is the characteristic length of a triangle element e in the direction of velocity vector, being approximated by (Tezduyar *et al.* [1992]):

$$h = 2\,\|\mathbf{V}\|\,(\sum_{a=1}^{3}\mathbf{V}\cdot\nabla N_a)^{-1} \tag{3-46}$$

where N_a is the interpolation function associated with node a and $\|\mathbf{V}\|$ is the norm of the average velocity vector. $\alpha = \lambda/(\rho_0\, c_p)$, being the thermal diffusivity.

Like in the nodal upwind resolution in section 3.3.1, the enthalpy H is chosen as the primary unknown, the temperature T is treated using its first order Taylor's expansion. Newton-Raphson method is used to solve the non-linear equation. Then the iterative resolution scheme can be written as follows:

$$\left(\left[\mathbf{M}_{\sup g}\right] + \left(\left[\mathbf{A}_{\sup g}\right] + [\mathbf{K}] \right) \left[\frac{\partial \mathbf{T}}{\partial \mathbf{H}}\right]^{(n)} \right) \{\delta H\} = -R(H^{(n)}, T^{(n)})$$

$$= -\left[\mathbf{M}_{\sup g}\right]\left\{H^{(n)} - H^0\right\} - \left(\left[\mathbf{A}_{\sup g}\right] + [\mathbf{K}] \right) \left\{T^{(n)}\right\} + \{F\} \qquad (3\text{-}47)$$

and $H^{(n+1)} = H^{(n)} + \eta\, \delta H$ with $0 < \eta \le 1$

As can be seen by comparing equation (3-34) with (3-47), to implement the SUPG formulation in R2SOL, we have just created a new module to compute the stiffness matrix and the residual at the element level. The organization of the code for solving the non-linear energy equation remains the same. For this reason, in the following text we focus on the nodal upwind method to discuss our improvement for the energy solver.

3.3.3 Improvement of convergence

- *Presentation of problems*

Because of the high non-linearity of the energy equation, the Newton-Raphson method may not converge if the starting point is far from the desired resolution even when using a non-symmetric consistent matrix, as mentioned above. In order to secure the convergence, we have rewritten the Newton-Raphson resolution with a line search scheme. The concept of the line search is to minimize the total potential energy, that is the work done by the unbalanced residual force due to the solution increment (Crisfield [1982]).

- *A line search scheme*

Newton-Raphson scheme for solving the energy equation has been given by equations from (3-33) to (3-36). With the line search scheme, the enthalpy H is updated by $H^{(n+1)} = H^{(n)} + \eta\, \delta H$. The value of η being different from the standard value 1 used in the standard method.

For the line search method, a suitable value of the scalar η must be found, such that the "work" done $s(\eta)$ by the unbalanced residual vector R^{n+1} in the direction of δH vanishes, that is to say:

$$s(\eta) = R(H^{(n)} + \eta \delta H) \cdot \delta H = 0 \qquad (3\text{-}48)$$

In the above equation, δH results from equation (3-33). Of course, it is not realistic to find the value of η that satisfies the condition of equation (3-48), *i.e.*, $R^{(n+1)} \equiv 0$ is achieved. For practical purpose, we try to find the value of η, such that the potential energy decreases:

$$\left| \frac{s(\eta)}{s(\eta=0)} \right| \le \beta_{tol} \qquad (3\text{-}49)$$

where β_{tol} is the line search tolerance, typically $\beta_{tol} = 0.8$ (Crisfield [1982]).

We define two inner products, s_0 and s_1, representing the bounds for the searching iterations.

$$s_0 = s(\eta = 0) \ = R^{(n)} \cdot \delta H \tag{3-50}$$

$$s_1 = s(\eta = 1) \ = R^{(+1)} \cdot \delta H \tag{3-51}$$

Following the work of Saleeb *et al.* [1998], the line search scheme is carried out to find the value of η between 0 and 1. Figure 3-3 and Figure 3-4 show four possibilities. But the case most frequently encountered is that shown in Figure 3-3, that is the case of $s_0 \cdot s_1 < 0$, indicating there exists a suitable value of η, such that the condition of equation (3-48) can be met. In the figures '0' denotes the point $s_0 = s(\eta = 0)$ and '1' denotes the point $s_1 = s(\eta = 1)$, the two points '0' and '1' are corresponding to the bounds for line search. As shown in Figure 3-3, the point '2' (denotes the point $\frac{s_2}{s_0}$) is found by using η_2, η_2 is computed by the interpolation using the values of the point '0' and the point '1'. The successive values η_i are then estimated according to the "secant" method that we have also used to solve some equations in our microsegregation models (see section 3.4.2).

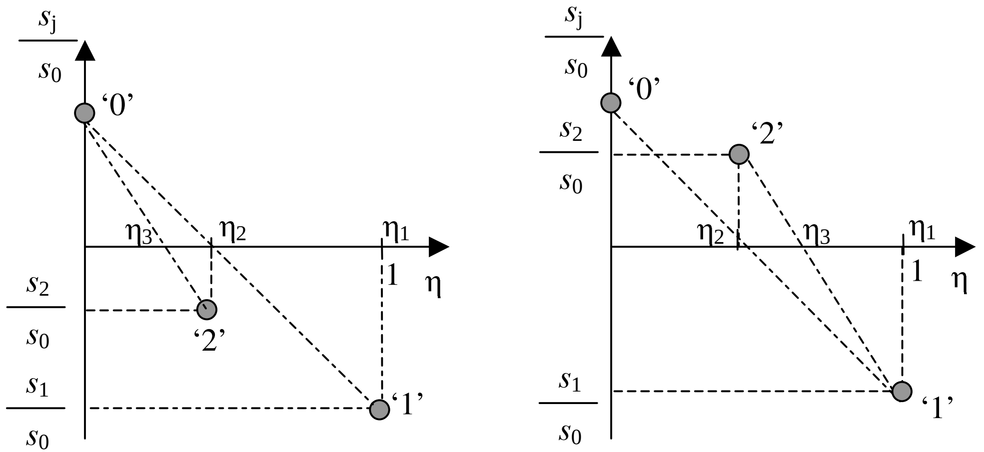

a) b)

Figure 3-3 Schematic for the interpolation

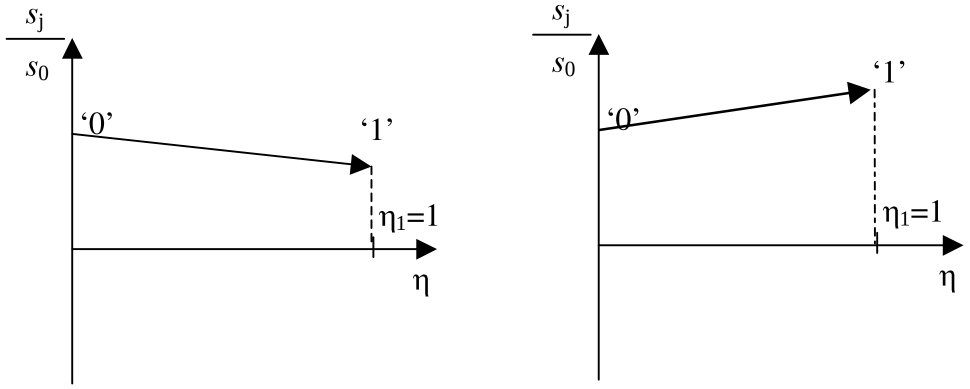

a) b)

Figure 3-4 Schematic for the extrapolation

Figure 3-4 shows the cases of extrapolation. Extrapolation could result in a very large value of η, leading to an excessive number of iterations or divergence. In the present work, a relaxation formulation is used to update the new value as follows:

$$H^{(n+1)} = H^{(n)} + 0.85\,\delta H \tag{3-52}$$

- *Convergence criterion for Newton-Raphson iterations*

The criterion to terminate Newton-Raphson iterations is as follows:

$$\left|\frac{H^{(n+1)} - H^{(n)}}{H^{(n)}}\right| \leq \varepsilon_{thermal}^{\text{tolerance}} \tag{3-53}$$

In equation (3-53), the condition denotes that the relative variation of enthalpy for each node is smaller than the prescribed tolerance value of $\varepsilon_{thermal}^{tolerance}$. For the solidification problem, the tolerance value of $\varepsilon_{thermal}^{tolerance}$ is in the range of $10^{-6} - 10^{-5}$.

3.3.4 Treatment of thermal shock

3.3.4.1 Presentation

Thermal shock, *i.e.*, the occurrence of steep thermal gradients near the boundaries, often appears in the modeling of solidification of casting. It causes temperature time and space-oscillations in the numerical resolution using the standard Galerkin finite element method with linear interpolation function (Menaï [1995]). The temperature oscillations lead to wrong solutions that do not satisfy the maximum principle (local extrema occur inside the domain). For the thermal mechanical analysis, the problem can be serious in some cases, as the material behavior is temperature and history dependent.

In practice, the following methods have been used to avoid spurious oscillations in heat conduction analysis.

- Adopt a sufficiently large time step, say Δt_{ts}, to satisfy the penetration depth condition (Menaï [1995]):

$$\Delta t_{ts} = \frac{1}{4}\,\frac{\rho c_p}{\lambda}\,\Delta x^2 \tag{3-54}$$

Where ρ, c_p and λ are the density, specific heat and thermal conductivity respectively. Δx is the mesh size in the first layer of elements near the boundary.

- Lump the capacity matrix, the off-diagonal terms being summed on the diagonal. The modified capacity matrix is then:

$$[\mathbf{M}]_{ij}^{L} = \delta_{ij} \sum_{k=1}^{3} [\mathbf{M}]_{ik} \tag{3-55}$$

Where δ_{ij} is the Kronecker delta, $\delta_{ij}=1$ if $i = j, \delta_{ij} = 0$ otherwise. It has been proved that "lumped capacity" in FEM is equivalent to FVM in the 2-dimensional problems (Rappaz *et al.* [2002]).

- Apply the so-called "Taylor Galerkin Discontinuous" (TGD) method (Pichelin [1998]). P0 elements are adopted, *i.e.*, the temperature within an element is constant. In the early work, we have used the explicit TGD approach to calculate the temperature at element level, then the temperature at each node is computed by a smoothing technique. However, the temperature field is not satisfying for the computation of macrosegregation (Liu [2003]).
- Based on the matrix theory (Ortega [1970]): an **M**-matrix (a real, non-singular $n\times n$ matrix **A** is an **M-**matrix if $\mathbf{A}^{-1}\geq 0$ and all its off-diagonal components are non-positive) satisfies the positive transmissibility condition, which guarantees to obtain the maximum/minimum of the solution only at the initial time or at the boundary. Putti and Cordes [1998], using 2-dimensional Delaunay meshes, has demonstrated that the linear Galerkin approach to the Laplace operator (the diffusion term) results in an **M**-matrix (the diffusion matrix). Further, by lumping the capacity matrix, the stiffness matrix (being the sum of the diffusion and capacity matrix) for a transient heat conduction problem becomes an **M**-matrix.
- At Cemef Fachinotti and Bellet[2004] proposed a so called "diffusion-split" method to overcome the difficulty in modeling of solidification with THERCAST®. This method has been implemented in R2SOL, and it is presented in the following text.

3.3.4.2 Diffusion-split method

For simplicity, let us consider the heat equation without phase change, with boundary conditions (3-20) and (3-21):

$$\rho_0\, c_p \frac{dT}{dt} - \nabla\cdot(\lambda\nabla T) = 0 \tag{3-56}$$

Applying the standard Galerkin method and the fully implicit scheme, the heat equation can be discretized as follows:

$$[\mathbf{M}]\frac{\{T\}-\{T^0\}}{\Delta t}+[\mathbf{K}]\{T\}-\{F\}=0 \tag{3-57}$$

where $[\mathbf{M}]$, $[\mathbf{K}]$and $\{F\}$are the heat capacity matrix, conductive matrix and thermal load vector respectively, and they have been already defined in equations (3-29), (3-30) and (3-31). $\{T\}$and$\{T^0\}$are the temperature vectors at time t and time $t-\Delta t$ respectively.

Recognizing that the thermal shock problems are associated with the stiffness matrix (Putti and Cordes [1998]), Fachinotti and Bellet [2004] proposed a method based on the splitting of the diffusion term, in order to improve the conductive matrix as follows:

$$[\mathbf{M}]\frac{\{T\}-\{T^0\}}{\Delta t}+[\mathbf{K}^*]\{T\}-\{F\}=\{S\} \tag{3-58}$$

Where

$$\{S\}=\left([\mathbf{K}^*]-[\mathbf{K}]\right)\{T^*\} \tag{3-59}$$

$$[\mathbf{K}^*]_{ij}=\int_\Omega \lambda^*\,\nabla N_i\cdot\nabla N_j\, d\Omega+\int_{\partial\Omega_c} hN_iN_j\, d\Gamma \tag{3-60}$$

$\{S\}$ as an explicit source term appears in equation (3-58). An augmented conductivity λ^* is defined to satisfy the penetration depth condition for Δt :

$$\lambda^* = \begin{cases} \lambda & \text{if} \quad \Delta t_{ts} \leq \Delta t \\ \\ \lambda \dfrac{\Delta t_{ts}}{\Delta t} & \text{if} \quad \Delta t_{ts} > \Delta t \end{cases} \tag{3-61}$$

The value of λ^* decreases linearly with time from the value given by equation (3-61) at $t=0$ to the real conductivity value λ when $t \geq \Delta t_{ts}$. The time step Δt_{ts} can be determined by equation (3-54) at the beginning of simulation.

Regarding the explicit source term $\{S\}$ that consists of a known temperature, T^0 at time $t-\Delta t$ can be used as an approximation, leading to:

$$\{S\} \approx \left([\mathbf{K}^*] - [\mathbf{K}] \right) \{T^0\} \tag{3-62}$$

It is interesting to note that during the early stages of the simulation, there is no sensible variation of the temperature outside the regions submitted to thermal shocks, and hence the approximation implied by equation (3-58) is local and temporary.

Also, it should be noted that a priori determination of the time step Δt_{ts} for a solidification problem might be more complicated. In this case, an effective heat capacity ρc_p^{eff} accounting for the latent heat release, instead of ρc_p , should be used in equation (3-54). In fact, for an element undergoing phase change, ρc_p is considerably greater than ρc_p , and it also varies greatly with time. Hence, Δt_{ts} should be determined at each time step until the thermal shock effects completely disappear. This makes it very difficult to estimate Δt_{ts} during the computation.

Fortunately, the thermal shock has a relative short-term effect, it disappears since the thermal diffusion has been developed in a few time steps. For a solidification problem, provided that the initial temperature is not too close to the liquidus temperature (*i.e.*, solidification does not occur during the first time steps of computation), the thermal shock can be controlled before the beginning of solidification. Hence, the determination of λ^* remains valid in this case.

In R2SOL, following the work of Victor Fachinotti, we rewrite equation (3-28) as:

$$[\mathbf{M}]\{H\} + [\mathbf{K}^*]\{T\} = [\mathbf{M}]\{H^0\} + [\mathbf{M}]\,\{\tilde{H}_l^0 - H_l^0\} + \{F\} + [\mathbf{K}_{add}]\{T^0\} \tag{3-63}$$

with

$$[\mathbf{K}^*]_{ij} = \int_\Omega \lambda^* \nabla N_i \cdot \nabla N_j d\Omega + \int_{\partial\Omega_c} h N_i N_j d\Gamma \tag{3-64}$$

$$[\mathbf{K}_{add}]_{ij} = \int_\Omega (\lambda^* - \lambda) \nabla N_i \cdot \nabla N_j d\Omega \tag{3-65}$$

In equation (3-63), $\mathbf{K}^*$ is the modified diffusion matrix, in which the conductivity λ^* has been augmented according to equations (3-54) and (3-61). The last right hand side term in equation (3-63) accounts for the additional splitting source term. The resolution is performed in the usual manner, by the Newton-Raphson method.

The solidification processes of a 3.3 ton steel ingot with insulated top surface have been simulated by R2SOL, using 1) the linear P1 elements (the standard Galerkin method with the diffusion split method); 2) the P0 elements (the explicit TGD method). Pure heat conduction with phase change, without fluid flow, is considered in the thermal analysis. The geometric and physical data of the ingot and the mold can be found in Appendix A. The computational results are shown in Figure 3-5. Figure 3-5 a) shows the temperature distribution in the ingot after 2 hours. The temperature field obtained by the TGD method is shown on the left hand, the result of the standard Galerkin method is shown on the right hand. The temperature profiles obtained at 15 s, 10 min, 1 hour, 2 hours and 6 hours, along a horizontal section at the height of 900 mm from the bottom of mold, are shown in Figure 3-5 b). The temperature fields obtained by the two methods are quite close, being free from temperature fluctuations.

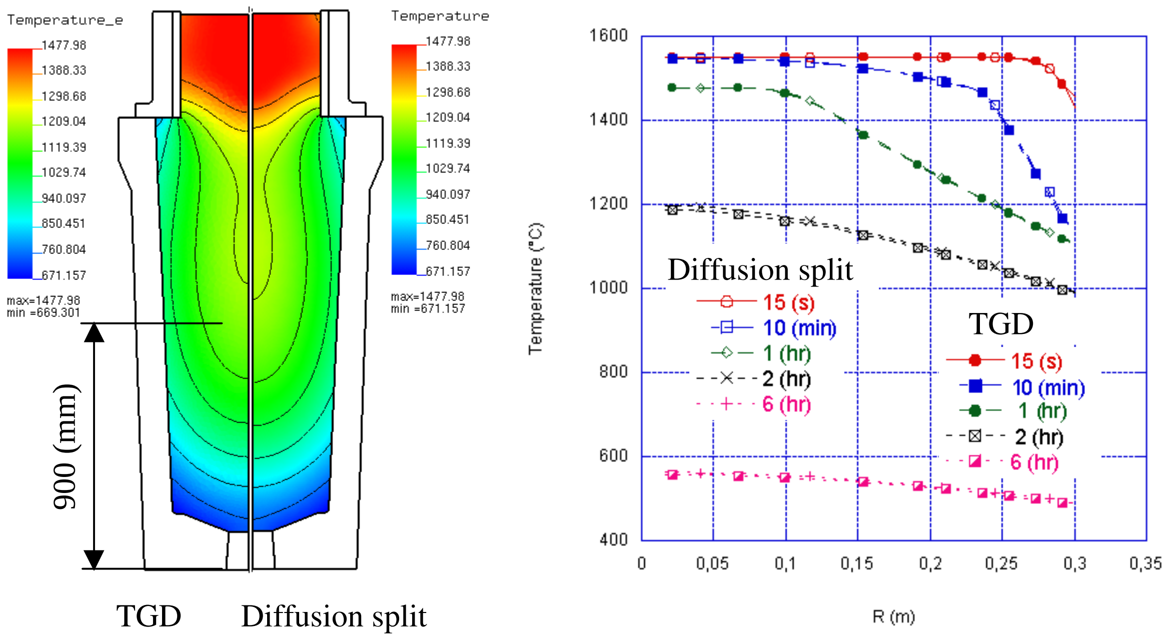

a) temperature in the ingot after 2 hours solidification

b) temperature profiles at different times

Figure 3-5 Comparison of the diffusion split method with the TGD method

To summarize the section 3.3, we would conclude that the energy equation is solved by an enthalpy scheme. In the nodal upwind approach, the equation is discretized spatially by the standard Galerkin method, and a fully implicit scheme is used for the temporal discretization. The convection term in the energy equation is treated by a nodal upwind scheme.

The new solver based on the SUPG formulation have been implemented in R2SOL.

The problem of thermal shock has been solved by the “diffusion-split” method.

Regarding the highly non-linear solidification problem, we have improved the Newton-Raphson method with a line search scheme. The PETSC solver has been implemented to solve the non-symmetric matrix equation. These improvements lead to a robust and efficient energy solver.

3.4 Resolution of microsegregation equations

In this section, we focus on the computation of thermal variables, such as the temperature T and the liquid fraction g_l *etc.*, knowing the average enthalpy H and the average concentration w. Following the work of Isabelle Vannier [1995] and its implementation in the finite volume software SOLID, two cases are considered hereunder. The first case is the solidification of a binary alloy with eutectic transformation. The second case is the solidification of steel and more generally, multicomponent alloys.

3.4.1 Binary alloys with eutectic transformation

The linearized phase diagram of a binary alloy is presented in Figure 3-6. For simplicity, it is assumed that the solute diffuses perfectly both in the solid and liquid phases, and then the lever rule applies. It is also assumed that the specific heat c_p is a constant. The evolution of the average enthalpy as a function of temperature is shown in Figure 3-7.

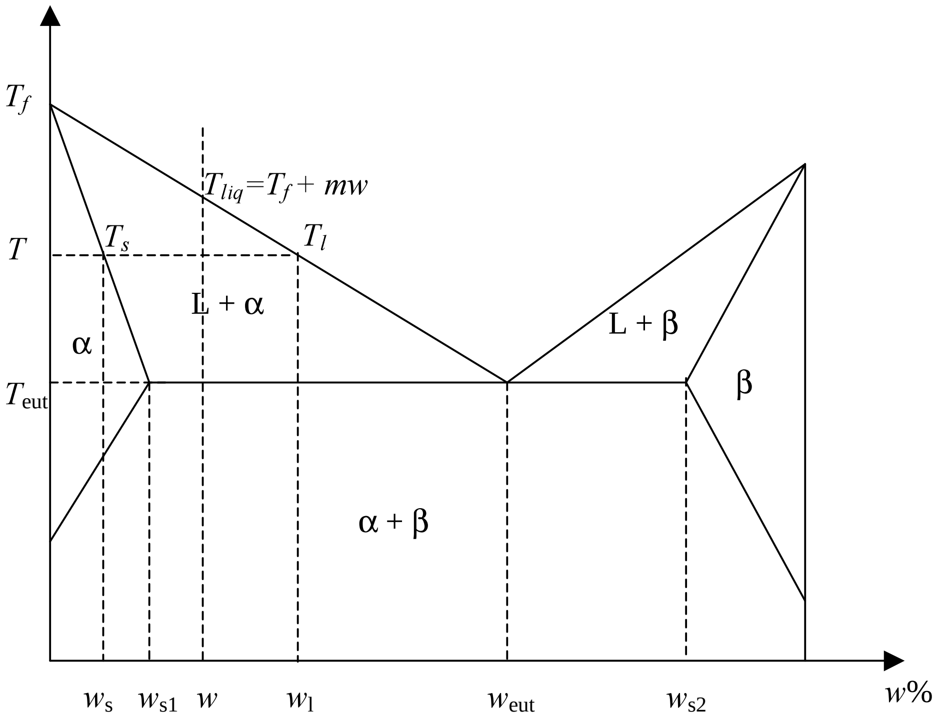

Figure 3-6 Phase diagram for a binary eutectic alloy. T_f is the melting temperature of the pure material. For an alloy with an average concentration w, solidification begins at temperature T_{liq} and ends at the eutectic temperature T_{eut}. At a given temperature T, we have the liquid phase with the concentration w_l and the solid phase α with the concentration w_s. While at the eutectic temperature T , the liquid phase with the concentration w transforms into two solid phases α and β, their concentrations being denoted by w_{s1} and w_{s2} respectively.

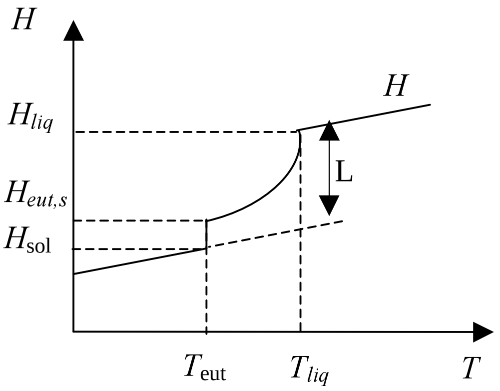

Figure 3-7 Relationship between average enthalpy and temperature. T_{liq} is the liquidus temperature, associated with the enthalpy H_{liq}. T_{eut} is the eutectic temperature. The eutectic transformation occurs in a range of enthalpies, it begins at $H_{eut,s}$ and ends at H_{sol}. L is the latent heat of fusion.

Now, we deduce the temperature, the liquid fraction and the concentration in the liquid phase, using the average enthalpy and the average concentration. This is achieved by two steps. Firstly, we determinate the important phase change points on the enthalpy-temperature curve as illustrated in Figure 3-7, so that the state of a point can be determined, either in the solid, liquid or mushy state. Then, we calculate the temperature T, the concentration in liquid phase w_l, the liquid fraction g_l and $\frac{\partial T}{\partial H}$.

- *Determination of the phase change points on the enthalpy-temperature curve*

The liquidus temperature T and associated enthalpy H can be computed by equations (3-66) and (3-67), using the thermal equilibrium hypothesis (3-5) and the definition of the average enthalpy (3-13).

$$T_{liq} = T_f + mw \tag{3-66}$$

$$H_{liq} = c_p T_{liq} + L \tag{3-67}$$

According to the average concentration, the solidus temperature T_{sol} is computed using either equation (3-68) or equation (3-69). The corresponding enthalpy H_{sol} is given by equation (3-70).

$$T_{sol} = T_f + m\frac{w}{k}, \qquad \text{if } w < w_{s1} \tag{3-68}$$

$$T_{sol} = T_{eut}, \qquad \text{if } w \geq w_{s1} \tag{3-69}$$

$$H_{sol} = c_p T_{sol} \tag{3-70}$$

Following the phase diagram, the liquid fraction $g^l_{eut,s}$, at the eutectic point can be calculated using equation (3-71). Equation (3-72) gives the enthalpy $H_{eut,s}$ below which the eutectic transformation takes place.

$$g^{l}_{eut,s} = \frac{w - w_{s1}}{w_{eut} - w_{s1}} \tag{3-71}$$

$$H_{eut,s} = c_p T_{eut} + L\, g^{l}_{eut,s} \tag{3-72}$$

- *Calculation of thermal parameters*

Knowing the values of enthalpy H_{liq}, $H_{,}$ and H_{sol}, we can identify 4 cases: 1) $H \geq H_{liq}$, the alloy is in the liquid state; 2) $H \leq H_{sol}$, in the solid state; 3) $H_{eut,s} \leq H < H_{liq}$, in the mushy state; and 4) $H_{sol} < H < H_{eut,s}$, in the eutectic transformation. According to these different states, the thermal parameters can be determined respectively.

1) $H \geq H_l$, the alloy is in the liquid state, we have:

$$g_l = 1 \tag{3-73}$$

$$w_l = w \tag{3-74}$$

$$T = \frac{H - H_{liq}}{c_p} + T_{liq} \tag{3-75}$$

$$\frac{\partial T}{\partial H} = \frac{1}{c_p} \tag{3-76}$$

2) $H \leq H_l$, the alloy is in the solid state. An additional test is done to identify if the alloy has already been in the solid before, *i.e.* $g_l^{t-\Delta t} = 0$. If the alloy was in the mushy state at the previous time step, we have two different cases according to the average concentration, $w < w_{s1}$ or $w > w_{s1}$.

For the case of $w < w_{s1}$, we have:

$$g_l = 0 \tag{3-77}$$

$$w_l = \frac{w}{k} \tag{3-78}$$

$$T = \frac{H - H_{sol}}{c_p} + T_{sol} \tag{3-79}$$

$$\frac{\partial T}{\partial H} = \frac{1}{c_p} \tag{3-80}$$

For the case of $w \geq w_{s1}$, we have:

$$g = 0 \tag{3-81}$$

$$w_l = w_{eut} \tag{3-82}$$

$$T = \frac{H - H_{sol}}{c_p} + T_{sol} \tag{3-83}$$

$$\frac{\partial T}{\partial H} = \frac{1}{c_p} \tag{3-84}$$

In the case where the alloy was already in the solid state at the previous time step, $g_l = 0$, and w_l does not change any more, it takes its value at the previous time step. T and $\frac{\partial T}{\partial H}$ are given by equations (3-83) and (3-84) respectively.

3) $H_{eut,s} \le H < H_{liq}$

In this case, we need to solve the following three equations with three unknowns g_l, w_l and T.

$$H = c_p T + g_l L \tag{3-85}$$

$$w = g_l w_l + (1 - g_l)\, k\, w_l \tag{3-86}$$

$$T = T_f + m\, w_l \tag{3-87}$$

Successive substitutions lead to a second order equation for g_l, which permits then to compute w_l using equation (3-86) and finally T using equation (3-87).

The derivation of equation (3-85) with respect to T, leads to:

$$\frac{\partial T}{\partial H} = \frac{1}{c_p + L \dfrac{\partial g_l}{\partial T}} \tag{3-88}$$

Combining equations (3-86) and (3-87), we find the temperature T as a function of the liquid fraction g_l and the average concentration w. Then $\frac{\partial T}{\partial g_l}$ can be deduced as follows:

$$\frac{\partial T}{\partial g_l} = \frac{m}{k + (1-k)\, g_l} \frac{\partial w}{\partial g_l} - \frac{(1-k)\, w\, m}{\left(k + (1-k)\, g_l\right)^2} \tag{3-89}$$

with

$$\frac{\partial w}{\partial g_l} = \frac{w - w^{t-\Delta t}}{g_l - g_l^{t-\Delta t}}, \qquad \text{if } g_l \ne g_l^{t-\Delta t} \tag{3-90}$$

$$\frac{\partial w}{\partial g_l} = 0, \quad \text{if } g_l = g_l^{t-\Delta t} \tag{3-91}$$

4) $H_{sol} < H < H_{eut,s}$, eutectic transformation occurs at this node. We have:

$$g_l = \frac{H - c_p T_{eut}}{L} \tag{3-92}$$

$$w_l = w_{eut} \tag{3-93}$$

$$T = T_{eut} \tag{3-94}$$

$$\frac{\partial T}{\partial H} = 0 \tag{3-95}$$

Remark

Regarding the method presented in this section, we note that an open system has been considered. The variation of average mass concentration affects the local solidification path, *i.e.*, the liquidus temperature T_{liq} and the solidus temperature T_{so} are considered as functions of the local average mass concentration. The lever rule is applied in the microsegregation model, the resolution of solute and the energy equations are consistent with the local thermal equilibrium. In the *full-coupling* approaches (with or without iterations), we have used this microsegregation model.

3.4.2 Multicomponent alloys

In the following text, we present the method developed by Isabelle Vannier [1995] that deals with the liquid-solid phase change in steels. The treatment of phase change is extended to the multi-component system.

- *Thermal equilibrium in the mushy zone*

Following the hypothesis of thermal equilibrium in the mushy zone, it is assumed that the temperature is equal to the liquidus temperature, which is approximated as a linear function of the liquid mass concentrations as follows:

$$T = T_f + \sum_{i=1}^{n} m^i w_l^i \tag{3-96}$$

Where n is the number of solute elements in the alloy; m^i is the slope of liquidus for the element i; w^i is the liquid mass concentration of the element i.

Let us denote $w_l^i(t_p)$ the liquid mass concentration of element i when the liquid just begins to solidify. The value of $w_l^l(t_p)$ can be different from the initial nominal concentration w_0^i, if the enrichment of the solute element i in liquid pool is taken into account. In the absence of enrichment, $w_l^i(t_p)=w_0^i$. Figure 3-8 shows the variation of concentration in the liquid pool.

Not taking the convection into account in the mushy state, after the beginning of solidification, that is for a local closed system, the lever rule and the Scheil equation give w^i as a function of $w_l^l(t_p)$.

- Lever rule for an element that diffuses perfectly both in the solid and liquid phases. This is the particular case of carbon in steel. Let the superscript c denote carbon, we have:

$$w_l^c = \frac{w_l^c(t_p)}{k^c + (1-k^c)\, g_l} \tag{3-97}$$

- Scheil's law for an element i that does not diffuse in the solid phase is expressed as:

$$w = w\,(t\ )\ g^{\ \ -1} \tag{3-98}$$

Substituting equations (3-97) and (3-98) into equation (3-96), then the temperature in the mushy zone can be expressed as:

$$T = T_f + \frac{m^c\, w_l^c(t_p)}{k^c + (1-k^c)\, g_l} + \sum_{i=1, i\neq c}^{n} m^i\, w_l^i(t_p) \left(g_l\right)^{k^i - 1} \tag{3-99}$$

The equation defines the solidification path, *i.e.*, $T = f(g\ )$. Consequently, $\frac{\partial T}{\partial g_l}$ can be deduced as follows:

$$\frac{\partial T}{\partial g_l} = \frac{m^c\, w_l^c(t_p)\,(k^c - 1)}{\left(k^c + (1-k^c)\, g_l\right)^2} + \sum_{i=1, i\neq c}^{n} m^i\, w_l^i(t_p)\,(k^i \text{ -}1) \left(g_l\right)^{k^i - 2} \tag{3-100}$$

Using this expression in equation (3-88), one can deduce the value of $\frac{\partial T}{\partial H}$ for the thermal analysis.

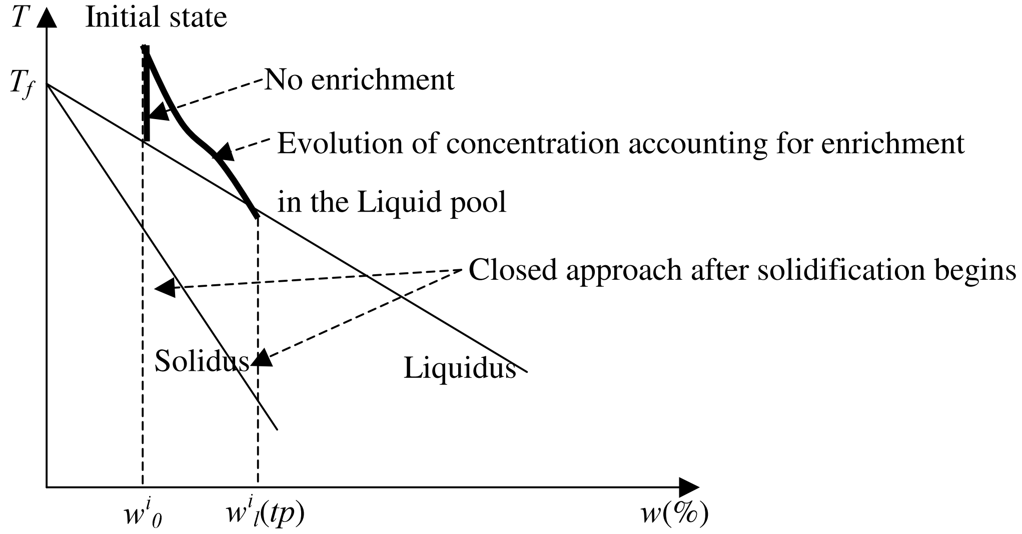

Figure 3-8 Schematic of the variation of concentration in the liquid pool (Isabelle Vannier [1995])

- *Determination of the liquidus temperature* T_{liq} *and the solidus temperature* T_{so}

In the liquid state, knowing $w^i \equiv w_l^i$, liquidus temperature T_{liq} is given by equation (3-96). Note that because of the closed-system hypothesis (at the level of the REV), this liquidus temperature does not change during solidification.

Regarding the end of solidification, Scheil's law gives a very large value of w_l^i when the fraction of liquid g_l tends to zero. It is then assumed that an artificial eutectic transformation occurs when $g_l \leq g_{ll}$. g_{lsol} is a small value, typically $g_{lsol} = 0.01$. g_{lsol} is applied in the equation (3-98) to truncate the liquid concentration.

The solidus temperature (the artificial eutectic temperature) T_{sol} is defined as a function of $w_l^i(t_p)$, which is a correlation obtained from experimental results:

$$T_{sol} = T_{sol}^{cor}\left(\, w_l^i(t_p)\right) \tag{3-101}$$

For steels, the correlation can be found in the original literature (Howe [1988]) and in the thesis of Isabelle Vannier [1995].

Corresponding to the temperature T_{sol}, one can find the fraction of liquid g_{lsol} at which the artificial eutectic transformation begins to take place. g_{lsol} is deduced from equation (3-99) by the secant method, knowing T_{sol} and $w_l^i(t_p)$ (Vannier [1995]).

- *Determination of the temperature* T *and the fraction of liquid* g_l

In order to compute the temperature T and the fraction of liquid g_l, firstly we compute the phase change points on the enthalpy-temperature curve using equations (3-11) to (3-13).

$$H_{liq} = H\,(T_{liq},\ g_l = 1) \tag{3-102}$$

$$H_{sol} = H\,(T_{sol},\ g_l = g_{lsol}) \tag{3-103}$$

$$H_{fin} = H\,(T_{sol},\ g_l = 0) \tag{3-104}$$

Knowing the average enthalpy H and the phase change points H_{liq}, H_{sol} and H_{fin}, providing that the specific heat c_p is a constant, we can identify 4 cases to compute the temperature T and the fraction of liquid g_l as follows:

1) $H \geq H$, the alloy is in the liquid state;

$$g_1 \ = 1 \qquad \text{and} \qquad T = \frac{H - L}{c_p} \tag{3-105}$$

2) $H \leq H$, in the solid state;

$$g_1 \ = \ 0 \qquad \text{and} \qquad T = \frac{H}{c_p} \tag{3-106}$$

3) $H_{fin} < H \leq H_{sol}$, in the artificial eutectic transformation;

$$g_1 \ = \ \frac{H \text{ - } c_p T_{sol}}{L} \qquad \text{and} \qquad T = T_{sol} \tag{3-107}$$

4) $H_{sol} < H < H_{fin}$, in the mushy state, T and g_l are computed from the equation (3-108) and the equation (3-99) by the secant method.

$$H(T, g_l) \text{ - } H = \ 0 \tag{3-108}$$

The computation of the parameter $\frac{\partial T}{\partial H}$ is achieved according to the 4 cases. If the alloy is in the liquid state or in the solid state, $\frac{\partial T}{\partial H} = \frac{1}{c_p}$. If it is in the artificial eutectic transformation, $\frac{\partial T}{\partial H} = 0$. In the mushy state, $\frac{\partial T}{\partial H}$ can be deduced from equations (3-88) and (3-100).

Remark

In this section, the treatment of solidification is extended to multicomponent systems. For simplicity, the solidification is considered locally as a closed system. T_{liq} and T_l are estimated locally, as functions of the local liquid average mass concentration before solidification, $w_l^l(t_p)$. That is to say the solidification path is fixed when the metal begins to solidify. Not accounting for the variation of concentration in the mushy zone, the energy equation is consistent with the local thermal equilibrium. We use this microsegregation model in the *no-coupling* approach.

3.5 Resolution of the solute transport equation

As mentioned above, the solute transport equation writes, for each alloying element considered:

$$\frac{\partial w}{\partial t} + \mathbf{V} \cdot \nabla w_l - \nabla \cdot (\varepsilon \nabla w_l) = 0$$

It is supposed that there is no solute exchange at the boundary of the computational domain $\partial\Omega$, that is:

$$\nabla w \cdot \mathbf{n} = 0 \quad \text{on} \quad \partial\Omega \tag{3-109}$$

where $\mathbf{n}$ is the outward normal on $\partial\Omega$.

It is also assumed that the initial concentration field is homogeneous:

$$w = w_0 \quad \text{at} \quad t = 0 \tag{3-110}$$

where w_0 is the nominal concentration of the alloy.

The fully implicit Euler-backward scheme is used for the time discretization. The linear triangle elements are used for the spatial discretization. Regarding the stabilization of the convection-diffusion equation of solute transport, the Streamline Upwind Petrov-Galerkin (SUPG) scheme is applied.

There are two unknowns in the solute transport equation (3-9): the average mass concentration in liquid w_l and the average mass concentration w. The relationships between w_l and w depend on the microsegregation model. The two unknowns can be chosen as the primary variable alternately, leading to two possibilities to solve the equation.

The first possibility is to choose w_l. In R2SOL we have implemented the resolution for w_l, following the work of Isabelle Vannier [1995] in the finite volume code SOLID.

The second possibility is to choose w. This is the case of the “split method” following the work of Prakash and Voller [1989], which we have also implemented in R2SOL.

In the *no-coupling* approach we solve for w_l as the primary unknown. In the *full-coupling* approach we solve for w as the primary unknown. We present the two approaches in the following text.

3.5.1 Approach 1 - resolution for the average mass concentration in liquid w_l

3.5.1.1 Lever rule

Lever rule states that the solutes in the solid and the liquid phases diffuse perfectly, according the equation (2-1). Substituting the lever rule into the solute transport equation (3-9), we have then:

$$\frac{\partial[(g_l+k(1-g_l))w_l]}{\partial t}+\nabla w_l\cdot\mathbf{V}-\nabla\cdot(\varepsilon\nabla w_l)=0 \tag{3-111}$$

As mentioned above, we solve for w_l, not coupling with the equations of energy and momentum. The velocity field obtained at previous time step $t-\Delta t$, $\mathbf{V}^{t-\Delta t}$, is used hereby. For clarity, this velocity is simply noted as $\mathbf{V}$ in this section. Since the solidification process is considered locally as a closed system in the *no-coupling* approach, the fraction of liquid g_l has been computed in the resolution of the energy equation. The liquid fraction at time t, g_l^t is then known in equation (3-111). Only one unknown w_l^t appears in the equation (3-111).

For stability, the SUPG test function φ_i instead of the standard interpolation function N_i is used for the spatial discretization. Using the finite element method, one can discretize the equation (3-111), leading to:

$$\begin{aligned}\forall i=1,N \qquad & \frac{1}{\Delta t}\left\{\int_\Omega \varphi_i N_j[(g_l+k(1-g_l))w_l]_j^t d\Omega-\int_\Omega \varphi_i w^{t-\Delta t}d\Omega\right\}+\int_\Omega \varphi_i\, V_m\frac{\partial N_j}{\partial x_m}(w_l)_j^t d\Omega \\ & +\int_\Omega \varepsilon\frac{\partial N_i}{\partial x_m}\frac{\partial N_j}{\partial x_m}(w_l)_j^t d\Omega \qquad \text{with } j=1,\ N\end{aligned} \tag{3-112}$$

In the above equations, N is the number of nodes; V_m is the m-th component of velocity vector $\mathbf{V}$, and it is computed by the linear interpolation $V_m=N_qV_m^q$; The superscript t and $t-\Delta t$ denote the time increment limits. The subscripts *i* and *j* denote the nodes. The SUPG test function φ has been given by equation (3-44). Regarding the stabilization parameter τ, we note that it is computed in the same way as that presented in section 3.3.2. However, this time, solute diffusion coefficient ε in stead of the thermal diffusivity α is used to compute the mesh Peclet number.

The linear equation (3-113) permits the computation of the average concentration in liquid w at each node:

$$A_{ij}(w_l)_j^t=B_i \tag{3-113}$$

where: $$A_{ij}=\frac{1}{\Delta t}\int_\Omega \varphi_i N_j[g_l+k(1-g_l)]_j^t d\Omega+\int_\Omega \varphi_i V_m\frac{\partial N_j}{\partial x_m}d\Omega+\int_\Omega \varepsilon\frac{\partial N_i}{\partial x_m}\frac{\partial N_j}{\partial x_m}d\Omega$$

$$B_i=\frac{1}{\Delta t}\int_\Omega \varphi_i w^{t-\Delta t}d\Omega$$

After the resolution of w_l, the average concentration w can be found by using the lever rule.

Remark

As it has been mentioned in section 3.1.2, ε is a diffusion coefficient. Usually the contribution of diffusion to the macrosegregation can be negligible. For numerical reasons, an arbitrarily small value ε, in the order of 10^{-9}, that is the order of magnitude of the physical diffusivity, can be used. In the present work, the diffusion terms are neglected.

3.5.1.2 Scheil's model

In the case of no diffusion in the solid phase and infinite diffusion in the liquid phase, the relation between w_l and w can be expressed by the Scheil's equation (2-2). Taking the time derivative of each side of the equation (2-2), we have:

$$\frac{\partial w}{\partial t}=\frac{\partial(g_l w_l)}{\partial t}-k w_l\frac{\partial g_l}{\partial t} \tag{3-114}$$

Substituting this equation into equation (3-9), one obtains:

$$\frac{\partial(g_l w_l)}{\partial t}-k w_l\frac{\partial g_l}{\partial t}+\nabla w_l\cdot\mathbf{V}-\nabla\cdot(\varepsilon\nabla w_l)=0 \tag{3-115}$$

For simplicity, we neglect the diffusion term in what follows (since it can be handled in the same way as we have presented for the lever rule). Using the same method as presented in last section 3.5.1.1, the following discretized equation for the Scheil's model can be obtained:

$$\begin{aligned}\forall i=1,N\quad &\frac{1}{\Delta t}\left\{\int_\Omega \varphi_i N_j (g_l w_l)^t_j\,d\Omega-\int_\Omega \varphi_i N_j (g_l w_l)^{t-\Delta t}_j\,d\Omega\right\}-\int_\Omega k\varphi_i N_j \left(\frac{\Delta g_l}{\Delta t}\right)_j (w_l)^t_j\,d\Omega\\ &+\int_\Omega \varphi_i V_m\frac{\partial N_j}{\partial x_m}(w_l)^t_j\,d\Omega=0 \qquad \text{with} \quad j=1,N\end{aligned} \tag{3-116}$$

After resolution for w_l, the local average mass concentration w can be calculated by equation (3-117). The equation is deduced from equation (3-114), using an explicit Euler time integration scheme (Vannier [1995]).

$$w^t-w^{t-\Delta t}=(g_l w_l)^t-(g_l w_l)^{t-\Delta t}-k(w_l)^t(g_l^t-g_l^{t-\Delta t}) \tag{3-117}$$

It can be seen that the lever rule and the Scheil's models are deeply involved in the solute transport equation, when solving for w_l.

3.5.2 Approach 2 - resolution for the average mass concentration w

In order to eliminate w_l in the solute equation, following the work of Voller *et al.* [1989] a "split operator" technique is used. Using the Euler backward scheme, the solute transport equation can be written as follows:

$$\frac{w^t-w^{t-\Delta t}}{\Delta t}+\nabla w^t\cdot\mathbf{V}-\nabla\cdot\left(\varepsilon\nabla w^t\right)=\nabla\left(w^*-w_l^*\right)\cdot\mathbf{V}-\nabla\cdot\left[\varepsilon\nabla\left(w^*-w_l^*\right)\right] \tag{3-118}$$

where: the superscript * refers: 1) the latest iterative value in the case of the *full-coupling* approach; 2) the value at the previous time instant $t-\Delta t$ in case of the *full-coupling* approach reduced to one iteration. The right hand side terms, that arise from the splitting of the advection and diffusion terms, appear as source terms.

The above equation has the great advantage of being able to treat any microsegregation model (lever rule, Scheil's model, or models accounting for the back diffusion in the solid phase) by the same transport equation at the macro scale. Indeed the microsegregation model can be treated individually in a different module, separately from the resolution for w.

The SUPG scheme is used to discretize equation (3-118). In the present work, the diffusion terms are neglected, leading to:

$$\forall i = 1,\ N \quad \frac{1}{\Delta t}\left\{\int_\Omega \varphi_i N_j w_j^t d\Omega - \int_\Omega \varphi_i N_j w_j^{t-\Delta t} d\Omega\right\} + \int_\Omega \varphi_i V_m \frac{\partial N_j}{\partial x_m} w_j^t d\Omega = \int_\Omega \varphi_i V_m \frac{\partial N_j}{\partial x_m} w_j^* d\Omega - \int_\Omega \varphi_i V_m \frac{\partial N_j}{\partial x_m} w_{l\,j}^* \mathrm{d}\Omega \qquad \text{with} \quad j = 1, N \tag{3-119}$$

In the above equations, φ_i is the SUPG test function, as defined by equation (3-44). The superscript t and $t-\Delta t$ denote the time increment limits. The subscript i and j denote the nodes. V_m is the m-th component of velocity vector $\mathbf{V}$. In the *full-coupling* approach, $\mathbf{V}$ is the current iterative estimation of the average liquid velocity. In the case of the *full-coupling* resolution reduced to *one iteration,* $\mathbf{V}$ is the velocity at previous time step.

As the approach 2 is more flexible, in the later stage of our work, we have focused on it. Now, only lever rule has been validated with the fully coupled resolution. We present the computational results in chapter 5.

3.6 Resolution of momentum equation

This section is dedicated to the resolution of fluid mechanics in the solidification process. We assume that the solid is fixed and non-deformable, the fluid flow is governed by the averaged momentum equation as follows:

$$\rho_0 \frac{\partial \mathbf{V}}{\partial t} + \frac{\rho_0}{g_l} \nabla \cdot (\mathbf{V} \times \mathbf{V}) = \nabla \cdot (\mu \nabla \mathbf{V}) - g_l \nabla p + g_l \rho\, \mathbf{g} - \frac{\mu}{\mathrm{K}} g_l \mathbf{V}$$

We also assume that the solid and liquid densities are equal and constant, except in the buoyancy term in the above equation. The mass conservation equation then gives:

$$\nabla \cdot \mathbf{V} = 0$$

In R2SOL, a nodal upwind approach has been developed by Gaston [1999], the governing equations are written alternatively as:

$$\begin{cases} \rho_0 \left(1 - \dfrac{1}{g_l}\right) \dfrac{\partial \mathbf{V}}{\partial t} + \dfrac{\rho_0}{g_l} \dfrac{d\mathbf{V}}{dt} - \nabla \cdot (\mu \nabla \mathbf{V}) + g_l \nabla p - g_l \rho \mathbf{g} + \dfrac{\mu}{K} g_l \mathbf{V} = 0 \\ \nabla \cdot \mathbf{V} = 0 \end{cases} \tag{3-120}$$

The total derivative of velocity is treated by a Lagrangian-type upwind scheme, which will be presented later. A velocity/pressure P1+/P1 formulation is used to solve the fluid mechanical problem. The present work has consisted of the implementation of the axisymmetric formulation in R2SOL and the improvement of the computation of the Darcy and inertia terms.

The previous work and the new development to solve mechanical problems are presented in section 3.6.1. Then, the implementation of axisymmetric formulation is introduced in section 3.6.2.

More recently, in collaboration with Victor Fachinotti and Michel Bellet, the SUPG-PSPG formulation has been implemented, which will be presented in section 3.6.3.

Finally, some validation test cases are presented in 3.7.

3.6.1 Resolution of fluid mechanics with the nodal upwind method

3.6.1.1 Weak form

In order to solve the mechanical problem, the classical principle of virtual work is applied. Multiplying the momentum equation by a virtual velocity $\mathbf{V}^*, \mathbf{V}^* \in \left\{\mathbf{v}, \mathbf{v} \in (H^1(\Omega))^2,\ \mathbf{v}\cdot\mathbf{n}=0 \text{ on} \partial\Omega\right\}$, and integrating over the domain Ω, after some calculations we obtain:

$$\begin{aligned}\forall \mathbf{V}^* \quad & \int_\Omega \frac{2\mu}{g_l}\dot{\boldsymbol{\varepsilon}}(\mathbf{V}):\dot{\boldsymbol{\varepsilon}}(\mathbf{V}^*)d\Omega - \int_\Omega p\nabla\cdot\mathbf{V}^* d\Omega - \int_{\partial\Omega} \frac{1}{g_l}\mathbf{T}\cdot\mathbf{V}^* d\Gamma - \int_\Omega \rho\mathbf{g}\cdot\mathbf{V}^* d\Omega \\ & + \int_\Omega \frac{\mu}{K}\mathbf{V}\cdot\mathbf{V}^* d\Omega + \int_\Omega \left[\frac{\rho_0}{g_l}\left(1 - \frac{1}{g_l}\right)\frac{\partial\mathbf{V}}{\partial t} + \frac{\rho_0}{g_l^{\ 2}}\frac{d\mathbf{V}}{dt}\right]\cdot\mathbf{V}^* d\Omega = 0\end{aligned} \tag{3-121}$$

where $\dot{\boldsymbol{\varepsilon}}(\mathbf{V})$ is the strain rate tensor associated with the averaged velocity field $\mathbf{V}$, $\dot{\varepsilon}_{ij}(\mathbf{V}) = \frac{1}{2}\left(\frac{\partial V_i}{\partial x_j} + \frac{\partial V_j}{\partial x_i}\right)$. ***T*** is the local contact surface force on the boundary. The notation ':' denotes the contracted product of tensors, $\dot{\varepsilon}(\mathbf{V}):\dot{\varepsilon}(\mathbf{V}^*) = \sum \dot{\varepsilon}_{ij}(\mathbf{V})\,\dot{\varepsilon}_{ij}(\mathbf{V}^*) = \sum \dot{\varepsilon}_{ij}(\mathbf{V})\frac{\partial V_i^*}{\partial x_j}$. The general procedure to get the weak form of the momentum equation can be found elsewhere (Rappaz *et al.* [2002]).

The equation (3-121) should be solved under the constraint of incompressibility for the liquid phase. In a mixed formulation, the pressure p appears as a Lagrange multiplier of the incompressibility constraint, and then we write:

$$\forall p^* \quad -\int_\Omega p^* \nabla\cdot\mathbf{V} dV = 0 \tag{3-122}$$

3.6.1.2 Time discretization

As it has been discussed before, here we assume that the computational domain is fixed, and the problem is solved by means of a Eulerian formulation on the fixed finite element mesh. The equations to be solved for $(\mathbf{V}, p)^t$, averaged liquid velocity and intrinsic liquid pressure fields at time t, can be expressed in the following way:

$$\begin{cases}\forall \mathbf{V}^* \ \displaystyle\int_\Omega \frac{2\mu}{g_l}\dot{\boldsymbol{\varepsilon}}(\mathbf{V}^t):\dot{\boldsymbol{\varepsilon}}(\mathbf{V}^*)d\Omega - \int_\Omega p^t\nabla\cdot\mathbf{V}^* d\Omega - \int_{\partial\Omega} \frac{1}{g_l}\mathbf{T}^t\cdot\mathbf{V}^* d\Gamma - \int_\Omega \rho\mathbf{g}\cdot\mathbf{V}^* d\Omega \\ \qquad + \displaystyle\int_\Omega \frac{\mu}{K}\mathbf{V}^t\cdot\mathbf{V}^* d\Omega + \int_\Omega \frac{\rho_0}{g_l\Delta t}\left(\mathbf{V}^t - \mathbf{V}^{t-\Delta t} + \frac{1}{g_l}(\mathbf{V}^{t-\Delta t} - \tilde{\mathbf{V}}^{t-\Delta t})\right)\cdot\mathbf{V}^* d\Omega = 0 \\ \\ \forall p^* \ -\displaystyle\int_\Omega p^*\nabla\cdot\mathbf{V} d\Omega = 0\end{cases} \tag{3-123}$$

where $\mathbf{V}^{t-\Delta t}$ denotes the velocity at the point $\boldsymbol{x}$ of the space, but at previous time step, whereas $\tilde{\mathbf{V}}^{t-\Delta t}$ denotes the velocity at time $t-\Delta t$ of the particle which, at time t, is at the same position $\boldsymbol{x}$. In other words, the total and partial derivative of the velocity are expressed as:

$$\frac{d\mathbf{V}}{dt}=\frac{1}{\Delta t}(\mathbf{V}^{t}-\tilde{\mathbf{V}}^{t-\Delta t}) \tag{3-124}$$

$$\frac{\partial\mathbf{V}}{\partial t}=\frac{1}{\Delta t}(\mathbf{V}^{t}-\mathbf{V}^{t-\Delta t}) \tag{3-125}$$

In sections 3.6.1 and 3.6.2, we will denote $\tilde{\boldsymbol{\gamma}}$ the following acceleration vector:

$$\tilde{\boldsymbol{\gamma}}=\frac{\rho_0}{g_l\Delta t}\left(\mathbf{V}^{t}-\mathbf{V}^{t-\Delta t}+\frac{1}{g_l}(\mathbf{V}^{t-\Delta t}-\tilde{\mathbf{V}}^{t-\Delta t})\right)$$

The particle velocity $\tilde{\boldsymbol{V}}^{t-\Delta t}$ is computed by a upwind transport approach that will be presented in the section 6.2.4.

3.6.1.3 P1+/P1 formulation

The finite element discretization spaces for the velocity and the pressure need to satisfy a compatibility condition, known as “Ladyzhenskaya-Babuska-Brezzi (LBB) condition” (Rappaz *et al.* [2002]). This is equivalent to the requirement of non-singularity of the matrix resulting from the discretized Navier-Stokes equations. In particular, this condition implies that the number of degrees of freedom of the velocity field should be higher than that of pressure field.

The so called P1+/P1 or “mini-element” formulation was adopted in the 3-dimensional code of THERCAST® (Jaouen [1998]) and the 2-dimensional code FORGE2® (Perchat [2000]), following the pioneering work of Arnold *et al.* [1984] and Fortin and Fortin [1985]. The pressure is discretized by polynomials of degree 1 (P1), while the velocity is also discretized by polynomials of degree 1 (P1), including additional degrees of freedom at the centre of the element (the bubble formulation).

In FORGE2®, the resolution of the mechanical problem is based on the one-phase continuum model, without the Darcy term. Clearly, some additional developments are needed in R2SOL due to the Darcy term.

In R2SOL, the P1+/P1 formulation was initially developed by Alban Heinrich (Heinrich [2003]), at the beginning of my work in September 2001. From then on , we have worked together on the implementation of P1+/P1 formulation.

As shown in Figure 3-9, for the sake of clarity we denote **w** the average liquid velocity $\boldsymbol{V}$. The velocity and the pressure are discretized by equations (3-126) and (3-127) respectively.

$$\mathbf{w}_h=\mathbf{v}_h+\mathbf{b}_h=\sum_{n=1}^{3}N_n\mathbf{V}^n+N^b\mathbf{B} \tag{3-126}$$

$$p_h=\sum_{n=1}^{3}N_nP^n \tag{3-127}$$

where N is the standard linear interpolation function. N^b is the linear bubble function defined in the three subtriangles, being equal to 1 at the center of the triangle and equal to 0 at the edges of the triangle.

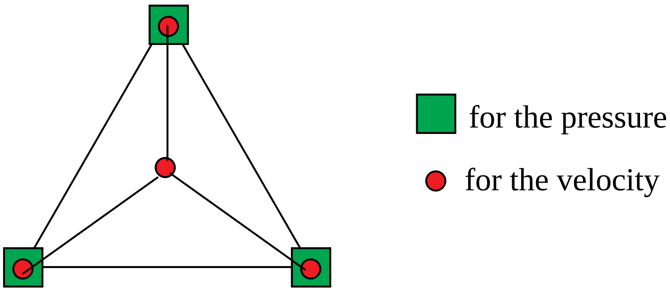

Figure 3-9 Representation of the mini-element. The value of the "bubble" interpolation function N^b is 1 at the triangle centre and 0 at its boundary. The central additional velocity degrees of freedom **B** permit a better control of the incompressibility constraint. This element satisfies the LBB condition (Rappaz *et al*. [2002]).

Since any virtual velocity field $\mathbf{w}^*$ can be decomposed as a sum $\mathbf{w}^* = \mathbf{v}^* + \mathbf{b}^*$, the equilibrium and incompressibility equations can be written as follows:

$$\begin{cases} \forall \mathbf{v}^* \ \int\limits_\Omega \frac{2\mu}{g_l} \dot{\boldsymbol{\varepsilon}}(\mathbf{w}) : \dot{\boldsymbol{\varepsilon}}(\mathbf{v}^*) d\Omega - \int\limits_\Omega p \nabla \cdot \mathbf{v}^* d\Omega - \int\limits_{\partial\Omega} \frac{1}{g_l} \mathbf{T} \cdot \mathbf{v}^* d\Gamma - \int\limits_\Omega \rho \mathbf{g} \cdot \mathbf{v}^* d\Omega + \int\limits_\Omega \frac{\mu}{K} \mathbf{w} \cdot \mathbf{v}^* d\Omega \\ \qquad + \int\limits_\Omega \frac{\rho_0}{g_l} \tilde{\boldsymbol{\gamma}}(\mathbf{w}) \cdot \mathbf{v}^* d\Omega = 0 \\ \forall \mathbf{b}^* \ \int\limits_\Omega \frac{2\mu}{g_l} \dot{\boldsymbol{\varepsilon}}(\mathbf{w}) : \dot{\boldsymbol{\varepsilon}}(\mathbf{b}^*) d\Omega - \int\limits_\Omega p \nabla \cdot \mathbf{b}^* d\Omega - \int\limits_\Omega \rho \mathbf{g} \cdot \mathbf{b}^* d\Omega + \int\limits_\Omega \frac{\mu}{K} \mathbf{w} \cdot \mathbf{b}^* d\Omega + \int\limits_\Omega \frac{\rho_0}{g_l} \tilde{\boldsymbol{\gamma}}(\mathbf{w}) \cdot \mathbf{b}^* d\Omega = 0 \\ \forall p^* \ -\int\limits_\Omega p^* \nabla \cdot \mathbf{w} d\Omega = 0 \end{cases} \tag{3-128}$$

Remark

The boundary integral disappears from the second equation. This is due to the properties of the bubble interpolation function whose value is zero on the edge of any triangle.

Actually, the spatial integration over an element of the product of the gradient of a bubble type function by a constant tensor is equal to zero. Then, it is interesting to decompose the term $\dot{\boldsymbol{\varepsilon}}(\mathbf{w})$ in a sum of two terms, one which will depend only on the linear part of the velocity field **v**, and the other one which will depend linearly on **b**. It is possible to take advantage of bubble properties to simplify the equations (Jaouen [1998], Perchat [2000]), leading to:

$$\begin{cases} \forall \mathbf{v}^* \quad \displaystyle\int_\Omega \frac{2\mu}{g_l}\dot{\boldsymbol{\varepsilon}}(\mathbf{v}):\dot{\boldsymbol{\varepsilon}}(\mathbf{v}^*)d\Omega - \int_\Omega p\nabla\cdot\mathbf{v}^* d\Omega - \int_{\partial\Omega}\frac{1}{g_l}\mathbf{T}\cdot\mathbf{v}^* d\Gamma - \int_\Omega \rho\mathbf{g}\cdot\mathbf{v}^* d\Omega + \int_\Omega \frac{\mu}{K}\mathbf{w}\cdot\mathbf{v}^* d\Omega \\ \qquad\qquad\qquad\qquad\qquad\qquad\qquad\qquad\qquad\qquad\qquad + \displaystyle\int_\Omega \frac{\rho_0}{g_l}\tilde{\boldsymbol{\gamma}}(\mathbf{w})\cdot\mathbf{v}^* d\Omega = 0 \\ \forall \mathbf{b}^* \quad \displaystyle\int_\Omega \frac{2\mu}{g_l}\dot{\boldsymbol{\varepsilon}}(\mathbf{b}):\dot{\boldsymbol{\varepsilon}}(\mathbf{b}^*)d\Omega - \int_\Omega p\nabla\cdot\mathbf{b}^* d\Omega - \int_\Omega \rho\mathbf{g}\cdot\mathbf{b}^* d\Omega + \int_\Omega \frac{\mu}{K}\mathbf{w}\cdot\mathbf{b}^* d\Omega + \int_\Omega \frac{\rho_0}{g_l}\tilde{\boldsymbol{\gamma}}(\mathbf{w})\cdot\mathbf{b}^* d\Omega = 0 \\ \forall p^* \quad -\displaystyle\int_\Omega p^*\nabla\cdot\mathbf{w}\, d\Omega = 0 \end{cases} \tag{3-129}$$

3.6.1.4 *Resolution by Newton-Raphson method*

- The matrix formulation

The Newton-Raphson method is used to solve equations (3-129). The residual vector R of equations (3-129) can be expressed as the sum of each integration term:

$$\begin{aligned} R^l &= R^{l,rheo} + R^{l,pre} + R^{l,t} + R^{l,grav} + R^{l,perm} + R^{l,iner} = 0 \\ R^b &= R^{b,rheo} + R^{b,pre} + R^{b,grav} + R^{b,perm} + R^{b,iner} = 0 \\ R^p &= R^{p,l} + R^{p,b} = 0 \end{aligned} \tag{3-130}$$

Equations (3-130) are solved by the Newton-Raphson method, and the linear system to be solved at each time step can be written in the matrix form (3-131):

$$\begin{bmatrix} H^{ll} & H^{lb} & H^{lp} \\ (H^{lb})^T & H^{bb} & H^{bp} \\ (H^{lp})^T & (H^{bp})^T & H^{pp} \end{bmatrix} \begin{bmatrix} \delta\mathbf{V} \\ \delta\mathbf{B} \\ \delta\mathbf{P} \end{bmatrix} = \begin{bmatrix} -R^l(\mathbf{V},\mathbf{B},\mathbf{P}) \\ -R^b(\mathbf{V},\mathbf{B},\mathbf{P}) \\ -R^p(\mathbf{V},\mathbf{B},\mathbf{P}) \end{bmatrix} \tag{3-131}$$

It is possible to eliminate the internal bubble degrees of freedom **B**, allowing a solution for the variables $\delta\mathbf{V}$ and $\delta\mathbf{P}$ only, at each Newton-Raphson iteration as follows.

$$\begin{bmatrix} H^{ll} - H^{lb}(H^{bb})^{-1}(H^{lb})^T & H^{lp} - H^{lb}(H^{bb})^{-1}H^{bp} \\ (H^{lp})^T - (H^{bp})^T(H^{bb})^{-1}(H^{lb})^T & -(H^{bp})^T(H^{bb})^{-1}H^{bp} \end{bmatrix} \begin{bmatrix} \delta\mathbf{V} \\ \delta\mathbf{P} \end{bmatrix} = \begin{bmatrix} -R^l + H^{lb}(H^{bb})^{-1}R^b \\ -R^p + (H^{bp})^T(H^{bb})^{-1}R^b \end{bmatrix} \tag{3-132}$$

Remark

The problem defined by equation (3-129) is linear. We have developed the code with the Newton-Raphson mothod, as if the problem would be non-linear. In fact, only one iteration will be sufficient for solving equation (3-129).

At the beginning of my work, $R^{b,perm}$ and $R^{b,iner}$ in equation (3-130) b) were omitted; in equation (3-130) a), the contribution of “bubble” component to $R^{l,iner}$, *i.e.* $H^{l,iner}\cdot\mathbf{B}$, was also omitted. Recognizing that the contribution of “bubble” component is important to the flow in the mushy zone, now these terms are taken into account and they are expressed as follows:

The term $R^{\ ,er}$

$$
\begin{aligned}
R^{b,perm} &= \int_{\Omega} \frac{\mu}{K}\,(\mathbf{v}+\mathbf{b})\cdot\mathbf{b}^{*}d\Omega = \int_{\Omega}\frac{\mu}{K}\,\mathbf{v}\cdot\mathbf{b}^{*}d\Omega + \int_{\Omega}\frac{\mu}{K}\,\mathbf{b}\cdot\mathbf{b}^{*}d\Omega \\
&= \qquad\qquad\qquad\qquad H^{bl,\,perm}\,\mathbf{V} \;+\; H^{bb,perm}\mathbf{B}
\end{aligned}
\tag{3-133}
$$

The term $R^{b,er}$

$$
\begin{aligned}
R^{b,iner} &= \int_{\Omega}\frac{\rho_0}{g_l}\,\tilde{\gamma}(\mathbf{v}+\mathbf{b})\cdot\mathbf{b}^{*}d\Omega \\
&= \int_{\Omega}\frac{\rho_0}{g_l}\,\frac{\mathbf{v}}{\Delta t}\cdot\mathbf{b}^{*}d\Omega + \int_{\Omega}\frac{\rho_0}{g_l}\,\left(\frac{-\mathbf{v}^{t-\Delta t}}{\Delta t}+\frac{1}{g_l}\frac{\mathbf{v}^{t-\Delta t}-\tilde{\mathbf{v}}^{t-\Delta t}}{\Delta t}\right)\cdot\mathbf{b}^{*}d\Omega + \int_{\Omega}\frac{\rho_0}{g_l}\,\frac{\mathbf{b}}{\Delta t}\cdot\mathbf{b}^{*}d\Omega \\
&= H^{bl,\,iner}\,\mathbf{V} \quad + \quad R^{b,iner0} \quad + \quad H^{bb,iner}\mathbf{B}
\end{aligned}
\tag{3-134}
$$

The term $R^{l,er}$

$$
\begin{aligned}
R^{l,iner} &= \int_{\Omega}\frac{\rho_0}{g_l}\,\tilde{\gamma}(\mathbf{v}+\mathbf{b})\cdot\mathbf{v}^{*}d\Omega \\
&= \int_{\Omega}\frac{\rho_0}{g_l}\,\left(\frac{\mathbf{v}-\mathbf{v}^{t-\Delta t}}{\Delta t}+\frac{1}{g_l}\frac{\mathbf{v}^{t-\Delta t}-\tilde{\mathbf{v}}^{t-\Delta t}}{\Delta t}\right)\cdot\mathbf{v}^{*}d\Omega + \int_{\Omega}\frac{\rho_0}{g_l}\,\frac{\mathbf{b}}{\Delta t}\cdot\mathbf{v}^{*}d\Omega \\
&= H^{ll,iner}\mathbf{V} \quad + \quad R^{l,\,iner0} \quad + \quad H^{lb,iner}\mathbf{B}
\end{aligned}
\tag{3-135}
$$

- Computation of R^{b}

As mentioned above, we need to eliminate the bubble degrees of freedom δ***B***, and solve only for the variables δ***P*** and δ***V*** at each node. Regarding equation (3-132), R^{b} should be eliminated. According to equation (3-130), we write the residual of R^{b} as follows:

$$
R^{b} = H^{bb,rheo}\mathbf{B} + H^{bp}\mathbf{P} + R^{b,grav} + (H^{lb,perm})^{T}\,\mathbf{V} + H^{bb,perm}\mathbf{B}
\tag{3-136}
$$

Substituting equation (3-136) into the left hand side of equation (3-132), then equation (3-132) reduces to:

$$
\begin{bmatrix}
H^{ll}-H^{lb}(H^{bb})^{-1}(H^{lb})^{T} & H^{lp}-H^{lb}(H^{bb})^{-1}H^{bp} \\
(H^{lp})^{T}-(H^{bp})^{T}(H^{bb})^{-1}(H^{lb})^{T} & -(H^{bp})^{T}(H^{bb})^{-1}H^{bp}
\end{bmatrix}
\begin{bmatrix}\delta\mathbf{V}\\ \delta\mathbf{P}\end{bmatrix}
=
\begin{bmatrix}
-R^{l}+H^{lb}(H^{bb})^{-1}\left\{H^{bp}P+R^{b,grav}+(H^{lb})^{T}\mathbf{V}\right\} \\
-R^{p}+(H^{bp})^{T}(H^{bb})^{-1}\left\{H^{bp}P+R^{b,grav}+(H^{lb})^{T}\mathbf{V}\right\}
\end{bmatrix}
\tag{3-137}
$$

Remark

The stiffness matrix for solving the mechanical problem is symmetric, the system can be solved using the direct symmetric solver with the skyline storage technique (Rappaz *et al.* [2002]), or using the external PETSC solver (PETSC [2003]).

In absence of the Darcy term, and neglecting the contribution of “bubble” component to the inertia term, then H^{lb} equals to zero, leading to the simplification equation (3-137):

$$\begin{bmatrix} H^{ll} & H^{lp} \\ (H^{lp})^T & -(H^{bp})^T(H^{bb})^{-1}H^{bp} \end{bmatrix} \begin{bmatrix} \delta \mathbf{V} \\ \delta \mathbf{P} \end{bmatrix} = \begin{bmatrix} -R^l \\ -R^p + (H^{bp})^T (H^{bb})^{-1} R^{b,grav} \end{bmatrix} \tag{3-138}$$

Equation (3-138) is used for the one-phase continuum model. But we have found that the term H^{lb} is of importance when Darcy terms are present.

3.6.2 Axisymmetric formulation

In many practical cases, the solidification of casting parts can be axially symmetric. If the loads and constraints are also axially symmetric, then the problem can be formulated using the two velocity components v_r and v_z. The subscripts r and z denote the radial and axial directions respectively. Although only two velocity components v_r and v_z need to be considered in the axisymmetric case, there are still some differences from the 2-dimensional plane case, which are presented as follows.

3.6.2.1 Additional term $\dot{\varepsilon}_{\theta\theta}$

Unlike the 2-dimensional plane case, the strain rate tensor for an axisymmetric problem takes the form:

$$\dot{\varepsilon} = \begin{bmatrix} \frac{\partial v_r}{\partial r} & 0 & \frac{1}{2}(\frac{\partial v_r}{\partial z} + \frac{\partial v_z}{\partial r}) \\ 0 & \frac{v_r}{r} & 0 \\ \frac{1}{2}(\frac{\partial v_r}{\partial z} + \frac{\partial v_z}{\partial r}) & 0 & \frac{\partial v_z}{\partial z} \end{bmatrix} \tag{3-139}$$

Comparing with the plane problem, it is then no longer possible to consider only the components of the r and z axes, the additional term, $\dot{\varepsilon}_{\theta\theta} = \frac{v_r}{r}$, must be considered. The new contributions to $R^{l,rheo}$ and $R^{b,rheo}$ appear in equation (3-129):

$$\dot{\varepsilon}_{\theta\theta}(\mathbf{v})\dot{\varepsilon}_{\theta\theta}(\mathbf{v}^*) \text{ and } \dot{\varepsilon}_{\theta\theta}(\mathbf{b})\dot{\varepsilon}_{\theta\theta}(\mathbf{b}^*) \tag{3-140}$$

and the additional term appears also in mass conservation equation:

$$\nabla \cdot \mathbf{v} = \frac{\partial v_r}{\partial r} + \frac{\partial v_z}{\partial z} + \frac{v_r}{r} \tag{3-141}$$

3.6.2.2 Computation of integration terms

The surface differentiation is $d\Omega = 2\pi r dr dz$ instead of $d\Omega = dxdy$ in Cartesian coordinates. This modifies the integration rules. For instance the integration of a linear function f will need three integration points in axisymmetric case instead of only one in the plane case. In order to integrate each terms in equations (3-129), we have adopted a similar strategy as Etienne Perchat [2000] used in the axisymmetric and the P1+/P1 version of FORGE2. In R2SOL, those three points have been chosen either as the usual Gaussian points or the three mid-points of each edge of the triangle.

As it has been mentioned above, the value of the "bubble" interpolation function N^b is 1 at the triangle centre and 0 at its boundary, and it is defined separately on each of the three subtriangles. So that the integration for the terms that comprises N^b has to be decomposed into the sum of three integrations on the sub-triangles shown in Figure 3-10. In this case, the three mid-edge integration points have been used. Three Gaussian integration points have been used when the term does not comprise N^b.

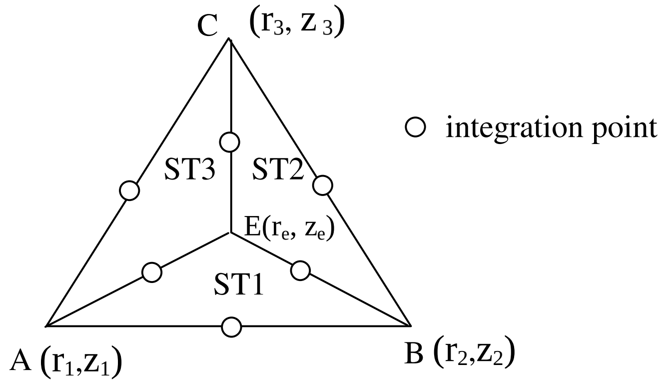

Figure 3-10 Schematic of the integration points

In the following paragraph, for example the computation of the Darcy term is presented to show the integration rule used in the axisymmetric case.

3.6.2.3 Computation of the Darcy term

Let us compute the Darcy term resulting from the "bubble" contribution, the matrix H^b and H^{bb}, which is important in the computation of macrosegregation.

- Term H^b

From equations (3-129) a) and (3-130) a), we find the residual, $R^{,}$, arising from the Darcy term as follows:

$$R^{l,perm}=\int\frac{\mu}{K}(\mathbf{v}+\mathbf{b})\cdot\mathbf{v}^{*}\,2\pi r\,dr\,dz=\int\frac{\mu}{K}\mathbf{v}\cdot\mathbf{v}^{*}\,2\pi r\,dr\,dz+\int\frac{\mu}{K}\mathbf{b}\cdot\mathbf{v}^{*}\,2\pi r\,dr\,dz \tag{3-142}$$

$$R^{ll,perm}=\int\frac{\mu}{K}\mathbf{v}\cdot\mathbf{v}^{*}\,2\pi r\,dr\,dz\,,\qquad R^{lb,perm}=\int\frac{\mu}{K}\mathbf{b}\cdot\mathbf{v}^{*}\,2\pi r\,dr\,dz \tag{3-143}$$

where the residual $R^{,}$ has been decomposed into two parts, $R^{ll,perm}$ and $R^{l\ ,perm}$. $R^{ll,perm}$ depends on the linear velocity field **v**, and $R^{l\ ,perm}$ depends on the bubble contribution **b**.

Then, the Hessian matrix with respect to the bubble contribution **b** gives:

$$H^{lb,perm}_{nk,l}=\frac{\partial R^{lb,perm}_{nk}}{\partial \mathbf{B}_l}=\int\frac{\mu}{K}N_n N^b\delta_{kl}\,2\pi r\,dr\,dz \tag{3-144}$$

where *n*, *k* and *l* are the degrees of freedom. δ is the Kronecker function.

$H^{lb,perm}_{nk,l}$ is integrated numerically in the three subtriangles of an element using the three mid-edge integration points.

- Term $H^{bb,perm}$

Regarding the residual $R^{b,perm}$ in equation (3-129) b) and (3-130) b), we have:

$$R^{b,perm}=\int\frac{\mu}{K}(\mathbf{v}+\mathbf{b})\cdot\mathbf{b}^{*}\,2\pi r\,dr\,dz=\int\frac{\mu}{K}\mathbf{v}\cdot\mathbf{b}^{*}\,2\pi r\,dr\,dz+\int\frac{\mu}{K}\mathbf{b}\cdot\mathbf{b}^{*}\,2\pi r\,dr\,dz \qquad (3\text{-}145)$$

$$R^{bb,perm}=\int\frac{\mu}{K}\mathbf{b}\cdot\mathbf{b}^{*}\,2\pi r\,dr\,dz, \qquad R^{bl,perm}=\int\frac{\mu}{K}\mathbf{v}\cdot\mathbf{b}^{*}\,2\pi r\,dr\,dz \qquad (3\text{-}146)$$

The Hessian matrix with respect to the bubble contribution **b** gives:

$$H_{k,l}^{bb,perm}=\frac{\partial R_{k}^{bb,perm}}{\partial \mathbf{B}_{l}}=\int\frac{\mu}{K}N^{b}N^{b}\delta_{kl}\,2\pi r\,dr\,dz \qquad (3\text{-}147)$$

Again, $H^{bb,perm}$ is integrated in the three subtriangles of an element using the three mid-edge integration points.

3.6.3 Resolution of momentum equation with the SUPG-PSPG formulation

Considering the momentum equation (3-8), let us assume that we have constructed the suitably defined function spaces S_v and S_p for the velocity and pressure respectively. The classical weak formulation for the fluid flow can be stated as: find $(\mathbf{V},p)\in S_v\times S_p$, such that for all the $(\mathbf{V}^{*},p^{*})\in S_v\times S_p$ the following holds:

$$\begin{cases}\forall\mathbf{V}^{*} & \displaystyle\int_{\Omega}\frac{\rho_0}{g_l}\left[\frac{\partial\mathbf{V}}{\partial t}+\frac{1}{g_l}(\nabla\mathbf{V})\mathbf{V}\right]\cdot\mathbf{V}^{*}d\Omega+\int_{\Omega}\frac{2\mu}{g_l}\dot{\boldsymbol{\varepsilon}}(\mathbf{V}):\dot{\boldsymbol{\varepsilon}}(\mathbf{V}^{*})d\Omega-\int_{\Omega}p\nabla\cdot\mathbf{V}^{*}d\Omega \\ & \displaystyle-\int_{\partial\Omega}\frac{1}{g_l}\mathbf{T}\cdot\mathbf{V}^{*}d\Gamma-\int_{\Omega}\rho\mathbf{g}\cdot\mathbf{V}^{*}d\Omega+\int_{\Omega}\frac{\mu}{K}\mathbf{V}\cdot\mathbf{V}^{*}d\Omega=0 \\ \forall p^{*} & \displaystyle-\int_{\Omega}p^{*}\nabla\cdot\mathbf{V}d\Omega=0\end{cases} \qquad (3\text{-}148)$$

Regarding the standard weak form of equation (3-148), the velocity and pressure fields need to be stabilized. The stabilization can be achieved using the SUPG-PSPG formulation.

3.6.3.1 The SUPG-PSPG formulation

Following the work of Tezduyar *et al*. [1992], Tezduyar and Osawa [2000], the SUPG-PSPG formulation writes:

$$\left\{\begin{aligned}
&\forall \mathbf{V}^* \quad \int_\Omega \frac{\rho_0}{g_l}\left[\frac{\partial \mathbf{V}}{\partial t} + \frac{1}{g_l}(\nabla \mathbf{V})\mathbf{V}\right]\cdot \mathbf{V}^* d\Omega + \int_\Omega \frac{2\mu}{g_l}\dot{\boldsymbol{\varepsilon}}(\mathbf{V}):\dot{\boldsymbol{\varepsilon}}(\mathbf{V}^*)d\Omega - \int_\Omega p\nabla\cdot\mathbf{V}^* d\Omega \\
&\qquad - \int_{\partial\Omega}\frac{1}{g_l}\mathbf{T}\cdot\mathbf{V}^* d\Gamma - \int_\Omega \rho\mathbf{g}\cdot\mathbf{V}^* d\Omega + \int_\Omega \frac{\mu}{K}\mathbf{V}\cdot\mathbf{V}^* d\Omega \\
&\qquad + \int_\Omega \tau_{SUPG}(\nabla\mathbf{V}^*)\mathbf{V}\cdot\left\{\frac{\rho_0}{g_l}\frac{\partial\mathbf{V}}{\partial t} + \frac{\rho_0}{g_l^2}(\nabla\mathbf{V})\mathbf{V} - \frac{1}{g_l}\nabla\cdot(\mu\nabla\mathbf{V}) + \nabla p - \rho\,\mathbf{g} + \frac{\mu}{\mathrm{K}}\mathbf{V}\right\}d\Omega \\
&\qquad + \int_\Omega \tau_{LSIC}\nabla\cdot\mathbf{V}^*\rho_0\nabla\cdot\mathbf{V}d\Omega = 0 \\
&\forall p^* \quad \int_\Omega -p^*\nabla\cdot\mathbf{V}d\Omega \\
&\qquad - \int_\Omega \tau_{PSPG}\frac{1}{\rho_0}\nabla p^*\cdot\left\{\frac{\rho_0}{g_l}\frac{\partial\mathbf{V}}{\partial t} + \frac{\rho_0}{g_l^2}(\nabla\mathbf{V})\mathbf{V} - \frac{1}{g_l}\nabla\cdot(\mu\nabla\mathbf{V}) + \nabla p - \rho\,\mathbf{g} + \frac{\mu}{\mathrm{K}}\mathbf{V}\right\}d\Omega = 0
\end{aligned}\right. \tag{3-149}$$

where, τ_{SUPG} is the SUPG (Streamline-Upwind/Petrov-Galerkin) stabilization parameter;

τ_{PSPG} is the PSPG (Pressure-Stabilizing/Petrov-Galerkin) stabilization parameter;

τ_{LSIC} is the LSIC (least-squares on incompressibility constant) stabilization parameter;

the brackets $\{\ \}$ denote the residual of the momentum equation.

Comparing with the standard weak form (3-148), three terms have been added, corresponding to the stabilizations of SUPG, PSPG and the incompressibility constraint respectively. The stabilization parameters will be introduced later in this section.

For the SUPG-PSPG stabilized formulation, one can use the equal-order interpolation function for the velocity and pressure. In the present work, linear triangle elements are used. The second-order terms $2\mu\,\dot{\boldsymbol{\varepsilon}}(\mathbf{V})$ in the the branket $\{\ \}$ associated with the SUPG and PSPG stabilizations vanish, just like the term $\nabla\cdot(\lambda\nabla T)=0$ in the SUPG stabilized energy equation (3-41). Regarding the temporal discretization, the Euler backward implicit scheme is used.

3.6.3.2 Stabilization parameters

Hereunder, we present the definitions of stabilization parameters, which are motivated by the work of Shakib *et al*. [1991], Tezduyar and Park [1986], Tezduyar and Osawa [2000]. The characteristic length of a triangle element along the flow direction, h, has been given by equation (3-46). To compute the stabilization parameters, we note that the known velocity $\mathbf{V}^{t-\Delta t}$ at the element center is used.

- τ_S and τ_S

As we have presented in section 3.3.2, the SUPG stabilization parameter for the energy transport equation is expressed by:

$$\tau_{SUPG} = \frac{\theta\,h}{2\|\mathbf{V}\|} \quad \text{with} \quad \theta = \coth(Pe_h) - \frac{1}{Pe_h}$$

In practice, several versions of stabilization parameter are used instead of the "optimal" coth function. The version of Shakib *et al.* [1991] with $\theta=(1+\frac{1}{Pe_h^2})^{-1/2}$ may be the most frequently used, that is:

$$\tau_{SUPG}=\frac{\theta\, h}{2\|\mathbf{V}\|}=\left[\left(\frac{2\|\mathbf{V}\|}{h}\right)^2+\left(\frac{4\alpha}{h^2}\right)^2\right]^{-1/2} \tag{3-150}$$

where α is the thermal diffusivity. For the momentum transport, the viscosity μ can be used instead of the diffusion coefficient α.

The two terms in the right-hand expression can be interpreted as the advection-dominated and diffusion-dominated limits (Tezduyar and Osawa [2000]). Accounting for the transient-dominated case, Tezduyar and Osawa [2000] supposed that:

$$\tau_{SUPG}=\left[\left(\frac{2}{\Delta t}\right)^2+\left(\frac{2\|\mathbf{V}\|}{h}\right)^2+\left(\frac{4\mu}{h^2}\right)^2\right]^{-1/2} \tag{3-151}$$

In the present work, equation (3-151) is used to compute the SUPG stabilization parameter τ_{SUPG}. Following Tezduyar and Park [1986], the PSPG stabilization parameter τ_{PSPG} is defined in the same way as τ_{SUPG}, *i.e.*, $\tau_{PSPG}=\tau_{SUPG}$.

- τ_{LSIC}

The LSIC stabilization parameter given by Tezduyar and Osawa [2000] is as follows:

$$\tau_{LSIC}=\frac{h}{2}\|\mathbf{V}\|\, z \tag{3-152}$$

where, z is a function of the element Reynolds number $R_e=\frac{\|\mathbf{V}\|\, h\rho_0}{2\mu}$, defined by:

$$z=\begin{cases}\frac{Re}{3} & if\;\; Re\le 3\\ 1 & if\;\; Re>3\end{cases} \tag{3-153}$$

3.6.3.3 Implementation of the SUPG-PSPG formulation

Regarding the SUPG-PSPG formulation in equation (3-149), the system is non-linear. The Newton-Raphson method is used. In the following text, firstly, we present the matrix formulation to solve equation (3-149). It is possible to linearize the equation, so that one can simplify the computation. Then, the linearized formulations are introduced. Finally, we present the differences between the axisymmetric and plane versions.

- **The matrix formulation**

According to equation (3-149) a), the residual vector for the velocity component can be expressed by the condensed form:

$$\begin{aligned}R^l=&R^{l,transient}+R^{l,adv}+R^{l,rheo}+R^{l,pre}+R^{l,t}+R^{l,grav}+R^{l,perm}\\&+R^{l,transient}_{SUPG}+R^{l,adv}_{SUPG}+R^{l,pre}_{SUPG}+R^{l,grav}_{SUPG}+R^{l,perm}_{SUPG}\\&+R^{l}_{LSIC}\end{aligned} \tag{3-154}$$

In the above equation, the terms in the first line on the right hand side denote the contributions associated with the transient, advection (inertia), rheology (diffusion), pressure, contact force on the boundary, gravity and Darcy terms respectively. These contributions are computed using the standard Galerkin test function. The terms in the second line denote the contributions of the SUPG stabilization. Comparing with the first line, we note that the rheology (diffusion) term vanishes, because this term related to the second order differential operator is identically zero for linear P1 elements. The term appearing in the third line presents the LSIC contribution.

According to equation (3-149) b), the residual vector for the pressure component can be expressed by:

$$R^{p} = R^{p,incomp} + R^{p,transient}_{PSPG} + R^{p,adv}_{PSPG} + R^{p,pre}_{PSPG} + R^{p,grav}_{PSPG} + R^{p,perm}_{PSPG} \tag{3-155}$$

In equation (3-155), $R^{p,incomp}$ denotes the traditional term arising from the contribution of the incompressibility constraint, the other terms express the contributions resulting from the PSPG stabilization.

To solve the equation (3-149) with the Newton-Raphson method, it is possible to write the following matrix formulation of the iterative corrections on nodal velocity and pressure to be calculated:

$$\begin{bmatrix} H^{ll} & H^{lp} \\ (H^{lp})^{T} & H^{pp} \end{bmatrix} \begin{bmatrix} \delta \mathbf{V} \\ \delta \mathbf{P} \end{bmatrix} = \begin{bmatrix} -R^{l} \\ -R^{p} \end{bmatrix} \tag{3-156}$$

Since the non-zero diagonal term H^{pp} in equation (3-156) is important to avoid a singular matrix, the term H^{pp} and the corresponding residual resulting from the contribution of PSPG stabilization $R^{p,pre}_{PSPG}$ are expressed as:

$$R^{p,pre}_{PSPG,\,l} = -\int_{\Omega} \frac{1}{\rho_0} \tau_{PSPG}\, \nabla p^{*} \cdot \nabla p \, d\Omega = -\int_{\Omega} \frac{1}{\rho_0} \tau_{PSPG} \frac{\partial N_l}{\partial x_k} \cdot \frac{\partial N_m}{\partial x_k} p_m \, d\Omega \tag{3-157}$$

and

$$H^{pp}_{l,m} = \frac{\partial R^{p,pre}_{PSPG,l}}{\partial p_m} = -\int_{\Omega} \frac{1}{\rho_0} \tau_{PSPG} \frac{\partial N_l}{\partial x_k} \cdot \frac{\partial N_m}{\partial x_k} d\Omega \tag{3-158}$$

where *l* and *m* denote the index of nodes. *N* is the linear interpolation function.

For the equation (3-156), we note that the stiffness matrix is non-symmetric.

- **The linearized formulation**

As equation (3-149) is non-linear, in order to simplify the computation, we have linearized the SUPG-PSPG formulation. The advection term $(\nabla \mathbf{V}^{t})\mathbf{V}^{t}$ has been linearized by computing $(\nabla \mathbf{V}^{t})\mathbf{V}^{t-\Delta t}$. While the SUPG term $\tau_{SUPG}(\nabla \mathbf{V}^{*})\mathbf{V}^{t}$ has been changed to $\tau_{SUPG}(\nabla \mathbf{V}^{*})\mathbf{V}^{t-\Delta t}$. For example, we present the linearized advection terms as follows.

The residual component, $R^{l,adv}$, arising from the advection term $(\nabla \mathbf{V})\mathbf{V}$ can be linearized by:

$$R^{l,adv} = \int_{\Omega} \frac{\rho_0}{g_l^{2}} (\nabla \mathbf{V}^{t}) \mathbf{V}^{t-\Delta t} \cdot \mathbf{V}^{*} d\Omega \tag{3-159}$$

The residual component, $R^{l,adv}_{SUPG}$, arising from the SUPG stabilization can be written as:

$$R^{l,adv}_{SUPG} = \int \tau_{SUPG} (\nabla \mathbf{V}^{*})\mathbf{V}^{t-\Delta t} \cdot \frac{\rho_0}{g_l^2}(\nabla \mathbf{V}^{t})\mathbf{V}^{t-\Delta t} d\Omega \tag{3-160}$$

For the component of the residual vector, $R^{l,adv}_{nk}$, which is associated with the node n and expresses the degree of freedom for the velocity in the direction k, we can express equation (3-159) in detail:

$$R^{l,adv}_{nk} = \int_{\Omega} \frac{\rho_0}{g_l^2} \underbrace{\frac{\partial N_m}{\partial x_j}(V_k^m)^t}_{(\nabla \mathbf{V})^t_{kj}} \cdot \underbrace{N_q (V_j^q)^{t\text{-}\Delta t}}_{\mathbf{V}_j^{t-\Delta t}} \; N_n d\Omega \tag{3-161}$$

where j and k vary from 1 to 2 for 2-dimensional problems. x_j denotes the spatial coordinate in the j direction. m, n and q denote the index of nodes, based on these nodal velocities, the velocity fields at time $t-\Delta t$ and, t, $\mathbf{V}^{t-\Delta t}$ and $\mathbf{V}^{t}$, are interpolated. N is the linear interpolation function.

The component of residual vector, $R^{l,adv}_{SUPG,nk}$, writes:

$$R^{l,adv}_{SUPG,nk} = \int_{\Omega} \tau_{\text{SUPG}} \frac{\rho_0}{g_l^2} \underbrace{\frac{\partial N_n}{\partial x_i}}_{(\nabla \mathbf{V}^{*})_{ni}} \underbrace{(N_m V_i^m)^{t\text{-}\Delta t}}_{\mathbf{V}_i^{t-\Delta t}} \cdot \underbrace{\frac{\partial N_q}{\partial x_j}(V_k^q)^t}_{(\nabla \mathbf{V})^t_{kj}} \; \underbrace{N_s (V_j^s)^{t\text{-}\Delta t}}_{\mathbf{V}_j^{t-\Delta t}} \; d\Omega \tag{3-162}$$

- **The axisymmetric formulation**

As it has been presented for the axisymmetric version of P1+/P1 formulation, following points need to be considered:

1) the additional term $\dot{\varepsilon}_{\theta\theta}$, $\dot{\varepsilon}_{\theta\theta} = \frac{v_r}{r}$, which appears in the rheology (diffusion) term;

2) the surface differentiation is $d\Omega = 2\pi r drdz$ instead of $d\Omega = dxdy$ in Cartesian coordinates.

These two points have been taken into account, regarding the implementation of the SUPG-PSPG formulation.

In addition, we have checked the SUPG-PSPG stabilized terms, arising from the perturbations of $\tau_{SUPG}(\nabla \mathbf{V}^{*})\cdot \mathbf{V}$ and $\tau_{PSPG}\frac{1}{\rho_0}\nabla P^{*}$: these terms are identical for the plane and axisymmetric cases, except the surface differentiation (the point 2 as presented above).

It should be noted that there are few differences in the computation of the LSIC contribution R^{l}_{LSIC}, between the plane and axisymmetric cases. The difference arises from the computation of $\nabla\cdot\mathbf{V}^{*}\ \nabla\cdot\mathbf{V}$. For the plane case, the residual component, R^{l}_{LSIC}, can be expressed by:

$$\begin{aligned} R^{l}_{LSIC,nk} &= \int_{\Omega} \tau_{LSIC}\, \rho_0 (\nabla\cdot\mathbf{V}^{*})\,(\nabla\cdot\mathbf{V}) d\Omega \\ &= \int_{\Omega} \tau_{LSIC}\ \rho_0 \frac{\partial N_n}{\partial x_k}\ \frac{\partial N_m}{\partial x_j}\,(\mathbf{V}_j^m) d\Omega \end{aligned} \tag{3-163}$$

where j and k vary from 1 to 2 for plane problems. m and n denote the index of nodes, N being the linear interpolation function.

For the axisymmetric case, $\nabla\cdot\mathbf{V}=\frac{\partial N_n}{\partial x_k}V_k^n+\frac{v_r}{r}$, leading to the difference to compute the term of R^l_{LSIC}, then we have:

$$
\begin{aligned}
R^l_{LSIC,nk} &= \int_\Omega \tau_{LSIC}\,\rho_0\,(\nabla\cdot\mathbf{V}^*)\,(\nabla\cdot\mathbf{V})d\Omega \\
&= \int_\Omega \tau_{LSIC}\,\rho_0 \left(\frac{\partial N_n}{\partial x_k}+\frac{N_n}{r}\delta_{k1}\right)\left(\frac{\partial N_m}{\partial x_j}V_j^m+\frac{N_m V_1^m}{r}\right)2\pi r\,dr\,dz
\end{aligned}
\tag{3-164}
$$

where, δ is the Kronecker function.

3.7 Validations

Firstly, we test the nodal upwind P1+/P1 formulation. Two cases have been considered. In the first case, a pure Navier-Stokes problem, without Darcy term, has been chosen to validate the code for additional term $\dot{\varepsilon}_{\theta\theta}$ and inertia term. In the second case, flow through a porous medium with a constant permeability has been considered to validate the Darcy term.

Secondly, we test the new developement of SUPG-PSPG formulation.

Finally, the solidification of a carbon steel alloy in a square cavity has been considered to validate the macrosegregation model, here the nodal upwind P1+/P1 formulation is used.

3.7.1 Axisymmetric formulation in the case of Navier-Stokes flow

The test of the Navier-Stokes problem is inspired from the De Vahl-Davis [1983] benchmark, which consists of a steady natural convection in a square cavity in plane strain conditions. Similarly we have chosen a hollow axisymmetric cavity, shown in Figure 3-11. The thermal boundary condition is as follows: the top and bottom are adiabatic; the temperature on the side walls is fixed: temperature on the inner wall is imposed to be 1.0°C, temperature on the outer wall is 0°C. As one can imagine when the inner radius R_{inner} tends to infinite, the computational result of such an axisymmetric problem should tend to that of the plane. So we choose testing cases as shown in Table 3-1. The computational result of case 1 is expected to be different from that of case 2, and case 2 should be very close to case 3. We use PHOENICS, a finite volume difference code, to recalculate case 1, the computational results obtained by PHOENICS and R2SOL (test 1) are expected to coincide. The physical data are shown in Table 3-2. They have been chosen to obtain a Rayleigh number equal to 10^4 (relatively high advection flow). Contact at walls is supposed to be sticky (no sliding velocity).

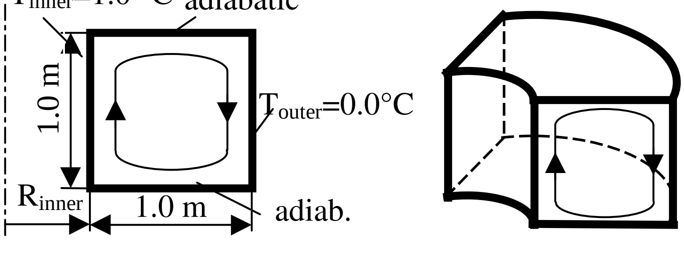

Figure 3-11 Schematic of the axisymmetric natural convection test

Table 3-1 Testing cases for Navier-Stokes flow

Case	1	2	3	4
R_{inner} (m)	1.0	1000.0	plane	1.0
Solver	R2SOL	R2SOL	R2SOL	PHOENICS

Table 3- 2 Data used for the computation

Physical properties	Initial and boundary temperatures
$\rho(T)=\rho_0(1-\beta_T(T-T_{init}))$	T_{init} = 0.5°C
ρ_0 = 1.0 kg. m^{-3}	
μ = 0.71 ×10^{-2} Pa.s	T_{inner} = 1.0°C
λ = 1.0 W. m^{-1}. K^{-1}	T_{outer} = 0.0°C
c_p = 100.0 J. kg^{-1}. K^{-1}	
β_T = 7.1 ×10^{-2} K^{-1}	

- Comparison between axisymmetric and plane flow (R2SOL computation)

The computational results of test cases 1 to 3 are shown in Figure 3-12. On the first line, the temperature field is shown. On the second one, velocity vectors and the third one, the vertical component of velocity.

First, and as expected, the results of case 2 (axisymmetrical computation with a huge radius) and case 3 (plane case) are identical. The only differences can be attributed to the convergence criterion for the obtention of a steady-state regime.

Let us come to the comparison between plane and axisymmetric cases. Near the inner wall, the temperature gradient is steeper in case 1 than in case 3 (or 2). This is due to axisymmetry: as the flow is convergent from the outer wall to the inner one, it is accelerated. The velocity is then higher near the inner wall than in the plane case (see line 3, test 1), seeing Figure 3-12, $V_z^{\max}=0.215(m\cdot s^{-1})$ in case 1, $V_z^{\max}=0.187(m\cdot s^{-1})$ in case 2(or 3) . The consequence is that the heat transfer is less diffusive – more advective – in this region, and therefore the normal gradient is higher. Conversely, the flow coming back to the outer wall at the top of the cavity is divergent and then decelerated, resulting in a lower velocity than in plane case in this region. The temperature distribution is then smoother in case 1 than in case 2, because the heat transfer is more diffusive. These expected effects can be clearly seen on the different figures.

Also it can be seen that the centre of the vortex in case 1 is slightly displaced upwards (in the plane case, it is located at the centre of the cavity). This is due to inertia effects associated with the non symmetrical velocity distribution.

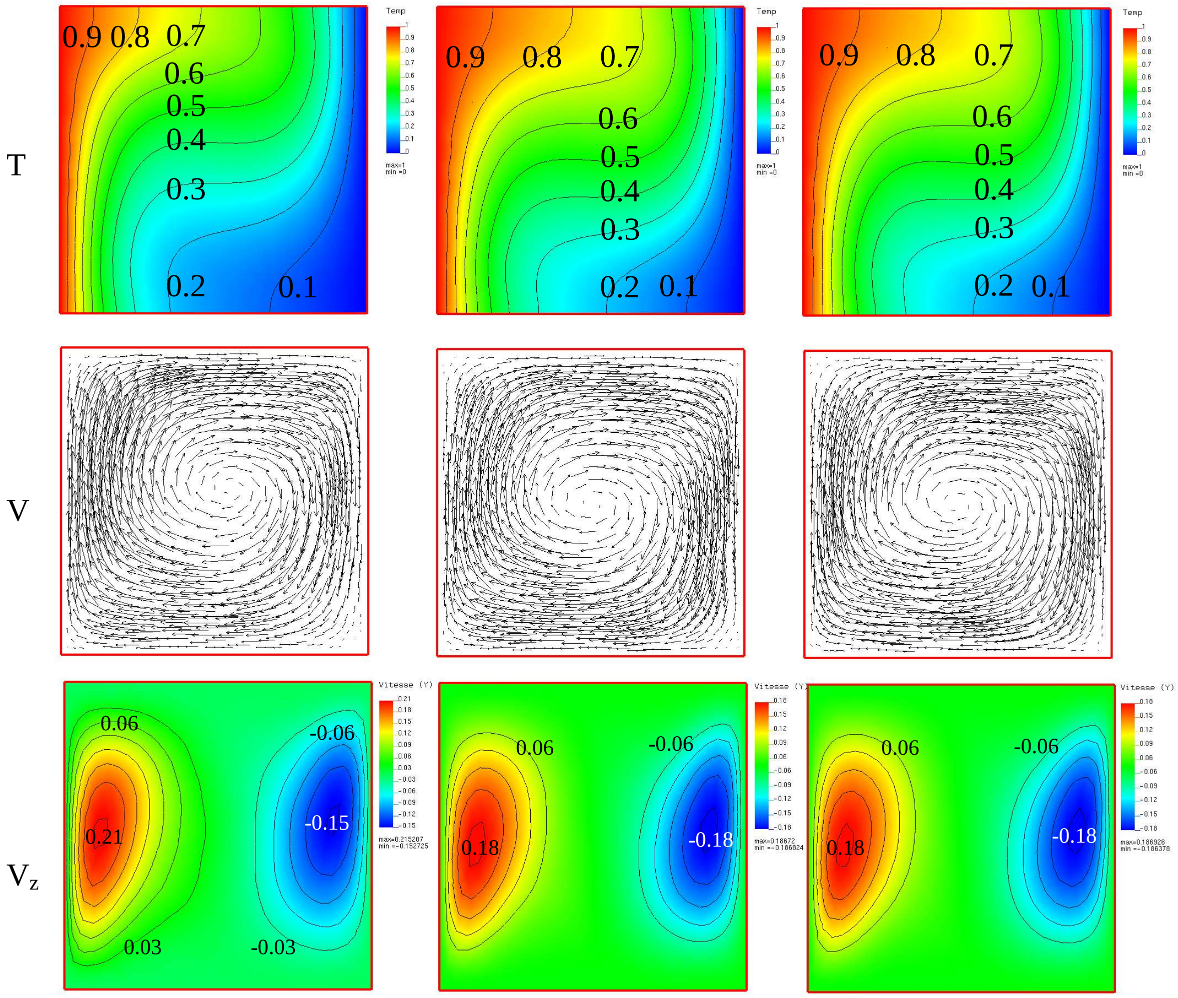

(a) Test case 1 (b) Test case 2 (c) Test case 3

R_{inner} = 1 m R_{inner} = 1000 m plane case

	Test case 1		Test case 2		Test case 3	
Velocities (m.s^{-1})	v_r	v_z	v_r	v_z	v_x	v_y
Max	0.169	0.215	0.155	0.187	0.154	0.187
Min	-0.134	-0.153	-0.156	-0.187	-0.155	-0.186

Figure 3-12 Comparisons of temperature fields and velocity vectors, test cases 1, 2 and 3 (R2SOL computation)

- Comparison between R2SOL and PHOENICS (axisymmetric case)

This comparison is achieved by means of test case 1 and test case 4. The comparison of the results is given in Figure 3-13 in which the picture of the temperature field obtained with PHOENICS is put over that of R2SOL properly. The contours of temperature obtained by R2SOL coincide with those of PHOENICS, as shown in Figure 3-13 (a). The velocity fields are compared by the distribution of component v_r shown in Figure 3-13 (b): the two pictures look alike each other. The quantitative comparison of velocity component is given in Table 3-3. The values of maximum and minimum velocity component obtained by R2SOL and PHOENICS are close to each other as well as their position.

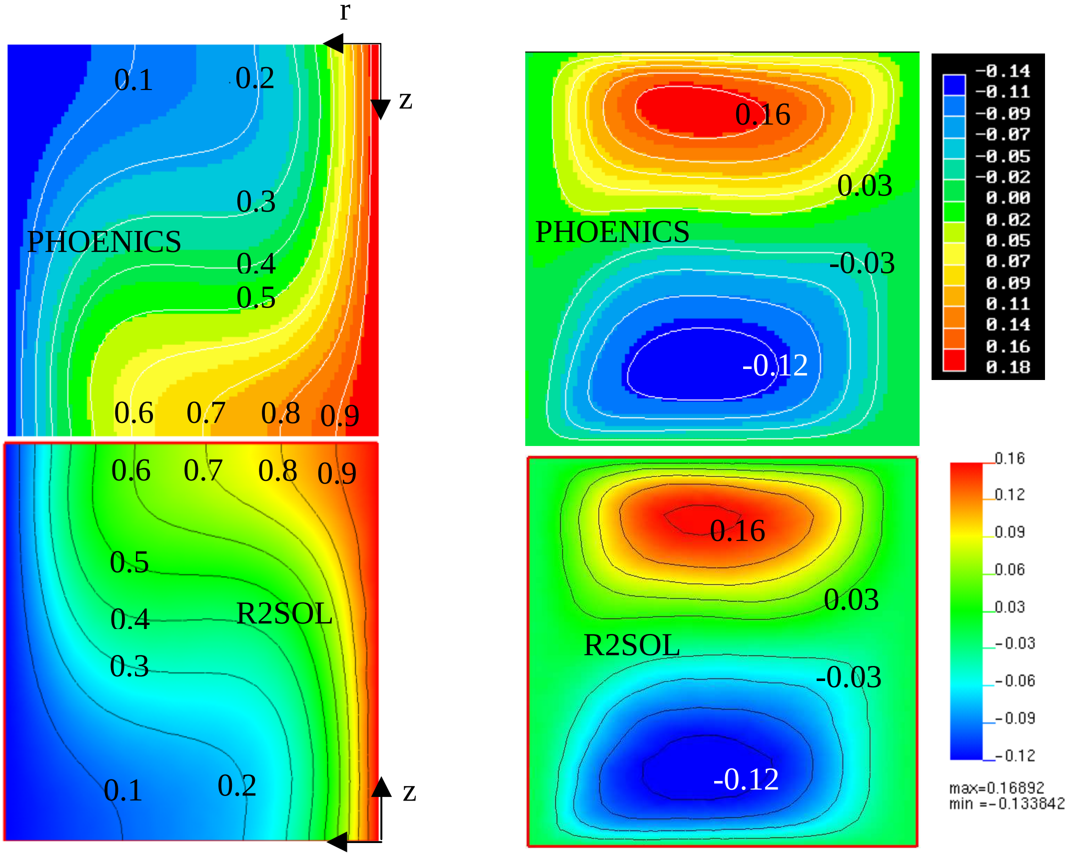

(a) Temperature (b) velocity component v_r

Figure 3-13 Comparison between R2SOL (test case 1) and PHOENICS (test case 4)

Table 3- 3 Velocities obtained by R2SOL and PHOENICS

	Max.v_z (m /s)	Position (r,z)(m)	Min. v_z (m /s)	Position (r,z) (m)	Max.v_r (m /s)	Position (r,z) (m)	Min. v_r (m /s)	Position (r,z) (m)
R2SOL	0.215	(1.12,0.50)	-0.153	(1.88,0.57)	0.169	(1.43,0.84)	-0.134	(1.46,0.19)
PHOENICS	0.236	(1.11,0.52)	-0.164	(1.89,0.57)	0.183	(1.42,0.86)	-0.137	(1.45,0.20)

3.7.2 Validation of Darcy term (axisymmetric case, computed by R2SOL and PHOENICS)

The test is similar to the test case 1 and test case 4 presented in section 3.7.1, but this time, we assume that the cavity is full of a porous medium, whose permeability K is uniform and constant, 1/K=100.0 m^{-2}. The comparison of the results is given in Figure 3-14, the upper figures are the results of PHOENICS, the lower are the ones of R2SOL. The contours of temperature obtained by R2SOL and PHOENICS coincide with each other as shown in Figure 3-14 (a). The velocity components v_r and v_z are shown in Figure 3-14 (b) and Figure 3-14 (c). The quantitative comparison of velocity component is given in Table 3-4. The computational results of R2SOL and PHOENICS are close to each other.

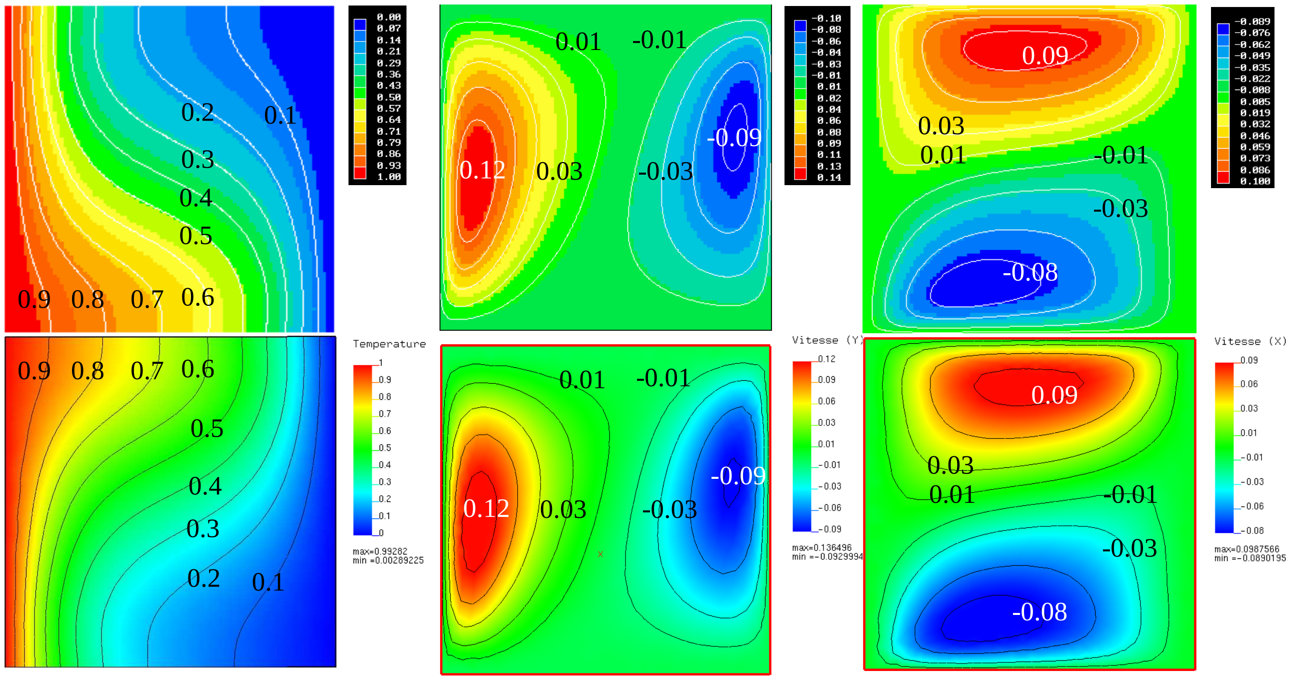

(a) Temperature (b) v_z (c) v_r

Figure 3-14 Comparison between R2SOL and PHOENICS, 1/K=100.0 m^{-2}

Table 3- 4 Velocities obtained by R2SOL and PHOENICS, 1/K=100.0 m^{-2}

	Max. v_z (m /s)	Position (r,z)(m)	Min.v_z (m /s)	Position (r,z) (m)	Max.v_r (m /s)	Position (r,z) (m)	Min. v_r (m /s)	Position (r,z) (m)
R2SOL	0.136	(1.10,0.43)	-0.093	(1.88,0.57)	0.099	(1.52,0.85)	-0.089	(1.34,0.15)
PHOENICS	0.144	(1.10,0.45)	-0.096	(1.90,0.60)	0.099	(1.47,0.87)	-0.089	(1.34,0.15)

The contribution of "bubble" component to the Darcy term has been tested by means of the new version of R2SOL. The computations taking into account or not the H^{lb} term have been carried out, the other conditions being the same as mentioned above. The computational results show that the contribution is less than 0.5% and can be neglected in the particular case of using a constant permeability. It should be noted that the permeability field in a solidifying casting is not homogeneous, the H^{lb} term can not be neglected. In this case, it has been found that the computation without accounting for the H^{lb} term, leads to a wrong solution.

3.7.3 Validations of the SUPG-PSPG formulation

3.7.3.1 Lid-driven cavity test

The evaluation of nodal-upwind P1+/P1 and SUPG-PSPG (P1) Navier-Stokes solvers has been done with a classical benchmark test, the lid-driven cavity test (Ghia *et al.* [1982]). Figure 3-15 presents the numerical setup, which consists of non-slip boundaries (zero velocity) everywhere except the top, on which a velocity is prescribed, shear forces driving the fluid flow within the cavity. In our computation, a square 0.1 × 0.1 m^2 is considered. The mesh is shown in Figure 3-16: fine elements are adopted near boundary (their size being 1.5 mm), coarse elements (size 3.0 mm) are used in the middle region.

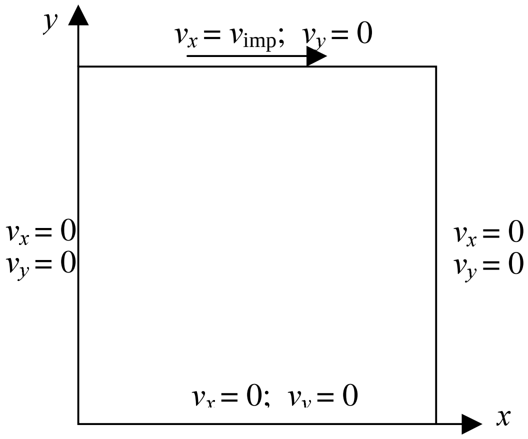

Figure 3-15 The numerical set up

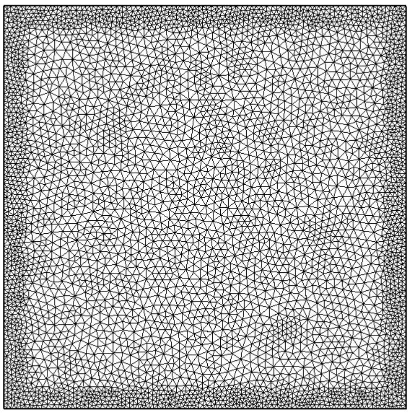

Figure 3-16 The mesh used in R2SOL

The computations with Re = 400 and Re = 1000 have been done by R2SOL, using the SUPG-PSPG and the nodal upwind P1+/P1 formulations. The results have been compared with those of Ghia *et al.* [1982], which are obtained by a second-order accurate finite difference multigrid method with a 129 ×129 grid. Typically, we compare the horizontal velocity component along the vertical center line of the cavity and the vertical velocity component along the horizontal center line of the cavity. Figure 3-17and Figure 3-18 present the results computed with Re = 400 and Re = 1000 respectively. Very good agreements with the reference resolutions have been achieved, using the SUPG-PSPG solver. There are some differences between the results computed with the nodal upwind P1+/P1 solver and the SUPG-PSPG solver. These differences grow with Re. According to Figure 3-17 b) and Figure 3-18 b), a quantitative comparison of maximum and minimum values of vertical velocity component v_y is given in Table 3-5. It seems that the P1+/P1 solver smoothes the velocity fields, with increasing Re number.

Table 3-5 Comparison of maximum and minimum values of v_y,

	Re = 400, Figure 3-17 b)					Re = 1000, Figure 3-18 b)			
	Max.v_y	position x	min.v_y	position x		max. v_y	position x	min. v_y	position x
P1+/P1	0.244	0.250	-0.383	0.850		0.285	0.222	-0.427	0.854
SUPG-PSPG	0.302	0.222	-0.450	0.871		0.376	0.159	-0.528	0.909
Error in v_y (%)	19.2		14.9			24.2		19.1	

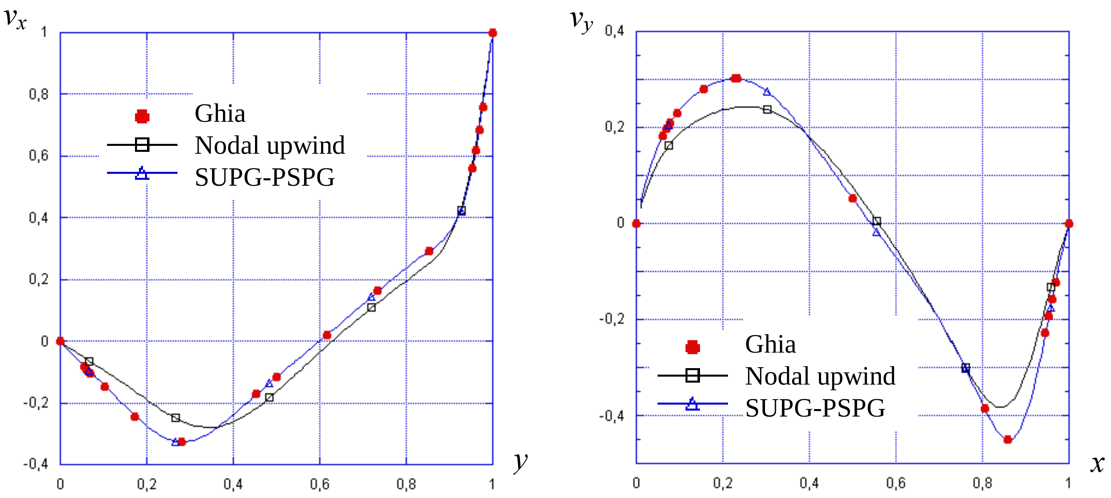

a) b)

a) Horizontal velocity component profiles along the vertical center line of the cavity

b) Vertical velocity component profiles along the horizontal center line of the cavity

Figure 3-17 Comparisons with the reference resolutions of Ghia *et al*. [1982], Re = 400

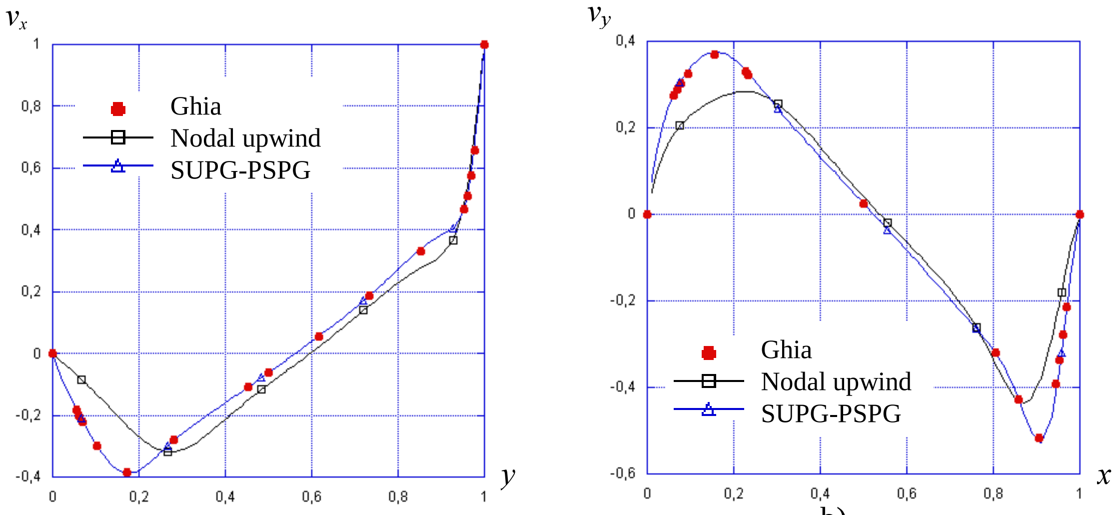

a) b)

a) Horizontal velocity component profiles along the vertical center line of the cavity

b) Vertical velocity component profiles along the horizontal center line of the cavity

Figure 3-18 Comparisons with the reference resolutions of Ghia *et al*. [1982], Re = 1000

For the two formulations, it would be interesting to complement these results with a study of the influence of mesh size and time step. Also, in the case of the nodal upwind P1+/P1 formulation, it would be very interesting to quantify separately the effects of the nodal upwind treatment for the advection terms on one hand, and the effects of the mini-element bubble formulation on another hand.

3.7.3.2 Fluid flow in the porous medium (axisymmetric case, buoyance force driven)

The test is to validate the axisymmetric version of the SUPG-PSPG formulation. Again, the case that has been presented in section 3.7.2 is considered. Here, we use the SUPG-PSPG solver to simulate the fluid flow in the porous medium, and the SUPG thermal solver is chosen to analysis the heat transfer. We also compare with the resolution of PHOENICS. In Figure 3-19, the upper figures are computed by PHOENICS, while the lower ones are computed by R2SOL. Once again, the results obtained by the new solver of R2SOL are quite close to those of PHOENICS.

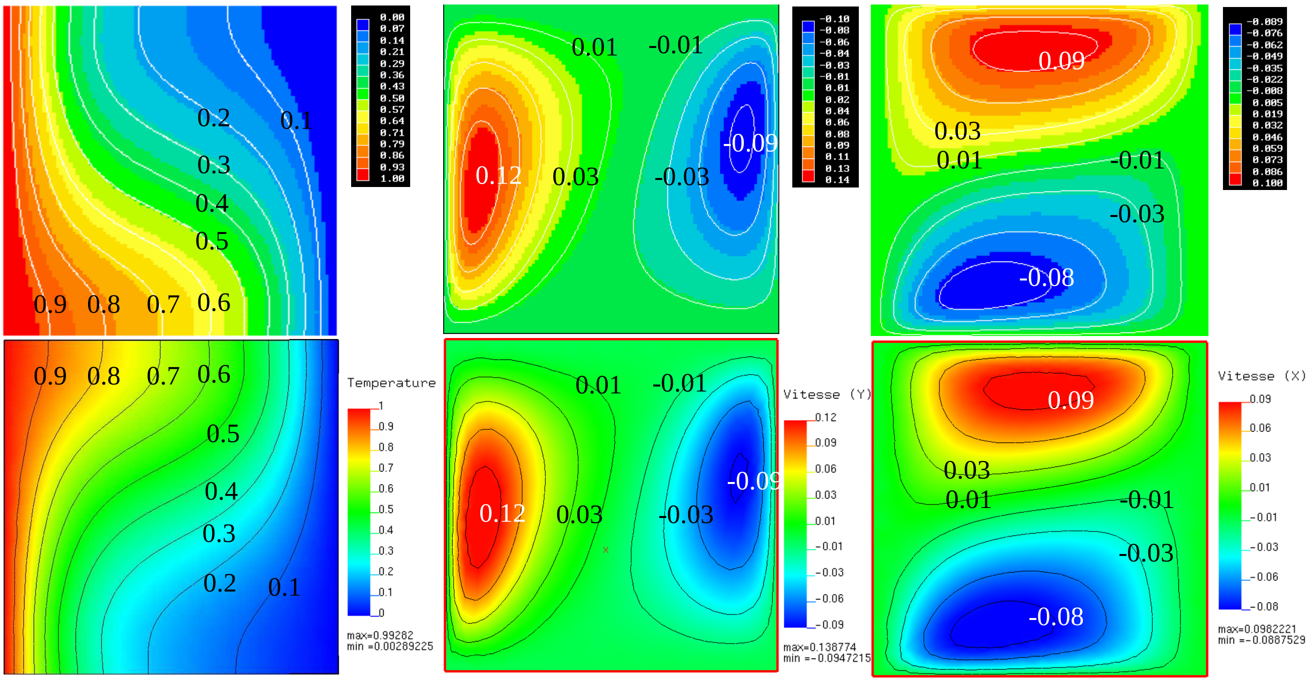

(a) Temperature (b) v_z (c) v_r

Figure 3-19 Comparison between R2SOL and PHOENICS, using the SUPG-PSPG formulation, $1/K=100.0\ m^{-2}$

3.7.4 A solidification test case

The validation test case is the solidification of a binary Fe-0.2%C alloy in a square cavity as shown in Figure 3-20 a). The objective of this test is to validate the computation of macrosegregation with lever rule and Scheil models. The computation is performed by R2SOL and SOLID using the non-coupling approach (locally closed system, no solute enrichment in liquid pool, resolution for w_l). The results are compared.

In the R2SOL computation, the cavity is discretized by a structured and symmetric mesh covering the whole domain, as illustrated in Figure 3-20 b). The mesh used in SOLID is structured with 50×50 nodes in the direction of x and y respectively. The data used in the computation are given in Table 3-6.

The diffusion terms in the solute transport equation have been neglected in R2SOL and SOLID. The results obtained by the lever rule are shown in Figure 3-21, and the Scheil's model in Figure 3-22 respectively.

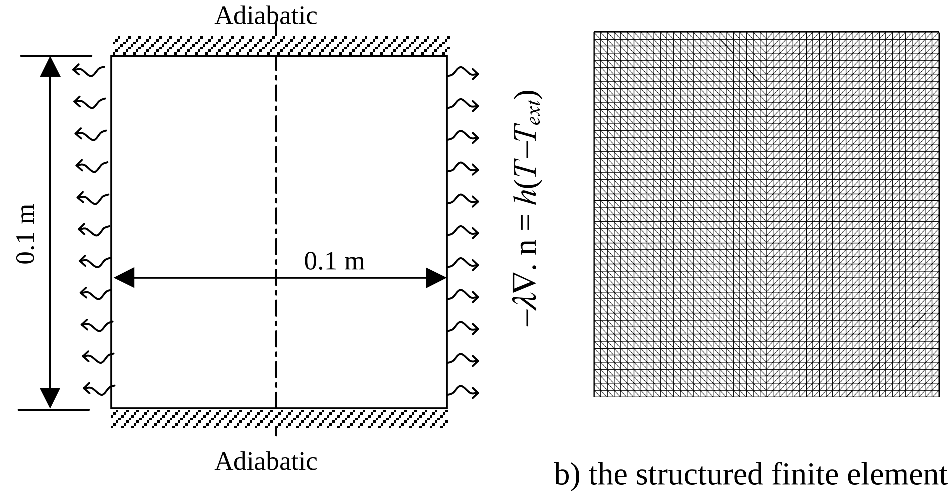

a) Schematics of the cavity test

b) the structured finite element mesh with 53 ×53 nodes (P1 triangle elements)

Figure 3-20 Schematic of the cavity test and the mesh used in R2SOL computation

Table 3- 6 Data used in the computation

Thermal conductivity λ	30 W.m^{-1}. K^{-1}	Initial temperature T_0	1523 ℃
Specific heat c_p	500 J.kg^{-1}.K^{-1}	Initial carbon mass concentration w_0	0.2 %C
Latent heat L	3.09×10^{5} J.kg^{-1}	Reference volumetric mass ρ_0	7060 kg. m^{-3}
Melting temperature T_f	1538 ℃	Dynamic viscosity μ	4.2×10^{-3} Pa.s
Liquidus slope m	-80 K.(%C)$^{-1}$	Secondary dendrite arm spacing λ_2	1×10^{-4} m
Partition coefficient k	0.18	Heat transfer coefficient h	100 W.m^{-2}.K^{-1}
Thermal expansion coefficient β_T	8.853×10^{-5} K^{-1}	External temperature T_{ext}	20 ℃
Solutal expansion coefficient β_w	4.164×10^{-2} (%C)$^{-1}$	Diffusion coefficient in liquid ε	1×10^{-9} m^{2}.s^{-1}

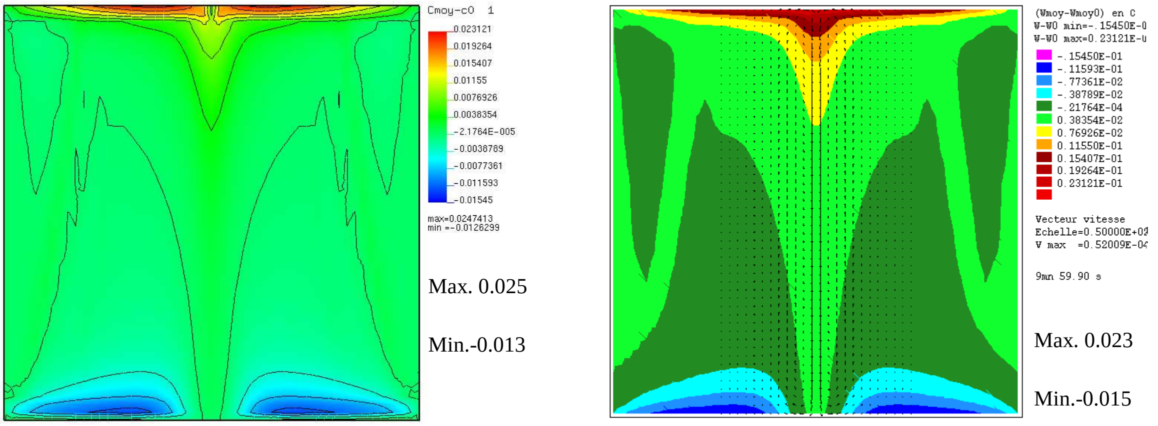

a) R2SOL

b) SOLID

Figure 3-21 The mass concentration distribution $w-w_0$ (%) obtained with the lever rule at 10 min.

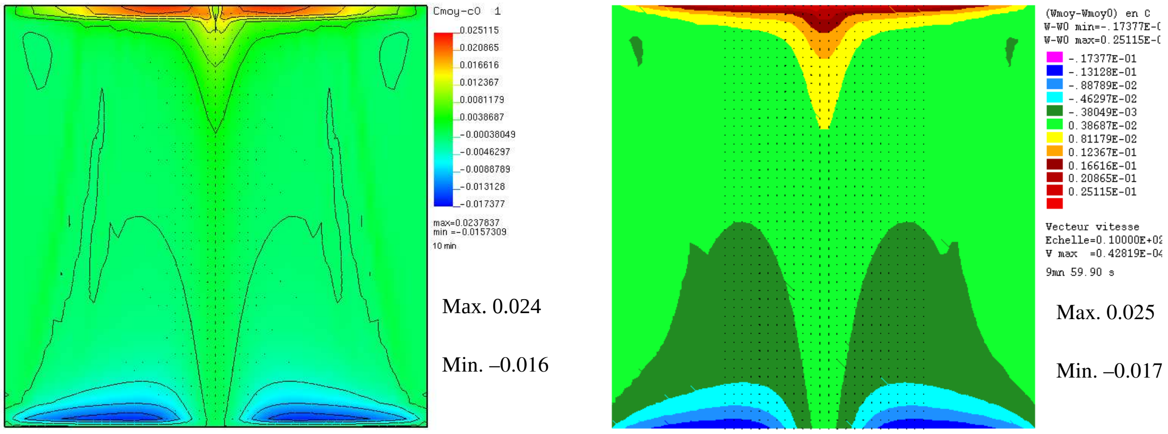

a) R2SOL b) SOLID

Figure 3-22 The mass concentration distribution $w-w_0$ (%) obtained with the Scheil's model at 10 min.

Comparing the segregation maps in Figure 3-21 and Figure 3-22 and results after complete solidification, one can find that a good agreement is obtained: the distributions of segregation (the shape and position of the contours) are very close, as well as the maximum and minimum values of variation of concentration. Since the local solidification time, and the global solidification time (about >15 min) are not as long, consequently the macrosegregation is not too serious. As expected, positive segregation appears at the top, while negative segregation at the bottom. This is due to the fact that the liquid enriched in carbon solute element in the mushy zone moves upward, leading to the top region enriched in carbon and the bottom region impoverished in carbon. The computational result is symmetric with respect to the center line, which is what we have expected for this symmetric solidification problem. It is interesting to note that the results of the lever rule are close to those of the Scheil's model.

To summarize this section, we would conclude that:

- The axisymmetric version of the P1+/P1 and SUPG-PSPG formulations for the Navier-Stokes problem has been implemented in R2SOL.
- The steady-state natural convection test in a cylindrical cavity at high Rayleigh has been chosen to validate the code. The new developments have been successfully validated: convergence towards the plane flow has been shown for very large radii and a successful quantitative comparison has been done with PHOENICS.
- The computation of Darcy term and inertia term in the mechanical solver have been improved.
- Macrosegregation in square cavity with a carbon binary steel alloy has been computed by R2SOL and SOLID using the no-coupling approach. The two codes give very close results.

Chapter 4

Mesh adaptation

Adaptation de maillage – Résumé en français

Le raffinement du maillage au front de solidification, précédemment évoqué, exige donc un remaillage dynamique du maillage d'éléments finis, de façon à accompagner l'avancée de la solidification dans la pièce. En l'absence d'estimateurs d'erreur avérés dans le cas de tels calculs fortement couplés, une approche pragmatique a été développée dans ce travail.

Pour raffiner le maillage au voisinage du liquidus dans la zone pâteuse, on utilise la norme du vecteur gradient de fraction solide. La taille de maille visée est alors directement fonction de cette norme. En aval du front dans le domaine purement liquide, c'est la distance à ce front qui est la variable pilotant la taille de maille visée. A l'aide de fonctions et de paramètres correctement choisis, on construit ainsi une méthode de remaillage dynamique isotrope, s'appuyant sur le module de remaillage existant du Cemef (module MTC).

Il peut être intéressant toutefois de générer des maillages anisotropes, de manière à capter une zone pâteuse étroite, ce qui est le cas notamment dans les premiers instants de la solidification, près de l'interface pièce-moule. Dans ce but, ou utilise alors l'orientation du vecteur gradient de fraction solide. La taille de maille visée est alors calculée selon cette direction, toujours en fonction de la norme du vecteur, tandis qu'un facteur d'anisotropie est déterminé en fonction de l'orientation du champ de vitesse. L'utilisation du remaillage anisotrope permet de diminuer considérablement le nombre d'éléments, à taille de maille données dans la direction du gradient de fraction solide.

L'organisation du chapitre est la suivante : le calcul de la distance au liquidus est exposé à la section 4.1. Les algorithmes de remaillage isotrope et anisotrope sont présentés aux sections 4.2 et 4.3 respectivement.

Chapter 4

Mesh adaptation

As discussed in the general introduction, fluid flow in the mushy zone close to the liquidus and in the liquid just ahead of the liquidus is most important to the formation of macrosegregation, and fine meshes are needed in these regions. In the deeper mushy zone close to solidus, fluid flow is very weak and the velocity is nearly equal to zero. Actually the solute concentration field in the deeper mushy zone and in the solid zone nearly does not change, we can properly use a rather coarse mesh. Because the solidification front moves during cooling, moving adaptive meshes are needed. So far no reliable error estimators have been evidenced for such highly coupled solidification problems. For this reason, we have decided to use a simple algorithm for the mesh adaptation.

A simple idea for the mesh adaptation is to generate fine elements in the critical regions. In the present study, the norm of the gradient of solid fraction is used as a parameter for piloting the remeshing in the mushy zone. The objective mesh size in the mushy zone is considered as a function of the solid fraction. For the mesh refinement in the liquid just ahead of the liquidus, we track the solidification front and compute the distance from each node to the front. Then, the objective mesh size ahead of liquidus can be determined as a function of the distance. An algorithm for isotropic remeshing has been proposed.

In the early solidification stage of ingots, extreme anisotropic cooling appears. Variations of temperature and fraction of liquid etc. are very large in the direction perpendicular to the mold wall, while variations are small in the other two directions. Therefore, anisotropic mesh adaptation seems quite appropriate in computation of ingots. The method for isotropic remeshing has been extended to the anisotropic case. Special attention is given regarding the solidification direction.

In this work, we have used the mesher "MTC", which has been initially developed by Thierry Coupez [1991] at CEMEF, and has been improved recently by Cyril Gruau [2004]. The algorithms of automatic mesh generation will not be presented in this document.

The organization of this chapter is as follows: we present a method to track the liquidus isotherm and compute the distance to it in section 4.1. The algorithms for isotropic and anisotropic mesh adaptation are presented in section 4.2 and section 4.3 respectively.

4.1 Tracking liquidus isotherm

Since the fraction of liquid, g , at each node has been computed by solving the energy equation with the microsegregation model, the liquidus isotherm can be determined by using g . For numerical reason, the liquidus isotherm is considered as the isoline with the value $g_l = 0.99$. The method to track the isoline is based on the following assumptions:

- the fraction of liquid is linear in each triangle element;

- an isoline can be either opened or closed as shown in Figure 4-1. An opened isoline has a starting point and an ending point on the boundary. A closed isoline is enclosed within the domain.

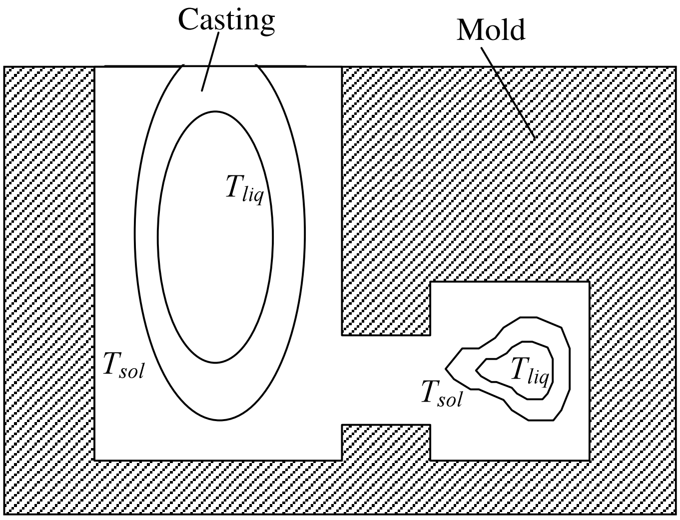

Figure 4-1 Illustration of solidification fronts with several closed or opened isolines

4.1.1 Tracking procedure

The procedure to track the liquidus isotherm is carried out as follows:

1) For simplicity, assuming that a given isoline never passes though the vertices of the triangle elements, it comes into a triangle from one edge, and leaves it from another edge. This simplification makes it easy to track the isoline from one element to its neighbor element. In practice, if the isoline just passes through the vertex, for instance through the node *i*, we change the value of the liquid fraction at the node *i* by adding an infinitesimal value (10^{-6}).

2) For each element (*e*), identify if the isoline passes through it, and initialize the indicator istate(*e*):

   istate (*e*) = 0, the isoline does not pass through the element *e*;

   istate (*e*) = 1, the isoline passes through the element *e*, as shown in Figure 4-2.

3) Search for the isoline that starts from the boundary. If there is an opened isoline, one can find an element *e* , such that:

   istate(*e*) = 1, and at least one edge of the element belongs to the boundary.

   Then, the coordinate of the starting point on the boundary can be determined by linear interpolation.

4) Extend the isoline from one element to its neighbor element. In step 3), we have found the element *e* as shown in Figure 4-2, and a starting point A on the boundary edge *i-j*. One can also find another point B on the edge *i-k* where the isoline leaves the element *e* . After connecting two points (that is to store the coordinates), change the value of the indicator, let istate(*e*) = 0. The next element *e*’ that the isoline goes into can be determined by the mesh topology and the indicator, istate(*e*’). All the points of the isoline can be found

consequently by a repeating procedure: connect a segment within an element; change the value of indicator; extend to the neighbor element. The repeating operation will be terminated when the isoline comes to the boundary again.

5) Repeat 3) and 4), until all the opened isolines have been found.

6) Search for the closed isolines inside the computational domain. After the step 5), there are only closed isolines left. One can find a closed isoline in the inner elements where istate(*e*) = 1. The tracking procedure is similar to that presented in step 4), one can track an isoline until it comes back to its starting point.

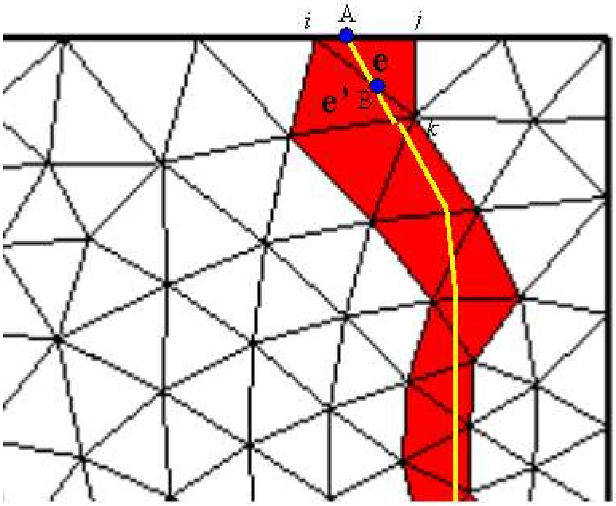

Figure 4-2 Schematic of an isoline. An opened isoline that starts from a point A on the boundary, and passes through the elements in red

4.1.2 Distance to liquidus isotherm

Regarding the tracking procedure, we note that the solidification front is approximated by a series of succesive segments as shown in Figure 4-3. These segments have not been oriented. Therefore, the liquid can be found either on the left or the right side of the contour. In order to compute the distance to the liquidus isotherm, for any node P in the liquid zone where g_l>0.99 we search for a point Q on the isotherm that is the nearest point to the node P. Then, this distance (from point P to point Q) is considered as the distance to the liquidus isotherm. The computation of distance from a point to a series of segments is a simple geometry problem. The distance can be calculated as follows:

- Computation of the perpendicular distance from the point P to the line passing the two points X_i and X_{i+1}

In order to compute this distance, we then define following vectors:

$$\mathbf{U}_{seg} = \mathbf{x}_{i+1} - \mathbf{x}_i = \begin{bmatrix} x_{i+1} - x_i \\ y_{i+1} - y_i \end{bmatrix} = \begin{bmatrix} a \\ b \end{bmatrix} \tag{4-1}$$

$$\mathbf{V}_{seg} = \begin{bmatrix} -b \\ a \end{bmatrix} \tag{4-2}$$

$$\mathbf{r}=\begin{bmatrix} x_i - x_p \\ y_i - y_p \end{bmatrix} \tag{4-3}$$

where $\mathbf{U}_{\text{seg}}$ is the vector from the point X_i to the point X_{i+1}; the vector $\mathbf{V}_{\text{seg}}$ is perpendicular to the vector $\mathbf{U}_{\text{seg}}$; $\mathbf{r}$ is the vector from the point P to the point X_i.

The perpendicular distance can be computed by projecting the vector $\mathbf{r}$ on the unit vector $\mathbf{V}_{\text{seg}}/|\mathbf{V}_{\text{seg}}|$, then we have:

$$d=\frac{|\mathbf{V}_{seg}\cdot\mathbf{r}|}{|\mathbf{V}_{seg}|}=\frac{|(x_{i+1}-x_i)(y_i-y_p)-(x_i-x_p)(y_{i+1}-y_i)|}{\sqrt{(x_{i+1}-x_i)^2+(y_{i+1}-y_i)^2}} \tag{4-4}$$

As shown in Figure 4-4, the location of the projecting point O, with respect to the point X_i can be found by projecting the vector $-\mathbf{r}$ on the unit vector $\mathbf{U}_{\text{seg}}/|\mathbf{U}_{\text{seg}}|$, leading to:

$$\xi=-\frac{\mathbf{U}_{seg}\cdot\mathbf{r}}{|\mathbf{U}_{seg}|^2}=-\frac{(x_{i+1}-x_i)(x_i-x_p)+(y_{i+1}-y_i)(y_i-y_p)}{(x_{i+1}-x_i)^2+(y_{i+1}-y_i)^2} \tag{4-5}$$

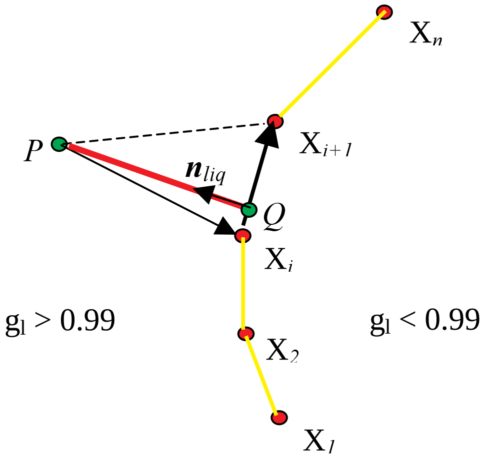

Figure 4-3 Distance from a point P to the solidification front. The solidification front is approximated by a series of segments (X_1 X_2), (X_2 X_3), … (X_i X_{i+1}), …, (X_{n-1} X_n)

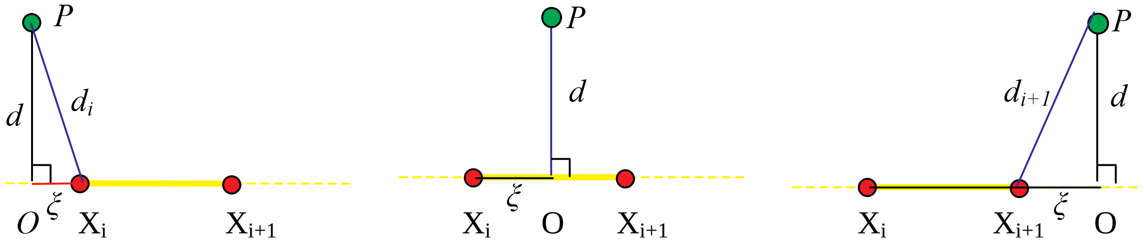

a) $\xi < 0.0$ b) $0.0 \le \xi \le 1$ c) $\xi > 1$

Figure 4-4 Schematic of the shortest distance from a point P to a segment X_iX_{i+1}

- Choosing of the shortest distance from the point *P* to the i^{th} segment X_iX_{i+1}, d_i^{seg}

As shown in Figure 4-4, the shortest distance from the point *P* to the i^{th} segment X_iX_{i+1} is determined by:

$$d_i^{seg} = \min(d, d_i, d_{i+1}) = \begin{cases} d_i & if \quad \xi < 0 \\ d & if \quad 0 \le \xi \le 1 \\ d_{i+1} & if \quad \xi > 1 \end{cases} \tag{4-6}$$

where d_i and d_{i+1} are the distances from the point *P* to the points X_i and X_{i+1} respectively; *d* is the perpendicular distance from the point *P* to the line passing the points X_i and X_{i+1}.

Meanwhile, the point q_i^{seg} on the i^{th} segment X_iX_{i+1}, which is the closest point to *P*, is chosen as follows:

$$q_i^{seg} = \begin{cases} X_i & if \quad \xi < 0 \\ O & if \quad 0 \le \xi \le 1 \\ X_{i+1} & if \quad \xi > 1 \end{cases} \tag{4-7}$$

- Determining the shortest distance from the point *P* to the liquidus isotherm

It is easy to find the distance to the liquidus isotherm, knowing the shortest distance from the point *P* to the i^{th} segment X_iX_{i+1}, d_i^{seg}. We write:

$$x_{liq}(P) = \min(d_i^{seg}) \tag{4-8}$$

And, the point *Q* on the isotherm that is the nearest point to *P* is chosen from the set of q_i^{seg}.

For the purpose of guiding anisotropic remeshing in the liquid zone, we also define a unit vector for each node *P*, $\mathbf{n}_{liq}(P)$. The vector follows the direction of the gradient of liquid fraction at the point *Q* which is the nearest to the point *P*. The vector $\mathbf{n}_{liq}(P)$ is considered to be a good approximation of the unit normal to liquidus isotherm. Its value is computed by the linear interpolation, knowing the coordinates of the point *Q* and the field of the gradient of liquid fraction.

Similarly, for guiding the derefinement in the solid-like zone where the solid fraction is great than a critical value g^{cr}, we track the isoline of g^{cr}, and compute the following parameters:

$x_{sol}(P)$, the shortest distance from each node *P* in the solid-like zone to the isotherm of g^{cr};

$\mathbf{n}_{sol}(P)$, the unit vector for each node *P* in the solid-like zone, following the direction of the gradient of solid fraction at the point *Q* on the isotherm of g^{cr}.

4.2 Isotropic remeshing

4.2.1 Definitions of isotropic mesh size

Definition 4.2.1 The mesh size for each element, h^T: let T be a triangle element with three vertices S_1, S_2 and S_3, as shown in Figure 4-5. Following the definition of mesh size in the mesher MTC, h^T is the average length of its edges S_1S_2, S_2S_3 and S_3S_1:

$$h^T = \left(\frac{1}{3}\sum_{i,j=1,3}\left\|s_i s_j\right\|^2\right)^{1/2} \tag{4-9}$$

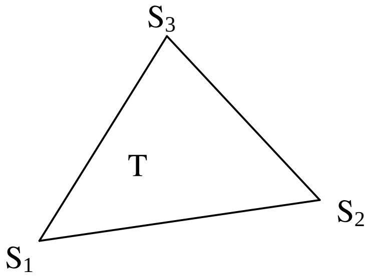

Figure 4-5 A triangle element with its vertices S_1, S_2 and S_3

Definition 4.2.2 The mesh size for each node, h^S: let T_k (with k = 1, n) be a triangle element sharing the common node S, as shown in Figure 4-6. h^S is the distance-weighted average of the sizes of elements T_k surrounding the node S, the weights being proportional to the inverse of square distance.

$$h^s = \frac{1}{\left(\sum_{k=1}^{n} l_k^{-2}\right)}\sum_{k=1}^{n} l_k^{-2} h_k^{T_k} \tag{4-10}$$

where, l_k is the distance from the node S to the center of triangle T_k

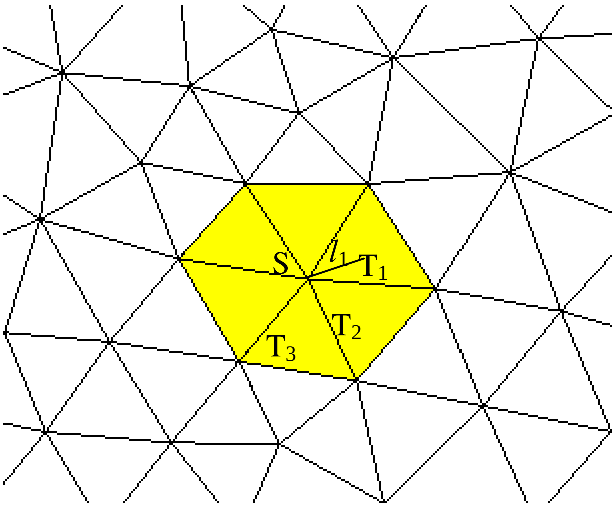

Figure 4-6 The triangle elements around a node S

As the objective mesh size that is used in the mesh generator “MTC” is defined at each node, we firstly evaluate the mesh size at each element using the definition 4.2.1, and then compute the mesh size at each node using the definition 4.2.2.

4.2.2 Domain decomposition

For the purpose of automatic remeshing, the computational domain is decomposed into three zones: 1) the liquid zone; 2) the mushy zone close to the liquidus, called the mushy zone for short; 3) the mushy zone close to the solidus and the solid zone, called the solid-like zone. A critical value, g , is used to distinguish the mushy zone and the solid-like zone.

The criterion to decompose the computational domain can be based on:

1) the solid fraction;
2) temperature;
3) the permeability, which is determined by the Carman-Kozeny relation as a function of the solid fraction;
4) the rate of variation of solute concentration in the case of a binary alloy, especially for the solid-like zone.

Since the liquidus and solidus temperature change with the local average solute concentration, a criterion based on the temperature would not be satisfying. For simplicity, in the present work we choose the solid fraction as the criterion. A critical value g prescribed by the user, typically $g \ \ = 0.4$ to 0.6, is used to distinguish the mushy zone and the solid-like zone. The liquidus isotherm, $g_l = 0.99$, is used to distinguish the mushy zone and the liquid zone.

4.2.3 Computation of the nodal objective mesh size

In order to control the mesh size at nodes, we define the following parameters:

$h_{current}$,	current local mesh size at nodes;
h_{obj},	objective mesh size at nodes;
$h_{\min\_mushy}$ and $h_{\max\_mushy}$,	two fixed values to bound the size in the mushy zone;
$h_{\min\_liq}$ and $h_{\max\_liq}$,	for the nodes in the liquid zone ;
$h_{\min\_sol}$ and $h_{\max\_sol}$,	for the nodes in the solid-like zone;
$\Delta g_s^{objective}$,	the objective variation of solid fraction in the mushy zone;
$\Delta \varepsilon_w^{objective}$,	the objective relative variation of average concentration.

$\Delta g_s^{objective}$ is used to guide remeshing in the mushy zone. Generally speaking, if $\Delta g_s^{objective} = 0.1$, we ask for about 10 elements in the mushy zone. $\Delta \varepsilon_w^{objective}$ is used to guide remeshing in the solid-like zone. As the field of solute concentration in the solid-like zone no longer changes, normally one can derefine the mesh. But if necessary we may like to use a fine mesh to keep the information of a segregated channel, where a great variation of solute concentration has formed. A priori estimation should be given to decide the value of $\Delta \varepsilon_w^{objective}$.

Before computing the objective mesh size at nodes, we compute the gradient of solid fraction, ∇g_s^e; and the gradient of average concentration, ∇w^e, in each element. Then, smoothed values of ∇g_s and ∇w can be obtained at each node (like smoothing the mesh size at each node by equation (4-10)). We identify the state of each node: it is either in the liquid, in the mushy or in the solid-like state. This can be achieved easily by testing the value of g_l at each node:

if $g_l \geq 0.99$, the node is in the liquid zone;

else if $g < 1 - g$, the node is in the solid-like zone;

else, the node is considered in the mushy zone.

Now let us compute the objective mesh size according to the state of each node as follows:

- ***Nodal objective mesh size in the mushy zone***

Two cases are considered:

1) the quantity $\|\nabla g_s\| h_{current}$ is lower than or equal to the prescribed value $\Delta g_s^{objective}$. In this case, we do not change the mesh size, hence:

$$\begin{aligned} & h_{obj}^{(1)} = \max(h_{current},\ h_{\min\_mushy}) \\ & \text{and } h_{obj} = \min(h_{obj}^{(1)},\ h_{\max\_mushy}) \end{aligned} \tag{4-11}$$

2) the quantity $\|\nabla g_s\| h_{current}$ is greater than $\Delta g_s^{objecte}$. In this case, refinement is needed, the objective mesh size is found as follows:

$$\begin{aligned} & h_{obj}^{(1)} = \min\Big(\frac{\Delta g_s^{objective}}{\|\nabla g_s\|},\ h_{\max\_mushy}\Big) \\ & \text{and } h_{obj} = \max(h_{obj}^{(1)},\ h_{\min\_mushy}) \end{aligned} \tag{4-12}$$

- ***Nodal objective mesh size in the liquid zone***

The objective mesh size is computed as a function of the distance x to the liquidus isotherm. We have selected the following Avrami-type function,

$$h_{obj} = h_{liq\_\max} + (h_{liq\_front} - h_{liq\_\max}) \exp\left[-5.0\left(\frac{x_{liq}}{x_{liq}^0}\right)^3\right] \tag{4-13}$$

which is illustrated in Figure 4-7. x_{liq}^0 is the prescribed distance, at which the objective mesh size reaches the value $h_{liq\_\max}$. h_{liq_front} is the current mesh size on the liquidus isotherm (with $g_l = 0.99$). For each node in the liquid zone, as we have found the nearest point on the liquidus isotherm, i.e., we know the coordinates of point Q (cf. section 4.1.2), h_{liq_front} can be interpolated by a linear function using the current mesh size.

Remarks

1) Fine objective mesh size near the liquidus isotherm can be achieved by the Avrami-type function, which is essential for modeling the macrosegregation. 2) The objective mesh size near the liquidus isotherm changes slightly, this character can prevent from too frequent triggering of the remeshing. 3) We desire to have fine elements ahead of the liquidus isotherm, so that the velocity field can be predicted with high accuracy. In the present work, x_{liq}^0 takes the value of $4 \times h_{liq\_\max}$.

At the beginning of computation, our domain usually is occupied by the liquid. In order to generate a good mesh, the distance to the boundary is computed instead of the distance to the liquidus isotherm. The objective mesh size on the boundary is considered as $h_{\min\_liq}$, and the Avrami-type function is used to define the objective mesh size near the boundary.

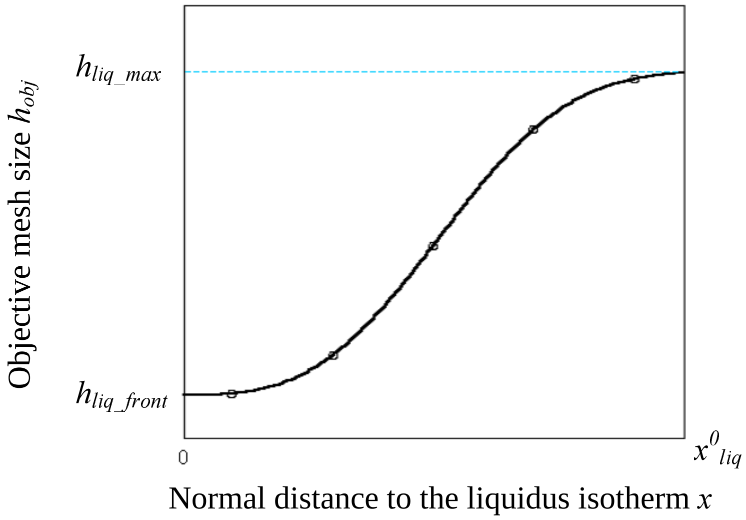

Figure 4-7 The objective mesh size as computed by the selected Avrami-type function

- ***Nodal objective mesh size in the solid-like zone***

For the solid-like zone, normally the mesh can be derefined according to the distance to the isotherm of g :

$$h_{obj} = h_{sol\_\max} + (h_{sol} - h_{sol\_\max}) \exp\left[-5.0\left(\frac{x_{sol}}{x^0_{sol}}\right)^3\right] \tag{4-14}$$

Where h_{sol} is the current mesh size at the isotherm of g ; x_{sol} is the distance to the isotherm of g ; x^0_{sol} is the prescribed distance, for which the objective mesh size reaches the value $h_{sol\_\max}$.

In order to keep the information regarding the segregated channels if necessary, we need to re-compute the objective mesh size. Similarly to the computation of objective mesh size in the mushy zone, two cases are considered:

1) the quantity $\dfrac{\|\nabla w\| h_{obj}}{w}$ is lower than or equal to the prescribed value $\Delta\varepsilon_w^{objective}$, and h_{obj} has been computed by equation (4-14). In this case, we accept the objective mesh size computed by equation (4-14).

2) the quantity $\dfrac{\|\nabla w\| h_{obj}}{w}$ is greater than $\Delta\varepsilon_w^{objective}$, then the objective mesh size is determined by:

$$\begin{gathered} h^{(1)}_{obj} = \min\left(\frac{\Delta\varepsilon_w^{objective} \cdot w}{\|\nabla w\|},\ h_{\max\_sol}\right) \\ \text{and} \quad h_{obj} = \max\left(h^{(1)}_{obj},\ h_{\min\_sol}\right) \end{gathered} \tag{4-15}$$

After the computation described above, finally we need to optimize the objective mesh size in order to create a new mesh with good quality. The variation of objective mesh size should be then controlled. Let h_{obj}^{k} be the objective mesh size at the *k*-th point in a triangle element, and let h_{obj}^{j} be the value at another point of the element. The ratio h_{obj}^{k}/h_{obj}^{j} should be in the range of (0.5, 2.0), so that the quality of mesh is guaranteed. An iterative procedure is performed to optimize the objective mesh size, in which we always decrease the larger objective mesh size, until this limit ratio is fulfilled for every node.

To summarize, the following procedures are performed for the adaptive remeshing:

- track the isotherms of liquidus and g^{c} , and compute the normal distance to the isotherms for each node;
- compute the objective mesh size at each node;
- optimize the objective mesh size by an iterative smoothing procedure, so that the maximum variation between two neighbor nodes is confined within the range of (0.5, 2.0);
- make a decision about remeshing. In order to avoid too frequent remeshing steps, we trigger the remeshing only when there is a certain number of nodes, typically 1%, for which the ratio of the objective mesh size to the current mesh size is out of the range [0.5, 2.0];
- create a new mesh by using the mesher “MTC”. Passing the objective mesh size to MTC, a new mesh can be created.
- Transport the variables that are needed in the further computation from the old mesh to the new mesh by the direct interpolation method. It is obvious that the solidification variables computed by direct interpolation will not satisfy the thermodynamic equilibrium due to the strong non-linearity of the problem. So, in a first step, values of enthalpy and average concentration are transported. Then, in a second step, the values of temperature, fraction of liquid, liquid concentration, liquidus and solidus temperature are deduced with the aid of the selected microsegregation model (in the present study, only lever rule is available to use the mesh adaptation).

In R2SOL, the organization for the dynamic mesh adaptation is summarized in Figure 4-8.

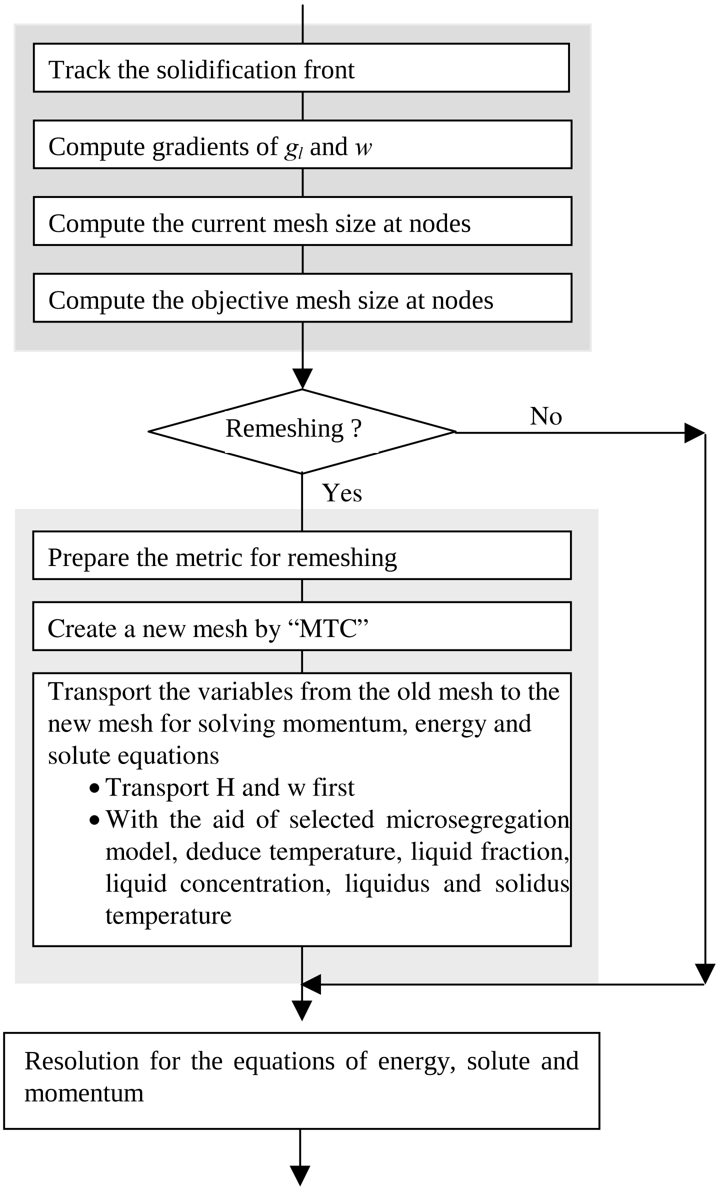

Figure 4-8 Organization for the dynamic mesh adaptation in R2SOL

4.3 Anisotropic remeshing

As it has been presented at the beginning of this chapter, in the solidification of ingots anisotropic cooling appears. Consequently, the gradient of quantities (such as temperature, liquid fraction, and velocity) is very large in one direction, and becomes small in the other directions. In order to match this strongly directional situation, it is desirable to use anisotropic meshes. A good anisotropic mesh that is adapted both in size and shape can improve the computational accuracy and reduce the computational cost. In general, a metric tensor is used to describe the objective mesh size and direction locally at each point in the computational domain. The present work is dedicated to introduce a metric tensor for guiding dynamic remeshing. While the anisotropic mesh is generated using the mesher "MTC".

As prior knowledge, the concept of metric tensor is briefly presented in section 4.3.1. Regarding the anisotropic remeshing, a similar strategy to the isotropic remeshing has been used to compute the objective mesh size. However, there are still some differences, and one should pay attention to the mesh orientation. This will be presented in section 4.3.2.

4.3.1 Metric tensor and anisotropic mesh

- ***Metric tensor***

Hereunder, we present the classical definition of the metric tensor for 2-dimensional anisotropic remeshing (Frey and George [1999]). A metric tensor is a positive symmetric definite tensor and its matrix **M** can be factorized as follows:

$$\mathbf{M}(x)=\mathbf{R}\boldsymbol{\Lambda}\mathbf{R}^T=\begin{bmatrix}\cos\theta & -\sin\theta \\ \sin\theta & \cos\theta\end{bmatrix}\begin{bmatrix}h_1(x)^{-2} & 0 \\ 0 & h_2(x)^{-2}\end{bmatrix}\begin{bmatrix}\cos\theta & \sin\theta \\ -\sin\theta & \cos\theta\end{bmatrix} \qquad (4\text{-}16)$$

where $\boldsymbol{\Lambda}=\begin{bmatrix}h_1(x)^{-2} & 0 \\ 0 & h_2(x)^{-2}\end{bmatrix}$ denotes the diagonal matrix formed by the eigenvalues of **M**(x). $\mathbf{R}=\begin{bmatrix}\cos\theta & -\sin\theta \\ \sin\theta & \cos\theta\end{bmatrix}$ presents the corresponding eigenvectors. The metric tensor **M**(x) defines a curved space (like an ellipse) as shown in Figure 4-9, the major radius and the minor radius are h_1(x) and h_2(x) respectively.

There are several possibilities to interpret the metric tensor. For instance, if the tensor **M** is a diagonal matrix as follows:

$$\mathbf{M}=\begin{bmatrix}h_{obj}(x)^{-2} & 0 \\ 0 & h_{obj}(x)^{-2}\end{bmatrix} \qquad (4\text{-}17)$$

Then, it defines a homogeneous space as a circle in Figure 4-10. That is the case for the isotropic mesh adaptation: the local objective mesh size, $h_{obj}(x)$, is only a function of the position, this function specifies the edge length in all directions.

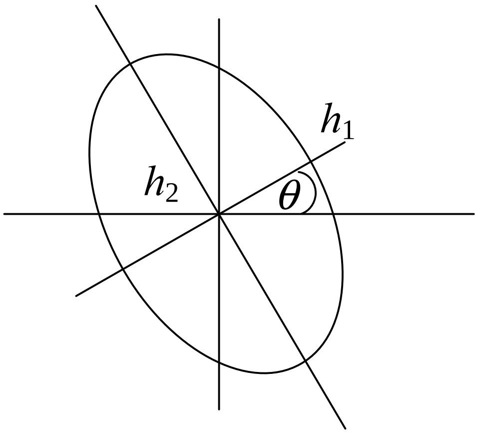

Figure 4-9 an ellipse

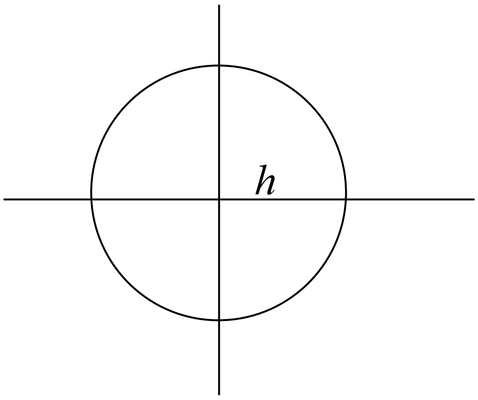

Figure 4-10 a circle

For the anisotropic meshes, the local metric tensor specifies an ellipse as shown in Figure 4-9. The objective mesh sizes in the two principal directions are the major radius h_1(x) and the minor radius h_2(x) respectively. The mesh orientation is specified by the angle θ.

Mathematically speaking, let $\Gamma(t)=(1-t)\,\mathbf{x}_0+t\,\mathbf{x}_1$ be a parametric description for the segment $\mathbf{x}_0\mathbf{x}_1$, in the space defined by the metric tensor **M**(x), the distance between two points $\mathbf{x}_0$ and $\mathbf{x}_1$ is then defined as:

$$l(\mathbf{x}_0,\mathbf{x}_1)=\int_0^1\sqrt{(\mathbf{x}_1-\mathbf{x}_0)^T\,\mathbf{M}\,(\Gamma(t))\,(\mathbf{x}_1-\mathbf{x}_0)}\;dt \tag{4-18}$$

By linearly interpolating the metric $\mathbf{M}(\Gamma(t))=(1-t)\,\mathbf{M}(\mathbf{x}_0)+t\,\mathbf{M}(\mathbf{x}_1)$, the length of segment $\mathbf{x}_0\mathbf{x}_1$ is approximated by (Frey and George [1999]):

$$l(\mathbf{x}_0,\mathbf{x}_1)=\frac{2}{3}\,\frac{l_0^2+l_0l_1+l_1^2}{l_0+l_1} \tag{4-19}$$

where $l_i=\int_0^1\sqrt{(\mathbf{x}_1-\mathbf{x}_0)^T\,\mathbf{M}\,(\mathbf{x}_i)\,(\mathbf{x}_1-\mathbf{x}_0)}\;dt\quad,\quad i=0,1\,.$

The distance in the equation (4-18) is the Euclidean distance when **M** is the identity matrix.

- ***Mesh size***

For an anisotropic mesh, using equation (4-19), the length of an edge (S_iS_j) in a triangle can be defined as follows with respect to the metric tensor **M**:

$$\left\|S_j-S_i\right\|_M^2=\frac{2}{3}\,\frac{\left\|S_j-S_i\right\|_{M(S_i)}^2+\left\|S_j-S_i\right\|_{M(S_i)}\cdot\left\|S_j-S_i\right\|_{M(S_j)}+\left\|S_j-S_i\right\|_{M(S_j)}^2}{\left\|S_j-S_i\right\|_{M(S_i)}+\left\|S_j-S_i\right\|_{M(S_j)}} \tag{4-20}$$

where $\left\|S_j-S_i\right\|_{\mathrm{M}}^2$ denotes the square of the distance from the point S_i to the point S_j according to the metric **M.**

In the mesher "MTC", the metric **M** is simply averaged to evaluate the edge length and the mesh size for an element. The definitions of mesh size are described as follows (Cyril Gruau [2004]):

The length of an edge:

$$\left\|\boldsymbol{S}_j-\boldsymbol{S}_i\right\|_M=\left\|\boldsymbol{S}_j-\boldsymbol{S}_i\right\|_{\frac{1}{2}(M(S_i)+M(S_i))} \tag{4-21}$$

The metric for an element *T*:

$$\mathbf{M}(T)=\frac{1}{3}\sum_{i=1,3}\mathbf{M}(\boldsymbol{S}_i) \tag{4-22}$$

The mesh size for an element *T*:

$$h_{\mathbf{M}(T)}=\left(\frac{1}{3}\sum_{i,j=1,3}\left\|\boldsymbol{S}_j-\boldsymbol{S}_i\right\|_M^2\right)^{1/2} \tag{4-23}$$

The mesher "MTC" creates automatically the new mesh by an iterative procedure, using a field of metric tensor defined at each node on the old mesh. Our task is then to introduce the metric tensor. In the following text we present an example of anisotropic mesh, and show what parameters are needed for guiding the remeshing.

- ***An example***

An anisotropic mesh used in the computation of solidification is shown in Figure 4-11. It can be seen that triangle elements in the mushy zone are elongated in the direction perpendicular to the gradient of liquid fraction, such that a layer of fine elements is located in the mushy zone. Ahead of mushy zone and toward to the bulk liquid zone, the anisotropic mesh becomes an isotropic mesh, being the isotropic mesh in the bulk liquid. The same feature can be seen in the solid zone.

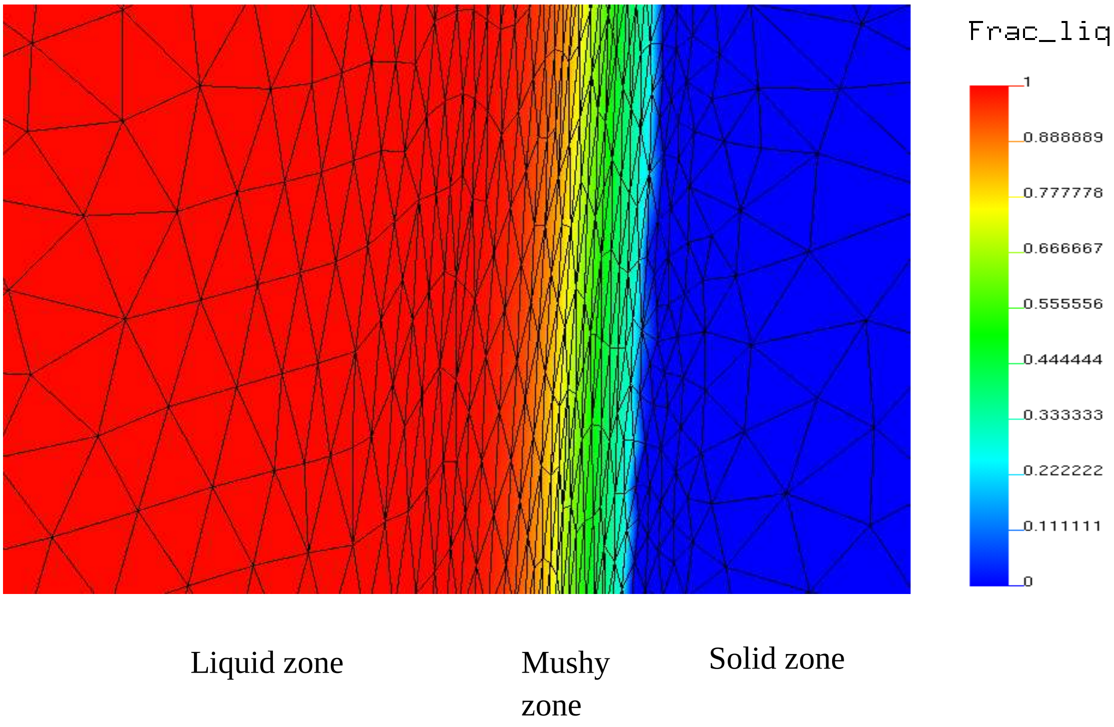

Figure 4-11 An example of anisotropic mesh

In order to create such meshes for the computation of macrosegregation, for each node we define the following parameters:

- the objective mesh size in the first principal direction h_{obj1};
- the objective mesh size in the second principal direction h_{obj2};
- the unit vector $\mathbf{n}1=\begin{bmatrix}\cos\theta\\ \sin\theta\end{bmatrix}$ that specifies the first principal direction.

The computation of these parameters is presented in the following sections.

4.3.2 Determination of parameters for anisotropic remeshing

4.3.2.1 Mesh orientation

- In the mushy zone, the mesh (according to the first principal direction) is oriented in the same direction as the gradient of solid fraction:

$$\cos\theta=\frac{(\nabla g_s)_x}{\|\nabla g_s\|} \quad \text{and} \quad \sin\theta=\frac{(\nabla g_s)_y}{\|\nabla g_s\|}\text{, that is } \mathbf{n}1=\frac{1}{\|\nabla g_s\|}\nabla g_s \tag{4-24}$$

- In the liquid zone and near the liquidus (within the prescribed distance x_{liq}^0), the mesh is oriented in the same direction as the liquidus isotherm (cf. section 4.1.2):

$$\mathbf{n}1 = \mathbf{n}_{liq} \tag{4-25}$$

  where $\mathbf{n}_{liq}$ is the unit norm of the liquidus isotherm at the point which is the nearest to the considered node, see Figure 4-3.

  For a node far from the liquidus isotherm, the mesh is isotropic, that is:

$$\cos\theta=1 \quad \text{and} \quad \sin\theta=0 \tag{4-26}$$

- In the solid-like zone and near the isotherm of g_s^{cr} (within the prescribed distance x_{so}^0), the mesh is oriented in the same direction of the isotherm of g_s^{cr}

$$\mathbf{n}1 = \mathbf{n}_{sol} \tag{4-27}$$

  where $\mathbf{n}_{sol}$ is the unit norm of the isotherm of g_s^{cr} at the point which is the nearest to the considered node.

  Otherwise the mesh is isotropic:

$$\cos\theta=1 \quad \text{and} \quad \sin\theta=0 \tag{4-28}$$

4.3.2.2 Objective mesh size

We adopt the same strategy as that for the isotropic mesh adaptation (described in section 4.2.3) to compute the objective mesh size in the first principal direction, h_{obj1}. The remained problem is to determine the objective mesh size in the second principal direction, h_{obj2}.

In the solid-like zone, h_{obj2}, is obtained by multiplying h_{obj1} with a given factor (typically, factor = 5), we have:

$$h_{obj2} = \min\left(h_{obj1} \times factor,\ h_{\max\_ol} \right) \tag{4-29}$$

In the mushy and liquid zones, three cases are considered as following:

In the first case as shown in Figure 4-12 a), the velocity vector is orthogonal with the first principal direction which has been determined in section 4.3.2.1. That is the ideal case, one can elongate an isotropic triangle element just following the fluid flow. h_{obj2}, is given by multiplying h_{obj1} with a given factor:

$$h_{obj2} = \min\left(h_{obj1} \times factor,\ h_{\max\_liq} \right), \quad \text{in the liquid zone} \tag{4-30}$$

$$h_{obj2} = \min\left(h_{obj1} \times factor,\ h_{\max\_muhy} \right), \text{ in the mushy zone}$$

In the second case as shown in Figure 4-12 b), $|\cos\alpha| \le 0.1$, α being the angle between vectors of velocity and the first principal. h_{obj2} is determined as a function of the angle α :

$$h_{obj2} = \min\left(h_{obj1} (factor + \frac{1-factor}{0.1} |\cos\alpha|),\ h_{\max\_liq} \right), \text{ in the liquid zone} \tag{4-31}$$

$$h_{obj2} = \min\left(h_{obj1}(factor + \frac{1-factor}{0.1}\left|\cos\alpha\right|),\ h_{\max\_mushy} \right),\ \text{in the mushy zone} \tag{4-32}$$

In the last case as shown in Figure 4-12 c), $\left|\cos\alpha\right| > 0.1$, We prefer to use the isotropic mesh, *i.e.*, $h_{obj2} = h_{obj1}$.

It is important to bound with $h_{\max\_liq}$ in equation (4-31), in order to get good transient meshes between fine meshes (in the mushy zone) and coarse meshes (in the bulk liquid zone).

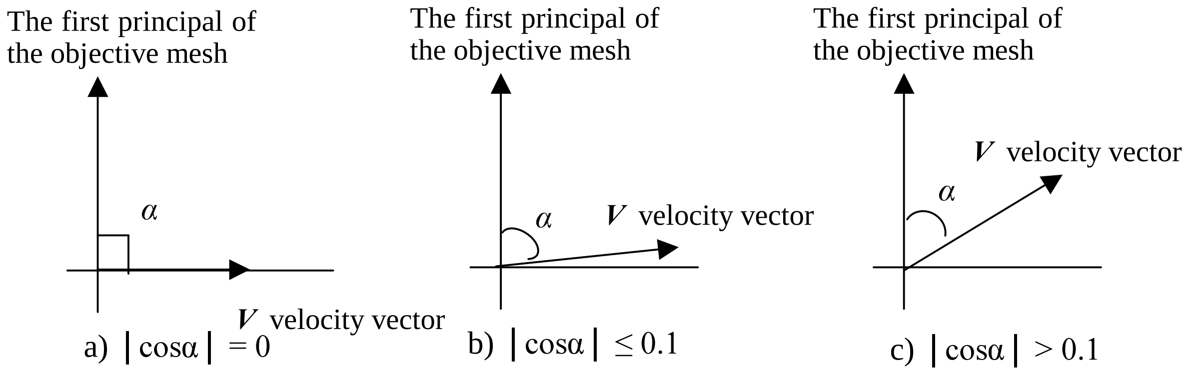

Figure 4-12 Schematic for the computation of objective mesh size

Remarks

It is very time consuming to track the isotherms and compute the distance to the isotherms, as well as to generate a new mesh and transport the variables from the old mesh to the new mesh. To prevent from doing too frequently the expensive operations, we compute the time interval Δt that is needed for the liquidus isotherm to travel through a mesh, as shown in Figure 4-13. During the time interval Δt, we do not perform the operations. In order to estimate the time interval Δt, let us consider the isotherm of $g_l = 1.0$:

$$\frac{dg_l}{dt} = 0 \quad \Rightarrow \quad \frac{\partial g_l}{\partial t} + \nabla \mathrm{g_l} \cdot \mathbf{U} = 0 \tag{4-33}$$

where $\mathbf{U}$ denotes the moving velocity of the liquidus isotherm. Knowing the gradient of liquid fraction in the element ∇g_l^e, and the average solidification rate in the element, $\left(\frac{\partial g_l}{\partial t} \right)^e$, the moving velocity of the liquidus isotherm can be deduced from 4-33. Then, the time interval Δt is estimated by the following equation:

$$\Delta t = \min\left(\frac{h^T \left\| \nabla g_l^e \right\|}{\left| \left(\frac{\partial g_l}{\partial t} \right)^e \right|} \right) \tag{4-34}$$

where, h^T is the mesh size of an element in the direction normal to the liquidus isotherm.

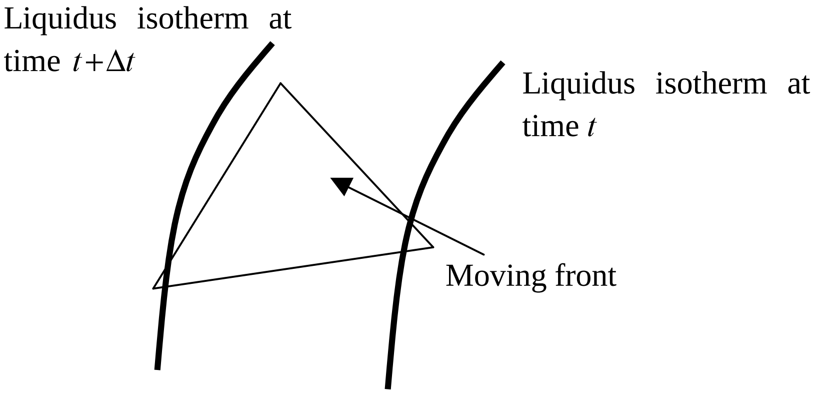

Figure 4-13 Schematic of the moving liquidus isotherm

Chapter 5

Numerical results of macrosegregation

Résultats numériques en macroségrégation – Résumé en français

Les modèles développés, intégrés dans le logiciel R2SOL, ont été appliqués à trois cas de macroségrégation. Le premier est le test de Hebditch et Hunt, consistant en la solidification de petits lingots parallélépipédiques d'alliages Sn-5%Pb et Pb-48%Sn. Ce test est intéressant car il a déjà fait l'objet d'études comparatives dans la littérature (Ahmad et al.) et il implique des tendances opposées en terme de convection thermo-solutale. Dans le cas du premier alliage, les convections thermique et solutale se conjuguent, donnant lieu à une forte tendance à la formation de canaux ségrégés. Dans le second cas, ces convections s'opposent, mais la macroségrégation est également marquée. L'accord entre simulation et mesures expérimentales est de bonne qualité. Les influences de la discrétisation spatiale et temporelle et des schémas de couplage sont alors discutées, notamment par rapport à la capacité de prédiction des canaux ségrégés. En outre, l'efficacité de l'adaptation de maillage est démontrée. Les résultats sont présentés dans les sections 5.1 à 5.3. On montre que les canaux ségrégés peuvent être détectés à condition d'utiliser des maillages et des discrétisations temporelles suffisamment fines et éventuellement un couplage fort entre les différentes résolutions incrémentales.

Le second cas étudié est un cas de solidification dirigée d'un alliage Pb-%10Sn. Au cours de la solidification dans un gradient de température positif, le liquide dans la zone pâteuse s'enrichit en soluté, ce qui donne lieu à des instabilités. Lorsque la vitesse de propagation du front est plus faible que la convection solutale dans la même direction, des canaux ségrégés se forment. La diffusion solutale étant beaucoup plus faible que la diffusion thermique, le liquide ségrégé garde une composition élevée en s'écoulant à travers la zone pâteuse vers des régions à température plus élevée. Le liquide enrichi peut alors retarder la croissance dendritique ou provoquer une refusion locale, créant ainsi des veines liquides verticales au travers de la zone pâteuse. Ces phénomènes complexes très fortement couplés ont pu être mis en évidence par le logiciel R2SOL en utilisant la formulation fortement couplée avec remaillage dynamique. Les résultats sont présentés à la section 5.4.

Finalement, du point de vue de l'application industrielle à l'échelle de lingots d'aciérie, la macroségrégation dans un lingot d'alliage binaire fer-carbone a été modélisée avec le logiciel, en utilisant le remaillage dynamique, ce qui a permis de mettre en évidence la formation de veines ségrégées de type « A » (section 5.5).

Chapter 5

Numerical results of macrosegregation

Macrosegregation resulting from the solidification of parallelepipedic ingot of Pb-48%Sn alloy and Sn-5%Pb alloys has been examined by Hebditch and Hunt [1974]. This test has already served as a benchmark to evaluate the computational codes (Ahmad *et al*. [1998], Desbiolles *et al*. [2003]). We have also adopted this test to validate R2SOL. A confrontation with the experimental results and numerical results obtained by the finite volume code SOLID has been done. We will present these results in sections 5.1 to 5.3.

In section 5.4, the ability of R2SOL to model the freckling phenomena, thanks to adaptive remeshing strategies, will be demonstrated

Finally, from the point of view of industrial applications, the macrosegregation in an industrial steel ingot has been studied. The computational results will be shown in section 5.5.

5.1 Benchmark test of Hebditch and Hunt

Hebditch and Hunt [1974] solidified a Pb-48%Sn alloy and a Sn-5%Pb alloy in a parallelepipedic cavity 0.06 m high, 0.1 m long and 0.013 m thick. The cavity was insulated on all surfaces except the thinnest lateral surface. Heat was extracted from only one (the left) surface as shown in Figure 5-1. After solidification, macrosegregations were measured by spectro-photometry. The concentration values were considered to be accurate to $\pm 2\,\%$ of the concentration values.

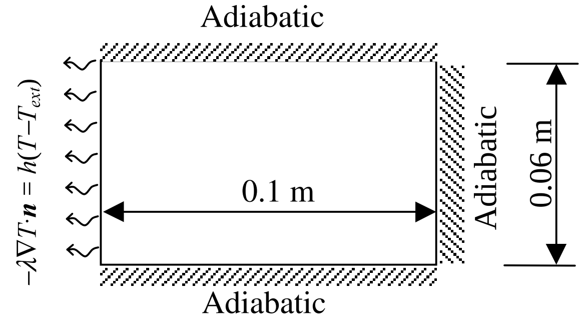

Figure 5-1 Schematics of the HH test

This setup of experiment was nearly 2-dimensional. Assuming that the fluid flow in the largest midplane section was not influenced by the two parallel walls of the cavity, the situation was considered to be a 2-dimensional problem. The macrosegregation in the largest midplane was simulated by Ahmad *et al*. [1998] using the finite element code CALCOSOFT developed at Ecole Polytechnique Fédérale de Lausanne and the finite volume code SOLID developed at Ecole des Mines de Nancy. The physical data and parameters used in the calculation are given in Table 5-1. The boundary conditions for the thermal analysis are illustrated in Figure 5-1: A Fourier condition is applied to the left wall, adiabatic conditions are imposed on the other three walls. The initial temperature field is assumed to be uniform, being at T_{init}. For solute transport analysis, there is no solute exchange through the boundaries, and the initial concentration field is supposed homogeneous, $w = w_0$. Zero initial velocity and a no slip boundary condition are applied for mechanical analysis. The numerical results obtained by the two codes, CALCOSOFT and SOLID, globally coincide with the experimental results. Ahmad *et al*. [1998] proposed then that Hebditch and Hunt test could be a classical benchmark test for macrosegregation computations.

It should be noted that the solidification times and thermal fields are not accurately reported in the article of Hebditch and Hunt [1974], except the initial temperature (being very close to the liquidus temperature). Some figures showing the advancement of the solidification front are presented, which are obtained by quenching the ingots at different times. Based on the advancement of the solidification front, cooling conditions (the heat exchange coefficient h and the external temperature T_{ext} in Table 5-1) have been estimated by Ahmad *et al*. [1998].

In the work of Ahmad *et al*. [1998], Carman-Kozeny relation (3-1) is used to compute the permeability of the mushy zone. A constant value of λ_2 (in Table 5-1) is used to fit the experimental segregation results.

Table 5- 1 Physical properties and computational parameters for the HH-test, Ahmad *et al*. [1998]

		Pb-48%Sn	Sn-5%Pb
Phase diagram data			
Nominal mass fraction, w_0	wt.pct	48.0	5.0
Melting temperature, T_f of the pure substance	°C	327.5	232.0
Eutectic temperature, T_{eut}	°C	183.0	183.0
Liquidus slope, m	$°C.(wt.pct)^{-1}$	-2.334	-1.286
Partition coefficient, k		0.307	0.0656
Eutectic mass fraction, w_{eut}	wt.pct	61.9	38.1
Thermal data			
Thermal conductivity, λ	$W.m^{-1}.K^{-1}$	50.0	55.0
Specific heat, c_p	$J.kg^{-1}.K^{-1}$	200.0	260.0
Latent heat, L	$J.kg^{-1}$	53550	61000
Other characteristics			
Reference density, ρ_0	$kg.m^{-3}$	9000	7000
Reference temperature, T_{ref}	°C	232	226
Thermal expansion coefficient, β_T	K^{-1}	1×10^{-4}	6×10^{-5}
Solutal expansion coefficient, β_w	$(wt.pct)^{-1}$	4.5×10^{-3}	-5.3×10^{-3}
Dynamic viscosity, μ	Pa.s	1×10^{-3}	1×10^{-3}
Secondary dendrite arm spacing, λ_2	m	40×10^{-6}	65×10^{-6}
Initial temperature, T_t	°C	216	226
Heat transfer coefficient, h	$W.m^{-2}.K^{-1}$	400	300
External temperature, T_{ext}	°C	25	25
Calculation parameters			
Time step	s	0.1	0.05
Gravity, $\|\mathbf{g}\|$	$m.s^{-2}$	9.81	9.81
Diffusion coefficient in liquid, ε	$m^2.s^{-1}$	1×10^{-9}	1×10^{-9}

In this test, horizontal gradients of temperature and solute concentration in the liquid are built up at the early stage of solidification. These two gradients lead to a horizontal gradient of the liquid density. Hence, thermal and solutal driven natural convection occurs in the cavity. It should be noted that natural convection occurring in the Pb-48%Sn alloy and the Sn-5%Pb alloy are different as shown in Figure 5-2. For the Sn-5%Pb alloy, the interdendritic liquid enriched in Pb becomes heavier. Combining with the temperature effect, the fluid flow is counterclockwise. However, for the Pb-48%Sn alloy, the interdendritic liquid being enriched in Sn, the effects of solute and temperature on the liquid density are opposite, but solute-induced convection dominates in this case, leading a clockwise fluid flow. At the beginning of solidification of the two alloys, it has been found that a solute difference Δw along the characteristic length (0.1 m) is about 10%, the solute Grashof number *Grc* ($G_{rc} = \frac{|g|\beta_w \Delta w L^3}{\nu^2} = \frac{9.8\times4.5\times10^{-3}\times0.1^3}{(10^{-3}/9000)^2} = 3.6\times10^9$, for the Pb-48%Sn alloy) is of the order of 10^9, this can cause a strong convection.

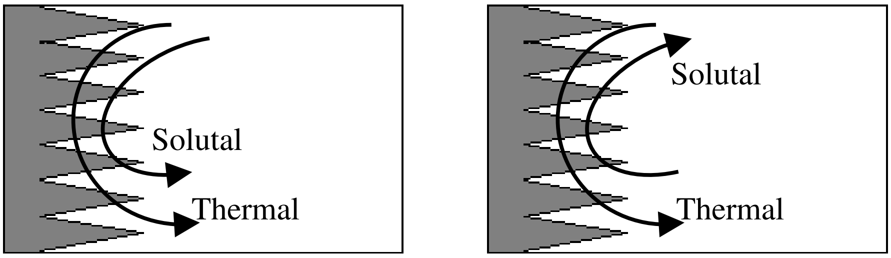

a) Sn-5%Pb alloy b) Pb-48%Sn alloy

Figure 5-2 Schematics of thermo-solutal convection, Ahmad *et al.* [1998]

5.2 Results for the Sn-5%Pb alloy

5.2.1 Numerical setup

Ahmad *et al.* [1998] computed the solidification of the Sn-5%Pb alloy using CALCOSOFT and SOLID. The governing equations used by Ahmad were exactly the same as those presented in chapter 3. Lever rule was considered as the microsegregation model. A structured mesh with 60×60 elements and a constant time step $\Delta t = 0.05\,s$ were used in the computation. *Full coupling* computations with iterations were performed. Macrosegregation maps at 400 *s* are shown in Figure 5-3. The computational result of SOLID, as shown in Figure 5-3 a), predicted the oscillation of average concentration in the middle region of the ingot, indicating the tendency to form segregated channels in this region. While CALCOSOFT predicted the oscillation only at the bottom of the ingot as shown in Figure 5-3 b).

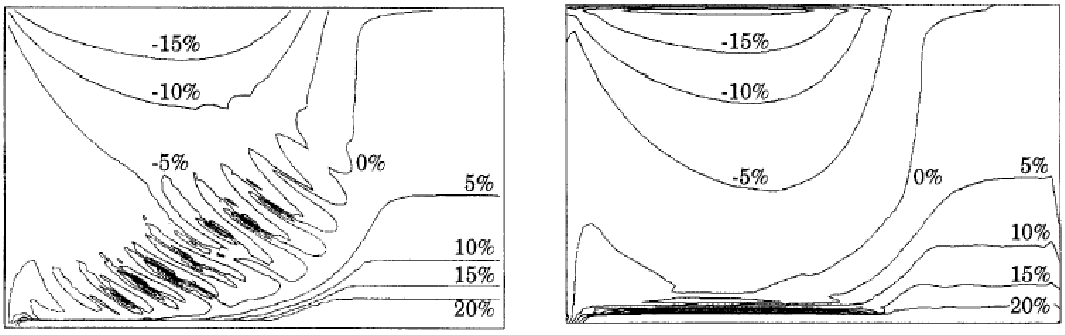

a) SOLID b) CALCOSOFT

Figure 5-3 The relative variation of the average concentration, (w-w_0)/w_0 at 400 s, from Ahmad *et al.* [1998]

Kämpfer [2002], using an improved version of CALCOSOFT with mesh refinement (see section 2.1.3) repeated the computation. The segregation map was similar to the map shown in Figure 5-3 b), the segregated channels being predicted along the bottom wall. Although a global agreement to the prediction of macrosegregation was achieved by the two codes, CALCOSOFT and SOLID, there are differences in the results.

Following the works of Ahmad *et al.* [1998] and Kämpfer [2002], we have performed numerical simulations of macrosegregation for this alloy with the codes R2SOL and SOLID, using the same physical parameters as presented in Table 5-1. The goals of the numerical tests are the followings:

- To study the mesh size influence. In this test, non-structured triangle meshes are used, the mesh sizes being given in Table 5-2. The time step is 0.05 *s*, taking the same value as the one used by Ahmad *et al.* [1998]. *Full coupling* computations have been carried out, *i.e.* in each time step iterations are performed to couple the velocity, temperature and concentration fields. The maximum number of iterations is limited to 30. The criteria to terminate the iterations are as follows:

  $$\left|\frac{T^{n+1}-T^{n}}{T^{n}}\right| \leq 1.0\times10^{-4} \text{ , for the resolution of energy equation}$$

  $$\text{and } \left|\frac{V^{n+1}-V^{n}}{V^{n}}\right| \leq 1.0\times10^{-4} \text{ , for the resolution of momentum equation}$$

  $$\text{and } \left|\frac{w^{n+1}-w^{n}}{w^{n}}\right| \leq 1.0\times10^{-4} \text{ , for the resolution of solute equation}$$

  n denoting the iteration number.

- To study the time step influence. Besides the standard time step 0.05 *s*, a larger and a smaller time steps, being 0.1 *s* and 0.025 *s*, are used. In this test, the *full coupling* approach is applied, but only one iteration is performed at each time step. The fixed mesh II is adopted (referring to Table 5-2).

- To study the influence of coupling iterations within each time step. In this test, a fixed mesh (Mesh II) is used, the time step being 0.05 *s*. Computations have been already done in the first and the second tests. Here, we compare the results obtained with iterations (the maximum number of iterations is 30, the criteria to terminate iterations are 10^{-4} for solving energy, solute and momentum equations respectively) and without iteration.

- To compare the results obtained by the *full coupling* approach and the *no-coupling* approach. The solidification of the Sn-5%Pb alloy has been re-computed with the no-coupling approach, using the fixed Mesh II and the time step $\Delta t = 0.05\,s$.

- To compare the results obtained by different solvers. Besides the traditional P1+/P1 formulation for solving the momentum equation, the so-called "P1/P1 SUPG-PSPG" formulation has been recently implemented in R2SOL. In addition, for the energy equation we have also implemented the "SUPG" method, which can be used instead of the nodal upwind method. We will compare the results obtained by the new solver, using the fixed Mesh II and the time step $\Delta t = 0.05\, s$ with the *full coupling* approach reduced to *one iteration*.

Table 5-2 Mesh size used in the computations

	Mesh I	Mesh II	Adaptive mesh
Mesh size	2.5 *mm*	1.3 *mm*	minimum 0.5 *mm* in the critical region, 1.3 *mm* in the solid-like and bulk liquid zones

Mesh I and Mesh II are the fixed meshes, whereas in the third case, the mesh is dynamically adapted. The mesh size of Mesh II is close to the mesh size used by Ahmad *et al*. [1998] (1.6 *mm* in the x-direction and 1 *mm* in the y-direction). For the adaptive mesh, the objective variation of solid fraction in each element is 0.02: we expect about 50 elements in the mushy zone. In fact, it is not necessary to apply fine elements covering all the mushy zone. We use fine elements in the critical region, i.e. in the mushy zone where $0.5 < g_l < 1$. The minimum mesh size is limited to 0.5 *mm*, to avoid extreme fine elements in the case of very large gradients of liquid fraction. In the zone with lower liquid fraction ($g_l < 0.5$) and in the liquid zone, the mesh size is 1.3 *mm*, being the original mesh size. In the solid-like zone, in order to keep the information on segregated channels, the objective relative variation of average concentration in each element is 1%.

In a first step, we present the results obtained in the different numerical tests (sections 5.2.2 to 5.2.7) hereunder. In a second step, we will discuss them in section 5.2.8.

5.2.2 Study of the mesh size influence

The test of the mesh size influence has been performed on the Sn-5%Pb alloy, using the *full coupling* approach. For the *full coupling* resolutions, the convergence has been achieved generally within 10 iterations, using the iterative criteria of 10^{-4} for coupling the energy, solute and momentum equations.

Figure 5-4 shows the results computed using the different meshes. The first column in Figure 5-4 presents the meshes. The second column shows the distribution of liquid fraction obtained at time *t* = 100 *s*. The third column shows the relative variation of average mass concentration, $(w - w_0)/w_0$, at time *t* = 400 *s*.

The first row shows the results calculated using a coarse mesh (Mesh I), the mesh size being 2.5 *mm*. The second row shows the results calculated using the standard mesh (Mesh II), the mesh size being equivalent to that used by Ahmad *et al*. [1998]. The computational results using an adaptive mesh, are shown on the third row. The fourth row shows the results computed by SOLID using a structured mesh with 60×60 elements, being progressively refined near the bottom wall. The last row shows the results computed by CALCOSOFT using a structured 60×60 quadrangle element mesh, with bilinear functions for all the fields except the pressure field, the pressure being assumed constant within each element (*i.e*., Q1-P0 element for the velocity-pressure fields).

Comparing the figures a), b) and c) in Figure 5-4 (showing the results obtained with R2SOL using different meshes), one find that the position and shape of the isoline $g_l = 0.5$ are very close. But some differences appear for the isolines $g_l = 0.9$ and $g_l = 0.99$: these isolines in the middle region become zigzagged with the mesh refinement. Seeing the segregation maps in the third column, a segregated channel near the bottom appears in the results of R2SOL. This has been already predicted by CALCOSOFT and SOLID. Besides, it is interesting to note that the tendency to form segregated channels in the middle region of the ingot has been captured by R2SOL, in particular using the adaptive mesh. This has been predicted by SOLID, but not by CALCOSOFT.

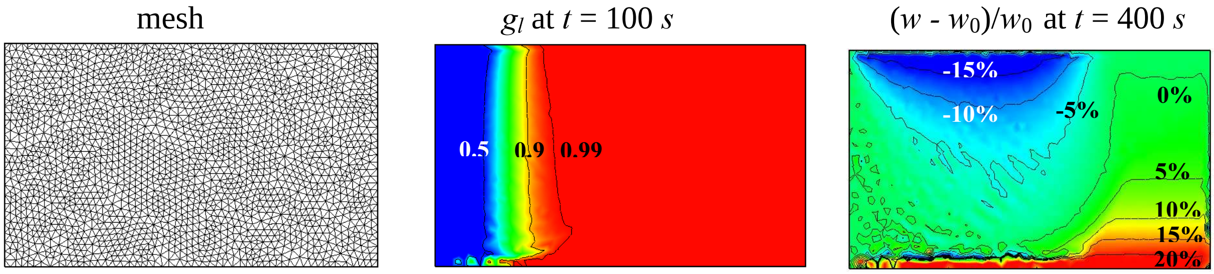

a) Mesh I, 2.5 *mm*

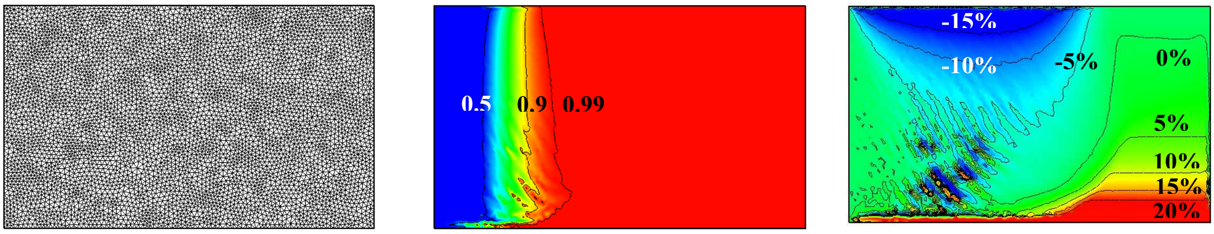

b) Mesh II, 1.3 *mm*

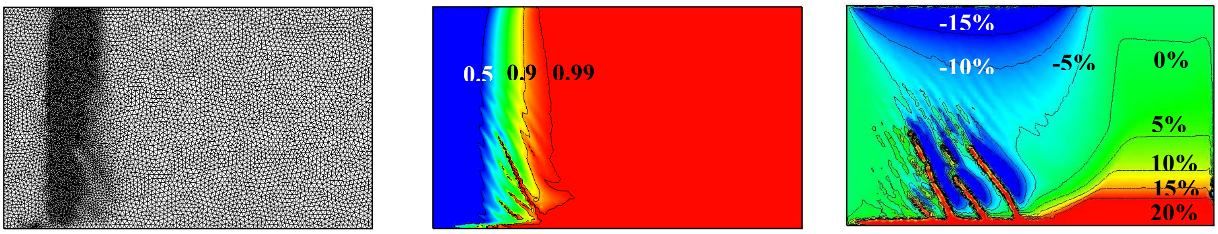

c) Adaptive mesh, at t = 100 s

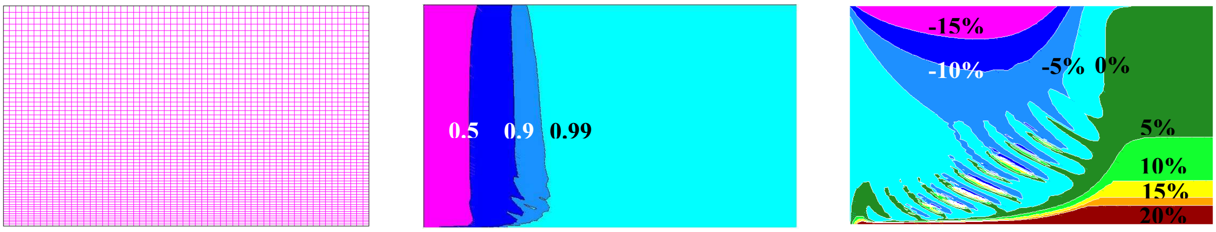

d) 60×60 structured mesh (fine at the bottom) used in SOLID computation

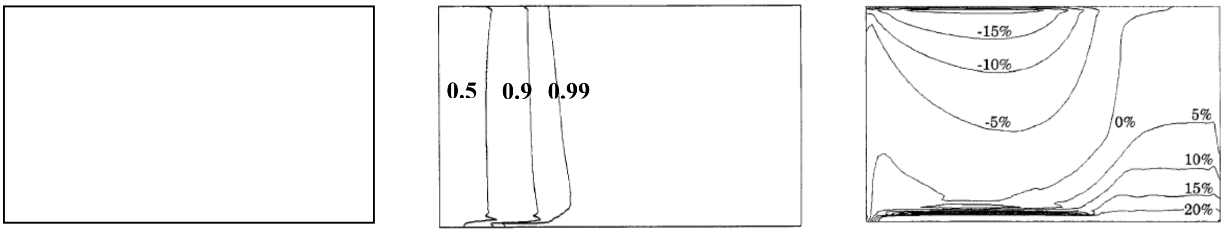

e) 60×60 structured mesh used in CALCOSOFT computation, from Ahmad *et al* [1998]

Figure 5-4 The *fully coupled* resolutions for the Sn-5%Pb alloy, showing the mesh influence

5.2.3 Study of the time step influence

In Figure 5-5 a), b) and c) we show the results computed with R2SOL using different time steps, Δt being 0.025 s, 0.05 s and 0.1 s respectively. The first column in Figure 5-5 shows the distribution of liquid fraction calculated at time t = 100 s. The second column shows the relative variation of the average mass concentration, $(w - w_0)/w_0$, at time t = 400 s.

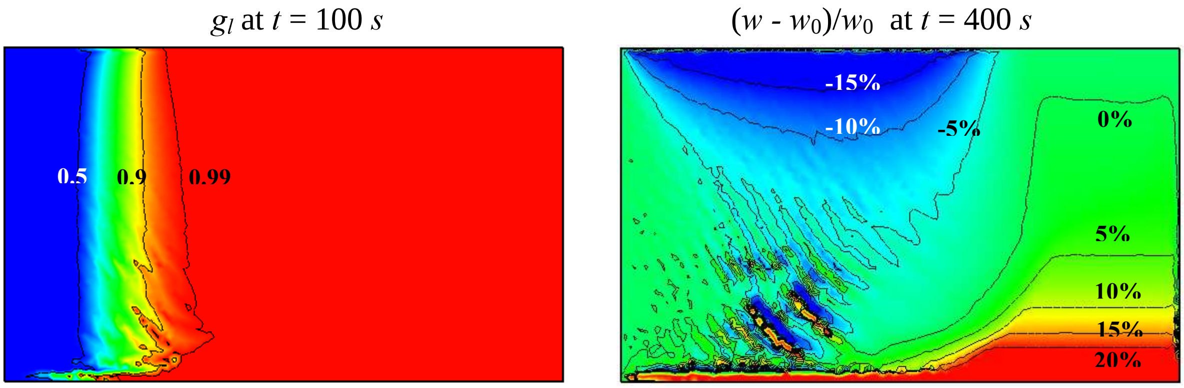
g_l at t = 100 s $(w - w_0)/w_0$ at t = 400 s

a) Δt = 0.025 s

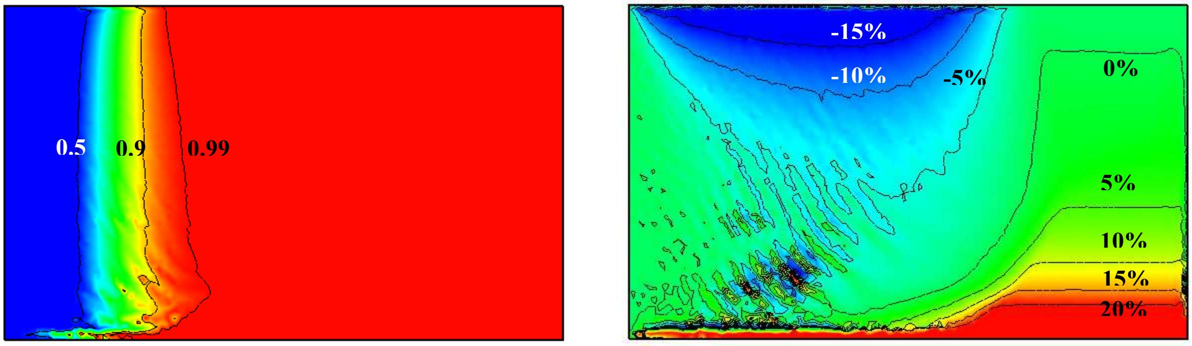

b) Δt = 0.05 s

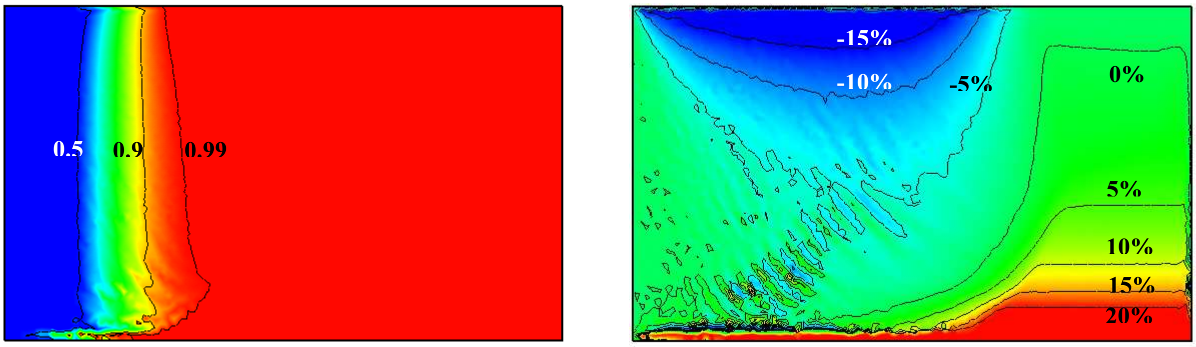

c) Δt = 0.1 s

Figure 5-5 *Fully coupled* resolutions limited to one iteration for the Sn-5%Pb alloy, showing the time step influence

Comparing the liquid fraction distribution at time t = 100 s, the isolines of liquid fraction become more instable in Figure 5-5 a) than in Figure 5-5 c); For segregation maps in the middle region at time t = 400, we note also that the variations of concentration in Figure 5-5 a) are greater than in Figure 5-5 c). It seems that the instabilities in the middle region can be captured properly using smaller time steps, comparing Figure 5-5 a), b) and c). The use of a larger time step, as shown in Figure 5-5 c), may smooth the liquid fraction and the average concentration fields.

5.2.4 Study of the influence of coupling iterations within each time step

In order to test the sensitivity to iterative coupling, let us compare the *fully coupled* and the *fully coupled reduced to one iteration* resolutions in Figure 5-6. The contours of $g_l = 0.99$ and

$g_l = 0.9$ shown in Figure 5-6 b) are smoother than those in Figure 5-6 a). This can be also seen in the segregation maps in Figure 5-6. It appears that the resolution is somewhat sensitive to the coupling iterations within each time step.

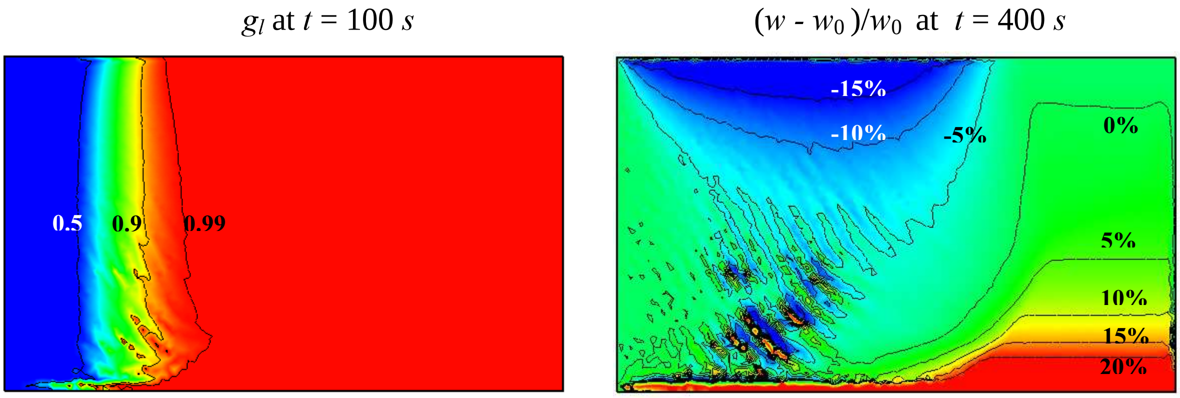

a) *fully coupled* resolutions (with iterations)

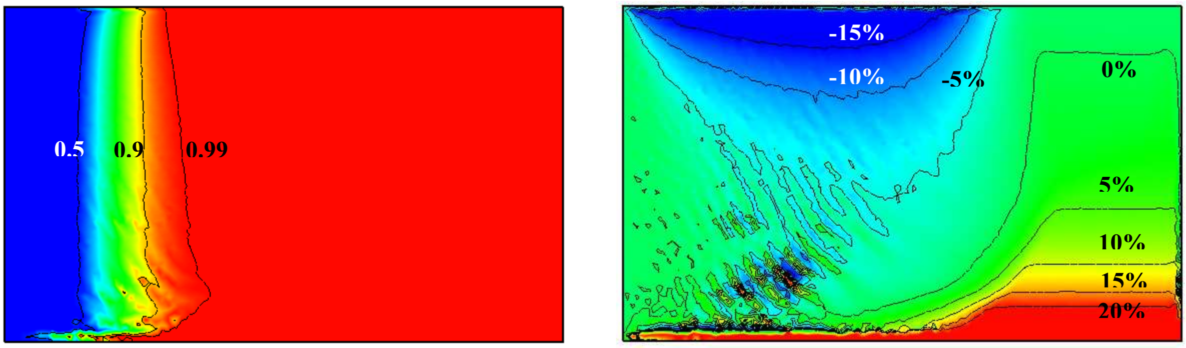

b) fully coupled resolutions *limited to one iteration*

Figure 5-6 Comparison between *fully coupled* and *fully coupled*, *limited to one iteration* resolutions, results calculated on Mesh II

5.2.5 No-coupling resolutions

The macrosegregation in the Sn-5%Pb alloy has been predicted by the *no-coupling* approach. In this computation, the enrichment of solute in the liquid pool is neglected. The map of liquid fraction at 100 s and the segregation pattern at 400 s are presented in Figure 5-7 a) and b) respectively. Comparing with the results obtained by the *full coupling* approach, it can be noticed that no segregated channels have been predicted by the *no-coupling* computation (cf. Figure 5-4 b)). However, the concentration pattern concerning the macrosegregation is very similar to that predicted by the fully coupled approach.

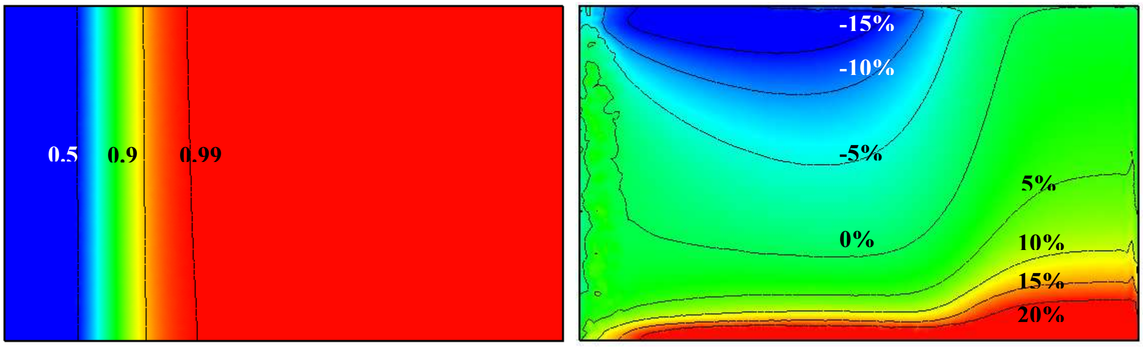

a) g_l at t = 100 s b) $(w- w_0)/w_0$ at t = 400 s

Figure 5-7 Numerical results obtained by the no-coupling approach using Mesh II, Δt = 0.05 s

5.2.6 Comparison between P1+/P1 and SUPG-PSPG formulations

In order to test the influence of different finite element schemes, we have used the P1/P1 SUPG-PSPG method to solve the momentum equation, and the SUPG method to solve the energy and solute equations. These methods are different from those used in the previous computations. Now the advection terms in momentum and energy equations are computed by the SUPG formulation, instead of the nodal upwind transport. For the momentum equation, the stabilization is achieved by the SUPG-PSPG method, instead of the P1+/P1 bubble formulation (cf. sections 3.6 and 3.7 for details). For the solute transport equation we use the same solver as the previous computations, being based on the SUPG method. The computation has been done on the fixed Mesh II with the *full coupling* approach reduced to *one iteration*. Figure 5-8 shows the map of liquid fraction at 100 s and the segregation pattern at 400 s. Comparing with Figure 5-6 b) obtained with the P1+/P1 nodal upwind solver, we note that the results obtained by those two finite element methods are very close.

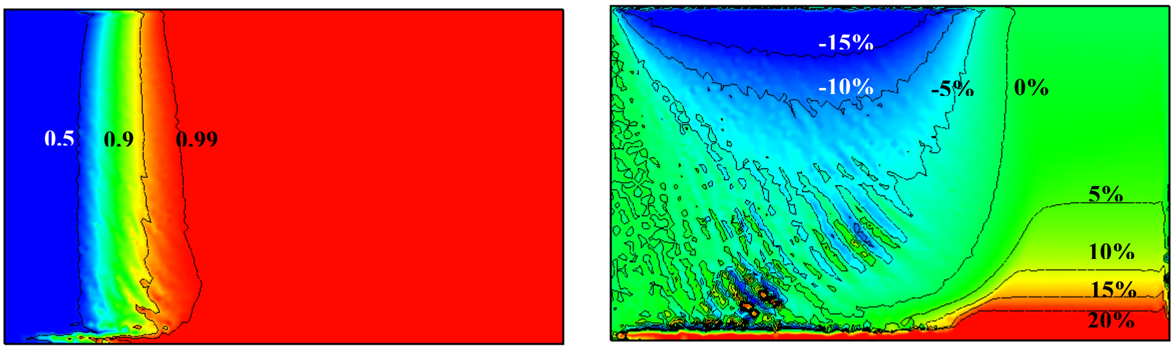

a) g_l at t = 100 s b) $(w- w_0)/w_0$ at t = 400 s

Figure 5-8 Results obtained by the P1/P1 SUPG-PSPG solver, using the full coupling approach reduced to one iteration with the fixed Mesh II and Δt = 0.05 s

5.2.7 Confrontation with experiments

The concentration profiles in different sections after complete solidification are shown in Figure 5-9. In the R2SOL and SOLID computations, the *full coupling* approaches have been used, and the same criteria to terminate iterations within each time step have been applied. Measurements and numerical predictions are in rather good agreement.

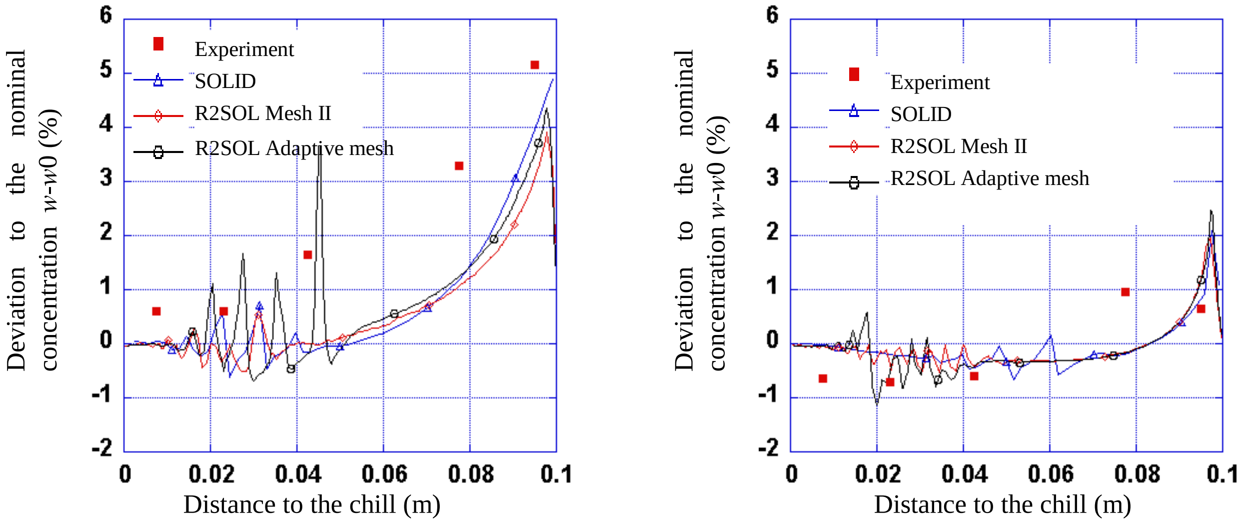

a) $y = 5$ *mm*

b) $y = 25$ *mm*

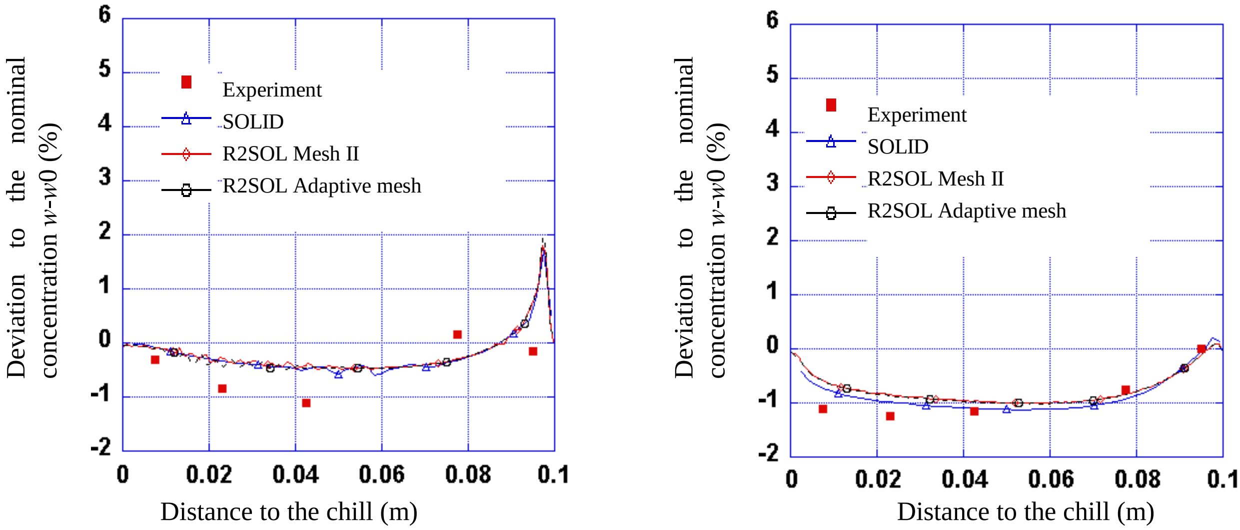

c) $y = 35$ *mm*

d) $y = 55$ *mm*

Figure 5-9 Profiles of the deviation to the nominal concentration ($w-w_0$ (%)) after solidification. Measurements and computational results obtained by R2SOL and SOLID using the full coupling approach with time step 0.05 *s*. These profiles correspond to various heights of the cavity: a) 5 *mm*, b) 25 *mm*, c) 35 *mm* and d) 55 *mm*. Sharp tips on the curves denote the occurrence of segregated channels.

5.2.8 Discussion on results for the Sn-5%Pb alloy

- **On the numerical models**

As it has been presented, two approaches, full coupling and no-coupling, have been used to predict the macrosegregation. In the no-coupling approach, locally the solidification path is fixed and the solidification is treated locally as a closed system. While in the full coupling approach, the solidification is treated as an open system. Observing the fact that segregated channels in the middle region have been predicted by the full coupling approach, but they have not been predicted by the no-coupling approach as shown in Figure 5-7, we note that an open system should be considered in order to predict these segregated channels.

However, regarding the global macrosegregation map obtained by the no-coupling computation, it is quite in agreement with that obtained by the full coupling computation. It appears then that the no-coupling approach can be used when the simulation of segregated channels is not of prime interest.

Regarding the different discretizations for the momentum equation in R2SOL, we have noted very few differences between P1+/P1 and P1/P1 SUPG-PSPG formulations. However, there are some differences between the results of R2SOL and CALCOSOFT, although these two codes are using finite elements and the same microsegregation model. The tendency to form segregated channels in the middle region has been captured by R2SOL, as with the finite volume code SOLID. This does not appear in the prediction of CALCOSOFT.

Here, we would like to recollect the discussion on the FVM and FEM formulations in the paper of Ahmad *et al.* [1998]. The authors proposed several possibilities to explain the differences observed in Figure 5-3:

- The treatment of the non-slip boundary condition. In the FEM formulation, the velocities are directly imposed and set to zero on the edges of the cavity. While in the FVM formulation, this boundary condition is expressed by using the tangential stress component. This leads to different velocities near the boundaries.
- The computation of the Darcy’s term. In the FEM, the Darcy’s term is integrated numerically at the Gauss points; In the FVM, the scalar quantities are computed at the center of each cell, while the velocities are computed on the faces of the cell. In order to compute the Darcy’s term, the permeability at the face center is interpolated by an average scheme. The computation of the Darcy’s term is different between the FEM and FVM schemes, which may lead to fairly large discrepancies between the two calculated velocity fields.
- The algorithms in the FEM and FVM. The meshes and the associated discretization schemes are different. The SIMPLEC algorithm is used in SOLID, therefore, staggered grids are employed for the discretization of the momentum equation. That is not the case in the FEM code. In addition, the upwind procedure in the FVM is not made along the streamlines as that in the FEM, which could add some numerical diffusion.

Since the inclined segregated channels in the middle region have been detected by R2SOL using FEM, it seems that these 3 points are definitely not the right explanation of the SOLID/CALCOSOFT differences.

Regarding the fact that segregated channels in the middle region have not been captured by CALCOSOFT with a structured mesh, we have also used a structured mesh (shown in Figure 5-10) to repeat the computation; and found that the tendency to form channels actually becomes very weak. These segregated channels are invisible in Figure 5-11 a), but can be shown in Figure 5-11 b) after changing the scale of the legend. It seems then that non-structured meshes are more sensitive to detect the freckles.

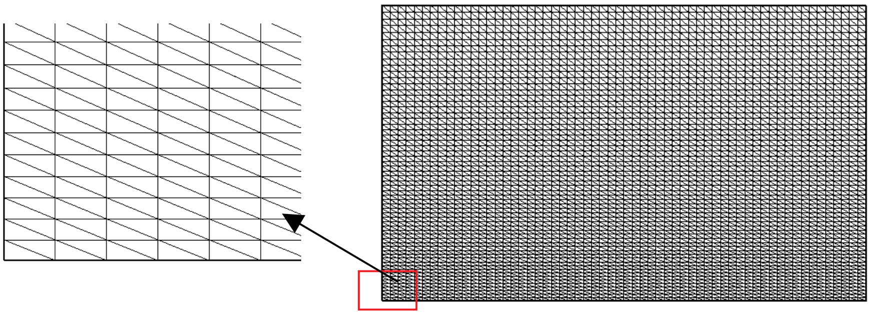

Figure 5-10 The structured mesh with 60×60 grids, used in R2SOL. In the vertical direction, the size increases geometrically by a factor of 1.0128, the minimum value being 0.67 mm; in the horizontal direction, the grids are uniform, the mesh size being 1.67 mm.

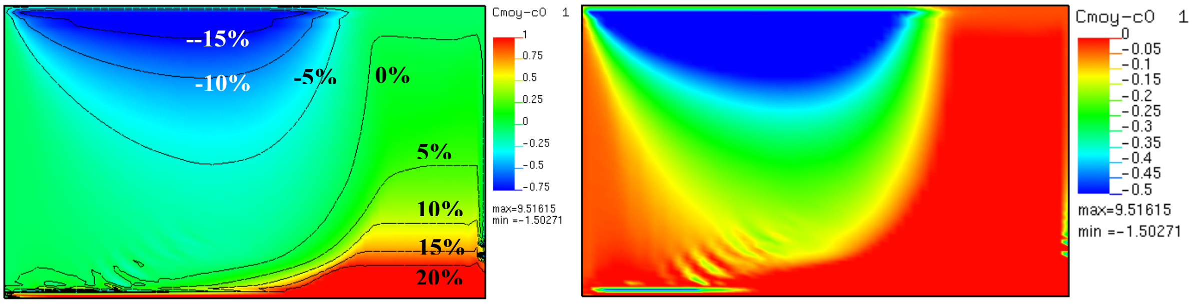

a) $(w - w_0)/w_0$ at $t = 400\ s$

b) negative segregation pattern $w - w_0$ at $t = 400\ s$

Figure 5-11 The segregation maps predicted by R2SOL. Using the full coupling approach with iterations, structured fixed mesh, $\Delta t = 0.05$ s

- **On time step, mesh size, and mesh refinement**

Comparing the results obtained by the different meshes and time steps in Figure 5-4 and Figure 5-5, we note that adequate fine mesh and small time step are necessary to capture segregated channels.

In order to discuss the mesh size influence on the segregated channels, we present the liquid fraction and velocity fields in Figure 5-12 and Figure 5-13 on next page. The results are obtained by the full coupling formulation using different meshes. Figure 5-12 shows the liquid fraction and the superimposed velocity field at $t = 100\ s$. The computation is performed using the coarse Mesh I. A segregated channel has been formed at the bottom. Consequently, strong flow at the bottom can be observed. Counterclockwise fluid flow occurs in the bulk liquid. Figure 5-13 presents the results calculated using the adaptive mesh: fine elements are used in the mushy zone. Besides the freckle at the bottom, several inclined freckles can be also observed. In the zoomed mushy region, one can observe that fluid within the freckles moves toward the bulk liquid with relative high velocity. Comparing Figure 5-12 and Figure 5-13, although the fluid flow in the bulk liquid is similar, the flow in the zoomed region is quite different.

It has been pointed out by Mehrabian *et al.* [1970] (referring to section 2.1.1), in the case of interdendritic fluid flow moving along the direction of temperature gradient (from lower temperature to higher temperature) and $\mathbf{v}\cdot\nabla T/\dot{T} < -1$, that remelting does occur and channels grow, leading to freckles opened to the bulk liquid. That is the case for the solidification of Sn-5%Pb alloy, in which counterclockwise fluid flow promotes the formation of freckles. Computational tests show that a fine mesh (and time step) is necessary to calculate the development of instabilities in interdendritic fluid flow, and then to capture the formation of freckles; while a coarse mesh (or time step) smoothes the velocity field, so that small perturbations cannot develop.

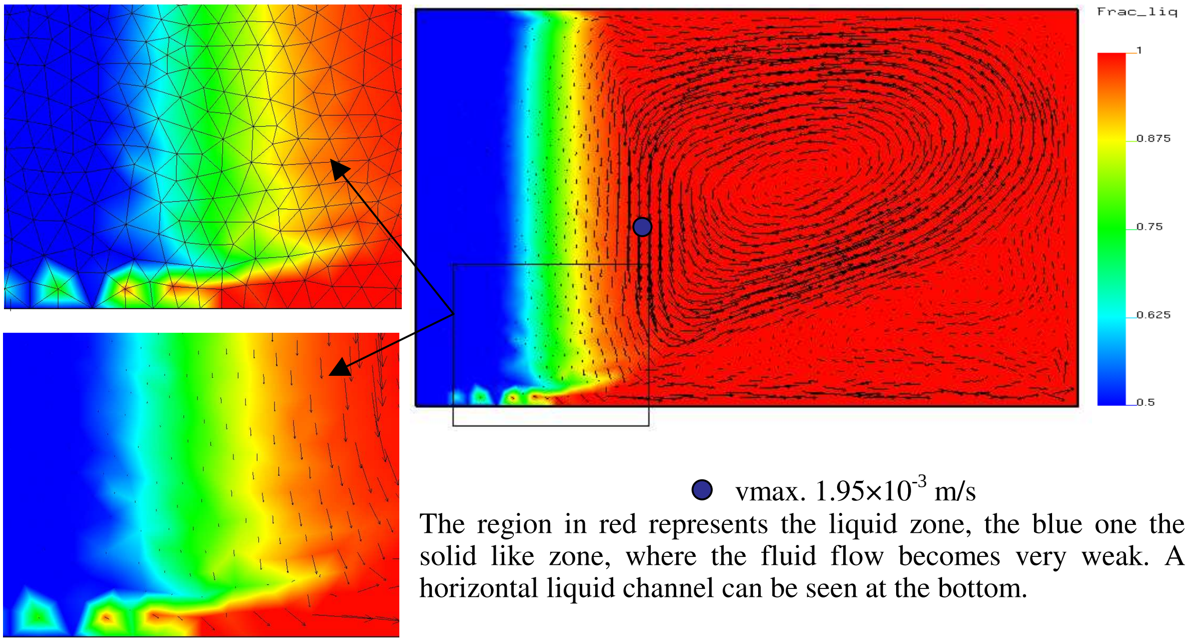

● vmax. 1.95×10^{-3} m/s

The region in red represents the liquid zone, the blue one the solid like zone, where the fluid flow becomes very weak. A horizontal liquid channel can be seen at the bottom.

Figure 5-12 The liquid fraction and velocity fields at 100 *s*, computed by the fully coupled approach on the coarse Mesh I, using Δt = 0.05 *s*

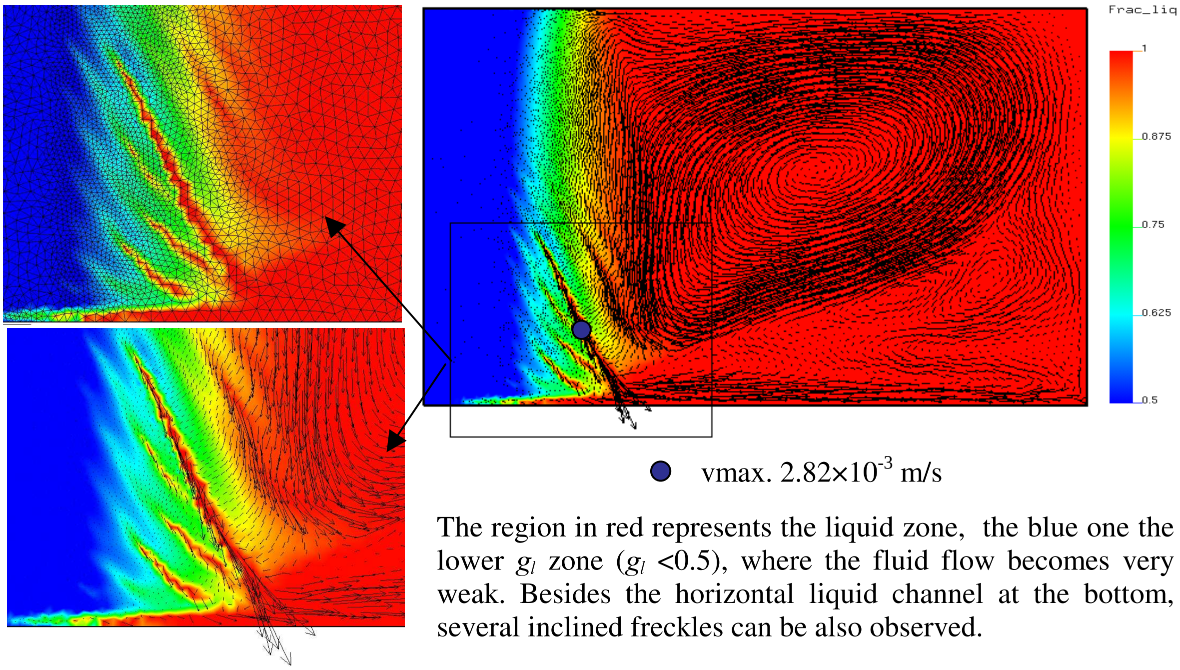

● vmax. 2.82×10^{-3} m/s

The region in red represents the liquid zone, the blue one the lower g_l zone (g_l <0.5), where the fluid flow becomes very weak. Besides the horizontal liquid channel at the bottom, several inclined freckles can be also observed.

Figure 5-13 The liquid fraction and velocity fields at 100 *s*, computed by the fully coupled approach on the adaptive mesh using Δt = 0.05 *s*

Figure 5-14 shows the results computed using the new version of CALCOSOFT developed by Kämpfer [2002], in which the momentum equations are solved by a Garlerkin least squares approach, including a mesh refinement technique (refer to section 2.1.3) . Kämpfer's results for the Sn-5%Pb alloy are similar to those of Ahmad *et al.* [1998] as shown in Figure 5-4 e).

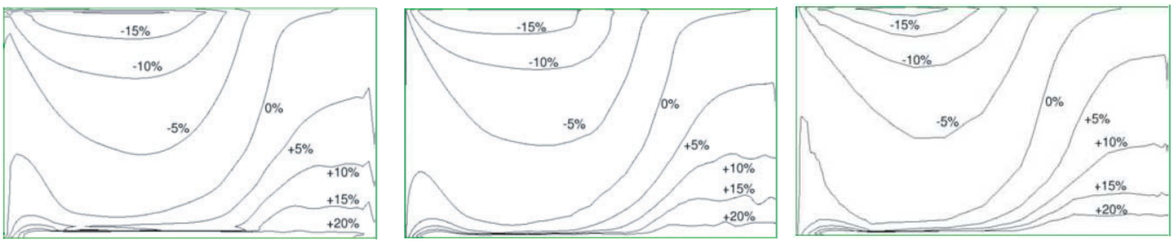

a) 60 ×60

b) 80 × 48

c) 40 ×24, adapted with refinement factor 2 in critical zone

Figure 5-14 CALCOSOFT results from Kämpfer [2002], showing segregation maps of $(w-w_0)/w_0$ at t = 400 *s*, using different structured meshes, Δt = 1 *s*. Small differences appear in the results using the 60×60 mesh and the 80×48 mesh. Results obtained in figure c) is comparable with those of the fixed mesh in figure b). Inclined segregated channels have not been captured.

- **On the coupling iterations within each time step**

We have found that the prediction of freckles is somewhat sensitive to computations with or without coupling iterations within each time step: see Figure 5-6. Since the *full coupling* resolution is costly, we would like to capture the freckles by using *one iteration*. Using the adaptive mesh and the time step $\Delta t = 0.05\,s$, the computation has been performed by the full coupling approach with only *one iteration*. The results are presented in Figure 5-15. Figure 5-15 a) shows the map of liquid fraction at t = 100 *s*, the zigzagged contour of $g_l = 0.9$ indicates the instabilities of interdendritic fluid flow. Figure 5-15 b) shows the map of $(w - w_0)/w_0$ at t = 400 *s*, revealing freckles. Comparing Figure 5-15 (one iteration resolution) and Figure 5-4 c) (iterative full coupling resolution), we note that the freckles can be predicted by the *one iteration* formulation when using the same adaptive remeshing strategy. However, further investigation would be needed to quantify the differences between the results

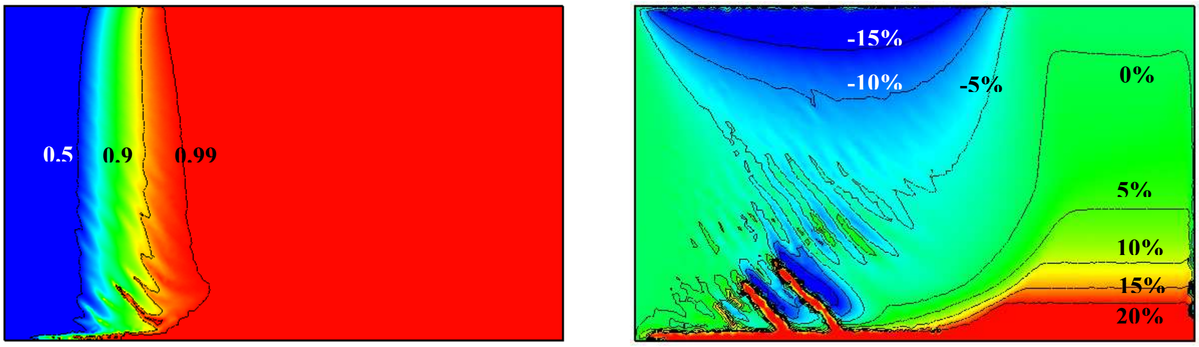

a) g_l at t = 100 *s*

b) $(w - w_0)/w_0$ at t = 400 *s*

Figure 5-15 Results obtained with the full coupling approach with only one iteration, using the adaptive mesh

In order to compare the computational cost, computations using full coupling with iterations and with only one iteration have been performed on a PC Pentium 4, 1.7 GHz processor and 1024MB RAM. Three meshes which have been presented before have been used, the time step being 0.05 *s* . Table 5-3 shows the computational time for 1000 time steps. The computational times of the one iteration resolution are about one half of the full coupling resolution.

Table 5-3 Computational times

Mesh	CPU time (s) /1000 time steps full coupling resolution	CPU time (s) /1000 time steps one iteration resolution
Mesh I	2968	1476
Mesh II	12218	6423
Adaptive mesh	26408	15673

5.3 Results for the Pb-48%Sn alloy

5.3.1 Numerical setup

A similar testing strategy has been applied to the Pb-48%Sn alloy:

- To study the mesh size influence, for simplicity the meshes described in Table 5-2 are used. In the computation with adaptive remeshing, the same parameters as those for Sn-5%Pb alloy are used. The time step is equal to 0.1 s, being the same value as that in the computation of Ahmad *et al*. [1998]. The *full coupling* computations have been carried out. As converged resolutions have been achieved within 10 iterations for the Sn-5%Pb alloy, this time the maximum number of iterations is limited to 10. The criteria to terminate the iterations are the same as defined for the Sn-5%Pb alloy, being 10^{-4} for coupling the energy, solute and momentum equations.
- To study the time step influence, three time steps, being 0.1 s, 0.05 s and 0.025 s, are used. The fixed mesh II is adopted (referring to Table 5-2). We compare the results obtained by the *full coupling* approach with one iteration.
- To study the influence of coupling iterations within each time step, we compare the results obtained with and without iterations, using the fixed Mesh II and the time step 0.1 s.
- To compare the results obtained by the *full coupling* approach, the computation has been done with the no-coupling approach, using the fixed Mesh II and the time step $\Delta t = 0.1 s$.

5.3.2 Mesh size influence

As it has been presented in section 5.1, the effects of solute and temperature on the liquid density are now opposite, leading to possibly more complex flow, resulting in some difficulties in the computation. In particular, at the beginning of solidification the convergence needs more than 10 iterations, but we skip out after 10 iterations. Figure 5-16 shows the results obtained with different meshes.

We have also computed this case with SOLID, using the same parameters as described in Table 5-1. A structured 50×40 element mesh is used. This time the mesh is progressively refined near the top wall, because there exists the tendency to the formation of a liquid channel. The results of CALCOSOFT from Ahmad *et al*. [1998] are also presented in Figure 5-16. Comparing the different results, it can be observed that the predictions of R2SOL and SOLID are very close: the shape of the contours of liquid fraction and concentration are similar, and their positions coincide. At the top of cavity the tendency to form a segregated channel appears in the results of R2SOL and

SOLID. Comparing the segregation patterns obtained using a coarse mesh and a fine adaptive mesh in Figure 5-16 a) and Figure 5-16 b), we notice that steep gradients occurring at the top can be better captured by mesh refinement.

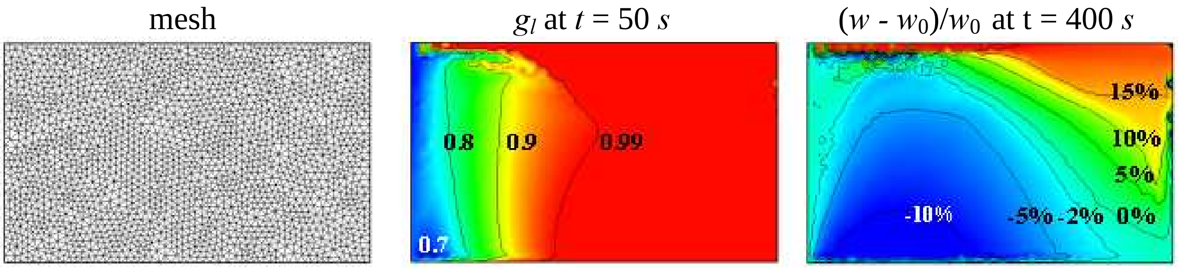

a) Mesh I, 2.5 *mm*

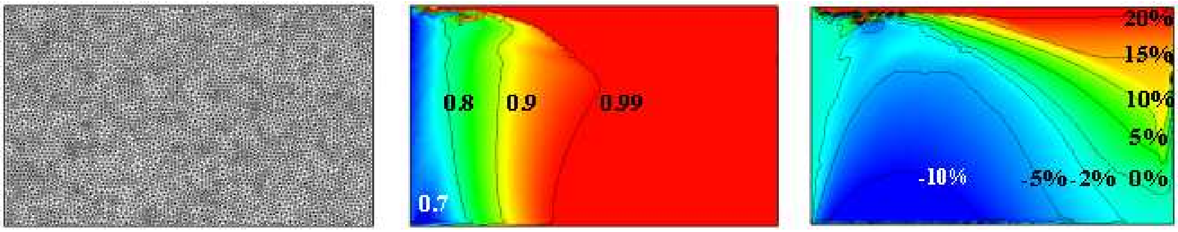

b) Mesh II, 1.3 *mm*

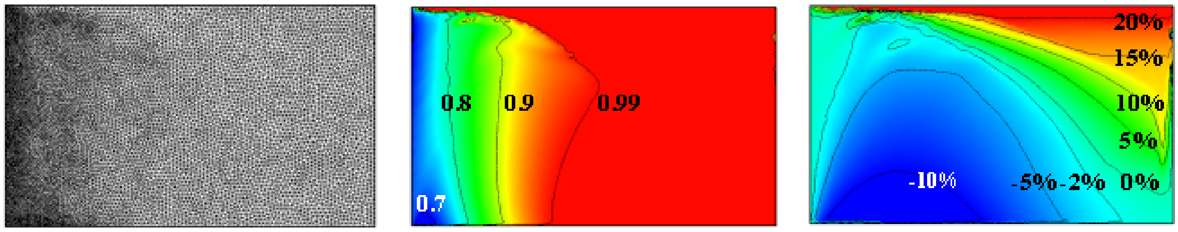

c) Adaptive mesh at $t = 50\ s$

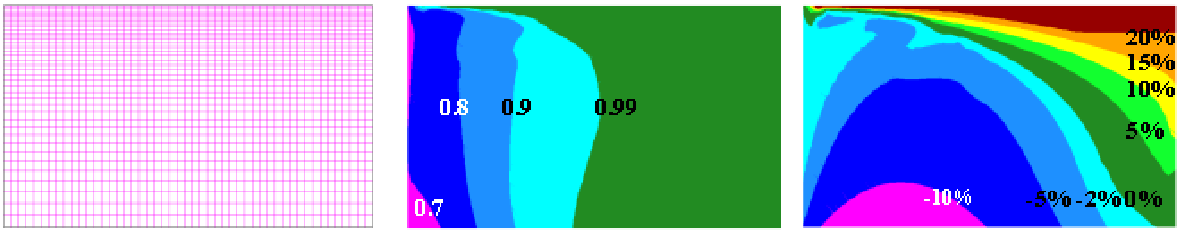

d) 50×40 structured mesh used
in SOLID computation

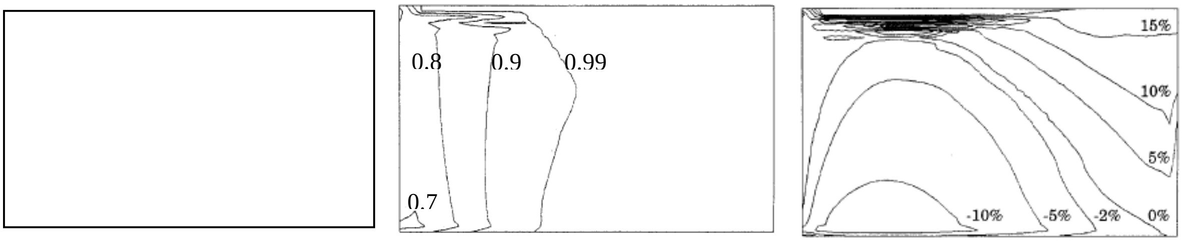

e) 50×40 structured uniform mesh used in CALCOSOFT computation, from Ahmad *et al* [1998]

Figure 5-16 The *fully coupled* resolutions for the Pb-48%Sn alloy, showing the mesh influence.

5.3.3 Time step influence

The test for time step influence has been performed using different time steps (being 0.025 *s*, 0.05 *s* and 0.1 *s*) on the same Mesh II. The results obtained with the *full coupling* resolutions (with only one iteration in each time step) are shown in Figure 5-17.

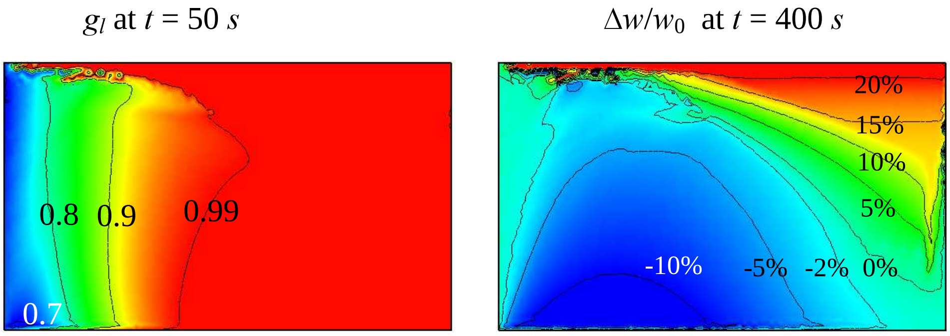

a) Δt = 0.025 s

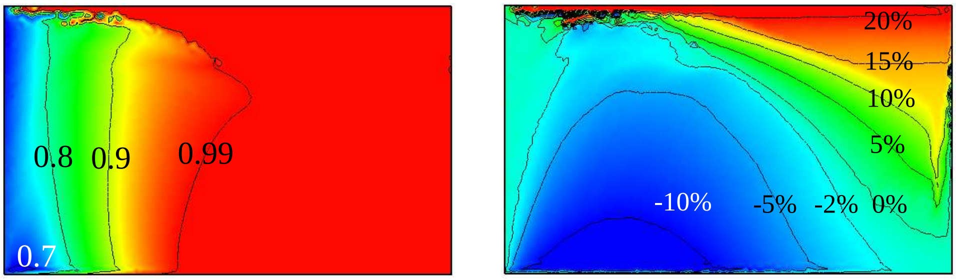

b) Δt = 0.05 s

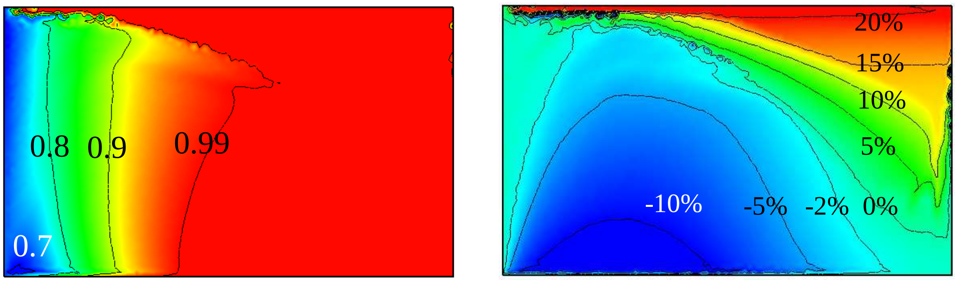

c) Δt = 0.1 s

Figure 5-17 *Fully coupled one iteration* resolutions for the Pb-48%Sn alloy, showing the time step influence

Looking at Figure 5-17 a) and b), only small differences can be found in the results calculated with time steps 0.025 *s* and 0.05 *s*. In addition, these results computed with only one iteration are very close to the full coupling results shown in Figure 5-16 b), indicating that the time step, Δt = 0.05 *s*, seems sufficiently small. Comparing Figure 5-17 a) and b) with c), there are some differences, a stronger tendency to the formation of freckles appearing in Figure 5-17 a) and b) than in Figure 5-17 c). Once again, we observe that smaller time steps favor the prediction of freckles.

5.3.4 Influence of coupling iterations within each time step

Let us compare the results obtained with and without iterations. The computational results obtained with Mesh II and the time step Δt = 0.1 *s*, are shown in Figure 5-18. As already noticed in the results of the Sn-5%Pb alloy, the prediction of freckles is somewhat sensitive to coupling iterations within each time step. The tendency to form freckles at the top of the cavity appearing in Figure 5-18 a) is stronger than that in Figure 5-18 b).

g_l at $t = 50$ *s* $(w - w_0)/w_0$ at $t = 400$ *s*

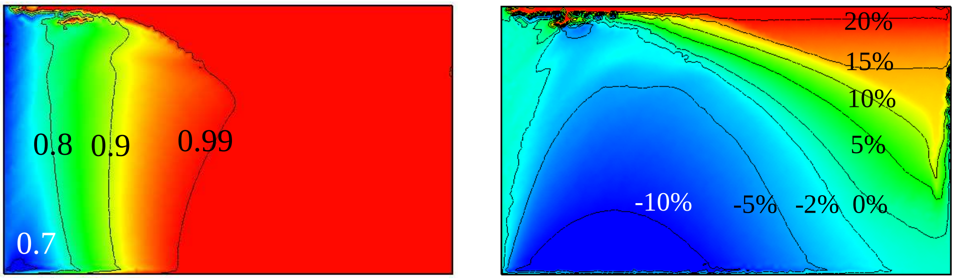

a) fully coupling resolutions (with iterations)

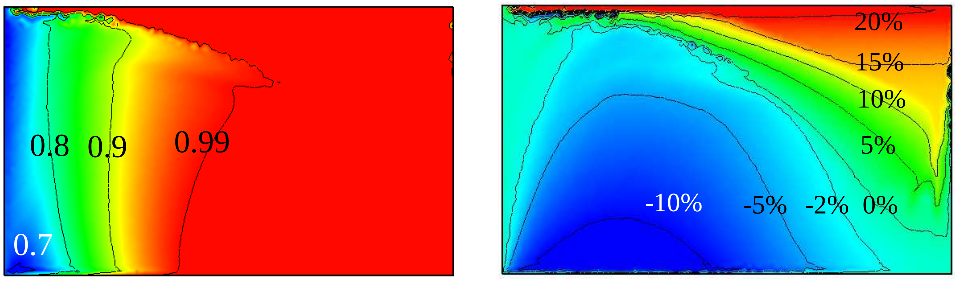

b) *one iteration* resolutions (without iteration)

Figure 5-18 Comparison between *fully coupled* and *one iteration* resolutions

5.3.5 No-coupling resolutions

We have also simulated the formation of macrosegregation in the Pb-48%Sn alloy, using the no-coupling approach and without accounting for the enrichment of solute in the liquid pool. The map of liquid fraction at 50 *s* and the segregation pattern at 400 *s* are presented in Figure 5-19. Comparing with the results obtained by the *full coupling* approach in Figure 5-16 b), one observe that the segregation patterns predicted by the no-coupling approach are not that far from those in Figure 5-16 b); but great differences appear in the distribution of liquid fraction.

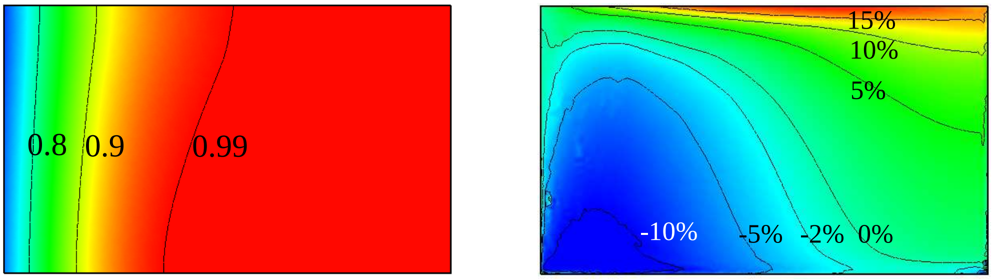

a) g_l at $t = 50$ *s* b) $(w - w_0)/w_0$ at $t = 400$ *s*

Figure 5-19 Results obtained by the no-coupling approach using the Mesh II, $\Delta t = 0.1$ *s*

5.3.6 Confrontation with experiments

A quantitative comparison between numerical and experimental results is shown in Figure 5-20, for which the concentration profiles in different sections after complete solidification are plotted. In the R2SOL and SOLID computations, the full coupling approaches are used, and the same computational parameters are applied. Measurements and numerical predictions are in rather good agreement, except in the top section, where the variations are important (as well as the measurement inaccuracy, particularly because of specimen deformation (Ahmad *et al*. [1998]).

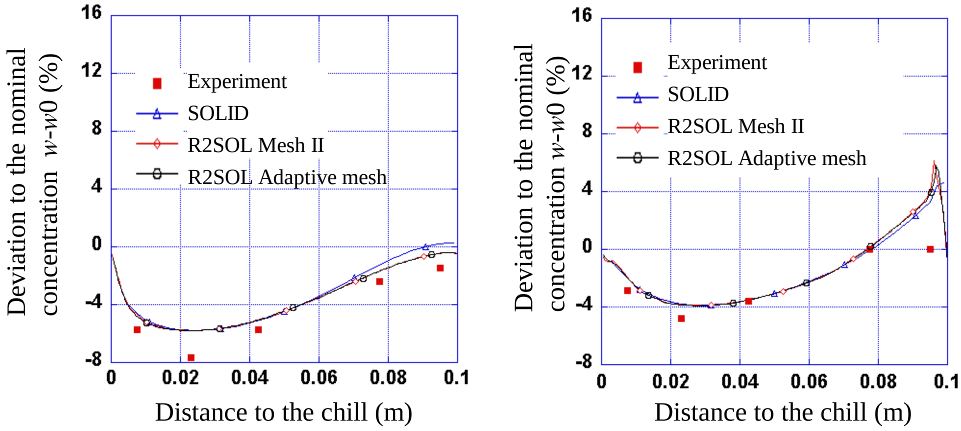

a) 5 mm b) 25 mm

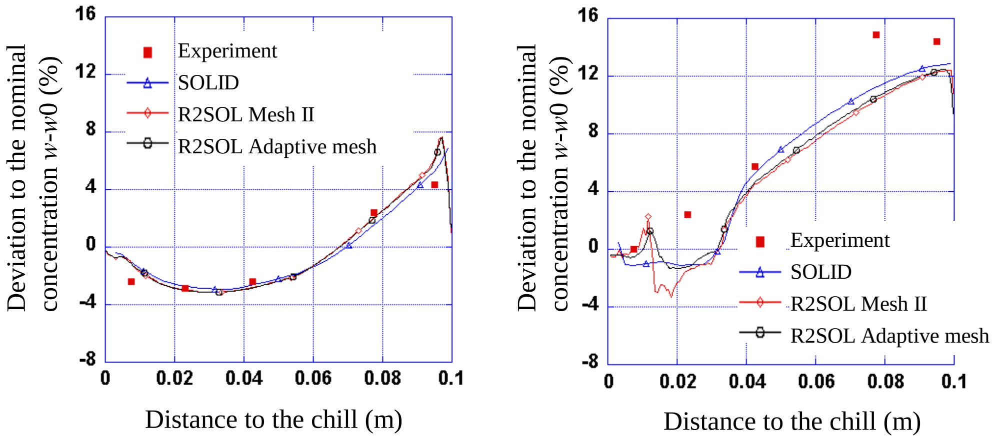

c) 35 mm d) 55 mm

Figure 5-20 Profiles of $w - w_0$ (%) after solidification. Measurements and computational results obtained by R2SOL and SOLID using the full coupling approach with time step 0.1 *s*. These profiles correspond to various heights of the cavity: a) 5 *mm*, b) 25 *mm*, c) 35 *mm* and d) 55 *mm*.

5.3.7 Concluding remarks

The numerical models presented in chapter 3 have been applied to the computation of macrosegregation in the Sn-5%Pb and Pb-48%Sn alloys. In the first alloy, the thermal and solutal convections are in the same direction, leading to a strong tendency to the formation of freckles. While in the second alloy, the effects of thermal and solutal gradients on the liquid density are opposite, but the last one dominates the fluid flow, and this alloy also exhibits a strong tendency to the formation of macrosegregation.

From the tests performed, we can conclude some points for the computation of macrosegregation as follows:

- The *full coupling* and *no-coupling* approaches have been validated by the benchmark test of Hebditch and Hunt. Since the thermal and solutal effects on solidification have been taken into account in the first approach (full coupling), it is able to predict the formation of segregated channels and freckles. While the global solute transport in the solidification has been treated by the second approach, leading to the prediction of the main spatial trends of macrosegregation.
- The computational tests for the two alloys show that the mesh size and time step influence the results. The computation with a coarse mesh and a large time step can not capture the localisations leading to segregated channels. Thus, in order to predict them, sufficient fine meshes and small time steps should be applied.
- Regarding the coupling itself, it appears that performing an iterative fully coupled resolution is desirable for the prediction of segregated channels. However, we have noted that they can be predicted by the one iteration resolution provided that an adaptive fine mesh and a smaller time step are used.

5.4 Modelling of freckles

"Freckle" in upward directional solidification of Ni-base superalloy turbine blades is a general cause of rejection. It has been reported that 40% of directional solidified blades are lost during casting (Frueh *et al.* [2002]), a blade that is rejected because of a casting defect, represents a loss of 49% when compared to overall production costs.

Motivated by industrial applications, researchers have investigated freckles for 30 years. Experiments with nonmetallic transparent systems have clearly shown that freckles are a direct consequence of upward liquid jets that emanate from the mushy zone (Copley *et al.* [1970]). During upward directional solidification with a positive temperature gradient, the liquid in the mushy zone may become instable due to chemical segregation. The buoyancy-driven convection is responsible for the formation of freckles. Since the solute diffusion is much lower than the thermal diffusion, the segregated liquid retains its composition as it flows upward through the mush into regions of higher temperature. There, the liquid enriched in solute elements can locally delay the growth of dendrites or remelt the solid, so that channels form in the mushy zone. Experiments with Pb-Sn alloys also show freckles formed by the same mechanism (Sarazin and Hellawell [1988]).

Considerable progress in numerical modeling of freckles has been achieved. Bennon and Incropera [1987B] have predicted the segregated channels in NH_4Cl-H_2O system. Felicelli *et al.* [1991] have simulated the formation of freckles in Pb-10%Sn alloys, following the experiments of Sarazin and Hellawell [1988]. Recently, several papers on the modeling of freckles (Felicelli *et al.* [1998], Frueh *et al.* [2002], Guo and Beckermann [2003]) have been published. These studies show that in order to predict freckles the mesh size should be sufficiently fine, being of the order of 0.1 mm.

Using a local refinement technique with non-confirming meshes, Kämpfer [2002] has simulated the formation of freckles in Pb-10%Sn alloys. The computation is based on the experimental study of Sarazin and Hellawell [1988] and the numerical modeling of Felicelli *et al.* [1991]. We have repeated the same computation. In this section, we present the numerical setup and our results.

5.4.1 Numerical setup

- Description of the problem

Felicelli *et al.* [1991] have simulated freckles in upward directional solidification of Pb-10%Sn alloy. In Felicelli's computation, a 2-dimensional domain of 5 mm in width and 10 mm in height is considered. The thermal conditions for the directional solidification are as follows: the side walls are insulated, and a vertical gradient of temperature, $\partial T/\partial z = G$, is imposed at the top boundary. At the bottom a time-dependant boundary condition, $T = T_0 + \dot{T}\,t$, is used, where T_0 is a reference temperature and $\dot{T}$ is the cooling rate. The thermal parameters T_0, $\dot{T}$ and G are selected from the experiments of Sarazin and Hellawell [1988].

Following Felicelli *et al.* [1991], Kämpfer has slightly changed the computation conditions to simulate the formation of freckles:

1) At the bottom, heat is extracted with a heat exchange coefficient of 20 W.m^{-2}.K^{-1} and an external temperature of 25°C. The reason to change the boundary condition is that: in the finite element code CALCOSOFT used by Kämpfer, the enthalpy is chosen as the primary unknown, and it is impossible to associate a unique enthalpy with each temperature during solidification. As shown in Figure 5-21, an approximate cooling rate of $\dot{T} = -0.015$ °C/s at the bottom boundary can be obtained using the heat exchange data proposed by Kämpfer. This cooling rate is comparable with that used by Felicelli, being $\dot{T} = -0.0167$ °C /s.

2) The mushy zone is modeled as an isotropic porous medium, its permeability is given by the Carman-Kozeny relation (3-1). In Felicelli *et al.* [1991], the mushy zone is considered as an anisotropic medium.

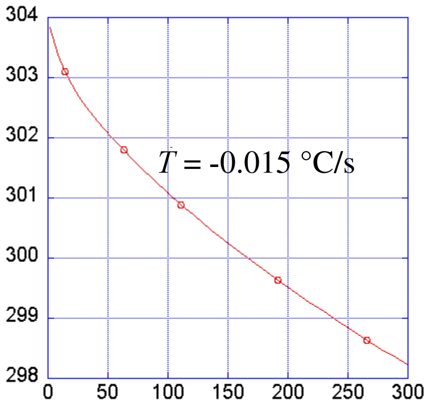

Figure 5-21 Temperature evolution at the center of the bottom wall.

Since the macrosegregation model in the present work is very close to that of Kämpfer [2002], we have adopted the same conditions. A computational domain of 30×50 mm^2 is considered, compared to 5 ×10 mm^2 used by Felicelli. The initial temperature field is linear in the vertical direction, 304°C at the bottom and 309°C at the top. During the upward solidification, a heat flux of 100 W/m^2 is imposed at the top surface, whereas heat is extracted at the bottom. We note that the thermal gradient in Kämpfer's work, being 0.1°C /mm, is smaller than that in Felicelli *et al.* [1991], being 1°C /mm, which could increase the tendency to freckles.

For the fluid flow, no-slip boundary conditions are imposed at the bottom and the lateral walls, while at the top an open cavity is simulated: the horizontal velocity component is imposed to be zero, $v_x = 0$, no condition on the vertical velocity component is prescribed.

The physical properties of the Pb-10%Sn alloy and the computational parameters are given in Table 5-4, which have been used by Kämpfer [2002].

Table 5-4 The physical properties and the computational parameters used for the freckles simulation

Phase diagram data		
Nominal mass fraction, w_0	wt.pct	10.0
Melting temperature, T_f of the pure substance	°C	327.5
Eutectic temperature, T_{eut}	°C	183.0
Liquidus slope, m	°C.(wt.pct)$^{-1}$	-2.334
Partition coefficient, k		0.307
Eutectic mass fraction, w_{eut}	wt.pct	61.9
Thermal data		
Thermal conductivity, λ	W.m^{-1}.K^{-1}	18.2
Specific heat, c_p	J.kg^{-1}.K^{-1}	167.0
Initial temperature T_{init} , linear	°C	304 at the bottom 309 at the top
Latent heat, L	J.kg^{-1}	26000
Thermal condition at bottom		
Heat transfer coefficient, h	W.m^{-2}.K^{-1}	20
External temperature, T_{ext}	°C	25
Thermal condition at top		
Heat flux, q	W.m^{-2}	100
Other characteristics		
Reference density, ρ_0	kg.m^{-3}	10100
Reference temperature, T_{ref}	°C	304
Thermal expansion coefficient, β_T	K^{-1}	1.2×10^{-4}
Solutal expansion coefficient, β_w	(wt.pct)$^{-1}$	5.15×10^{-3}
Dynamic viscosity, μ	Pa.s	2.4947×10^{-3}
Secondary dendrite arm spacing, λ_2	m	40×10^{-6}
Calculation parameters		
Time step	s	1.0
Gravity, $\|\mathbf{g}\|$	m.s^{-2}	9.81
Diffusion coefficient in liquid, ε	m^2.s^{-1}	3×10^{-9}

- Computational test cases

In Kämpfer's [2002] work, firstly, as a reference computation, a structured mesh with 30×40 elements was used. As expected, this simulation was not able to predict correctly the formation of freckles, as shown in Figure 5-22 (since we have not gotten the original paper from Kämpfer, the photocopy of the picture is not clear).

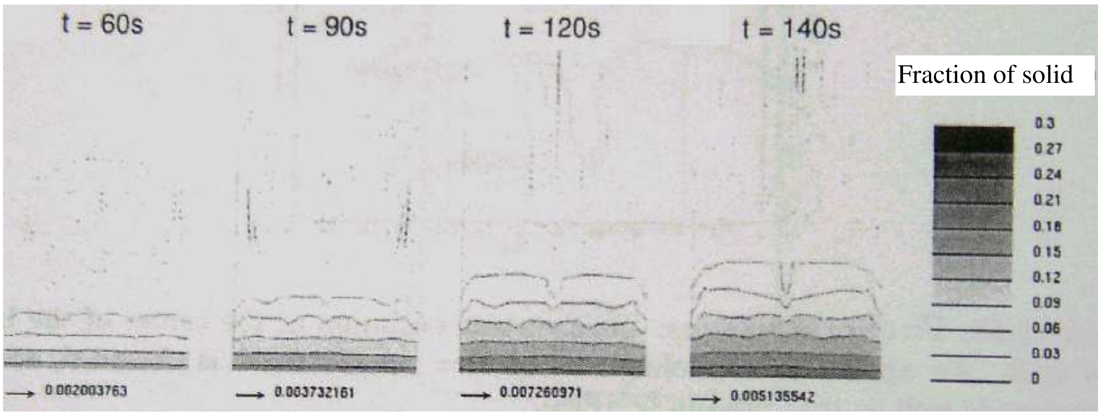

max. velocity $2. \times 10^{-3}$ (m/s) 3.7×10^{-3} 7.3×10^{-3} 5.1×10^{-3}

Figure 5-22 Results obtained by CALCOSOFT using a 30×40 structured mesh, from Kämpfer [2002]. Fraction of solid from 0 to 0.3, and the velocity fields together with the maximum velocity for t = 60, 90, 120 and 140 s respectively. The last figure, for t = 140 s, shows the tendency to the formation of freckles at the center and near the side walls.

Secondly, starting from time t = 60 s, the coarse structured mesh was refined by a factor of 2 in the critical mushy zone near the solidification front, the fine mesh sizes in the two directions being 0.25 mm × 0.31 mm respectively. Figure 2-5 in section 2.1.3 shows the mesh at t = 125 s, being structured but refined. With such a mesh refinement, freckles have been predicted as shown in Figure 5-23.

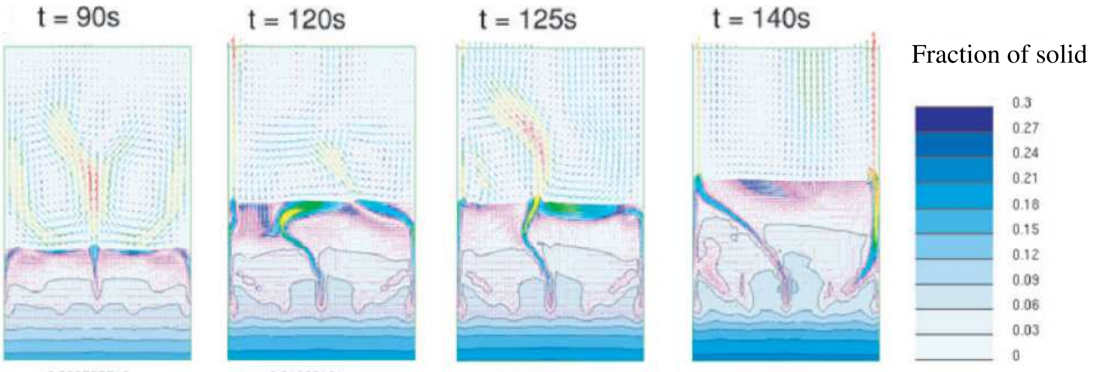

max. velocity 6.8×10^{-3} (m/s) 1.0×10^{-2} 1.4×10^{-2} 2.0×10^{-2}

Figure 5-23 Freckles simulated by CALCOSOFT using a local refinement technique with non conforming meshes, from Kämpfer [2002]. Fraction of solid from 0 to 0.3, the velocity fields together with the maximum velocity for t = 90, 120, 125 and 140 s respectively.

Compared to the work of Kämpfer, three meshes are considered in the present study, as shown in Figure 5-24. The first mesh is a structured and symmetric mesh with 32×40 elements, this mesh has a characteristic size comparable to the coarse mesh used by Kämpfer. The second mesh is non-structured, its size being 1 mm and comparable to the first one. The last mesh is an adaptive mesh: for the mushy zone close to the liquidus isotherm (where $0.95<g_l<1.0$), fine and uniform elements are used, their size being 0.25 mm. Near the boundaries fine elements are also used. Wheras coarse elements are used in the bulk liquid, the size being 1 mm. Unlike Kämpfer's computation, in our computation the mesh adaptation (introduced in chapter 4) has been applied since the beginning of computation.

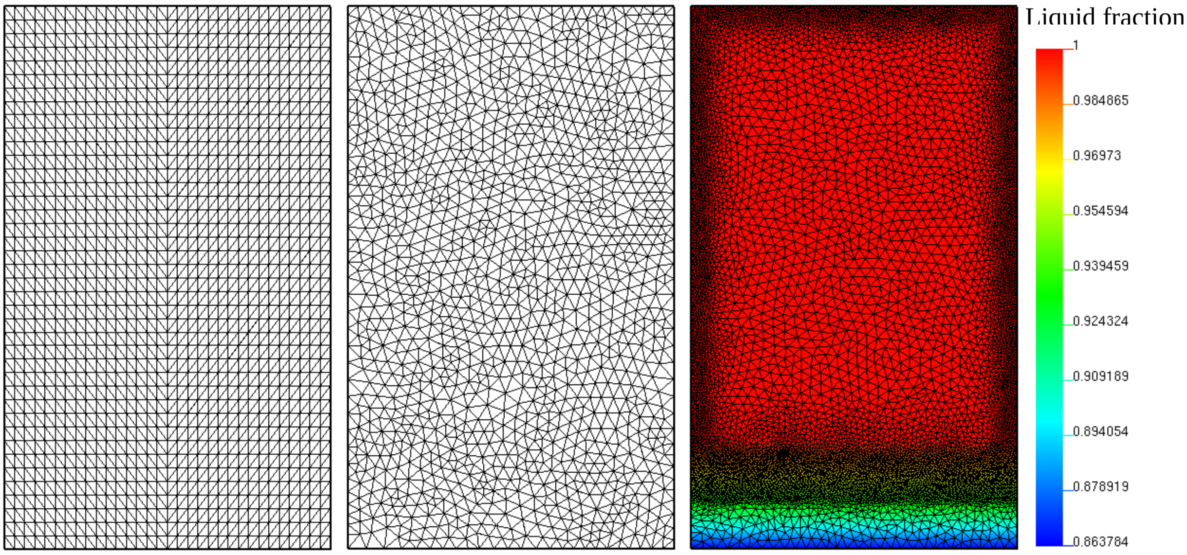

a) structured mesh b) non-structured mesh c) adaptive mesh

Figure 5-24 Meshes used in the simulation of freckles

The *full coupling* computations have been carried out with three meshes. The maximum number of iterations is limited to 30. The criteria to terminate the iterations are the same as in the tests of Hebditch and Hunt (10^{-4}). Firstly, we simply reproduce the Kämpfer's computation using the structured coarse mesh. Then, the second computation is performed with the non-structured coarse mesh, the influence of non-structured mesh is examined. Finally, the last computation with the mesh adaptation is run, aiming at showing the ability to capture freckles.

5.4.2 Results

Figure 5-25 shows the results obtained with the coarse structured mesh (see Figure 5-24 a)). Comparing with the results obtained by Kämpfer in Figure 5-22, the liquid fraction and the velocity field are presented for t = 30, 60, 90, 120 and 140 *s* respectively. It is interesting to note that the maximum velocities have different orders of magnitude, being from 10^{-5} to 10^{-3} (m/s) at different times. The development of a liquid jet at the center can be shown in the simulation with R2SOL. That is not the case in the prediction of CALCOSOFT, as shown in Figure 5-22, where the maximum velocity being of the same order at different times.

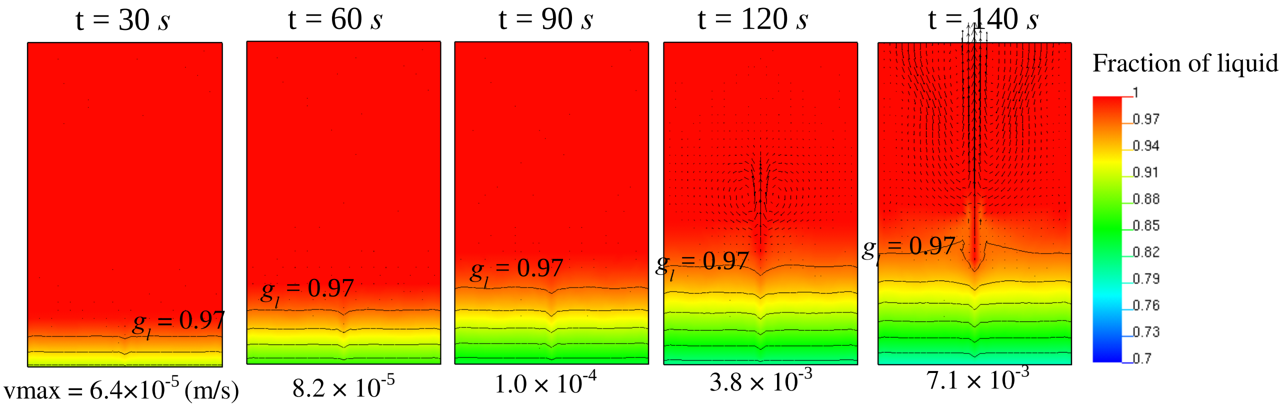

Figure 5-25 Freckles simulated by R2SOL using the coarse structured mesh: fraction of liquid and the velocity field at t = 30, 60, 90, 120 and 140 *s* respectively

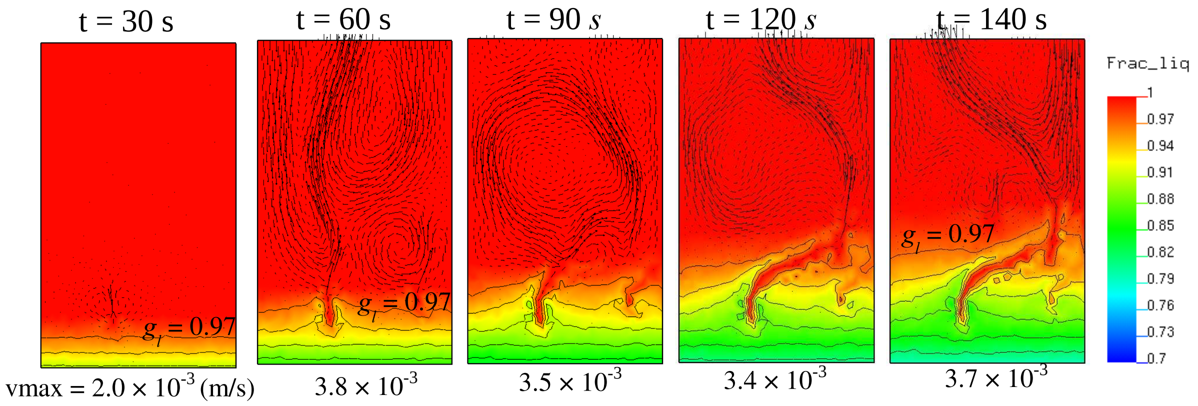

Figure 5-26 Freckles simulated by R2SOL using the coarse non-structured mesh

Figure 5-26 shows the results obtained with the coarse non-structured mesh (seeing Figure 5-24 b)). Comparing with Figure 5-25, it can be seen that the solidification front predicted using the non-structured mesh is more irregular. It seems that numerical perturbations resulting from the coarse non-structured mesh induce the instabilities of liquid, leading to a strong tendency to the formation of a freckle.

The freckles predicted by R2SOL using the adaptive mesh are shown in Figure 5-27. We present the isolines of liquid fraction and the velocity field at *t* = 90, 120, 130 and 140 *s* respectively. The instabilities near the solidification front appear at 120 *s*, leading to two freckles formed at 140 *s*. The segregated concentration fields together with the isolines of liquid fraction at *t* = 130, 140 and 165 *s* are shown in Figure 5-28. Clearly, one can see the development of freckles in these figures. For details, a zoom into the region where a freckle has been formed is presented in Figure 5-29. The ability to capture the freckling phenomena is here clearly demonstrated.

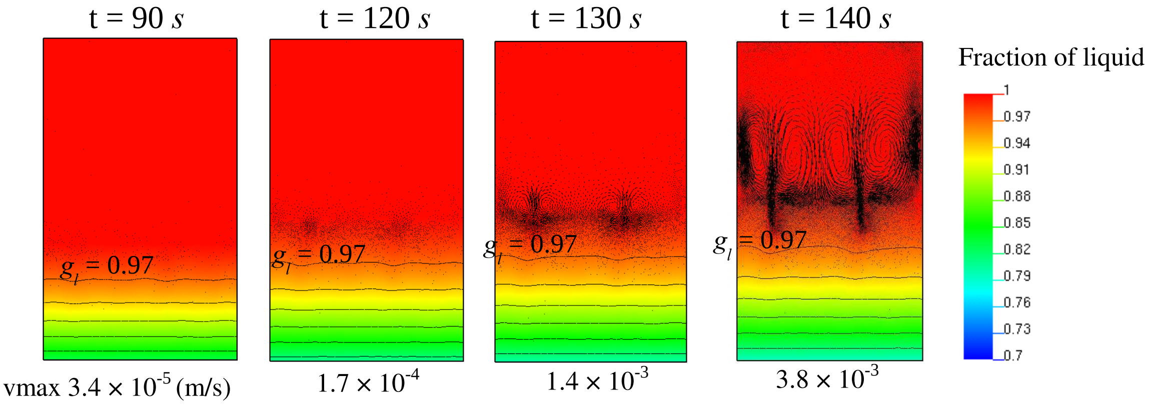

Figure 5-27 Freckles simulated by R2SOL using an adaptive mesh: liquid jets near the solidification front

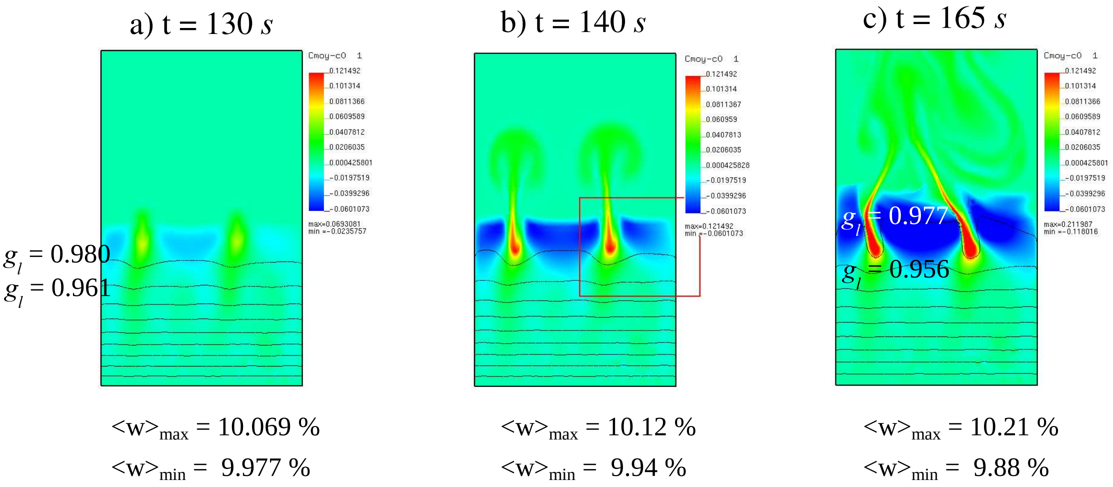

Figure 5-28 Freckles simulated by R2SOL using an adaptive mesh: segregated channels, the positive segregation regions presented in red, the negative segregation regions in blue. A zoom for the region in the red box, at *t* = 140 *s*, is presented in Figure 5-29

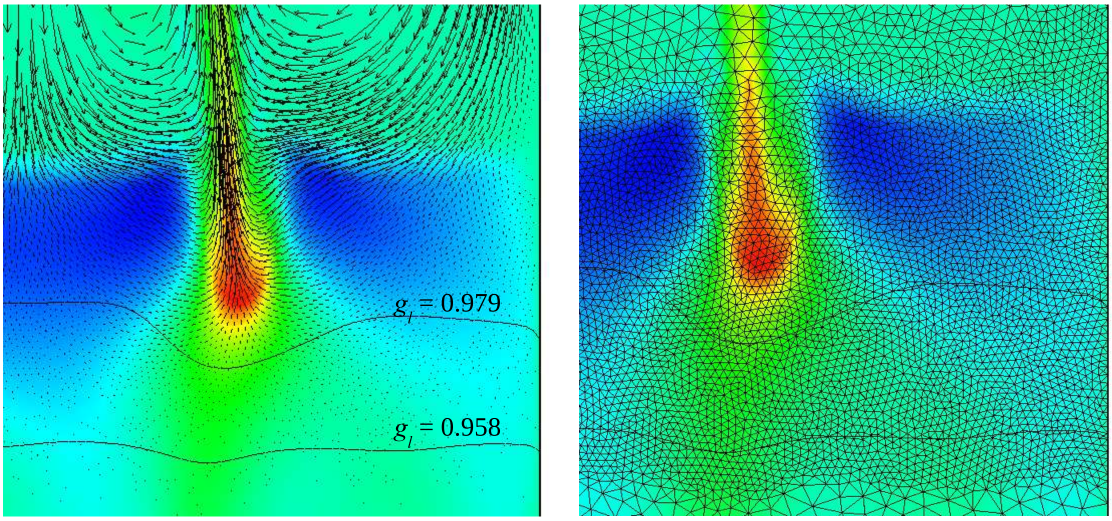

Figure 5-29 A zoom into a region where a freckle has been predicted by the adaptive mesh: on the left panel, the velocity vectors indicate the upward liquid jet. The mesh for the prediction of a freckle is presented in the right. As a background, the concentration field (deviation to the nominal concentration <w>-w0) is shown in colours, the solidification front is presented with the isolines of liquid fraction.

Comparing Figure 5-27 and Figure 5-23, we note that the maximum velocity calculated by R2SOL, at t = 140 s being 3.8×10^{-3} (m/s), is lower than that obtained by Kämpfer, being 2.0×10^{-2}

(m/s); consequently, the intensity of segregation calculated by R2SOL is lower. At t = 140 s, the maximum and minimum values of the average concentration obtained by R2SOL are 10.12% and 9.94% respectively, compared to 11.05% and 9.83% calculated by CALCOSOFT.

5.4.3 Discussion

Observing the results calculated with the coarse structured and non-structured meshes, one can find that the fluid flow in the mushy zone is not correctly predicted, although the tendency to freckles has been revealed. Comparing Figure 5-25 with Figure 5-26, we note that the non-structured coarse mesh introduces strong perturbations due to numerical reasons, leading to a strong tendency to freckles.

The prediction of freckles can be improved with adaptive remeshing, seeing Figure 5-29. In the present work, the mesh size near the solidification front is 0.25 mm, which may be not sufficiently fine. According to recent studies (Frueh *et al*. [2002], Guo and Beckermann [2003]), in order to accurately simulate the formation of freckles, the mesh size in the horizontal direction should be of the order of the primary dendrite spacing λ_1, being about 100 μm; in the vertical direction, the size should be comparable to D/R, being about 40 μm, where D is the diffusivity of solute element and R is the moving velocity of solidification front. Beyond the present work, it would be necessary to investigate more precisely the sensitivity of such results to time step, mesh size and remeshing parameters

5.5 Application to a steel ingot

For simplicity, we considered the solidification of a binary carbon steel alloy in a cylindrical ingot, which is similar to the octogonal 3.3 ton ingots produced by AUBERT & DUVAL. The geometry of the solidification system is shown in Figure 5-30, the weight of the studied ingot is 3.31 tons.

The mesh sizes for the mold and refractory are 15 and 5 (mm) respectively, and anisotropic adaptive meshes are used in the domain of ingot. The objective mesh size in the first principal direction is defined as follows:

- in the mushy zone, at the beginning of computation the minimum mesh size is 1 mm and it can be increased to 3 mm at the end of computation for saving CPU time, the maximum mesh size is 3 mm;
- in the liquid zone, the mesh size is in the range 1 to10 mm;
- in the solid zone, the mesh size is in the range 10 to 30 mm. A ratio factor of 5 is used to determine the objective mesh size in the second principal direction.

The detail of mesh adaptation can be referred to chapter 4.

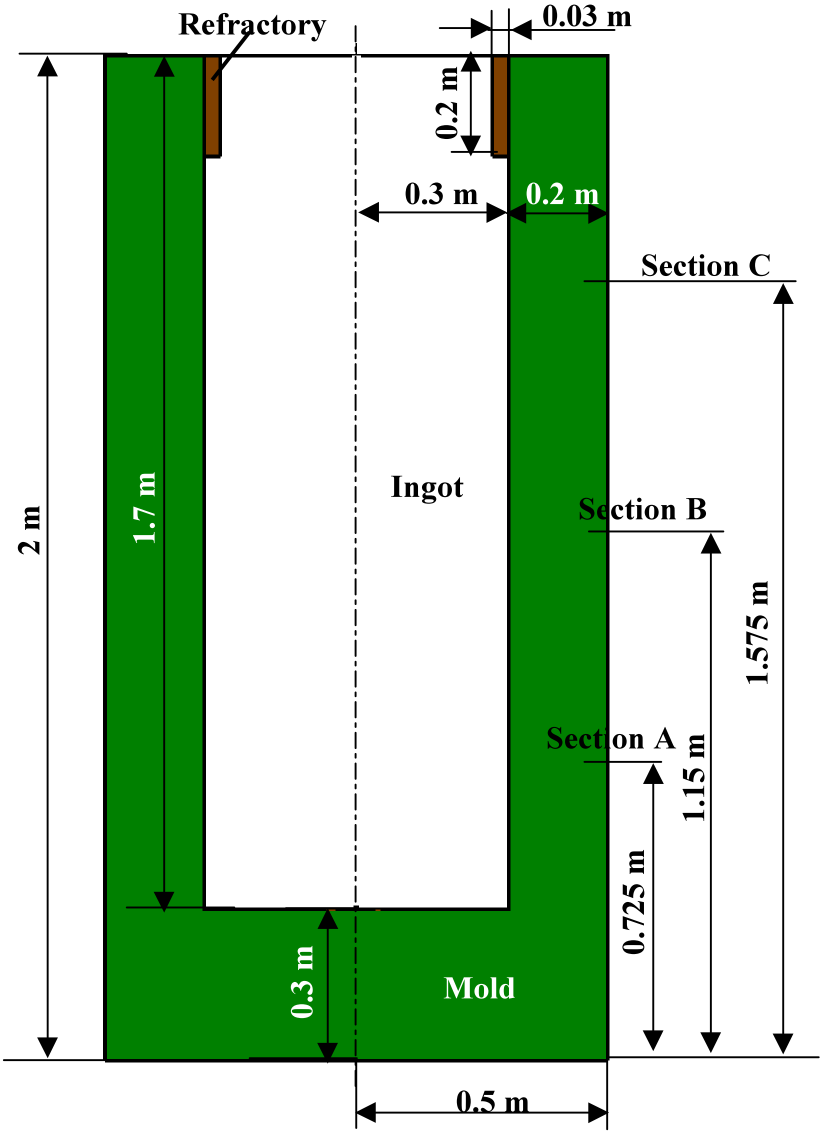

Figure 5-30 Schemetic of the geometry of ingot and mold (axisymmetric model)

We assume that the top surface of ingot is isolated. The heat transfer coefficients between ingot and mold, ingot and refractory are constant, being 500 W.m^{-2}.K^{-1}. The heat transfer coefficient of 100 W.m^{-2}.K^{-1} and the external temperature of 50 °C are used for heat exchange between mold and air, refractory and air. The physical properties of ingot, mold and refractory and calculation parameters are given in Table 5-5 and Table 5-6.

Table 5-5 Physical properties and calculation parameters of the steel ingot

Phase diagram data		
Nominal mass fraction, w_0	wt.pct	0.38
Melting temperature, T_f	°C	1538
Eutectic temperature, T_{eut}	°C	1338
Liquidus slope, m	$°C.wt.pct^{-1}$	-80
Partition coefficient, k		0.18
Eutectic mass fraction, w_{eut}	wt.pct	2.5
Thermal data		
Thermal conductivity, λ	$W.m^{-1}.K^{-1}$	35
Specific heat, c_p	$J.kg^{-1}.K^{-1}$	715
Latent heat, L	$J.kg^{-1}$	0.309×10^{6}
Other characteristics		
Reference volumetric mass, ρ_0	$Kg.m^{-3}$	7060
Reference temperature, T	°C	1522
Thermal expansion coefficient, β_T	K^{-1}	8.85×10^{-5}
Solutal expansion coefficient, β_w	$wt.pct^{-1}$	4.1643×10^{-2}
Dynamic viscosity, μ	Pa.s	0.42×10^{-2}
Secondary dendrite arm spacing, λ_2	m	1.0×10^{-4}
Calculation parameters		
Initial temperature	°C	1525
Time step	s	0.1
Heat transfer coefficient, h between ingot/mold, ingot/refractory	$W.m^{-2}.K^{-1}$	500
Gravity, $\mathbf{g}$	$m.s^{-2}$	9.81
Diffusion coefficient in liquid, D	$m^2.s^{-1}$	1×10^{-9}

Table 5-6 Physical properties and calculation parameters of the mold and refractory

Thermal data		Mold	Refractory
Thermal conductivity, λ	$W.m^{-1}.K^{-1}$	30	0.7
Specific heat, c_p	$J.kg^{-1}.K^{-1}$	540	1050
Volumetric mass, ρ_0	$Kg.m^{-3}$	7000	1300
Calculation parameters			
Initial temperature	°C	250	250
Heat transfer coefficient, h between mold/air, refractory/air	$W.m^{-2}.K^{-1}$	100	100
External temperature, T	°C	50	50

Initially, it is assumed that temperature fields in the ingot, mold and refractor are uniform, and that there is a homogeneous concentration field in the ingot, the values being given in Table 5-5 and Table 5-6. For fluid flow, zero initial velocity is applied, no-slip boundary conditions are imposed where the liquid is in contact with the mold and refractory. At the top, the vertical velocity component is imposed to be zero, no condition on the horizontal velocity component is prescribed. The time step varies from 0.05 *s* at the beginning of computation to 0.2 *s* at the end. The *full* *coupling* resolution reduced to one iteration has been done. The segregated concentration maps are shown in Figures from Figure 5-31 to Figure 5-33.

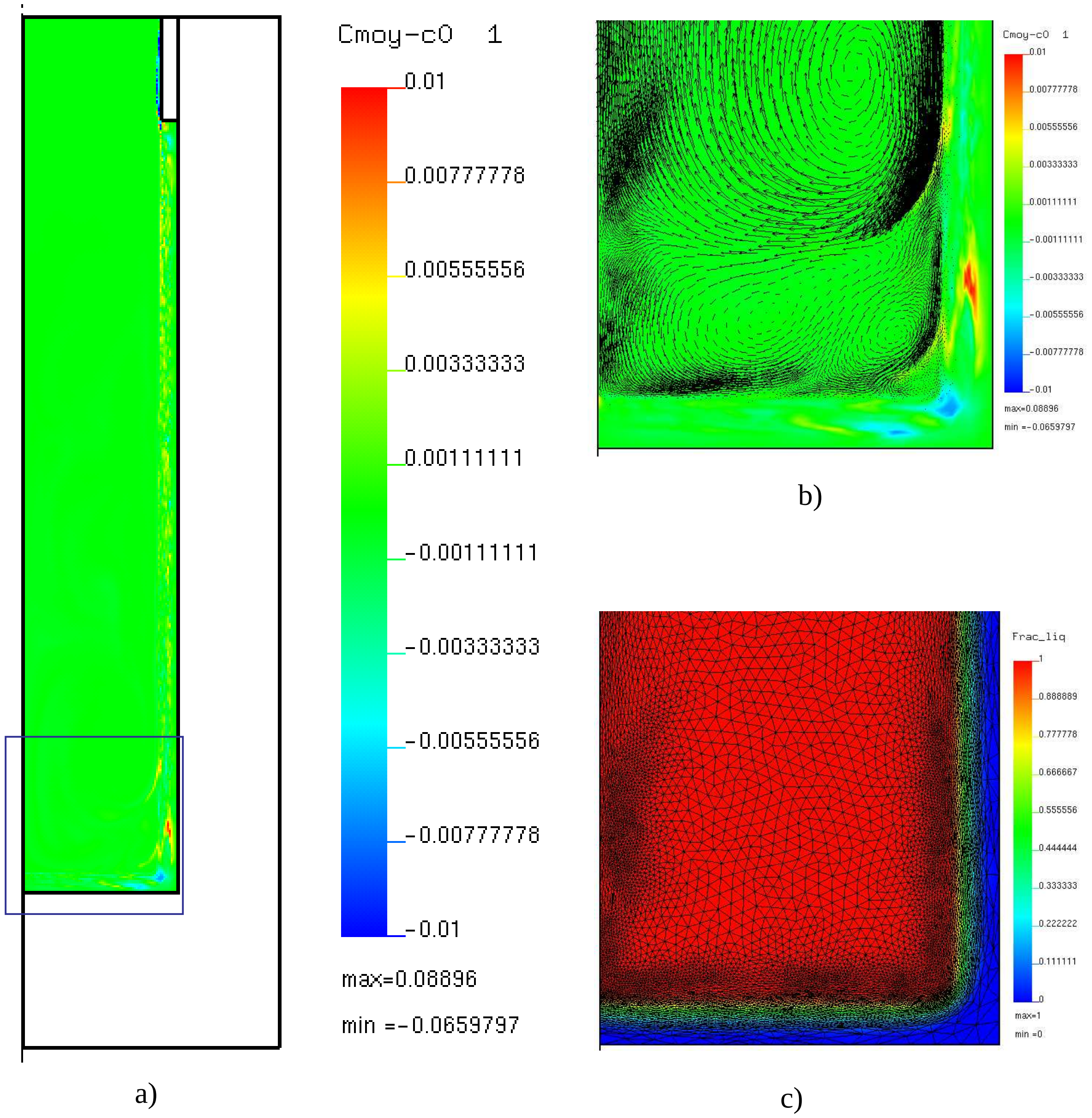

a)

b)

c)

Figure 5-31 The liquid fraction, velocity and segregated concentration $(w - w_0)$% fields at $t = 3$ *min*. A zoom in the bottom region is presented in b) and c). The velocity vectors are plotted in b), and the liquid fraction field and the mesh are shown in c).

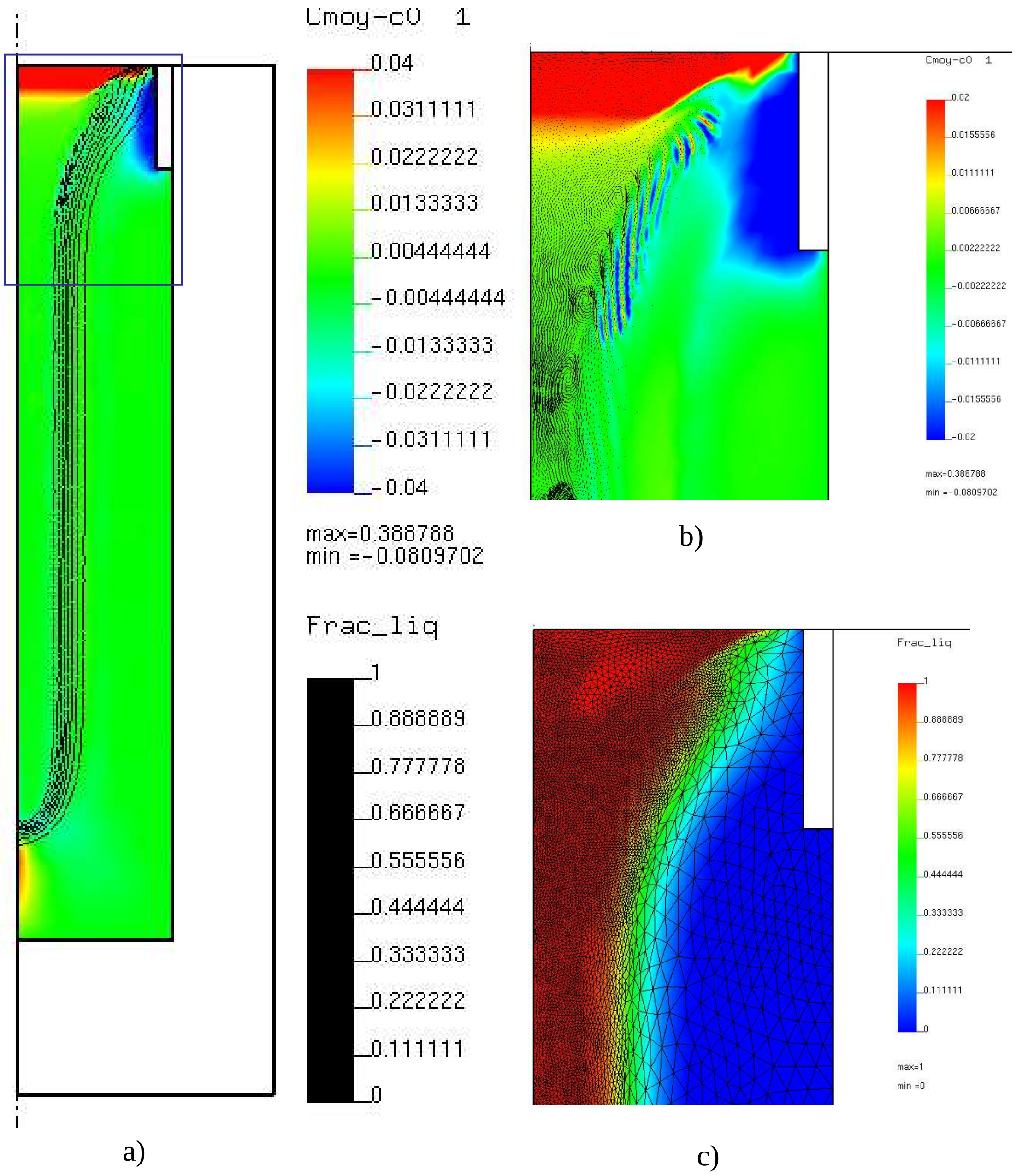

Figure 5-32 The liquid fraction, velocity and segregated concentration (w - w_0)% fields at t = 1 *hr*. Segregated concentration field (w - w0)% and the isolines of liquid fraction are shown in a), a zoom to the top region is presented in b) and c). The velocity vectors are plotted in b), showing the tendency to the “A-type” segregated channels, and the liquid fraction field is shown in c) with the mesh. It is interesting to observe a positive segregation zone at the bottom of the ingot and near the axis, this is caused by a freckle at the initial stage.

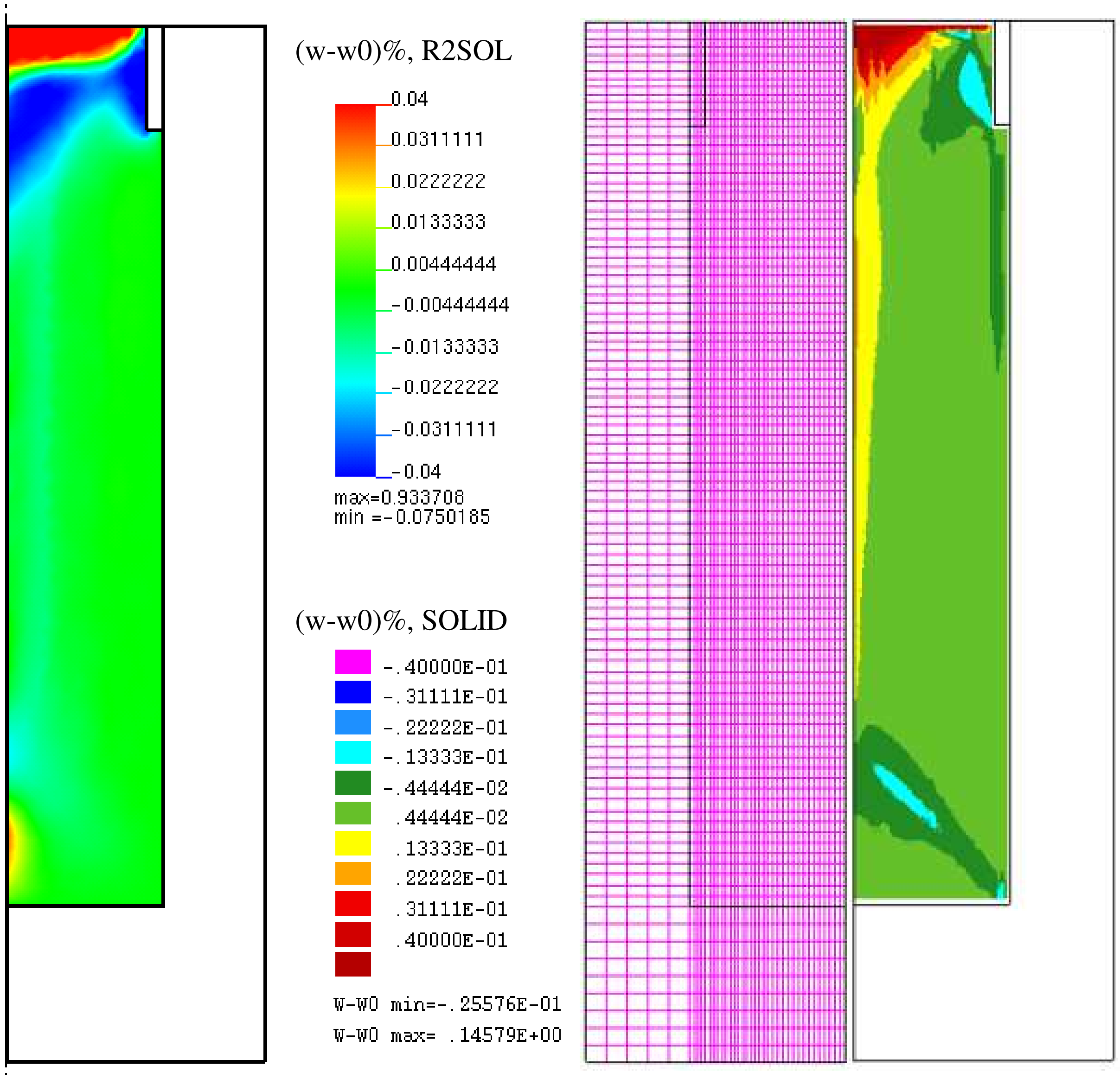

a) b)

Figure 5-33 The segregated concentration (w - w_0)% field after complete solidification. a) result of R2SOL at t = 2 hr 50 min, the maximum and minimum deviations to the nominal concentration are 0.934 and –0.075 (%) respectively. b) result of SOLID, the maximum and minimum values are 0.146 and –0.026 (%) respectively. The mesh used in SOLID consists of 3900 nodes, 39 nodes in the radial direction, and 100 nodes in the vertical direction.

We have re-computed the solidification of the test ingot with SOLID, using full coupling approach with only one iteration; however, the mesh is fixed and not adapted. The final segregated map after complete solidification is shown in Figure 5-33 b), compared with the result of R2SOL in Figure 5-33 a). At the top of ingot, oscillation of concentration appears in Figure 5-33 b), indicating the tendency to the formation of segregated channels.

A quantitative comparision of segregation intensity along the central axis is given by Figure 5- 34. It can be seen that the shapes of the two curves are similar, but the variation of concentration predicted by R2SOL is greater than that of SOLID. Profiles of $w - w_0$(%) in three horizontal sections, at ¼, ½ and ¾ heights of the ingot as shown in Figure 5-30, are presented in Figure 5- 35. It can be seen that the segregation intensity along horizontal sections is not as severe as along the axis. There are some differences between the predictions of R2SOL and SOLID. For the result of SOLID, near the center line slightly positive segregation is observed, near the surface of ingot negative segregation is observed, which is just opposite to the result of R2SOL.

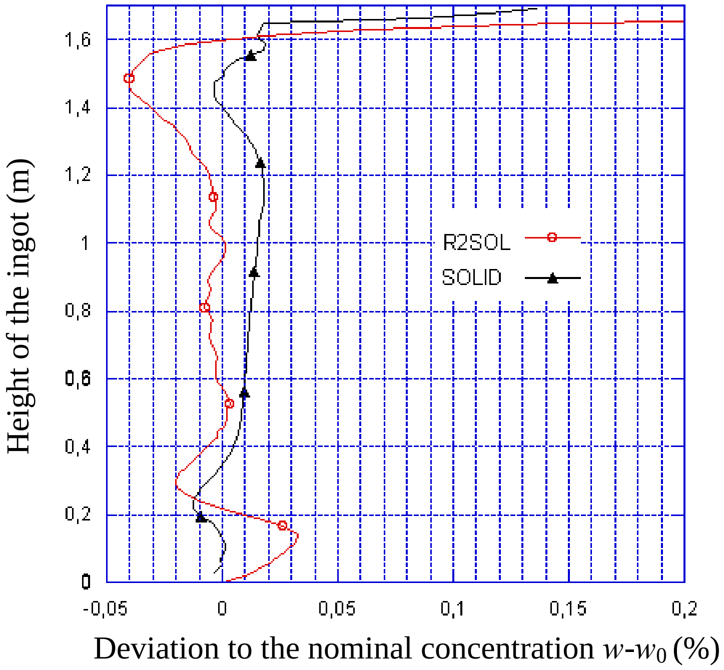

Figure 5- 34 Evolution of deviation to the nominal concentration w-w_0 (%) along the axis

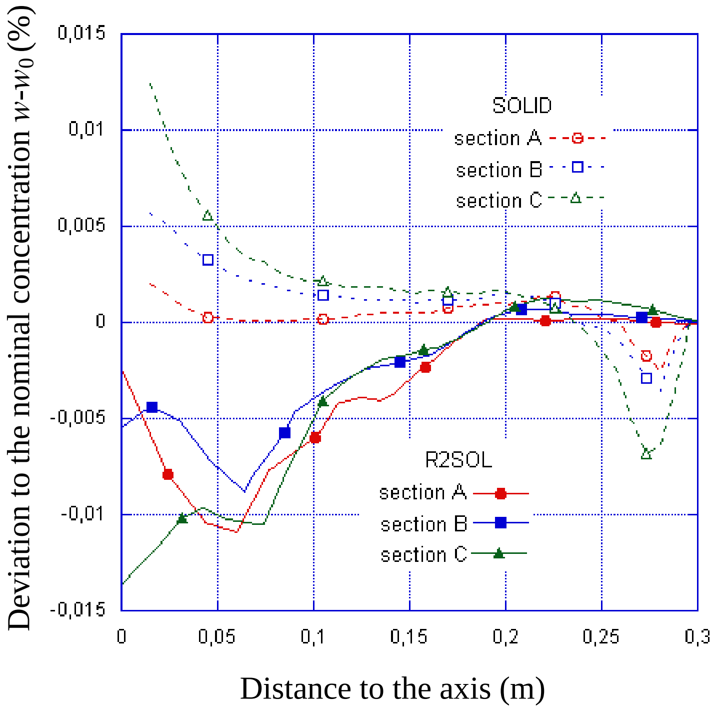

Figure 5- 35 Profiles of $w-w_0$ (%) after solidification

Remark

In the computation of R2SOL, the maximum number of nodes in the domain of ingot is 25816, and the maximum number of elements is 50890. The computation has taken about 3 weeks on a PC.

At the beginning of solidification, the temperature-induced convection dominates the fluid flow. The maximum downward velocity is observed at 33 s, being 83 mm/s, the reference Reynolds number for such a fluid flow is given by:

$$Re = \frac{|\mathbf{v}|\, L}{\mu/\rho} = \frac{0.083\times0.6}{0.42\times10^{-2}/7060} \cong 8.4\times10^{4}$$

and taking the superheat temperature as the temperature difference (17.4°C), the reference Rayleigh number is given by:

$$Ra = \frac{\rho^{2}|\mathrm{g}|\, \beta_{\mathrm{T}}\Delta T L^{3} c_{p}}{\mu\, \lambda} = \frac{7060^{2}\times9.8\times8.85\times10^{-5}\times17.4\times0.6^{3}\times715}{0.42\times10^{-2}\times35} \cong 7.9\times10^{8}$$

indicating that turbulent flow might appear. However the computation has been done with the laminar assumption.

Since the present macrosegregation model does not account for the solid movement and the growth of equiaxed grains, the negative segregation zone at the bottom of ingot cannot be predicted (cf. section 1.2.3). There are also some differences in the boundary and initial conditions between the test case and the industrial production. Despite these approximations, this case could consist in a valuable benchmark test to compare different simulation codes.

Regarding the difference between computations of R2SOL and SOLID, a further investigation is needed to check the influence of mesh size.

Chapter 6

Thermomechanical stress-strain modeling

Modélisation thermomécanique – Résumé en français

A la suite des travaux de Jaouen et Bellet dans le code THERCAST au Cemef, un modèle thermo-mécanique similaire a été implanté dans le logiciel R2SOL. Le matériau est alors considéré comme newtonien au-dessus du liquidus, comme viscoplastique entre le liquidus et une température critique T_C, et comme élasto-viscoplastique en-dessous de T_C. Le modèle est présenté à la section 6.1. Dans ce travail, nous avons notamment étendu la formulation, initialement en déformation plane, au cas axisymétrique (section 6.2.3). Le modèle est complété par une formulation eulérienne-lagrangienne (section 6.2.4). Les régions solides sont alors traitées en formulation lagrangienne, le maillage suivant les déformations de la matière, de façon à bien représenter la formation des lames d'air. Les régions liquides et pâteuses sont quant à elles traitées en approche eulérienne-lagrangienne, ce qui permet de modéliser la convection thermique et l'abaissement de la surface libre liquide, conséquence du retrait et ainsi de modéliser la formation des retassures primaires.

Quelques test de validation et tests comparatifs sont alors présentés (sections 6.3 et 6.4.1). La section 6.4.2 illustre le défaut majeur des analyses de formation de retassure qui affectent en totalité le changement de volume dû au retrait à la formation des retassures primaires (comme évoqué dans la revue bibliographique du chapitre 2). Pour ce faire on compare deux calculs pour une même simulation de refroidissement d'un lingot d'acier : un calcul réalisé en condition de contact unilatéral, c'est-à-dire en autorisant le formation de lames d'air entre pièce et moule et l'autre en condition de contact bilatéral, c'est-à-dire sans autoriser le décollement et donc la formation de lame d'air. La simulation met clairement en évidence la profondeur largement surestimée de la retassure primaire dans le second cas.

Chapter 6

Thermomechanical stress-strain modeling

In this chapter, we focus on the simulation of thermo-mechanics during the solidification of castings. A thermomechanical model has been implemented in the three dimensional finite element code THERCAST® (Jaouen [1998]), for stress strain calculations during the solidification of castings. The goal of the present work is to implement this model in the two-dimensional code R2SOL, and to predict the shrinkage pipe, air gap, strains and stresses during the solidification of ingots. For the purpose, we have implemented an elastic-viscoplastic constitutive behaviour, using axisymmetrical coordinates system. We assume that the mold is rigid (non-deformable), the thermal stresses and strains in the solid phase can be then modeled.

At the beginning of this chapter, we present the thermomechanical model in section 6.1. The resolution of mechanics is introduced in section 6.2, in which we focus on the implementation of thermo-elastic-viscoplastic (THEVP) model in R2SOL. Validation tests are shown in section 6.3, followed by an application to industrial ingots in section 6.4.

6.1 Thermal mechanical model

6.1.1 The mechanical equilibrium

Consider a part solidified in a rigid mold, *i.e.*, we consider only the mechanical problem of the solidifying part. We assume that the mold is initially full of the liquid alloy at rest and in contact with the mold. During the solidification of the part, the mechanical equilibrium is governed by the momentum equation:

$$\rho\boldsymbol{\gamma}=\nabla\cdot\boldsymbol{\sigma}+\rho\mathbf{g} \tag{6-1}$$

where $\mathbf{g}$ is the gravity; $\boldsymbol{\gamma}$ is the acceleration vector. $\boldsymbol{\sigma}$ is the Cauchy stress tensor, the stress tensor is generally decomposed into the spherical, $p\mathbf{I}$, and deviatoric, $\mathbf{s}$, components as follows:

$$\boldsymbol{\sigma}=-p\mathbf{I}+\mathbf{s} \tag{6-2}$$

Let Ω be the domain occupied by the part, its boundary can be specified by the two regions $\partial\Omega_m$ and $\partial\Omega_p$. The region $\partial\Omega_m$ is the part of boundary facing the mold, and $\partial\Omega_p$ is the free surface, which is not facing the mold. The mechanical boundary conditions are expressed as follows:

- Unilateral contact condition on the boundary $\partial\Omega_m$, that is:

$$\begin{cases}\boldsymbol{\sigma}\,\mathbf{n}\cdot\mathbf{n}\leq 0\\ \delta\geq 0\\ (\boldsymbol{\sigma}\,\mathbf{n}\cdot\mathbf{n})\cdot\delta=0\end{cases} \tag{6-3}$$

where $\mathbf{n}$ is the local outward unit normal to the part; δ is the local airgap width, being positive when the airgap exists effectively. The contact can be treated by a penalty method (Rappaz *et al.* [2002]), we then have:

$$\mathbf{T}=\boldsymbol{\sigma}\,\mathbf{n}=-\chi_p\left\langle(\mathbf{v}-\mathbf{v}_{mold})\cdot\mathbf{n}\right\rangle\mathbf{n} \tag{6-4}$$

In the condition (6-4), χ_p is the penalty coefficient; the bracket, $\langle\ \rangle$, denotes the following notation:

$$<x>=x \text{ if } x\geq 0 \qquad \text{and} <x>=0 \text{ if } x<0 \tag{6-5}$$

- Bilateral contact condition

In contrast to the unilateral contact, the so-called "bilateral contact condition" can be alternatively applied to the boundary $\partial\Omega_m$, which is the case when $\delta=0$, being always in contact with the mold. The penalty formulation can be written as:

$$\mathbf{T}=\boldsymbol{\sigma}\,\mathbf{n}=-\chi_p((\mathbf{v}-\mathbf{v}_{mold})\cdot\mathbf{n})\mathbf{n} \tag{6-6}$$

The tangential friction effects between part and mold are neglected.

- Free surface boundary $\partial\Omega_p$

The atmospheric pressure P_{atm} (or a prescribed pressure) is applied, that is:

$$\mathbf{T}=\boldsymbol{\sigma}\,\mathbf{n}=-P_{atm}\mathbf{n} \tag{6-7}$$

6.1.2 Constitutive equations

In a foundry process, a part is usually cooled over a large range of temperature, and the metallic material undergoes liquid-solid phase change. Thereby, the material behavior is quite changing and temperature-dependant. Following Jaouen [1998]), a thermo-viscoplastic (THVP) model is used to describe the behavior of the liquid and mushy states, and a small strains thermo-elastic-viscoplastic (THEVP) model is used for the solid (seeing Figure 1-5).

The rate of deformation of the metal $\dot{\boldsymbol{\varepsilon}}$ is decomposed into a viscoplastic part $\dot{\boldsymbol{\varepsilon}}^{vp}$, an elastic part $\dot{\boldsymbol{\varepsilon}}^{el}$ and a thermal part $\dot{\boldsymbol{\varepsilon}}^{th}$ as follows:

$$\dot{\boldsymbol{\varepsilon}}=\dot{\boldsymbol{\varepsilon}}^{vp}+\dot{\boldsymbol{\varepsilon}}^{el}+\dot{\boldsymbol{\varepsilon}}^{th} \tag{6-8}$$

One can decompose the deformation rate tensor into spherical and deviatoric parts. Since $\dot{\boldsymbol{\varepsilon}}^{th}$ and $\dot{\boldsymbol{\varepsilon}}^{vp}$ are purely spherical and purely deviatoric tensors respectively, one writes:

$$\begin{cases}\dot{\mathbf{e}}=\dot{\mathbf{e}}^{vp}+\dot{\mathbf{e}}^{el}\\ Tr(\dot{\boldsymbol{\varepsilon}})=Tr(\dot{\boldsymbol{\varepsilon}}^{el})+Tr(\dot{\boldsymbol{\varepsilon}}^{th})\end{cases} \tag{6-9}$$

where $\dot{\mathbf{e}}$ denotes the deviatoric deformation rate tensor.

- **Viscoplastic deformation**

We assume that the viscoplastic behavior of metal obeys the law of Norton-Hoff, which writes:

$$\dot{\boldsymbol{\varepsilon}}^{vp} = \dot{\lambda}\mathbf{s} \qquad \text{with} \quad \dot{\lambda} = \frac{\sqrt{3}}{2\sigma_{eq}} \left\langle \frac{\sigma_{eq} - \sigma_s}{K(T)\sqrt{3}} \right\rangle^{\frac{1}{m(T)}} \tag{6-10}$$

where, K(*T*) is the viscoplastic consistency of the material, depending on the temperature *T*. *m*(*T*) the strain rate sensitivity coefficient. The brackets present the positive convention defined by equation (6-5). σ_s is the stress threshold, under which the behavior of the metal is elastic. The equivalent stress of Von Mises σ_{eq} is defined by:

$$\sigma_{eq} = \sqrt{\frac{3}{2}\mathbf{s}:\mathbf{s}} \tag{6-11}$$

The equivalent one-dimensional relation to (6-10) can then be obtained:

$$\sigma_{eq} = \sigma_s + K(T)\sqrt{3}^{\,m(T)+1}\dot{\bar{\varepsilon}}^{\,m(T)} \tag{6-12}$$

where $\dot{\bar{\varepsilon}}$ is the equivalent viscoplastic strain rate, and is given by:

$$\dot{\bar{\varepsilon}} = \sqrt{\frac{2}{3}\dot{\boldsymbol{\varepsilon}}^{vp}:\dot{\boldsymbol{\varepsilon}}^{vp}} \tag{6-13}$$

In R2SOL, the following model for strain hardening is available Costes [2004]:

$$\dot{\boldsymbol{\varepsilon}}^{vp} = \frac{\sqrt{3}}{2\sigma_{eq}} \left\langle \frac{\sigma_{eq} - \sigma_s}{K(T)\,\bar{\varepsilon}^n\sqrt{3}} \right\rangle^{\frac{1}{m(T)}} \mathbf{s} \tag{6-14}$$

- **Elastic deformation**

The elastic behavior can be described by Hooke's law:

$$\dot{\boldsymbol{\sigma}} = \mathbf{D}^{el}\dot{\boldsymbol{\varepsilon}}^{el} = \frac{E}{(1+\nu)}\dot{\boldsymbol{\varepsilon}}^{el} + \frac{E\nu}{(1-2\nu)(1+\nu)}Tr(\dot{\boldsymbol{\varepsilon}}^{el})\mathbf{I} \tag{6-15}$$

where $\mathbf{D}^{el}$ is the elasticity tensor of 4th order, depending on the Young modulus, *E*, and the Poisson coefficient, ν. The Hooke's law can also be written in the following form:

$$\dot{\boldsymbol{\varepsilon}}^{el} = (\mathbf{D}^{el})^{-1}\dot{\boldsymbol{\sigma}} \tag{6-16}$$

If the Young modulus and the Poisson coefficient vary as temperature changes, taking account for the variation in physical properties, equation (6-16) then becomes:

$$\dot{\boldsymbol{\varepsilon}}^{el} = (\mathbf{D}^{el})^{-1}\dot{\boldsymbol{\sigma}} + \dot{T}\frac{\partial(\mathbf{D}^{el})^{-1}}{\partial T}\boldsymbol{\sigma} \tag{6-17}$$

Equation (6-17) accounts for the influence of coupling effect in the thermal mechanical problems. Consequently, the deviatoric strain rate $\dot{\mathbf{e}}^{el}$ and its associated spherical part $Tr(\dot{\boldsymbol{\varepsilon}}^{el})$ are expressed as follows:

$$\begin{cases} \dot{\mathbf{e}}^{el} = \dfrac{\dot{\mathbf{s}}}{2\mu} - \dot{T}\dfrac{1}{2\mu^2}\dfrac{\partial\mu}{\partial T}\mathbf{s} & \text{with } \mu = \dfrac{E}{2(1+\nu)} \\ Tr(\dot{\boldsymbol{\varepsilon}}^{el}) = -\dfrac{\dot{p}}{\chi} + \dot{T}\dfrac{1}{\chi^2}\dfrac{\partial\chi}{\partial T}p & \text{with } \chi = \dfrac{E}{3(1-2\nu)} \end{cases} \tag{6-18}$$

where μ is Lamé coefficient, also called shear modulus. χ is the bulk modulus.

From equation (6-18), one obtains the spherical and deviatoric components of the stress rate:

$$\begin{cases} \dot{\mathbf{s}} = 2\mu\dot{\mathbf{e}}^{el} + \dot{T}\dfrac{1}{\mu}\dfrac{\partial\mu}{\partial T}\mathbf{s} \\ \dot{p} = -\chi Tr(\dot{\boldsymbol{\varepsilon}}^{el}) + \dot{T}\dfrac{1}{\chi}\dfrac{\partial\chi}{\partial T}p \end{cases} \tag{6-19}$$

- **Thermal deformation**

The thermal deformation is decomposed into two parts, the linear thermal expansion and solidification shrinkage.

$$\dot{\boldsymbol{\varepsilon}}^{th} = \alpha\dot{T}\mathbf{I} + \frac{1}{3}\dot{g}_s\Delta\varepsilon^{tr}\mathbf{I} \tag{6-20}$$

where, $\dot{T}$ is the temperature rate, α the thermal linear expansion coefficient. $\dot{g}_s$ is the rate of massic fraction of solid, and $\Delta\varepsilon^{tr}$ the relative volume change from liquid to solid.

Remark

As it has been presented in general introduction, segregation is neglected in the computation of deformation. Therefore, the liquidus and solidus temperatures are fixed. In order to compute the solidification shrinkage, we define two densities, ρ_L and ρ_S, corresponding to the values at liquidus and solidus temperature. During the solidification, the density of the liquid and solid mixture is given by:

$$\rho = g\ \rho\ + g\ \rho\ = g\ (\rho\ - \rho\ ) + \rho \tag{6-21}$$

where g and g_l are the mass fraction of solid and mass fraction of liquid respectively. Then the deformation due to solidification shrinkage can be defined by:

$$\dot{\boldsymbol{\varepsilon}}^{th} = -\frac{1}{3\rho}\frac{d\rho}{dt}\mathbf{I} = -\frac{1}{3\rho}\frac{d\rho}{dg_s}\dot{g}_s\mathbf{I} = -\frac{1}{3}\frac{\rho_s - \rho_l}{\rho}\dot{g}_s\mathbf{I} \approx -\frac{1}{3}\frac{\rho_S - \rho_L}{\rho_L}\dot{g}_s\mathbf{I} = \frac{1}{3}\dot{g}_s\Delta\varepsilon^{tr}\mathbf{I} \tag{6-22}$$

The resolution of constitutive equations in THERCAST® has been presented by Jaouen [1998] and Aliaga [2000]. In order to introduce our adaptations to the two dimensional problems, as an example, in the following text we present the resolution of THEVP system.

6.1.3 Local resolution of constitutive equations

The method that deals with the small strains THEVP constitutive equations in THERCAST® is summarized as follows.

Substituting equations (6-9) and (6-10) into equation (6-18), we obtain:

$$\begin{cases} \dot{\mathbf{s}}=2\mu(\dot{\mathbf{e}}-\dot{\lambda}(\mathbf{s})\mathbf{s})+\dot{T}\dfrac{1}{\mu}\dfrac{\partial\mu}{\partial T}\mathbf{s} \\ \dot{p}=-\chi(Tr(\dot{\boldsymbol{\varepsilon}})-3\alpha\dot{T}-\dot{g}_s\Delta\varepsilon^{tr})+\dot{T}\dfrac{1}{\chi}\dfrac{\partial\chi}{\partial T}p \end{cases} \tag{6-23}$$

A general (θ-type) time integration scheme is applied to discretize equation (6-23), leading to:

$$\begin{cases} \dfrac{\mathbf{s}_{n+1}-\mathbf{s}_n}{\Delta t}=\theta 2\mu_{n+1}(\dot{\mathbf{e}}_{n+1}-\dot{\lambda}_{n+1}\mathbf{s}_{n+1})+(1-\theta)2\mu_n(\dot{\mathbf{e}}_n-\dot{\lambda}_n\mathbf{s}_n)+\dfrac{\mu_{n+1}-\mu_n}{\mu_n\Delta t}\mathbf{s}_n \\ \dfrac{p_{n+1}-p_n}{\Delta t}=-\theta\chi_{n+1}(Tr(\dot{\boldsymbol{\varepsilon}}_{n+1})-3\alpha\dot{T}_{n+1}-\dot{g}_{s\,n+1}\Delta\varepsilon^{tr})-(1-\theta)\chi_n(Tr(\dot{\boldsymbol{\varepsilon}}_n)-3\alpha\dot{T}_n-\dot{g}_{s\,n}\Delta\varepsilon^{tr}) \\ \qquad +\dfrac{\chi_{n+1}-\chi_n}{\chi_n\Delta t}p_n \end{cases} \tag{6-24}$$

where the subscription n denotes the time increment, and Δt is the time step. $\mu_{n+1}=\mu(T_{n+1})$, $\chi_{n+1}=\chi(T_{n+1})$. The parameter θ takes its value in the range of 0 to 1, and $\theta=1$ is the implicit scheme. Following the previous work in THERCAST®, the implicit scheme is used in R2SOL.

Within each time step $[t,\ t+\Delta t]$, knowing the initial state of stress and deformation at time t_n, $\mathbf{s}_n$, p_n, $\dot{\mathbf{e}}_n$, and $\dot{\lambda}_n$, we assume that the deformation rate is constant in each element, and proposed that $\dot{\mathbf{e}}_{n+1}(\mathbf{v}_{n+1})$ is known, then, the resolution of equation (6-24) can be done.

The second equation in (6-24) is linear, once the value of $\mathbf{v}_{n+1}$ is known, p_{n+1} can be computed directly. Whereas, the first equation in (6-24) is nonlinear, where $\dot{\lambda}_{n+1}$ and $\mathbf{s}_{n+1}$ are the two unknowns. In order to determine $\dot{\lambda}_{n+1}$, the Von Mises criterion (6-11) is considered, we write:

$$\mathbf{s}_{n+1}:\mathbf{s}_{n+1}-\frac{2}{3}\sigma_{eq}^2(\bar{\varepsilon}_{n+1},\Delta\bar{\varepsilon}_{n+1})=0 \quad \text{with} \quad \Delta\bar{\varepsilon}_{n+1}=\bar{\varepsilon}_n+\Delta t\,\dot{\bar{\varepsilon}}_{n+1} \tag{6-25}$$

Applying $\theta=1$ to the first equation in (6-24), and after some computations, then we have:

$$\mathbf{s}_{n+1}=\frac{2\mu_{n+1}\Delta t\dot{\mathbf{e}}_{n+1}+G_{n+1}\mathbf{s}_n}{1+2\mu_{n+1}\Delta t\dot{\lambda}_{n+1}} \tag{6-26}$$

where $G_{n+1}=\dfrac{\mu_{n+1}}{\mu_n}$.

Inserting equation (6-26) into equation (6-25), one can obtain the following nonlinear scalar equation, which has a single unknown $\dot{\lambda}_{n+1}$:

$$\begin{aligned} F(\dot{\lambda}_{n+1})=&\,2\mu_{n+1}\Delta t\sigma_{eq}(\bar{\varepsilon}_{n+1})\dot{\lambda}_{n+1}+\sigma_{eq}(\bar{\varepsilon}_{n+1}) \\ &-\sqrt{\frac{3}{2}(2\mu_{n+1}\Delta t\dot{\mathbf{e}}_{n+1}+G_{n+1}\mathbf{s}_n):(2\mu_{n+1}\Delta t\dot{\mathbf{e}}_{n+1}+G_{n+1}\mathbf{s}_n)}\ =\ 0 \end{aligned} \tag{6-27}$$

We introduce a scalar B_0:

$$B_0=\sqrt{\frac{3}{2}(2\mu_{n+1}\Delta t\dot{\mathbf{e}}_{n+1}+G_{n+1}\mathbf{s}_n):(2\mu_{n+1}\Delta t\dot{\mathbf{e}}_{n+1}+G_{n+1}\mathbf{s}_n)} \qquad (6\text{-}28)$$

and considering the following relation:

$$\dot{\bar{\varepsilon}}=\frac{2}{3}\dot{\lambda}\sigma_{eq} \qquad (6\text{-}29)$$

then, equation (6-27) can be written as:

$$3\mu_{n+1}\Delta t\dot{\bar{\varepsilon}}_{n+1}+\sigma_{eq}(\bar{\varepsilon}_{n+1})-B_0=0 \qquad (6\text{-}30)$$

Remark

The scalar B_0 defined in equation (6-28) is the Von Mises equivalent stress associated with the pure elastic estimation. If $\dot{\lambda}_{n+1}=0$, *i.e.*, $\dot{\mathbf{e}}^{vp}=0$ and $\dot{\mathbf{e}}^{el}=\dot{\mathbf{e}}$. Then, equation (6-26) reduces to the pure elastic estimation of $\mathbf{s}_{n+1}$.

In practice, if $\sigma_{eq}(\bar{\varepsilon}_n)>B_0$, the deformation is purely elastic, the estimated value is the resolution. If $\sigma_{eq}(\bar{\varepsilon}_n)<B_0$, the deformation is elastic viscoplastic. It has been demonstrated (Simo and Taylor [1985], Bellet *et al.* [1996]) that the nonlinear equation (6-30) has a unique resolution for all the cases, $\dot{\lambda}>0$. The detail for the resolution of $\dot{\bar{\varepsilon}}_{n+1}$ can be found in the thesis of Aliaga [2000]. When $\dot{\bar{\varepsilon}}_{n+1}$ is obtained, $\dot{\lambda}_{n+1}$ is then deduced from equation (6-29). Finally, $\mathbf{s}_{n+1}$ can be found using equation (6-26).

The expression of the tangent modulus $\partial\mathbf{s}/\partial\dot{\boldsymbol{\varepsilon}}$ which is necessary to express the tangent matrix in the Newton-Raphson resolution (see next section) can be found in Appendix C.

6.2 Resolution of mechanics

6.2.1 Weak form and time discretization

A velocity/pressure P1+/P1 formulation is used to solve the mechanical problem.

We start from the equilibrium equation (6-1):

$$\nabla\cdot\mathbf{s}-\nabla p+\rho\mathbf{g}-\rho\boldsymbol{\gamma}=0 \qquad (6\text{-}31)$$

where the deviatoric stress $\mathbf{s}$ can be determined by either the elastic-viscoplastic constitutive equation, $\mathbf{s}=\mathbf{s}^{evp}(\dot{\lambda}(\dot{\mathbf{e}}(\mathbf{v})),\dot{\mathbf{e}}(\mathbf{v}))$, or the viscoplastic equation $\mathbf{s}=\mathbf{s}^{vp}(\mathrm{dev}(\dot{\boldsymbol{\varepsilon}}(\mathbf{v})))$.

The constraint of incompressibility of the viscoplastic deformation can be expressed by:

$$\begin{aligned} Tr(\dot{\boldsymbol{\varepsilon}}^{vp}) &= Tr(\dot{\boldsymbol{\varepsilon}})-Tr(\dot{\boldsymbol{\varepsilon}}^{el})-Tr(\dot{\boldsymbol{\varepsilon}}^{th}) \\ &= \nabla\cdot\mathbf{v}+\frac{3(1-2\nu)}{E}\dot{p}-3\alpha\dot{T}-\dot{g}_s\Delta\varepsilon^{tr}=0 \end{aligned} \qquad (6\text{-}32)$$

The weak form is applied to solve equations (6-31) and (6-32), then we have:

$$\begin{cases} \forall \mathbf{v}^* & \int\limits_{\Omega} \begin{Bmatrix} \mathbf{s}^{evp} \\ \mathbf{s}^{vp} \end{Bmatrix} : \dot{\boldsymbol{\varepsilon}}^* d\Omega - \int\limits_{\Omega} p \nabla \cdot \mathbf{v}^* d\Omega - \int\limits_{\partial\Omega} \mathbf{T} \cdot \mathbf{v}^* d\Gamma - \int\limits_{\Omega} \rho \mathbf{g} \cdot \mathbf{v}^* d\Omega + \int\limits_{\Omega} \rho_0 \boldsymbol{\gamma} \cdot \mathbf{v}^* d\Omega = 0 \\ \forall p^* & -\int\limits_{\Omega} p^* (\nabla \cdot \mathbf{v} + \begin{Bmatrix} 3\dot{p}(1-2\nu)/E \\ 0 \end{Bmatrix} - 3\alpha \dot{T} - \dot{g}_s \Delta\varepsilon^{tr}) d\Omega = 0 \end{cases} \tag{6-33}$$

The first equation is the weak form of the momentum equation. The second expresses the incompressibility of the plastic deformation. The brackets in equation (6-33) allow the choice between THEVP and THVP according to the temperature T_C as shown in Figure 1-5.

In equation (6-33), $\dot{T}$ and $\dot{g}_s$ are provided by the thermal resolution. The time derivatives of pressure and velocity are approximated by implicit Euler backward scheme:

$$\dot{p}^t = \frac{1}{\Delta t}(p^t - p^{t-\Delta t}) \tag{6-34}$$

$$\boldsymbol{\gamma}^t = \frac{1}{\Delta t}(\mathbf{v}^t - \mathbf{v}^{t-\Delta t}) \tag{6-35}$$

where $p^{t-\Delta t}$ and $\mathbf{v}^{t-\Delta t}$ denote the values associated with the particle at time $t-\Delta t$, which can be computed by an upwind transport approach that will be presented in section 6.2.4.

Given the configuration Ω occupied by the part at time $t-\Delta t$, the equations to be solved for $(\mathbf{v}, p)^t$, velocity and pressure fields at time t, can be expressed in the following way (for the sake of clarity, we take the case of THEVP behaviour, in the sequel).

$$\begin{cases} \forall \mathbf{v}^* & \int\limits_{\Omega} \mathbf{s}^{evp}(\mathbf{v}^t) : \dot{\boldsymbol{\varepsilon}}^* d\Omega - \int\limits_{\Omega} p^t \nabla \cdot \mathbf{v}^* d\Omega - \int\limits_{\partial\Omega} \mathbf{T}^t \cdot \mathbf{v}^* d\Gamma - \int\limits_{\Omega} \rho(T^t) \mathbf{g} \cdot \mathbf{v}^* d\Omega + \int\limits_{\Omega} \rho_0 \frac{\mathbf{v}^t - \mathbf{v}^{t-\Delta t}}{\Delta t} \cdot \mathbf{v}^* d\Omega = 0 \\ \forall p^* & -\int\limits_{\Omega} p^* (\nabla \cdot \mathbf{v}^t + \frac{3(1-2\nu)}{E} \frac{p^t - p^{t-\Delta t}}{\Delta t} - 3\alpha \dot{T} - \dot{g}_s \Delta\varepsilon^{tr}) d\Omega = 0 \end{cases} \tag{6-36}$$

6.2.2 P1+/P1 formulation

We have presented the mini-element P1+/P1 formulation for computing the Navier-Stokes flow in section 3.6.1. Similarly, the weak form of equation (6-36) can be solved using the following mini-element P1+/P1 formulation:

$$\begin{cases} \forall \mathbf{v}^* & \int\limits_{\Omega} \mathbf{s}^{evp}(\mathbf{w}) : \dot{\boldsymbol{\varepsilon}}(\mathbf{v}^*) d\Omega - \int\limits_{\Omega} p \nabla \cdot \mathbf{v}^* d\Omega - \int\limits_{\partial\Omega} \mathbf{T} \cdot \mathbf{v}^* d\Gamma - \int\limits_{\Omega} \rho \mathbf{g} \cdot \mathbf{v}^* d\Omega + \int\limits_{\Omega} \rho_0 \boldsymbol{\gamma}(\mathbf{w}) \cdot \mathbf{v}^* d\Omega = 0 \\ \forall \mathbf{b}^* & \int\limits_{\Omega} \mathbf{s}^{evp}(\mathbf{w}) : \dot{\boldsymbol{\varepsilon}}(\mathbf{b}^*) d\Omega - \int\limits_{\Omega} p \nabla \cdot \mathbf{b}^* d\Omega - \int\limits_{\Omega} \rho \mathbf{g} \cdot \mathbf{b}^* d\Omega + \int\limits_{\Omega} \rho_0 \boldsymbol{\gamma}(\mathbf{w}) \cdot \mathbf{b}^* d\Omega = 0 \\ \forall p^* & -\int\limits_{\Omega} p^* (\nabla \cdot \mathbf{w} + \frac{3(1-2\nu)}{E} \dot{p} - 3\alpha \dot{T} - \dot{g}_s \Delta\varepsilon^{tr}) d\Omega = 0 \end{cases} \tag{6-37}$$

where the velocity field $\mathbf{w}$ is linear continuous, including additional degrees of freedom at the center of element, $\mathbf{w} = \mathbf{v} + \mathbf{b} = \sum_{n=1}^{3} N_n \mathbf{V}^n + N^b \mathbf{B}$; the pressure is linear continuous, given by a linear interpolation function, $p = \sum_{n=1}^{3} N_n P^n$.

Following the previous works of CEMEF (Menaï [1995], Jaouen [1998], Aliaga [2000]), the deviatoric stress tensor, $\mathbf{s}(\dot{\lambda}(\dot{\mathbf{e}}(\mathbf{w})),\dot{\mathbf{e}}(\mathbf{w}))$, can be decomposed into a non-linear part and a complementary linear part, that is:

$$\mathbf{s}(\dot{\lambda}(\dot{\mathbf{e}}(\mathbf{w})),\dot{\mathbf{e}}(\mathbf{w}))=\underbrace{\mathbf{s}^{v}(\dot{\lambda}(\dot{\mathbf{e}}(\mathbf{v})),\dot{\mathbf{e}}(\mathbf{v}))}_{non-linear\ part}+\underbrace{\mathbf{s}^{b}(\dot{\lambda}(\dot{\mathbf{e}}(\mathbf{v}),\dot{\mathbf{e}}(\mathbf{b}))}_{linear\ part} \tag{6-38}$$

The deviatoric stress tensor, $\mathbf{s}^{v}(\mathbf{v})$ and $\mathbf{s}^{b}(\mathbf{b})$ can be computed using equation (6-26), leading to:

$$\mathbf{s}^{v}_{n+1}(\dot{\lambda}(\dot{\mathbf{e}}(\mathbf{v}_{n+1})),\dot{\mathbf{e}}(\mathbf{v}_{n+1}))=\frac{2\mu_{n+1}\Delta t\dot{\mathbf{e}}(\mathbf{v}_{n+1})+G_{n+1}\mathbf{s}^{v}_{n}}{1+2\mu_{n+1}\Delta t\dot{\lambda}(\mathbf{v}_{n+1})} \tag{6-39}$$

$$\mathbf{s}^{b}_{n+1}(\dot{\lambda}(\dot{\mathbf{e}}(\mathbf{v}_{n+1})),\dot{\mathbf{e}}(\mathbf{b}_{n+1}))=\frac{2\mu_{n+1}\Delta t\dot{\mathbf{e}}(\mathbf{b}_{n+1})}{1+2\mu_{n+1}\Delta t\dot{\lambda}(\mathbf{v}_{n+1})} \tag{6-40}$$

where $\mathbf{s}^{b}$ in equation (6-40) can be considered as a correction of the deviatoric stress tensor.

Taking the advantage of bubble properties (seeing section 3.6.1), we can simplify equation (6-37), leading to:

$$\begin{cases}\forall\mathbf{v}^{*}\ \int_{\Omega}\mathbf{s}^{v}(\mathbf{v}):\dot{\boldsymbol{\varepsilon}}(\mathbf{v}^{*})d\Omega-\int_{\Omega}p\nabla\cdot\mathbf{v}^{*}d\Omega-\int_{\partial\Omega}\mathbf{T}\cdot\mathbf{v}^{*}d\Gamma-\int_{\Omega}\rho\mathbf{g}\cdot\mathbf{v}^{*}d\Omega+\int_{\Omega}\rho_{0}\boldsymbol{\gamma}(\mathbf{v}+\cancel{\mathbf{b}})\cdot\mathbf{v}^{*}d\Omega=0\\ \forall\mathbf{b}^{*}\ \int_{\Omega}\mathbf{s}^{b}(\mathbf{b}):\dot{\boldsymbol{\varepsilon}}(\mathbf{b}^{*})d\Omega-\int_{\Omega}p\nabla\cdot\mathbf{b}^{*}d\Omega-\int_{\Omega}\rho\mathbf{g}\cdot\mathbf{b}^{*}d\Omega+\cancel{\int_{\Omega}\rho_{0}\boldsymbol{\gamma}(\mathbf{v}+\mathbf{b})}\cdot\mathbf{b}^{*}d\Omega=0\\ \forall p^{*}\ -\int_{\Omega}p^{*}(\nabla\cdot(\mathbf{v}+\mathbf{b})+\frac{3(1-2\nu)}{E}\dot{p}-3\alpha\dot{T}-\dot{g}_{s}\Delta\varepsilon^{tr})d\Omega=0\end{cases} \tag{6-41}$$

Comparing with equation (3-129), the terms $2\mu\dot{\boldsymbol{\varepsilon}}(\mathbf{v}):\dot{\boldsymbol{\varepsilon}}(\mathbf{v}^{*})$ and $2\mu\dot{\boldsymbol{\varepsilon}}(\mathbf{b}):\dot{\boldsymbol{\varepsilon}}(\mathbf{b}^{*})$ have been replaced respectively by $\mathbf{s}^{v}(\mathbf{v}):\dot{\boldsymbol{\varepsilon}}(\mathbf{v}^{*})$ and $\mathbf{s}^{b}(\mathbf{b}):\dot{\boldsymbol{\varepsilon}}(\mathbf{b}^{*})$, which present the non-linear rheology behaviour. Since equation (6-41) is non-linear, the Newton-Raphson method is used. As presented in section 3.6.1, the system to be solved can be written in a matrix form:

$$\begin{bmatrix}H^{ll} & H^{lb} & H^{lp}\\ (H^{lb})^{T} & H^{bb} & H^{bp}\\ (H^{lp})^{T} & (H^{bp})^{T} & H^{pp}\end{bmatrix}\begin{bmatrix}\delta\mathbf{V}\\ \delta\mathbf{B}\\ \delta\mathbf{P}\end{bmatrix}=\begin{bmatrix}-R^{l}(\mathbf{V},\mathbf{B},\mathbf{P})\\ -R^{b}(\mathbf{V},\mathbf{B},\mathbf{P})\\ -R^{p}(\mathbf{V},\mathbf{B},\mathbf{P})\end{bmatrix} \tag{6-42}$$

In equation (6-41) a), neglecting the contribution of "bubble" component in the inertia term, and neglecting the inertia contribution in the "bubble" equation (6-41) b), as it has been presented in section 3.6.1, equation (6-42) can be written as:

$$\begin{bmatrix}H^{ll} & H^{lp}\\ (H^{lp})^{T} & -(H^{bp})^{T}(H^{bb})^{-1}H^{bp}\end{bmatrix}\begin{bmatrix}\delta\mathbf{V}\\ \delta\mathbf{P}\end{bmatrix}=\begin{bmatrix}-R^{l}\\ -R^{p}+(H^{bp})^{T}(H^{bb})^{-1}R^{b,grav}\end{bmatrix} \tag{6-43}$$

In each Newton-Raphson iteration, it is possible to compute the correction of solution, $\delta\mathbf{V}$ and $\delta\mathbf{P}$, and the velocity and pressure at each node $\mathbf{v}_{n+1}$ ($\mathbf{v}_{n+1}=\mathbf{v}_{n}+\delta\mathbf{v}$) and p_{n+1} ($p_{n+1}=p_{n}+\delta p$). Consequently, the stress and deformation can be obtained by the local resolution of constitutive equations.

6.2.3 Implementation of axisymmetric formulation

Compared with the incompressible Newtonian model for the liquid phase, the THEVP model is more complicated. In this section we introduce the tangent modulus to treat the non-linear rheology behaviour, and we show how the adaptation from 3D to 2D axisymmetry should be done. We present the computation of $H^{ll,rheo}$, which shows some differences between the axisymmetric and plane cases.

Let us consider the rheology term in equation (6-41), which is expressed by:

$$R^{l,rheo} = \int_{\Omega} \mathbf{s}^{v}(\mathbf{v}):\dot{\boldsymbol{\varepsilon}}(\mathbf{v}^{*})d\Omega = \int_{\Omega} \mathbf{s}^{v}(\mathbf{v}):\nabla\mathbf{v}^{*}d\Omega \tag{6-44}$$

In the axisymmetric case, for the degrees of freedom *nk* (node *n*, the *k*th velocity component), the residual vector $R_{nk}^{l,rheo}$ can be expressed by:

$$R_{nk}^{l,rheo} = \int_{\Omega} s_{kj}\frac{\partial N_n}{\partial x_j}2\pi r drdz + \int_{\Omega} s_{\theta\theta}\frac{1}{r}N_n\delta_{k1}2\pi r drdz \tag{6-45}$$

where the indexes *k* and *j* vary from 1 to 2. N is the interpolation function. δ is the Kronecker function.

The Hessian matrix with respect to the degrees of freedom *ml* (node *m*, the *l*th velocity component, and *l* varies from 1 to 2), $H_{nk,ml}^{ll,rneo}$, is then given by:

$$H_{nk,ml}^{ll,rheo} = \frac{\partial}{\partial v_{ml}}\left[\int_{\Omega} s_{kj}\frac{\partial N_n}{\partial x_j}2\pi r drdz + \int_{\Omega} s_{\theta\theta}\frac{1}{r}N_n\delta_{k1}2\pi r drdz\right] \tag{6-46}$$

In order to compare with the plane strain case, the two terms in equation (6-46) are integrated individually. The first integration gives:

$$H_{nk,ml}^{ll,rheo1} = \int_{\Omega}\frac{\partial s_{kj}}{\partial\dot{\varepsilon}_{gh}}\frac{\partial\dot{\varepsilon}_{gh}}{\partial v_{ml}}\frac{\partial N_n}{\partial x_j}2\pi r drdz + \int_{\Omega}\frac{\partial s_{kj}}{\partial\dot{\varepsilon}_{\theta\theta}}\frac{\partial\dot{\varepsilon}_{\theta\theta}}{\partial v_{ml}}\frac{\partial N_n}{\partial x_j}2\pi r drdz \tag{6-47}$$

where the indexes *g* and *h* vary from 1 to 2. $\frac{\partial s_{kj}}{\partial\dot{\varepsilon}_{gh}}$ denotes the components of the tangent modulus. The definition of the tangent modulus can be referred to the Appendix C. The first integration in equation (6-47) provides the usual terms that need to be considered in the plane strain case, the corresponding components are as follows: $\frac{\partial\mathbf{s}_{11}}{\partial\dot{\boldsymbol{\varepsilon}}_{11}}$, $\frac{\partial\mathbf{s}_{22}}{\partial\dot{\boldsymbol{\varepsilon}}_{22}}$, $\frac{\partial\mathbf{s}_{11}}{\partial\dot{\boldsymbol{\varepsilon}}_{22}}$ and $\frac{\partial\mathbf{s}_{12}}{\partial\dot{\boldsymbol{\varepsilon}}_{12}}$. While the second integration presents the additional terms for the axisymmetric case, the associated components being $\frac{\partial\mathbf{s}_{11}}{\partial\dot{\boldsymbol{\varepsilon}}_{33}}$ and $\frac{\partial\mathbf{s}_{22}}{\partial\dot{\boldsymbol{\varepsilon}}_{33}}$.

In addition, the second integration in equation (6-46) can be written as:

$$H_{nk,ml}^{ll,rheo2} = \int_{\Omega}\frac{\partial s_{\theta\theta}}{\partial\dot{\varepsilon}_{gh}}\frac{\partial\dot{\varepsilon}_{gh}}{\partial v_{ml}}N_n\delta_{k1}2\pi drdz + \int_{\Omega}\frac{\partial s_{\theta\theta}}{\partial\dot{\varepsilon}_{\theta\theta}}\frac{\partial\dot{\varepsilon}_{\theta\theta}}{\partial v_{ml}}N_n\delta_{k1}2\pi drdz \tag{6-48}$$

equation (6-48) gives the additional terms associated with $\frac{\partial\mathbf{s}_{33}}{\partial\dot{\boldsymbol{\varepsilon}}_{11}}$, $\frac{\partial\mathbf{s}_{33}}{\partial\dot{\boldsymbol{\varepsilon}}_{22}}$ and $\frac{\partial\mathbf{s}_{33}}{\partial\dot{\boldsymbol{\varepsilon}}_{33}}$.

Considering the deformation rate $\dot{\boldsymbol{\varepsilon}}$ is a constant within each element, in the context of P1+/P1 formulation, only one Gaussian integration point is used to compute the term $H^{ll,rheo}$.

Regarding the rheology term $H^{bb,rheo}$, the related code has been rewritten using the tangent modulus. Since the rule for computing $H^{bb,rheo}$ according to the constitutive equation is similar to that of $H^{ll,rheo}$, we do not repeat it.

Since the "bubble" interpolation function is defined on the three subtriangles (seeing sections 3.6.1 and 3.6.2), again, $H^{bb,rheo}$ is integrated over the three subtriangles of an element using the three mid-edge integration points. We have written the code, carefully considering the additional terms in the axisymmetric case. As it is a very technical task, we will not enter here into details.

6.2.4 ALE formulation

The pipe formation in ingots is characterized by the fluid flow and free surface. To simulate this complicated problem, a purely Eulerian scheme (fixed mesh) is not satisfying, since it cannot provide enough precision for the evolution of the free surfaces. The classical Lagrangian scheme (convected mesh) would lead to mesh degeneracy in the liquid pools. Therefore, a specific arbitrary Lagrangian-Eulerian scheme (ALE) is used in the liquid and the mushy zones (called "liquid-like" zones), where the material behavior is Newtonian or viscoplastic. The Lagrangian scheme is used in the solid zone, a Lagrangian-type mesh updating permitting to describe the movement of the solidified shell. This is essential to treat the airgap opening between the mold and the ingot.

The ALE method is between the Lagrangian method ($\mathbf{v}_{\text{msh}} = \mathbf{v}_{\text{mat}}$) and the Eulerian one ($\mathbf{v}_{\text{msh}} = 0$). The basic principle of the ALE method is to separate clearly the mesh velocity field $\mathbf{v}_{\text{msh}}$ from the material velocity field $\mathbf{v}_{\text{mat}}$. In this way it is possible to retain a good mesh quality even at large material distortion. To simulate the mold filling process, the ALE formulation was initiated by Gaston [1997] in R2SOL, and complemented by Bellet *et al.* [2004]. So, we will not discuss here the details of the ALE formulation, but only the main lines of the formulation.

1) computation of the mesh velocity field $\mathbf{v}_{\text{msh}}$;
2) accounting for the velocity difference $\mathbf{v}_{mat} - \mathbf{v}_{msh}$ in energy and momentum equations;
3) determination of the areas of the computational domain that should be treated by the Lagrangian and Lagrangian-Eulerian schemes.

- **Computation of mesh velocity**

The computation of $\mathbf{v}_{\text{msh}}$ consists in regularizing the position of nodes in order to minimize the deformation of the mesh. Knowing the time step Δt, the mesh velocity is defined by the relation:

$$\mathbf{x}^{t+\Delta t} = \mathbf{x}^{t} + \Delta t\,\mathbf{v}_{msh} \qquad (6\text{-}49)$$

where $\mathbf{x}^{t+\Delta t}$ are the new locations of nodes. These new positions are determined by an iterative procedure, which aims at positioning each node at the center of gravity of the set of its neighbors. This is done under the constraint of conservation of material flux through the domain surface:

$$\mathbf{v}_{ms}\,.\mathbf{n} = \mathbf{v}_{mat}\,.\mathbf{n} \qquad (6\text{-}50)$$

where **n** is the outward unit normal. This constraint is enforced by a local penalty technique.

- **Treatment of advection terms**

Knowing the mesh velocity, it is now necessary to transport the nodal fields, for instance the temperature *T*. For each node, this is done by:

$$T^{t+\Delta t} = T^{t} + \frac{\partial_g T}{\partial t}\Delta t \tag{6-51}$$

where the time derivative of *T* with respect to the grid, that is the rate of variation of the temperature at a given node of the moving mesh, can be expressed as follows:

$$\frac{\partial_g T}{\partial t} = \frac{dT}{dt} - (\mathbf{v}_t \quad - \mathbf{v} \quad).\nabla T \tag{6-52}$$

Once the heat transfer problem has been solved on the time increment, the total (material) time derivative of the temperature is known at each node. After computation of $\mathbf{v}_{mat}$ and $\mathbf{v}_{msh}$, the updating of the temperature field can be obtained using equations (6-51) and (6-52), for which one only requires the nodal temperature gradient. Using an upwind technique, this nodal gradient is computed in the upstream element, according to the advection velocity $\mathbf{v}_{mat}$ - $\mathbf{v}_{msh}$ (see Figure 6-1).

In order to express the acceleration terms in the momentum equation, a transport of the material velocity field is necessary. In equation (6-36), the velocity $\mathbf{v}^{t-\Delta t}$ is the material velocity of the particle at the previous time level $\mathbf{v}_{mat}^{t-\Delta t}$. Hence, after configuration updating, this requires a pure transport of the velocity field. This is achieved by a similar scheme as that presented by equations (6-51) and (6-52), but in which the material derivative is taken equal to zero:

$$\mathbf{v}_{mat}^{t}(\mathbf{x}^{t+\Delta t}) = \mathbf{v}_{mat}^{t}(\mathbf{x}^{t}) - [\nabla\mathbf{v}_{mat}^{t}(\mathbf{x}^{t})](\mathbf{v}_{mat}^{t}(\mathbf{x}^{t}) - \mathbf{v}_{msh})\Delta t \tag{6-53}$$

Referring to Figure 6-1, it can be seen that equation (6-53) is nothing but a first order spatial development of the material velocity field in the upstream element associated with the nodal position $\mathbf{x}^{t}$.

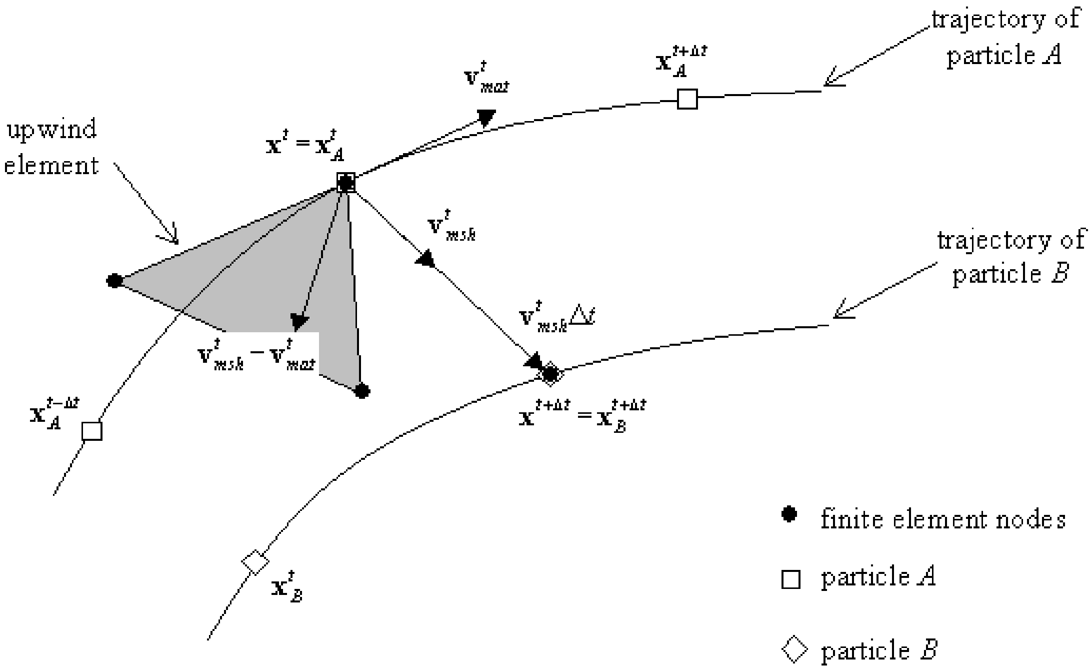

Figure 6-1 Updating of the location of a finite element node and subsequent identification of the upwind element. The materialization of the trajectory of two material particles A and B helps in the interpretation of (6-53), from Bellet *et al.* [2004]

- **Lagrangian and Eulerian-Lagrangian zones**

Regarding now the global treatment of viscoplastic and elastic viscoplastic models, the idea consists in defining the solidified regions as Lagrangian (convected mesh) and the liquid or mushy ones as Eulerian-Lagrangian. Therefore each node is affected to one of the two classes, according to the following rule, as illustrated in Figure 6-2.

1) Each node belonging at least to one solid-like element (*i.e.*, whose constitutive equation has been chosen elastic-viscoplastic) is treated as Lagrangian (mesh velocity equals material velocity).

2) All other nodes, which then belong to liquid-like elements only, are treated as Eulerian-Lagrangian (mesh velocity calculated independently of the material velocity).

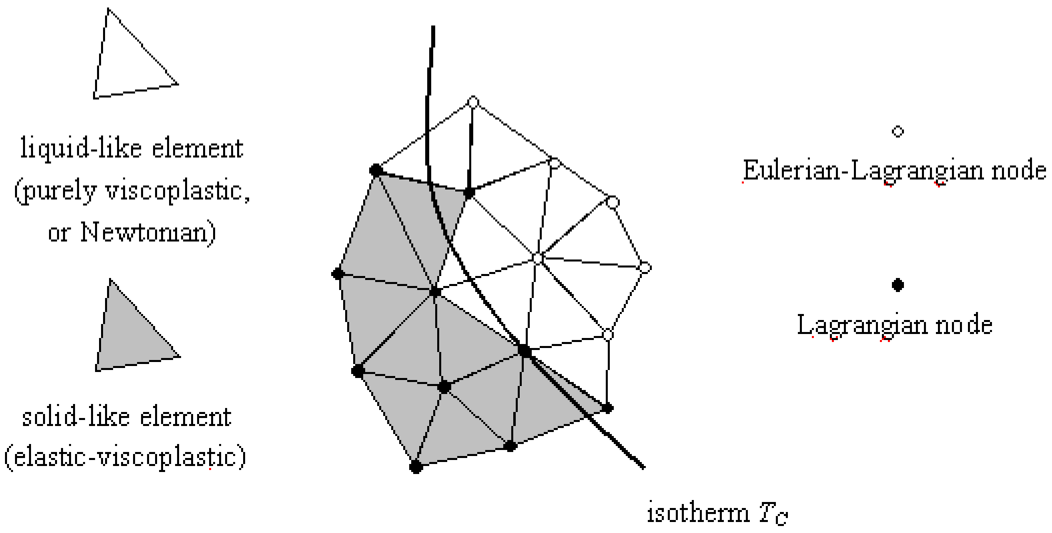

Figure 6-2 Lagrangian and Eulerian-Lagrangian nodes, as determined by their belonging to solid-like and liquid-like finite elements, from Bellet *et al*. [2004]

6.3 Validations

6.3.1 Thermoelastic test

This test aims at the validation of the dilation term in equation (6-33). Let us consider a cylinder which is constrained between two rigid tools as shown in Figure 6-3. A sliding contact is applied at the top and the bottom surfaces. We assume that the cylinder is cooled down uniformly at a constant cooling rate $\dot{T}=-5°C/s$, and the behavior of the material is elastic, with Young modulus $E=1000\,(\mathrm{MPa})$, and Poisson coefficient $\nu=0.3$. The thermal expansion coefficient $\alpha=1.068\times10^{-5}(1/°C)$.

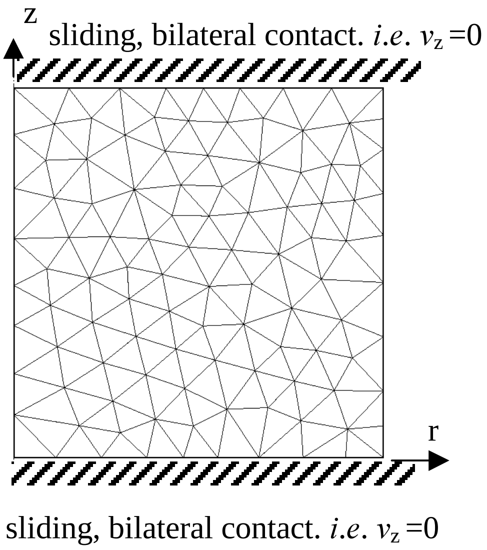

Figure 6-3 The mesh of the sample

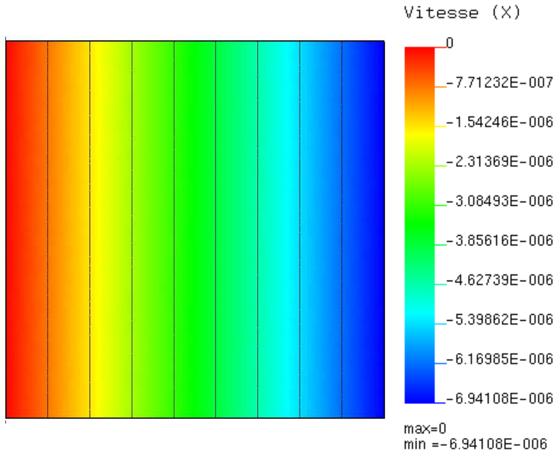

Figure 6-4 The radial velocity field

The strain is assumed to be homogeneous in the sample, such that:

$$v_r = v_r(r) \quad v_\theta = 0 \quad v_z = 0$$

The analytical resolution of such a problem is as follows:

$$\dot{\sigma}_{\theta\theta} = \dot{\sigma}_{rr} = 0, \text{ and } \dot{\sigma}_{zz} = -E\alpha\dot{T}$$

$$v_r = (1+\nu)\alpha\dot{T}r$$

Asuming the height of the sample is 0.1 (m) and the radius is 0.1 (m), taking the time step $\Delta t = 1(s)$, the numerical simulation has been carried out. The velocity field is shown in Figure 6-4. The Minimum velocity $v_r = -6.942\times10^{-6}(m/s)$ is expected by analytical resolution at $r = 0.1(m)$. The numerical result $v_r = -6.941\times10^{-6}(m/s)$ coincide with the analytical one. The comparison of stress σ_{zz} verus time t between the analytical result and the numerical one is shown in Figure 6-5.

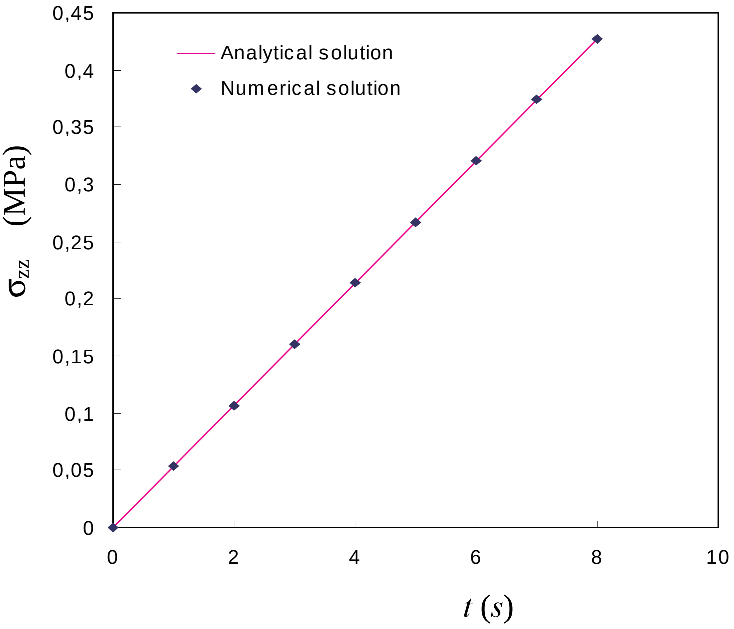

Figure 6-5 Comparison between numerical and analytical solutions

6.3.2 Uniaxial tension test

The uniaxial tension test is used to validate the implementation of the elastic viscoplastic behavior. Consider a cylindrical sample shown in Figure 6- 6. Its initial length is l_0 ($l_0 = 50\,mm$), and its initial radius r_0 ($r_0 = 5\,mm$). The work hardening obeys equation (6-14). The rheology parameters are selected from Kozlowski *et al.* [1992] and given in Table 6-1, the equivalent stress is then defined by:

$$\sigma_{eq} = \sigma_s + K\dot{\bar{\varepsilon}}_{eq}{}^m \bar{\varepsilon}_{eq}{}^n$$

Table 6-1 Rhoelogy parameters

K(MPa .s^m)	m	n	σ_s (MPa)	ν	E(GPa)
252	0.2	0.25	20	0.3	25

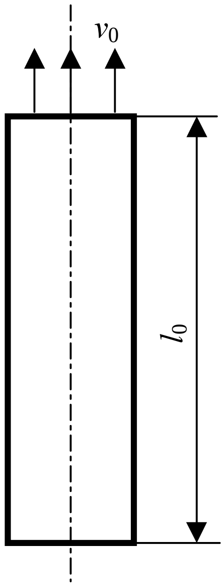

Figure 6- 6 Schematic of the uniaxial tension test

A constant velocity v_0 is imposed at the top surface. The equivalent strain rate is then: $\bar{\varepsilon}_{eq} = v_0 / l_0$. Numerical tests have been done under different equivalent strain rate. The numerical results are shown in Figure 6-7. It can be seen that the relationship between strain and stress is linear when the stress is under the initial threshold σ_s. It is nonlinear when the stress exceeds the initial threshold because the work hardening occurs. It can be seen also that the threshold is less sensitive with increasing strain rate, that is the behavior can be modeled either elastic or elastic-viscoplastic when the strain rate is very high. The numerical solution coincide with the analytical solution.

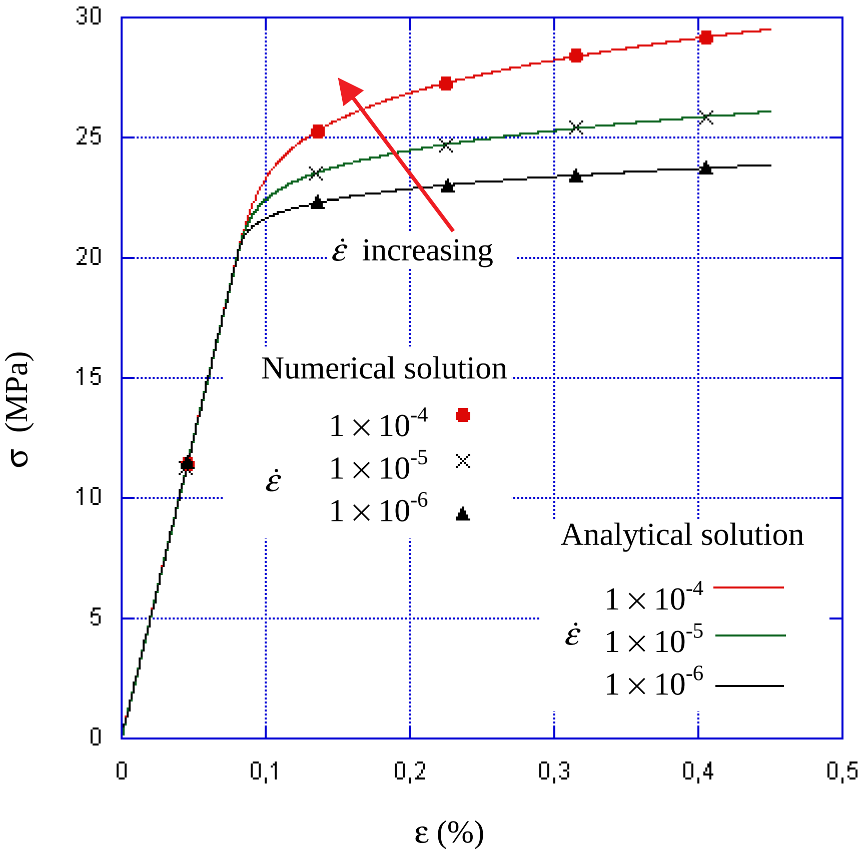

Figure 6-7 Relationship between strain and stress for different nominal strain rates v_0/l_0

6.4 Applications

6.4.1 Svensson solidification test

- **Description of the problem**

This test has been designed by Svensson to validate computational codes (Bellet *et al*. [1996]). The experimental set-up is shown in Figure 6-8. The mold was made from a low alloy steel. The height of the mold was 100 mm. The outer and inner diameters of the mold were 250 mm and 150 mm respectively. The core was a quartz tube filled with oil bound sand, its diameter was 24 mm. Insulating material was placed in the bottom and in the top of the set up. Al-7%Si-Mg alloy was cast in the cavity. A series of thermocouples and displacement sensors (linear variable differential transducers, LVDTs) were used to measure the temperature and the air gap width during solidification. The heat transfer coefficient (HTC) at the interface between the part and mold was deduced from the measured temperatures, as shown in Figure 6-9. The details of the test can be referred to Bellet *et al*. [1996] and Kron *et al*. [2004].

The thermo-mechanical modeling of solidification of the part have been done with R2SOL, compared to three codes: CASTS, MAGMA and PROCAST. For the details of computational conditions and parameters, one can refer to Kron *et al*. [2004]. Hereunder, we briefly introduce the numerical computations.

As a first step, pure heat transfer analyses of the solidification problem were done with a constant HTC between the part and mold. The maximum value of measured HTC was used in the computations. This academic study served as a comparison between the heat transfer solvers of the different numerical codes.

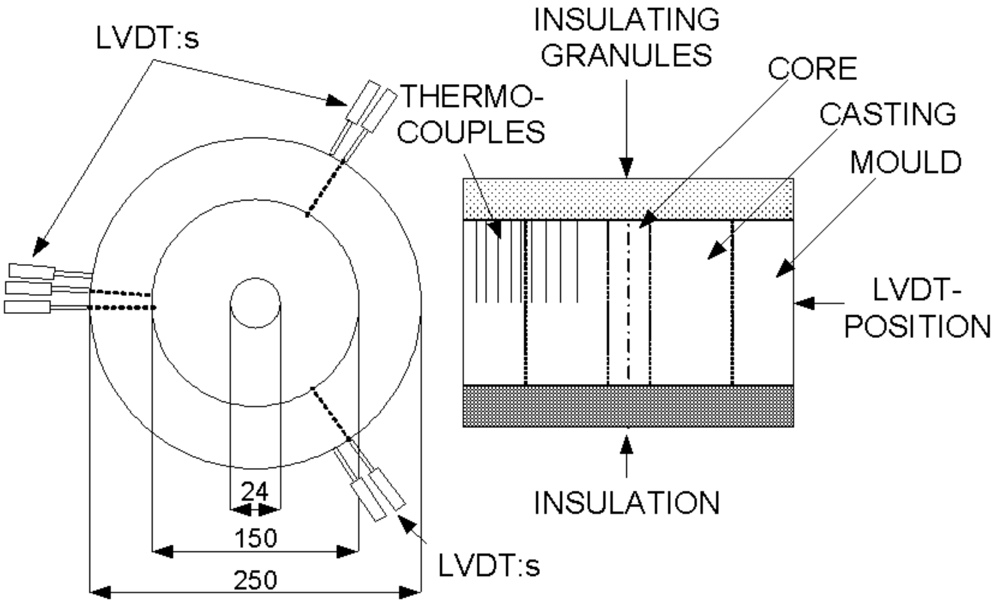

Figure 6-8 Top and side view of experimental set-up, from Kron *et al.* [2004]

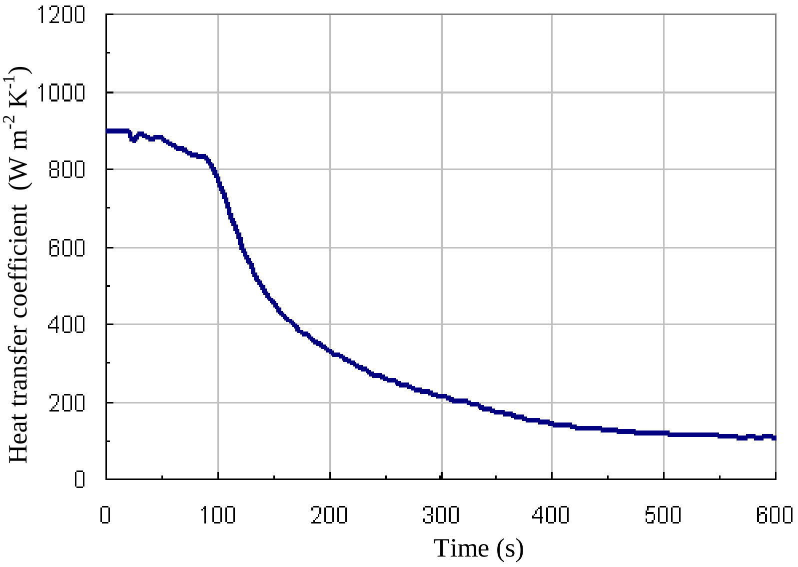

Figure 6-9 The measured heat transfer coefficient HTC from Kron *et al.* [2004], and the constant value used for pure heat transfer calculation (h = 898 W.m^{-2}.K^{-1})

In the second step, thermo-mechanical calculations were performed. The time-dependent HTC as obtained from experiments was used for the heat transfer analysis (this time-dependent heat transfer coefficient was assumed uniform on the whole interface). So, there was no effective coupling from the mechanical calculation towards the heat transfer calculation. Only the coupling from the thermal calculation towards the mechanical calculation was taken into account through the temperature dependence of constitutive parameters. For these computations, we compare predictions of the air gap.

It should be noted that in R2SOL the mold, the core and the insulating materials are assumed rigid, the same assumptions are adopted in the computation of CASTS. While MAGMA, PROCAST and THERCAST permit computing the deformations in the mold. In MAGMA, since the thermal and mechanical modules are separated, firstly the program makes thermal calculations and then uses the calculated temperature field as in-data for the mechanical calculations. The calculation of the air gap is done in two steps: firstly, the displacement of the casting is calculated, and then the displacement of the mold is calculated. In the computation of PROCAST, the core and the insulating material are considered rigid, the mold linear elastic, the part elastic-plastic. PROCAST permits coupling the thermal and mechanical analyses simultaneously, as well as THERCAST.

- **Results of the pure heat transfer computations**

As presented before, the first step computations have been carried out using the maximum heat transfer coefficient. The cooling curve measured in the part at mid-height (z = 50 mm) and near the outer surface (r = 69 mm) is shown in Figure 6-10. It is compared with the computational results obtained by R2SOL and the other codes. It can be seen that the computational result of R2SOL is close to the others. The computational cooling curves coincide with the experimental result at the beginning of solidification. But they deviate from the experimental result in the later stage. In fact, the heat transfer coefficient between the part and mold decreases when the gap grows. This is not taken into accout in the computations, and leads logically to an underestimation of temperature.

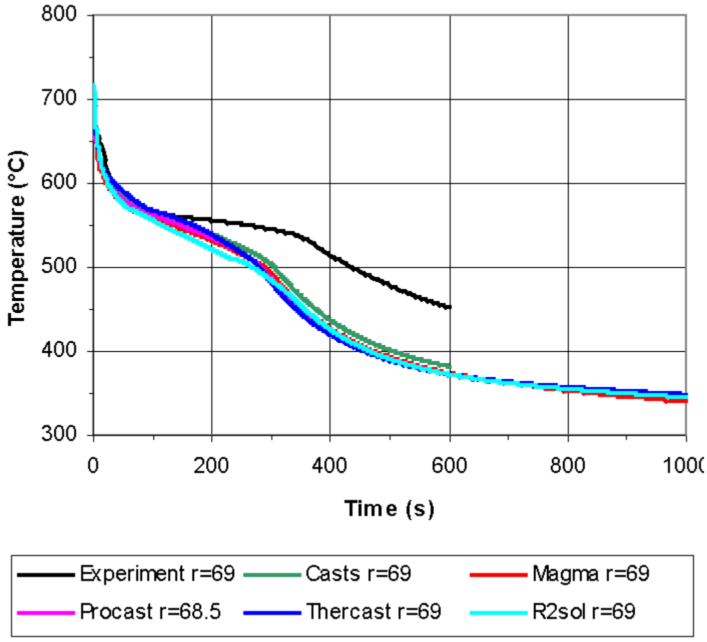

Figure 6-10 Comparison of cooling curves between measured and calculated, pure heat analyses

- **Results of the thermo-mechanical computations**

Besides the heat transfer computations, an elastic-plastic model (Ramberg-Osgood stress-strain model) is applied (Kron *et al*. [2004]) to compute the stresses and strains in the solidifying part. The core and the insulation are assumed rigid. In the computation of R2SOL, the mold is also assumed rigid. But the deformations in the mold are computed with MAGMA and PROCAST.

Compared to Figure 6-10, the cooling curves are again shown in Figure 6-11. It can be seen that the computational results are in good agreement with the experimental one. This is quite normal since the computations have used the measured HTC directly.

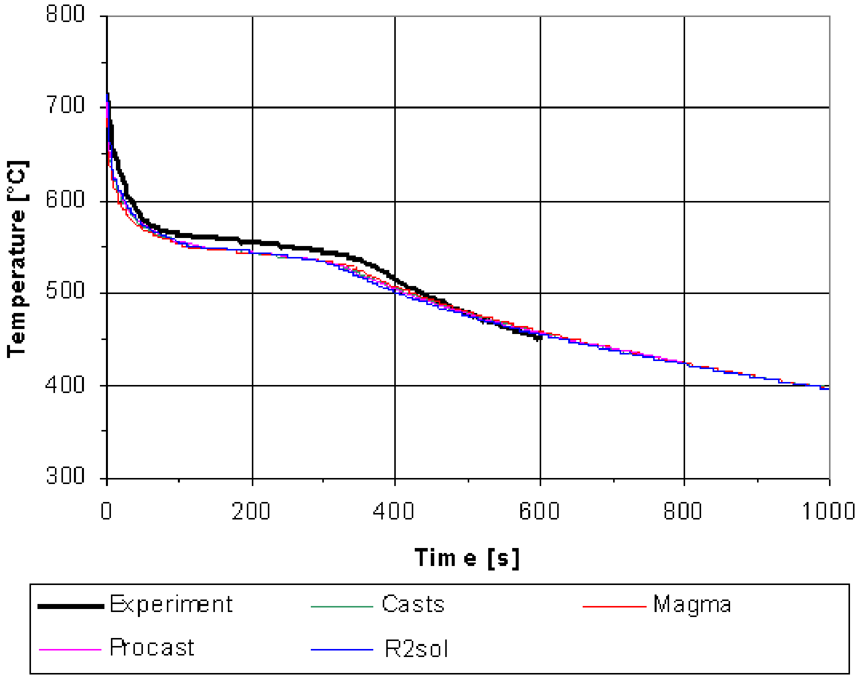

Figure 6-11 Measured and calculated cooling curves, thermo-mechanical analyses, from Kron *et al*. [2004]

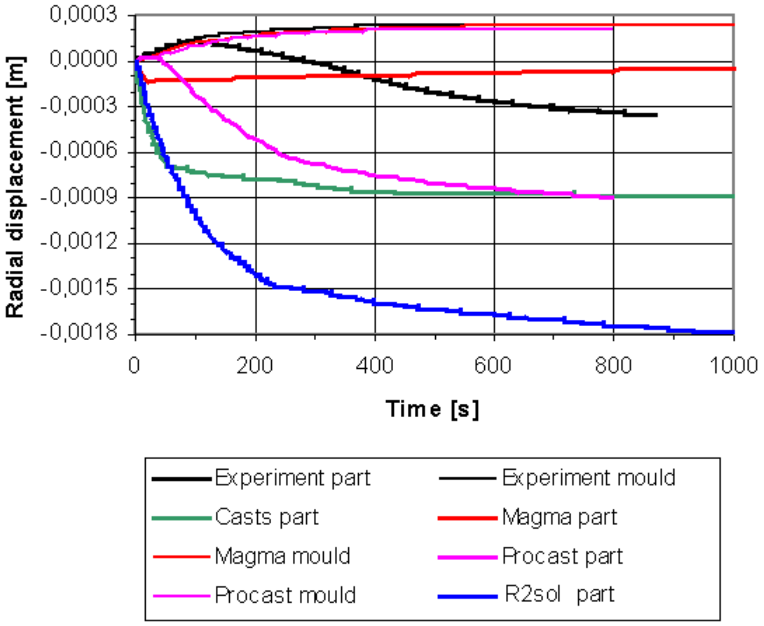

Figure 6-12 Evolution of the displacement of the part and mold surfaces, from Kron *et al*. [2004]

Regarding the mechanical computations, Figure 6-12 shows the evolution of the displacement of the part and mold surfaces at the mid-height of the casting. The experimental curves show the mold expansion, which stabilises at 400 s. The part surface follows this expansion at the beginning of cooling, up to 100 s, which is the air gap formation time. The mold expansion has been correctly predicted by MAGMA and PROCAST, using the thermo-elastic model. Comparing the curves of displacement of the part, a huge disparity can be observed in the numerical results. This disparity has been explained by Kron *et al*. [2004], the main causes may be found in the constitutive equation and the corresponding parameters. It should be noted that the given constitutive law cannot be used directly in different codes, except for MAGMA. For instance, in R2SOL the elastic viscoplastic behavior is described by equations presented in section 6.1.2. In order to use the Ramberg-Osgood model, a fitting has been done to approach as best as possible the stress-strain curves. This might be a source of differences between the different computations.

6.4.2 Solidification of industrial ingots

In this section, we present the results obtained by coupled thermo-mechanical simulations. The first case is an octogonal 3.3 ton steel ingot produced by AUBERT & DUVAL. The ingot is considered axisymmetric, the geometry is shown in Figure 6-13. The computational system consists of the ingot and four subdomains of mold. The ingot has a height of 1.83 m, and the maximum radius is 0.331 m. It is discretized with 7236 triangle elements, the mesh size varies from 2.5 to 25 mm. Coupled thermomechanical simulations have been performed with R2SOL. In the computation, the mold is considered rigid. A unilateral contact condition is applied to the boundary of the ingot and mold, the deformation in the solidified ingot is computed with the method as presented before. For heat transfer analysis, a constant heat transfer coefficient at the interface between the ingot and mold is used before the formation of an airgap. When an airgap with a thickness δ locally appears, heat exchange between the ingot and mold mainly arises from heat conduction and radiation through the airgap. Therefore, an equivalent local heat transfer coefficent h can be computed by:

$$\frac{1}{h}=\frac{1}{h_{cond}+h_{rad}} \quad \text{with} \quad h_{cond}=\frac{\lambda_{air}}{\delta} \quad \text{and} \quad h_{rad}=\sigma_B\frac{(T_1^{\,2}+T_2^{\,2})(T_1+T_2)}{(\frac{1}{\varepsilon_1}+\frac{1}{\varepsilon_2}-1)} \qquad \text{if} \quad \delta\geq\delta_{\min} \tag{6-54}$$

$$h=h_0 \qquad \text{if} \quad \delta<\delta_{\min} \tag{6-55}$$

where λ_{air} denotes the thermal conductivity of air, T_1 and T_2 the surface temperatures of the ingot and mold respectively, ε_1 and ε_2 their emissivities and σ_B the constant of Stefan-Boltzmann.

In addition, in order to consider the natural convection (due to the density gradient caused by the temperature gradient) in the bulk liquid, we have used an augmented viscosity of the liquid (μ = 1 Pa. s).

Regarding the natural convection flow in the liquid pool, we have not been able to use the nominal viscosity of liquid steel (say 10^{-3} Pa.s) which has resulted in loss of convergence for the resolution of our non-linear problem. In our opinion, the following cause can be invoked. The use of low viscosity results in great variations of the rheological contributions that are assembled around nodes belonging to the mushy zone. This leads to very badly conditioned sets of linear equations at each Newton-Raphson iteration, causing non-convergence. This would need further investigation. This limitation might also be overcome by using finer meshes in the mushy zone. From this point of view the tools we have developed to control automatic remeshing (cf. chapter 4) could be very profitable, but this has not been tested in the frame of our Ph.D. work.

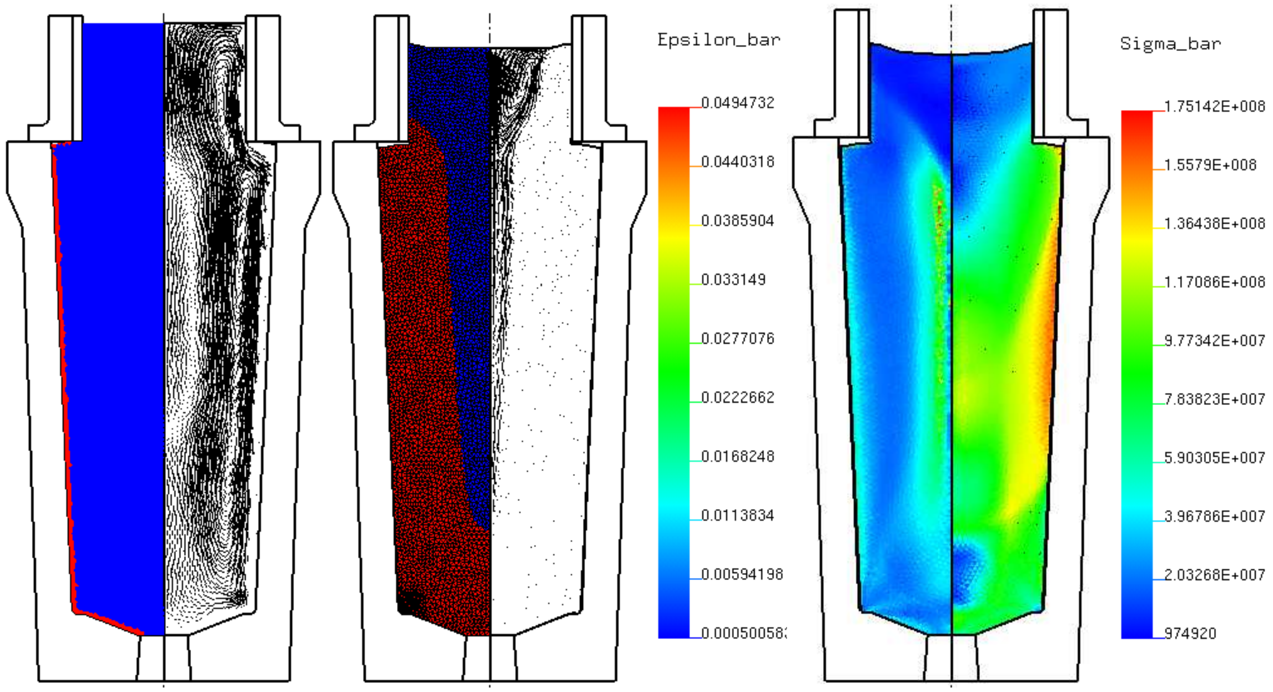

a) 1 min b) 1 h 15 min c) 5 h

Figure 6-13 Illustration of the solidification of a 3,3 ton steel ingot. a) the liquid zone in blue, the solid zone in red, and the velocity vector at 1 min (the maximum velocity, 37.8 mm/s); b) the mesh superimposed on the liquid and solid zone at 1 h 15 min, maximum velocity 1 mm/s; c) distribution of the cumulated plastic deformation and the Von Mises equivalent stress (Pa) at 5 h, end of the solidification at 3 h 25 min.

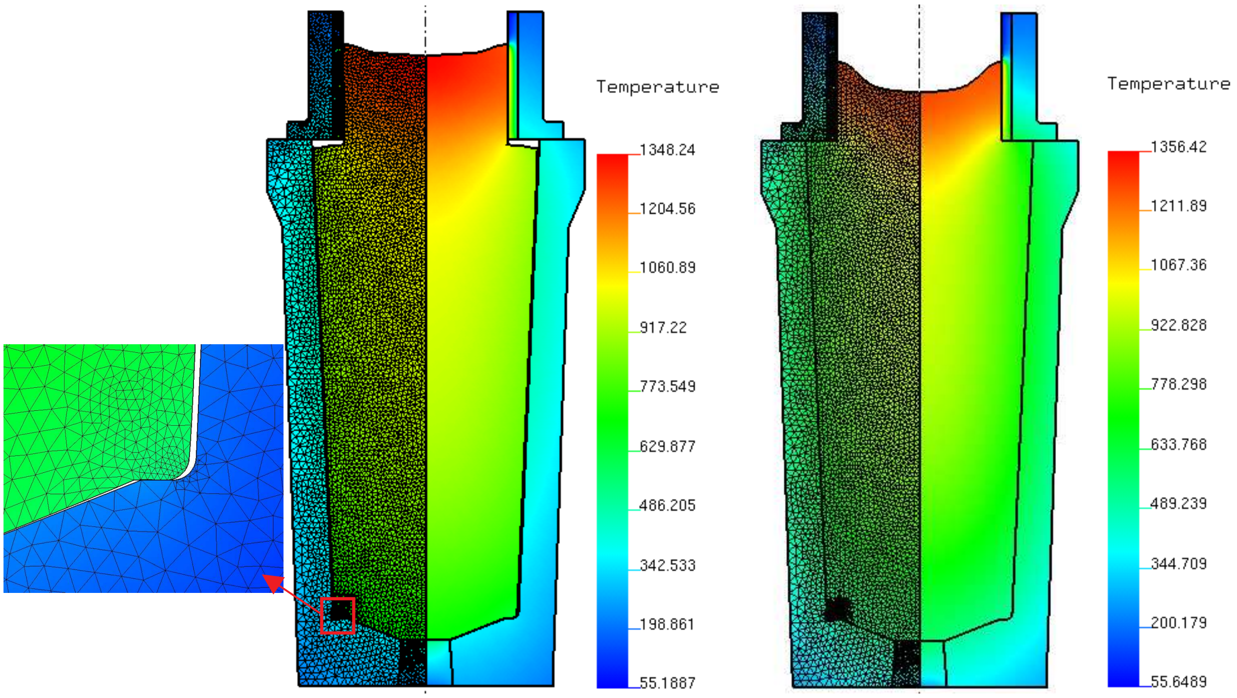

a) unilateral contact
end of solidification: *t* = 3 h 25 min

b) bilateral contact
end of solidification: *t* = 2 h 25 min

Figure 6-14 Comparison of results calculated with unilateral and bilateral contact for a 3.3 ton steel ingot. a) the heat transfer coefficient at the interface between the ingot and mold depends on the airgap width, which is computed with a unilateral contact condition; b) the heat transfer coefficient is a constant, without airgap, a bilateral contact condition is applied.

Using an augmented viscosity can also avoid treating turbulent flow that can appear during the solidification. In the current computation, the maximum velocity of fluid flow is 5.5×10-2 m/s (observed at 30 s), the associated Reynolds ($Re = \frac{|\mathbf{v}|\, L}{\mu / \rho} = \frac{0.055 \times 0.6}{1.0/7060} \cong 230$) number is about 230. Taking the superheat temperature as the temperature difference (72°C), the reference Rayleigh number is given by:

$$Ra = \frac{\rho^2 |\mathrm{g}|\, \beta_{\mathrm{T}} \Delta T L^3 c_p}{\mu\, \lambda} = \frac{7052^2 \times 9.8 \times 7.55 \times 10^{-5} \times 72 \times 0.6^3 \times 672}{1. \times 35} \cong 1.1 \times 10^7$$

The solidification process of the ingot is illustrated in Figure 6-13. Solidification phenomena, such as the natural convection in the liquid due to temperature gradient, the deformation in the solid due to thermal contraction and the solidification shrinkage, can be observed simultaneously in the figures. One can clearly see the fall of liquid level at the top of ingot, which results from the solidification shrinkage and the thermal contraction in the solid and liquid phases. One also observes the air gap at the interface between ingot and mold. It is about 4.0 mm around the body of the ingot, and a maximum value of 25 mm is observed on the shoulder of ingot.

It should be noted that the air gap takes a considerable volume, this volume is about 1.33×10^{-2} m^3 ($2\pi \times 0.33 \times 1.6 \times 0.004$), which may influence the prediction of the shrinkage pipe. Assumed that this volume is compensated by the liquid in the hot riser, then the descent level of liquid can be 73 mm ($1.33 \times 10^{-2} / (\pi 0.24^2)$).

Following this consideration, we found interesting to compare simulations accounting for or not the airgap. We have performed a second calculation in which it is supposed that no airgap is formed during the solidification: this more restrictive calculation has been done with a condition of bilateral contact and a constant heat transfer coefficient at the interface between ingot and mold ($h = h_0$ in equation (6-55)). The comparison is shown in Figure 6-14. As expected, in this second calculation, the pipe is deeper, as can be seen in Figure 6-14 b). The depth of the defect is augmented by 121 mm in the center and 66 mm in the periphery, which is consistent with our previous calculation. Let us notice, additionally, that the final mass of the ingot in these two calculations is the same, the mass loss in the calculations being very low (about 0.3 %): it is then clear that the difference can be attributed to numerical errors.

We can also note that the solidification time is shorter in this second computation (2 h 25 min instead of 3 h 25 min). This is consistent with the choice of a constant heat transfer coefficient h_0 (corresponding to a no-gap situation in the first calculation). It can be seen that the contact condition affects not only the cooling of the ingot, but also the shape of the shrinkage pipe.

A similar comparison as mentioned above is done with a larger steel ingot (height 5 m, maximum radius 1.40 m, 164 tons) produced by Industeel Creusot. In a first step, a unilateral contact condition is applied to the mechanical simulation, and the heat transfer coefficient between the ingot and mold (considering the formation of air gap) is defined by equations (6-54) and (6-55). In a second step, a bilateral contact condition is applied, and a time-dependent heat transfer coefficient (HTC) is used. This time-dependent HTC is obtained from the first computation as follows. At mid-height of the ingot and at different times, knowing the gap size and the surface temperatures, it is possible to deduce a HTC by applying equations (6-54) and (6-55). In the second calculation this time-dependent HTC is applied to the whole interface between mould and ingot.

This is to ensure that the temperature history in the ingot is approximately the same whatever the contact option chosen (either unilateral or bilateral).

The solidification process of the ingot simulated with a unilateral contact condition is illustrated in Figure 6- 15. The evolutions of surface temperatures of the ingot and the mold at the mid-height of the ingot are shown in Figure 6- 16, as well as the growth of the local air gap. Figure 6-17 shows the formation of air gap at the bottom of the ingot. It can be seen that a 17 mm air gap is formed during solidification.

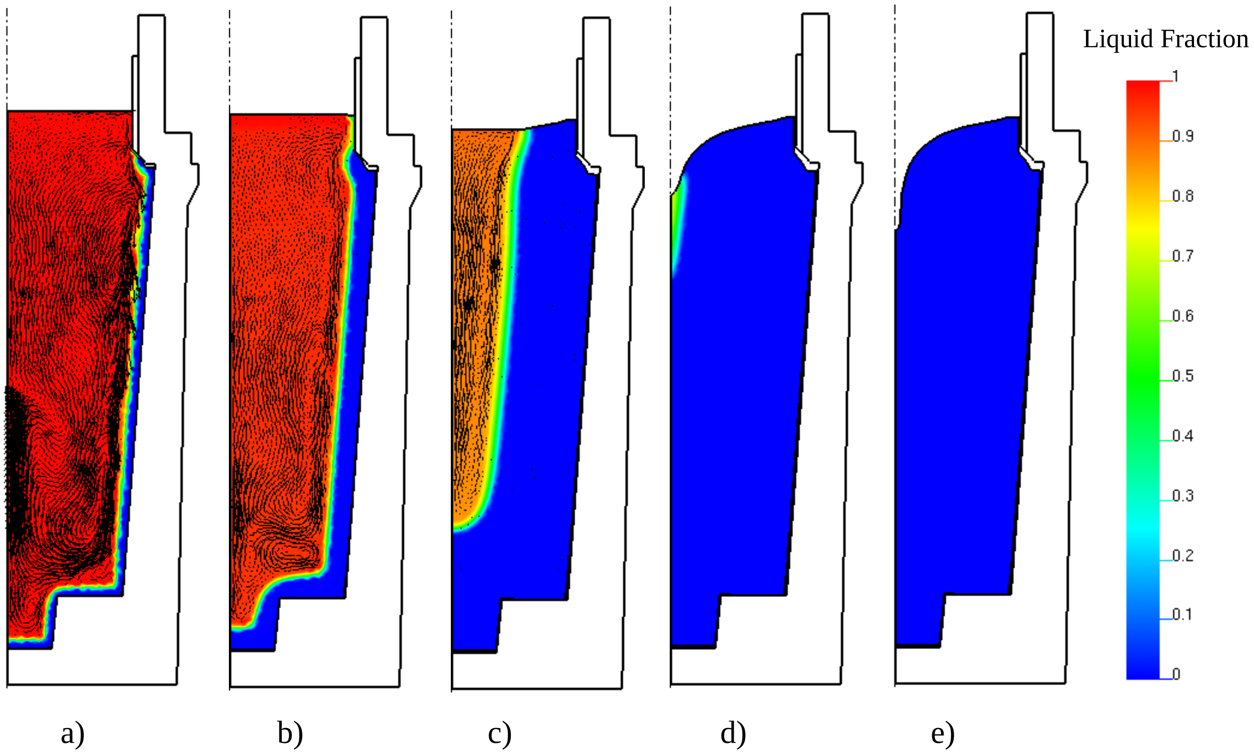

Figure 6- 15 The solidification process of a 165 ton steel ingot. a) the liquid fraction field and velocity vectors at 10 min, the maximum velocity, 47.47 mm/s; b) at 1 h, maximum velocity 10.92 mm/s; c) at 10 h, maximum velocity 0.22 mm/s; d) at 20 h; e) at 20 h 50 min, end of solidification.

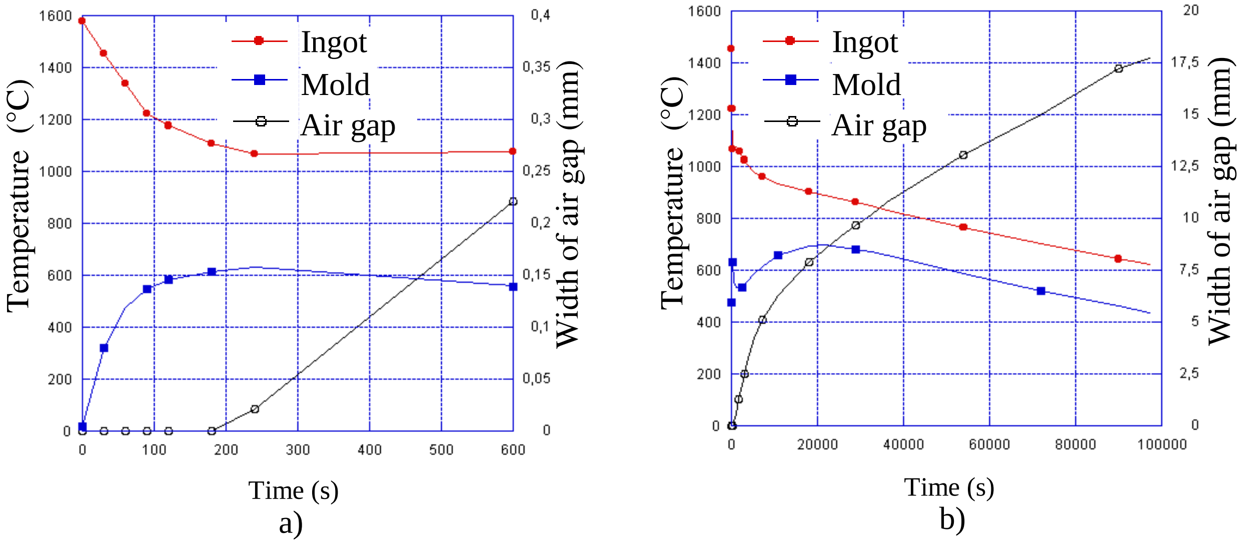

Figure 6- 16 Evolutions of surface temperatures and the air gap: a) at the beginning; b) during the solidification.

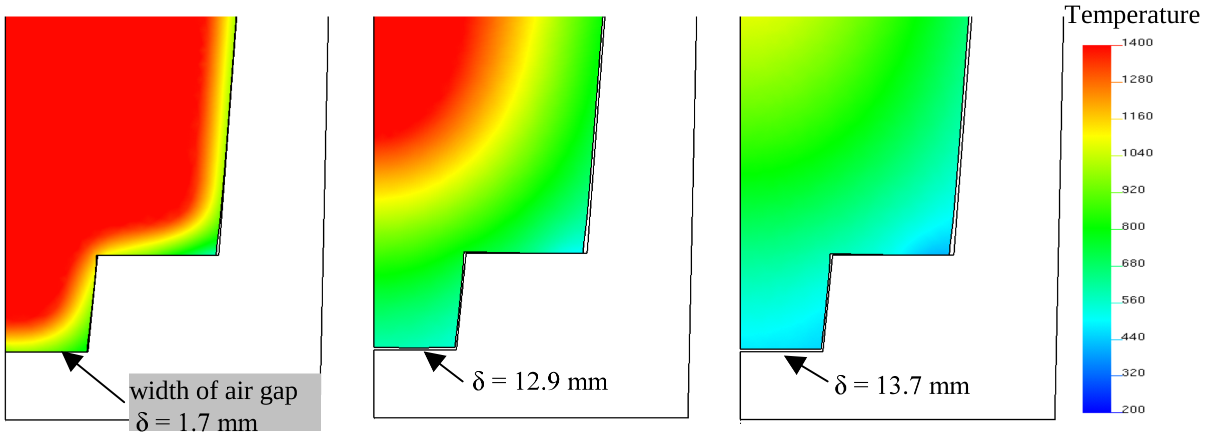

a) time = 1 h b) time = 10 h c) time = 20 h

Figure 6-17 Formation of the air gap at the bottom of the ingot

As expected the solidification time of the second case is 20 h 10 min, compared to the first case, 20 h 50 min. However, regarding the shrinkage pipe and stresses, the results calculated with a bilateral contact condition are very impressive as shown in Figure 6-18 and Figure 6-19. Blocking the movement of the periphery of ingot with a bilateral contact condition, dramatically causes a deep shrinkage pipe that reaches the mid-height of the ingot, and very large stresses at the bottom and the corners. For the simulation with a bilateral contact, one can imagine that the volume of the shrinkage pipe increases in order to compensate the volume of the air gap. A downward and outward feeding flow can be observed in the mushy zone in Figure 6-18 b), which leads to the formation of shrinkage pipe. Considering the air gap at the bottom of the ingot in Figure 6-17, the maximum width being 13.7 mm, this contraction is constrained in the computation with a bilateral contact condition, leading to larger stresses and strains as shown in Figure 6-19.

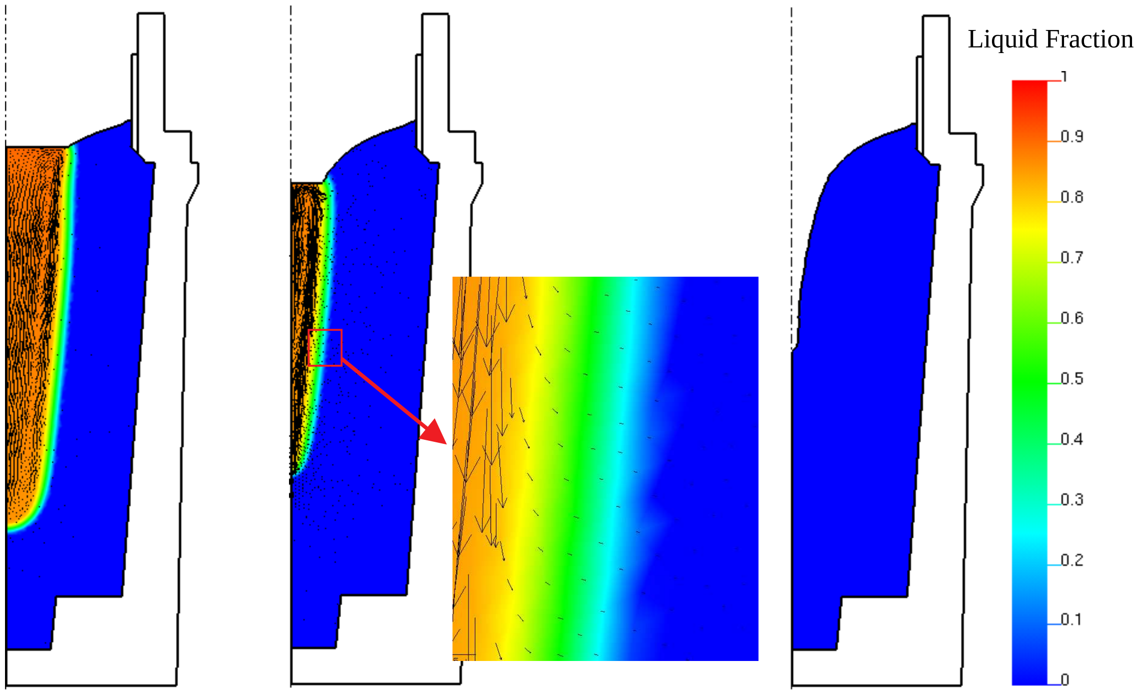

a) b) c)

Figure 6-18 The solidification process of a 165 ton steel ingot simulated with a bilateral contact condition. a) the liquid fraction field and velocity vectors at 10 min, the maximum velocity, 0.27 mm/s; b) at 15 h, maximum velocity 0.14 mm/s, a zoom to the flow in the mushy zone is presented; c) at 20 h 10 min, the end of solidification.

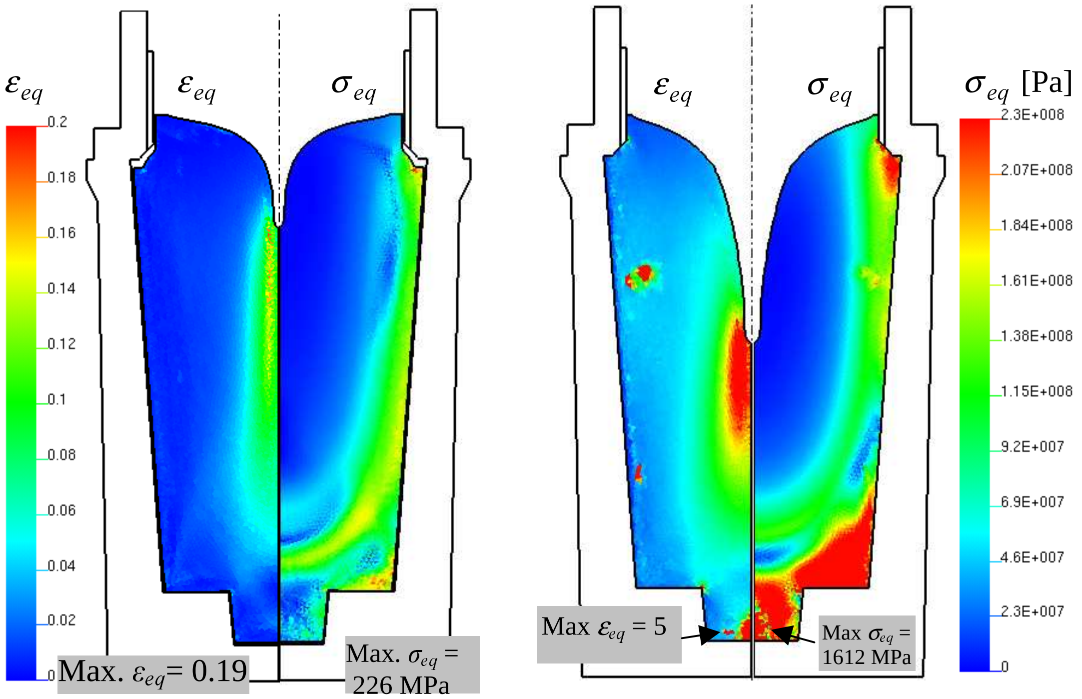

a) unilateral contact, end of solidification: 20 h 50 min b) bilateral contact, end of solidification: 20 h 10 min

Figure 6-19 Comparison of results calculated with the unilateral and bilateral contact for a 165 ton steel ingot. The distribution of equivalent plastic deformation is shown on the left part, and the equivalent stress on the right part.

We have checked the mass conservation for the thermal mechanical simulations, comparing with the initial mass, the maximum difference is less than 0.68%.

Regarding the prediction of the formation of shrinkage pipe in large ingots, we note that the volume of air gap must be taken into account. However, in many references of the literature (refer to the bibliographic review in section 2.2), only fluid mechanical models are used without considering the deformation in solid zones. These models can not predict the formation of air gap, therefore the contribution of air gap to the shrinkage pipe is neglected.

6.5 Conclusion

A thermo-elastic-viscoplastic (THEVP) model and a thermo-viscoplastic (THVP) model have been implemented in R2SOL. The alloy in the liquid or mushy states is modeled using the THVP law, depending on the temperature, the model can be either Newtonian for the pure liquid, or viscoplastic for the mushy state. Fluid flow induced by the temperature gradient and solidification shrinkage can be simulated. Below a critical temperature, the alloy is considered by the THEVP constitutive law, which allows to compute stresses and strains in the solid.

Our personal contribution to the new version of R2SOL has consisted in extending the material behavior from Newtonian to elastic viscoplastic. In collaboration with Alban Heinrich, the P1+/P1 formulations for thermo-mechanical problems have been implemented. In this work, adaptation from 3D to 2D axisymmetric formulation was a delicate issue, which needed a careful consideration of the additional terms. A thermo-dilation and an uniaxial tension test have been done to validate the new code.

Numerical simulations of solidification of Svensson test and industrial steel ingots demonstrate the new computational capacity of R2SOL, being able to predict the shrinkage pipe, air gap, strains and stresses. These academic computations show important effects of air gap during the solidification of ingots. Beyond our numerical contribution, complementary work is needed to evaluate in a more quantitative manner the capacity of the models developed.

Chapter 7

Conclusion and perspectives

The present work aimed at developing numerical models in the two dimensional finite element code R2SOL, in order to compute: 1) macrosegregation associated with the thermo-solutal convection in the liquid and mushy zones; and 2) stresses and strains in the solid phases during solidification of castings. The thermal mechanical models are summarized as follows.

➢ Modeling of macrosegregation

Macrosegregation in columnar dendritic solidification has been simulated following the works of Isabelle Vannier [1995] in SOLID and Laurence Gaston [1999] in R2SOL. We assume that the solid phase is fixed and rigid, therefore, only fluid mechanics is considered. The liquid flow is laminar, Newtonian, with a constant viscosity. The mushy zone is considered as an isotropic porous medium whose permeability is defined by Carman-Kozeny relation. In order to calculate the drag force exerted on the interdendritic liquid, Darcy's law is applied. The Boussinesq approximation is adopted in the momentum equation for the liquid phase. The averaged conservation equations of energy, solute and momentum are used for modeling of the macroscopic transport phenomena. Regarding microsegregation, the lever rule and Scheil models are considered in the present work.

Following the work of Isabelle Vannier [1995] in finite volumes, on the coupling resolutions for the macroscopic conservation equations and microscopic solidification models, we have implemented the following two approaches in the context of finite elements:

- *Full coupling* approach to a binary alloy with eutectic transformation. In this approach, the solidification in the whole casting is considered as an open system, the lever rule is used for modeling microsegregation. Iterations are performed within each time step until convergence resolutions that satisfy the macroscopic conservation equations for energy, solute and momentum, as well as the local thermodynamic equilibrium with the lever rule. One can also solve the governing equations with only one iteration within each time step (full coupling reduced to one iteration).
- *Non-coupling* approach for multi-component alloys. This time, the solidification is considered locally as a closed system in the mushy zone, *i.e.*, the solidification path is fixed when the metal begins to solidify. The liquidus and solidus temperatures are estimated locally as a function of the local liquid average concentration just before solidification. The lever rule and Scheil models are used for modeling microsegregation.

From the point of view of numerical analysis, a nodal upwind P1+/P1 and a SUPG-PSPG methods are used for the discretization of Navier-Stokes equations. A nodal upwind P1 and the SUPG method are used for the energy equation. The SUPG method is also applied to the solute transport equation. Since solidification shrinkage is not taken into account, the computational domain is fixed. Therefore, the Eulerian scheme can be used. Our personal contribution to the new version of R2SOL can be summarized as follows:

- Regarding the highly non-linear solidification problem, we have improved the energy solver with a line search scheme. The PETSC solver has been used to solve the non-symmetric matrix equation, leading to a robust and efficient energy solver.
- Regarding fluid mechanics, the computation of Darcy and inertia terms in the P1+/P1 formulation has been improved, and the axisymmetric formulation has been implemented in R2SOL. Following Tezduyar [2000], the SUPG-PSPG approach has also been implemented in the axiymmetric version of R2SOL.
- In order to improve the computational accuracy, algorithms for isotropic and anisotropic mesh adaptations have been proposed. In the present study, the norm of the gradient of solid fraction is used as a parameter for piloting the mesh refinement in the mushy zone. The objective mesh size ahead of the liquidus isotherm is defined as a function of the distance to the liquidus isotherm. The adaptive mesh is then created using the mesher "MTC".

The *full coupling* and *no-coupling* approaches have been validated by the benchmark test of Hebditch and Hunt. It has been demonstrated that the prediction of segregated channels needs a *full coupling* computation, for which the thermal and solutal coupling effects on the solidification have been taken into account. While the main spatial trends of macrosegregation can be predicted by the *no-coupling* approach.

The mesh size and time step influence studies on the test of Hebditch and Hunt show that sufficient fine meshes, small time steps and possibly coupling iterations within each time step should be used in order to predict the segregated channels. This has also been demonstrated in the prediction of freckles during upward directional solidification. Macrosegregation in an industrial dimensional steel ingot has been simulated with mesh adaptation, fine meshes being applied in the critical region near the liquidus isotherm, and coarse meshes being used in the bulk liquid and in the solid. 'A-type' segregation is captured with the mesh refinement, the efficiency of mesh adaptation is illustrated.

Perspectives

From the point of view of physical models, the following points that affect macrosegregation would be considered in the future work, in order to improve the prediction of macrosegregation in industrial ingots:

- Equiaxed solidification. In the present work the solid is assumed stationary, the columnar dendritic solidification is modeled. This leads to failure in the prediction of the negative macrosegregation zone at the bottom of an ingot (also called the sedimentary equiaxed cone). Equiaxed crystals solidified in the early stage with poor solute content settle down to the bottom, resulting in this negative segregation cone. In order to simulate the equiaxed dendritic solidification, one needs to model the nucleation, the movement and the growth (or remelting) of grains. This could be a challenging issue (Boubeker Rabia [2004]).
- Solidification shrinkage. It is well known that shrinkage is a driving force for the interdendritic liquid movement. However, in the current model, densities of the liquid and

the solid are equal and constant, except in the buoyancy term. We will come back to this point at the end of the conclusion when dealing with coupling with solid deformation.

- Microstructure. Microstructure affects microsegregation and permeability of the mushy zone. Consequently it affects macrosegregation. In the current computations, a constant secondary arm spacing, λ_2, is used in the Carman-Kozeny relation. This could be improved by a variable λ_2, which can be as a function of, a first approximation, the local solidification time. Besides the lever rule and Scheil models, a back-diffusion model would be developed, considering the diffusion of solute elements in the solid and peritectic transformation for multicomponent steels (Thuinet et al. [2003]).

From the point of view of numerical computation, the following points remain to be investigated:

- Optimisation of remeshing algorithms. For the current version of R2SOL, it takes more CPU time to compute the distance to the liquidus isotherm, because the comparison test to find the shortest distance (cf. section 4.1.2) is very time consuming. This needs to be improved. Moreover, a direct linear interpolation is used to transport the concentration field from the old mesh to the new one. Then, information of segregated channels can be lost when derefining the mesh, which can be observed in results of an industrial ingot as presented in section 5.5. This may result in loss of accuracy. Besides the method that is defined by equation (4-15), we need an additional development to keep the memory of the local concentration near a segregated channel, avoiding use of fine meshes.
- Deeper confrontation of the nodal upwind P1+/P1 and SUPG-PSPG stabilization. Regarding the lid-driven cavity test in section 3.7.3, it appears that the nodal upwind P1+/P1 solver gives a smooth velocity field. It would be necessary to quantify separately the effects of the nodal upwind treatment for the advection terms and the bubble-type P1+/P1 formulation.

➢ Modeling of solid deformation

The goal of this part of work is to predict the shrinkage pipe, air gap, strains and stresses during the solidification of ingots. A single continuum medium is considered in the thermo-mechanical analysis. Unlike modeling of macrosegregation, we assume that in the mushy zone the solid and the liquid move together with the same velocity. For simplicity, the liquidus and solidus temperatures of an alloy are fixed according to its nominal concentration. During solidification the different behaviors of the alloy are clearly distinguished by a critical temperature. Following the work of Jaouen [1998] in THERCAST, a thermo-viscoplastic (THVP) model is used for the liquid and the mushy metal, in particular, the liquid can be Newtonian. A thermo-elastic-viscoplastic (THEVP) model is used for the solid.

Fluid flow induced by the temperature gradient and solidification shrinkage is simulated using an ALE scheme. A pure Eulerian scheme is not satisfying to model the evolution of free surface due to solidification shrinkage and the air gap formation. While a Lagrangian scheme can not be used to simulate the strong natural convection in the liquid pool, since the Lagrangian-type mesh updating could lead to mesh degeneracy. The Lagrangian scheme is used in the solid zone, where the Lagrangian-type mesh updating can track the movement of the solidified shell. This is essential to the prediction of air gap opening between ingot and mold.

In collaboration with Alban Heinrich, our contribution to the new version of R2SOL has consisted in extending the material behavior from Newtonian to elastic viscoplastic, using the P1+/P1 formulation. In this work, adaptation from 3D to 2D axisymmetric formulation is a delicate issue. The new code has been validated by a thermo-dilation and an uniaxial tension tests.

Now it is possible to calculate simultaneously fluid flow in the liquid pool and deformation in the solid, coupling with thermal analysis. The coupling from the thermal calculation towards the mechanical calculation is taken account through the temperature dependence of constitutive parameters; on the other hand, the mechanical calculation provides the size of local air gap, which changes the heat transfer coefficient at the interface between ingot and mold and consequently affects thermal analysis. Academic computations of Svensson test clearly show the importance of thermal mechanical coupling. An application to industrial steel ingots demonstrates predictions of the shrinkage pipe, air gap, strains and stresses.

Perspectives

In order to increase the accuracy, adaptive remeshing could be used for computing the deformation in the mushy zone in the future. Great variations of rheological properties appear during the liquid-solid phase change, this may need sufficient fine meshes in the mushy zone. We have proposed algorithms for piloting automatic remeshing in the computation of macro-segregation, which could be also used in the stresses and strains computation.

Finally, regarding the two models as mentioned above, it would be very interesting to merge the two computations. We expect that fluid flow induced by thermo-solutal convection and solidification shrinkage could be computed in the ALE frame instead of the Eulerian frame, so that macrosegregation and deformation in solid could be simultaneously predicted. The main difficulty remains in the treatment of mushy zone.

References

Ahmad *et al*. [1998]	N. Ahmad, H. Combeau, J.-L. Desbiolles, T. Jalanti, G. Lesoult, J. Rappaz, M. Rappaz and C. Stomp. Numerical simulation of macrosegregation: a comparison between finite volume method and finite element method predictions and a confrontation with experiments. Metall. and Mat. Trans., **29A**, 617-630, 1998
Aliaga [2000]	Charles Aliaga. Simulation numérique par éléments finis en 3D du comportement thermomécanique au cours du traitement thermique d'aciers: application à la trempe de pièces forgées ou coulées. Thèse de doctorat, Ecole des Mines de Paris. 2000
Arnold *et al*. [1984]	D. N. Arnold, F.Brezzi and M.Fortin. A stable finite element for the Stokes equations. Calcoco, **21**, 337-344, 1984
Barkhudarov *et al.* [1993]	M. Barkhudarov, H.You, J. Ortega, J. Beech, S. B. Chin, D. H. Kirkwood. Experimental validation and development of Flow-3D for casting problems. Proc. VI Int. Conf. on Modeling of Casting, Welding and Advanced Solidification Processes. T.S.Piwonka, V.Voller and L.Katgerman, TMS, 423-434, 1993
Beckermann and Viskanta [1988]	C. Beckermann and R. Viskanta. Double diffusive convection during dendritic solidification of a binary mixture. PhysicoChemical Hydrodynamics, **10**, 195-213, 1988
Beckermann [2000]	C. Beckermann. Modeling of macrosegregation: past, present and future. Flemings Symposium, Boston, MA. June, 2000
Beckermann [2001]	C. Beckermann. Macrosegregation, in Encyclopedia of Materials: Science and Technology. Elsevier Science Ltd., 4733-4739, 2001
Bellet *et al*. [1996]	M.Bellet, F.Decultieux, M.Menai, F.Bay, C.Levaillant, J.L.Chenot, P.Schmidt and I.L.Svensson. Thermomechanics of the cooling stage in casting processes: 3D finite element analysis and experimental validation. Met. Trans., **27**B, 81-100, 1996
Bellet *et al*. [2004]	Michel Bellet, Victor D. Fachinotti. ALE method for solidification modelling. Comput. Methods Appl. Mech. Engrg., **19**, 4355-4381, 2004
Bennon and Incropera [1987A]	W.D.Bennon and F.P.Incropera. A continuum model for momentum, heat and species transport in binary solid-liquid phase chang systems -I. Model formulation. Int. J. Heat Mass Transfer, **30**, 2161-2170, 1987
Bennon and Incropera [1987B]	W. D. Bennon and F. P. Incropera. The evolution of macrosegregation in statically cast binary ingots. Metall. Trans, **B**, **18B**, 611-616, 1987
Bousquet-Melou *et al.* [2002]	P.Bousquet-Melou, B.Goyeau, M.Quintard, F.Fichot, D.Gobin. Average momentum equation for interdendritic flow in a solidifying columnar mushy zone. Int. J. Heat Mass Transfer, **45**, 3651-3665, 2002

Chiang and Tsai [1992A]	K.C.Chiang and H.L.Tsai. Shrinkage-induced fluid flow and domain change in two-dimensional alloy solidification. Int. J. Heat Mass Transfer, **35**, No.7, 1763-1770, 1992
Chiang and Tsai [1992B]	K.C.Chiang and H.L.Tsai. Interaction between shrinkage-induced fluid flow and nature convection during alloy solidification. Int. J. Heat Mass Transfer, **35**, No.7, 1771-1778, 1992
Combeau et al. [1998]	H. Combeau, B. Appolaire and G. Lesoult. Recent progress in understanding and prediction of macro and mesosegregation. Modeling of Casting, Welding and Advanced Solidification Processes-VIII, TMS. B. G. Thomas and C. Beckermann, 245-256, 1998
Copley et al. [1970]	S.M. Copley, Anthony F. Giamei, S.M.Johnson, and M.F. Hornbecker. Metall. Trans., **1**, 2193-2204, 1970
Costes [2004]	Frédéric Costes. Modélisation thermomécanique tridimensionnelle par élément finis de la coulée continue d'aciers. Thèse de doctorat, Ecole des Mines de Paris. 2004
Coupez [1991]	Thierry Coupez. Grandes transformations et remaillage automatique. Thèse de doctorat, Ecole des Mines de Paris. 1991
Crisfield [1982]	M.A. Crisfield. Accelerated solution techniques and concrete cracking. Comput. Meth. Appl. Mech. Eng., **33**, 585-607, 1982
Desbiolles et al. [2003]	J.L. Desbiolles, P. Thevoz, M. Rappaz. Micro-/macrosegregation modeling in casting: a fully coupled 3D model. Proc. of Modeling of Casting, Welding and Advanced Solidification Processes X, TMS, 245-252, 2003
De Vahl-Davis [1983]	G. De Vahl Davis. Natural convection of air in a square cavity: A bench mark numerical solution. International Journal for Numerical Methods in Fluids, **3**, 249-264, 1983
Ehlen et al. [2000]	G.Ehlen, A.Schweizer, A.Ludwig, P.R.Sahm. Free surface model to predict the influence of shrinkage cavities on the solute redistribution in castings. Proc. IX Int. Conf. on Modeling of Casting, Welding and Advanced Solidification Processes, Peter R.Sahm, Preben N.Hansen and James G.Conley, TMS, 633-639, 2000
Fachinotti and Bellet [2004]	V.D. Fachinotti, M. Bellet. A diffusion-split method to deal with thermal shocks using standard linear tetrahedral finite elements. Proc. NUMIFORM'2004, 8th Int. Conf. on Numerical Methods in Industrial Forming Processes. Columbus (OH, USA), June 2004. S. Ghosh, J.M. Castro & J.K. Lee (eds.), American Institute of Physics, New York, 2258-2263, 2004.
Felicelli et al. [1991]	S.D. Felicelli, J.C. Heinrich and D.R..Poirier. Simulations of freckles during vertical solidification of binary alloys. Metall. Trans. B, **22B**, 847-859, 1991
Felicelli et al. [1998]	S.D. Felicelli, D.R. Poirier, and J.C. Heinrich. Three-dimensional simulations of freckles in binary alloys, J. Cryst.Growth, 191, 879-888, 1998

Flemings et al. [1967]	M.C. Flemings and G.E. Nereo. Macrosegregation: Part I, Trans. AIME, **239**, 1449-1461, 1967
Flemings et al. [1968A]	M.C. Flemings, R.Mehrabian and G.E.Nereo. Macrosegregation: Part II, Trans. AIME, **242**, 41-49, 1968
Flemings et al. [1968B]	M.C. Flemings and G.E.Nereo. Macrosegregation: Part III, Trans. AIME, **242**, 50-55, 1968
Flemings [1974]	M. C. Flemings. Solidification processing. 31-35, New York, McGraw Hill, 1974
Fortin and Fortin [1985]	M. Fortin and A. Fortin. Newer and newer element for incompressible flow. Finite element in fluids, **6**, 171-187, 1985
Frey and George [1999]	Pascal Jean Frey and Paul-Louis George. Maillages, applications aux éléments finis. Hermes Science Publications, Paris, 1999
Fries et al. [2004]	Thomas-Peter Fries *et al.* A Review of Petrov-Galerkin Stabilization Approaches and an Extension to Meshfree Methods. http://opus.tu-bs.de/opus/volltexte/2004/549/
Frueh et al. [2002]	C. Frueh, D.R. Poirier, S.D. Felicelli. Predicting freckle-defects in directionally solidified Pb-Sn alloys. Materials Science and Engineering, **A328**, 245-255, 2002
Fujii et al. [1979]	T. Fujii, D.R. Poirier and M.C. Flemings. Macrosegregation in a multi-component low alloy steel. Metall. Trans., B, **10B**, 331-339, 1979
Ganesan and Poirier [1990]	S. Ganesan and D.R. Poirier. Conservation of mass and momentum for the flow of interdendritic liquid during solidification. Metall. Trans.B, **21B**, 173-181, 1990
Gaston [1997]	Laurence Gaston. Simulation numérique par éléments finis bidimensionnels du remplissage de moules de fonderie et étude expérimentale sur maquette hydraulique. Thèse de doctorat, Ecole Nationale Supérieure des Mines de Paris. 1997
Gaston [1999]	Laurence Gaston. Résolution numérique par éléments finis d'un modèle de solidification pour alliages métalliques multiconstitués. CEMEF internal report, 1999
Ghia [1982]	U. Ghia, K.N. Ghia and C.T. Shin. High-Re solutions for incompressible flow using the Navier-Stokes equations and a multigrid method. Journal of Computational Physics, **48**, 387-411, 1982
Gray [1975]	W. G. Gray. A derivation of the equations for multi-phase transport. Chem. Engng. Sci., **30**, 229-233,1975
Gray [1983]	W. G. Gray. General conservation equations for multi-phase systems: 4. Constitutive theory including phase change. Adv. Water Resources, **6**, 130-140,1983
Gruau [2004]	Cyril Gruau. Génération de métriques pour adaptation anisotrope de

	maillages, applications à la mise en forme des matériaux. Thèse de doctorat, Ecole Nationale Supérieure des Mines de Paris. 2004
Gu and Beckermann[1999]	J.P. Gu and C. Beckermann. Simulation of convection and macrosegregation in a large steel ingot. Metall. Mater. Trans, A, **30**, 1357-1366, 1999
Guo and Beckermann [2003]	J. Guo and C. Beckermann. Three dimensional simulation of freckle formation during binary alloy solidification: effect of mesh spacing. Numerical Heat Transfer, Part A, **44**, 559-576, 2003
Hassanizadeh and Gray [1979]	M. Hassanizadeh and W.G. Gray. General conservation equations for multi-phase systems: 1. Averaging procedure. Adv. Water Resources, **2**, 131-144, 1979
Hebditch and Hunt [1974]	D.J. Hebditch, J.D. Hunt. Observations of ingot macrosegregation on model systems. Metall. Trans., **5**, 1557-1564, 1974
Heinrich [2003]	Alban Heinrich. Modélisation thermomécanique de la coulée continue d'acier en deux dimensions. Thèse de doctorat, Ecole Nationale Supérieure des Mines de Paris, 2003
Hughes and Brooks [1979]	T. J. R. Hughes and A. Brooks. A multi-dimensional upwind scheme with no cross wind diffusion, in Finite Elements for Convection Dominated Flows. ed. T. J. R Hughes, AMD 34, ASME, 1979
Howe [1988]	H.M. Howe. Iron Making and Steel Making., **15**, 136, 1988
Jaouen [1998]	Olivier Jaouen. Modélisation tridimensionnelle par éléments finis pour l'analyse thermo-mécanique du refroidissement des pièces coulees. Thèse de doctorat, Ecole des Mines de Paris, 1998
Kämpfer [2002]	Thomas U. Kämpfer. Modeling of macrosegregation using an adaptive domain decomposition method. Thèse de doctorat, Ecole Polytechnique Fédérale de Lausanne, 2002
Kim and Ro [1993]	C.J.Kim and S.T.Ro, Shrinkage formation during the solidification process in an open rectangular cavity, Journal of Heat Transfer, **115**,1078-1081,1993
Kou *et al*. [1978]	S. Kou, D.R. Poirier and M.C. Flemings. Macrosegregation in rotated remelted ingots, Metall. Trans., B, **9B**, 711-719, 1978
Kozlowski *et al* [1992]	P. F. Kozlowski, B. G. Thomas, J. A. Azzi and H. Wang. Simple constitutive equations for steel at high temperature, Metall. Trans. A, **23**A, 903-918, 1992
Kron *et al*. [2004]	J. Kron, M. Bellet, A. Ludwig, B. Pustal, J. Wendt and H. Fredriksson. Comparison of numerical simulation models for predicting temperature in solidification analysis with reference to air gap formation. International Journal of Cast Metals Research, **17**, 295-310, 2004
Liu [2003]	W. Liu. Computation of macrosegregation in R2SOL. CEMEF report for the OSC project, March, 2003
Mehrabian *et al*. [1970]	R. Mehrabian, M. Keane and M.C. Flemings. Interdendritic fluid flow and macrosegregation, influence of gravity, Metall. Trans., **1**, 1209-1220, 1970

Menaï [1995]	Mamar Menaï. Simulation numérique tridimensionnelle du refroidissement des pièces en fonderie: approche thermomécanique. Thèse de doctorat, Ecole des Mines de Paris, 1995
Mencinger [2004]	Jure Mencinger. Numerical simulation of melting in two-dimensional cavity using adaptive grid. Journal of Computational Physics, **198**, 243-264, 2004
Naterer [1997]	G.F.Naterer. Simultaneous pressure-velocity coupling in the two-phase zone for solidification shrinkage in an open cavity. Modelling Simul. Mater. Sci. Eng. **5**, 595-613, 1997
Ortega [1970]	J. M. Ortega. Marix theory. Plenum Press, New York, 1987
Perchat [2000]	Etienne Perchat. Mini-élément et factorisations incomplètes pour la parallélisation d'un solveur de Stokes 2D, application au forgeage. Thèse de doctorat, Ecole des Mines de Paris, 2000
PETSC [2003]	http://www-unix.mcs.anl.gov/petsc. Portable extensible toolkit for scientific computation, 2003
Pichelin [1998]	E. Pichelin. Calcul par éléments finis du remplissage 3D pour des fluides visqueux incompressibles. Application à l'injection. Thèse de doctorat, Ecole des Mines de Paris, 1998
Prakash and Voller [1989]	C. Prakash and V. Voller. On the numerical solution of continuum mixture model equations describing binary solid-liquid phase change. Num. Heat Transfer, **15B**, 171-189, 1989
Prescott *et al.* [1991]	P. J. Prescott, F. P. Incropera and W.D.Bennon. Modeling of dendritic solidification systems: reassessment of the continuum momentum equation. Int. J. Heat Mass Transfer, **34**, 2351-2359, 1991
Putti and Cordes [1998]	M. Putti and C. Cordes. Finite element approximation of the diffusion operator on tetrahedra. SIAM J. Sci. Comput. **19**, No.4, 1154-1168, 1998
Rabia [2004]	Boubeker Rabia. La formation des structures équiaxes: mouvement des grains, croissance-refusion, consequences sur les macroségrégations. Thèse de doctorat, Institut National Polytechnique de Lorraine, 2004.
Rappaz *et al.* [2002]	M. Rappaz, M. Bellet and M. Deville. Numerical modeling in materials science and engineering. Springer-Verlag Berlin Heidelberg, 2002
Ridder *et al.* [1981]	S.D. Ridder, S.Kou and R.Mehrabian. Effect of fluid flow on macro-segregation in axi-symmetric ingot. Metall. Trans., B, **12B**, 435-447, 1981
Roch *et al.* [1991]	F. Roch, H. Combeau, J.-C. Chevrier and G. Lesoult. Numerical model for prediction of the final composition and pipe formation of heavy steel ingots. Proc. 5th Int. Conf. on Modeling of Casting, Welding and Advanced Solidification Processes. M. Rappaz, M.R. Ozgü and K.W. Mahin, TMS, 789-795, 1991
Saleeb *et al.* [1998]	A. F. Saleeb, T. E. Wilt, W. Li. An implicit integration scheme for generalized viscoplasticity with dynamic recovery. Computational Mechanics, **21**, 429-440, 1998.

Sarazin and Hellawell [1988]	J. R. Sarazin and A. Hellawell. Metall. Trans. A, **19**A, 1861-1871, 1988
Shakib *et al*. [1991]	F. Shakib, T.J.R. Hughes and Z. Johan. A new finite element formulation for computational fluid dynamics: X. The compressible Euler and Navier-Stokes equation. Comp. Methods Appl. Mech. Engrg., 89, 141–219, 1991
Simo and Taylor [1985]	J.C. Simo and R.L. Taylor. Consistent tangent operators for rate-independent elastoplasticity. Computer Methods in Applied Mechanics and Engineering, **48**, 101-118, 1985
Szabó and Babuška [1991]	Barna Szabó and Ivo Babuška. Finite element analysis. John Wiley & Sons, Inc. 1991
Tezduyar and Park [1986]	T.E. Tezduyar, Y.J. Park. Discontinuity capturing finite element formulations for nonlinear convection-diffusion-reaction problems. Comput. Methods Appl. Mech. Engrg., **59**, 307-325, 1986
Tezduyar *et al*. [1992]	T.E. Tezduyar, S. Mittal, S.E. Ray, R.Shih. Incompressible flow computations with stabilized bilinear and linear equal-order-interpolation velocity-pressure elements. Comput. Methods Appl. Mech. Engrg., **95**, 221-242, 1992
Tezduyar and Osawa [2000]	T.E. Tezduyar, Y. Osawa. Finite element stabilization parameters computed from element matrices and vectors. Comput. Methods Appl. Mech. Engrg., **190**, 411-430, 2000
Thuinet et al. [2003]	L. Thuinet, G. Lesoult, H. Combeau. Computer simulation of micro-segregation in th case of columnar growth involving a peritectic transformation for multicomponent steels. Proc. MCWASP X, 10th Int. Conf. on Modeling of Casting, Welding and Advanced Solidification Processes, Destin (Floride, USA), 25-30 May 2003, D. M. Stefanescu, J. A. Warren, M. R. Jolly & M. J. M. Krane (eds.), The Minerals, Metals and Materials Society, Warrendale, Pennsylvania, USA, 237-244, 2003.
Vannier [1995]	Isabelle Vannier. Modélisation de la solidification des lingots d'acier. Thèse de doctorat, Institut National Polytechnique de Lorraine, 1995
Verhoeven [1975]	John D. Verhoeven. Fundamentals of physical metallurgy. 285-287, John Wiley & Sons, 1975
Voller and Prakash [1987]	V.R. Voller and C. Prakash. A fixed grid numerical modelling methodology for convection-diffusion mushy region phase-change problems. Int. J. Heat Mass Transfer, 30, no.8, 1709-1719, 1987
Voller *et al*. [1989]	V.R. Voller, A.D. Brent and C. Prakash. The modelling of heat, mass and solute transport in solidification system. Int. J. Heat Mass Transfer, **32**, 1719-1713, 1989
Zienkiewicz and Taylor [1989]	O.C.Zienkiewicz and R.L. Taylor. The Finite Element Method, Volume 2, solid and fluid mechanics dynamics and non-linear. Fourth Edition, McGraw-Hill Press, London, 438-456, 1989

Appendix A Data for the validation of diffusion split method

- **Geometry of the ingot and the mold**

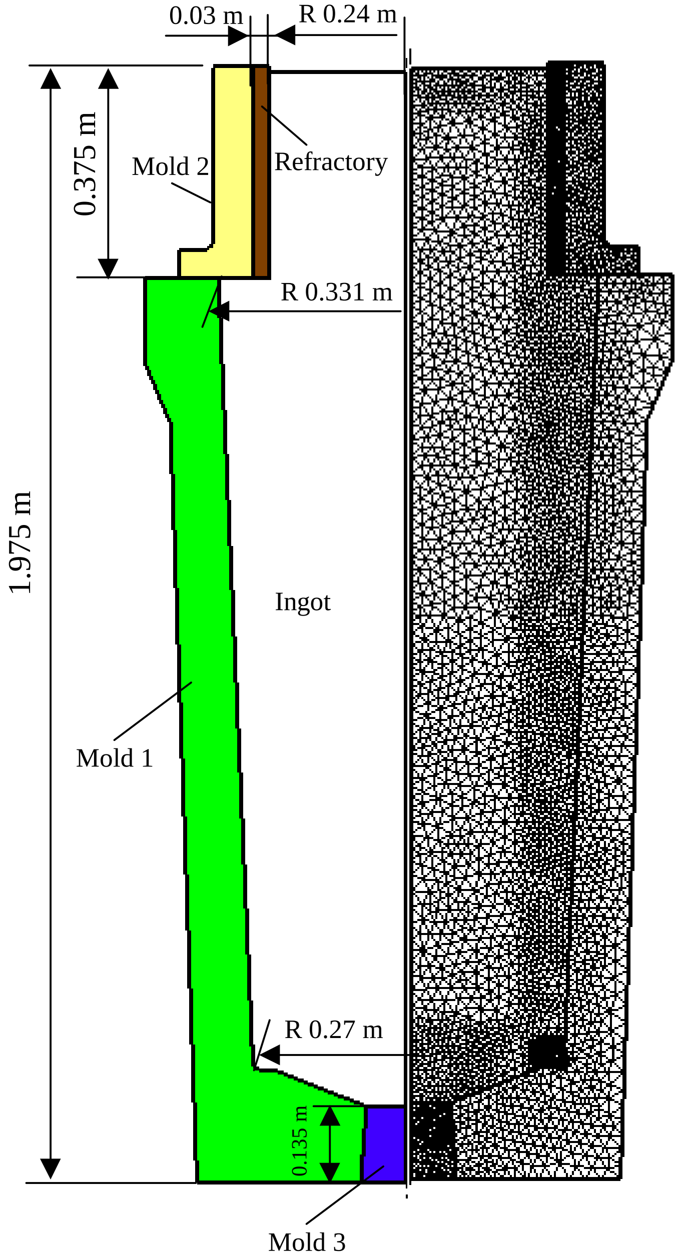

- **Physical data and calculation parameters**

Table A-1 Physical properties and calculation parameters of the steel ingot (a carbon binary alloy)

Phase diagram data		
Nominal mass fraction, w_0	wt.pct	0.38
Melting temperature, T_f	°C	1538
Liquidus slope, m	°C.wt.pct^{-1}	-80
Partition coefficient, k		0.18
Thermal data		
Thermal conductivity, λ	W.m^{-1}. K^{-1}	35
Specific heat, c_p	J.kg^{-1}. K^{-1}	672
Latent heat, L	J.kg^{-1}	0.309×10^6
Density, ρ_0	Kg.m^{-3}	7060
Calculation parameters		
Initial temperature	°C	1550
Time step	s	0.1
Heat transfer coefficient, h between ingot/mold, ingot/refractory	W.m^{-2}. K^{-1}	1000

Table A-2 Physical properties and calculation parameters of the mold and refractory

Thermal data		Mold 1 and Mold 2	Mold 3	Refractory
Thermal conductivity, λ	W.m^{-1}. K^{-1}	30	2	0.45
Specific heat, c_p	J.kg^{-1}. K^{-1}	540	1100	868
Density, ρ_0	Kg.m^{-3}	7000	2135	1600
Calculation parameters				
Initial temperature	°C	250	250	250
Heat transfer coefficient, h between mold/air, refractory/air	W.m^{-2}. K^{-1}	50	40	40
External temperature, T_{ext}	°C	50	50	50

Appendix B Organization for Macrosegregation computation

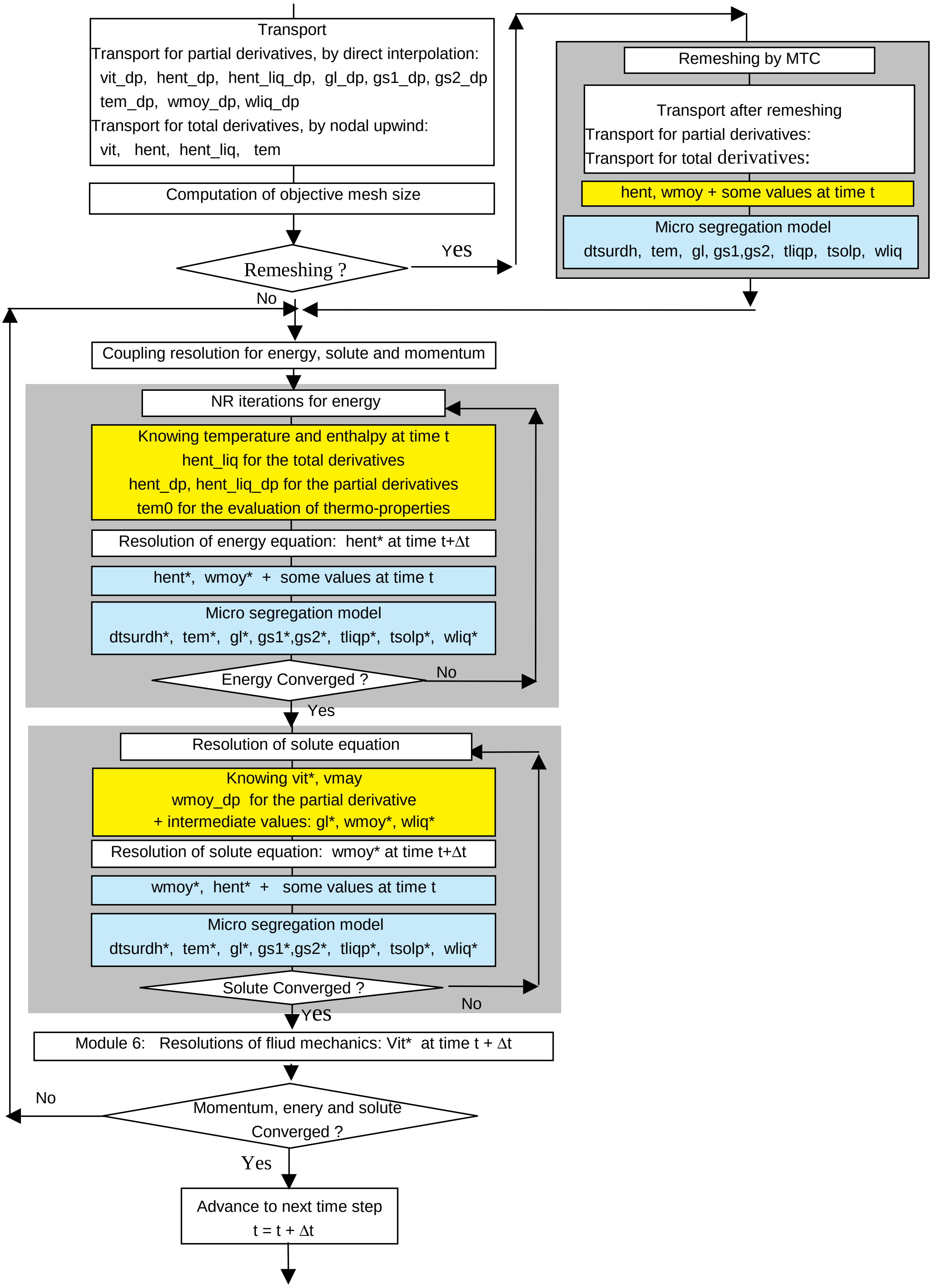

Appendix C Tangent modulus

- **Tangent modulus for the THEVP model**

Because the THEVP model is nonlinear, the global resolution of the mechanical problem should be done by an iterative procedure. The Newton-Raphson method is applied. In order to compute the Hessian matrix $\mathbf{H}$ for the Newton-Raphson iteration, the so-called "tangent modulus" is introduced in R2SOL. Therefore, the code is more general regarding the constitutive equations selected.

The tangent modulus is defined by:

$$\mathbf{C}^{d}_{n+1} = \frac{\partial \mathbf{s}_{n+1}}{\partial \dot{\boldsymbol{\varepsilon}}_{n+1}} \tag{C-1}$$

For the THEVP model, the tangent modulus of fourth order may be expressed by (Jaouen [1998]):

$$\mathbf{C}^{d}_{n+1} = 2\mu_{n+1}\alpha[\,\mathbf{I} - \frac{1}{3}\mathbf{I}\otimes\mathbf{I}\,] - \gamma\,\mathbf{s}_{n+1}\otimes\mathbf{s}_{n+1} \tag{C-2}$$

where

$$\alpha = \frac{\sigma_{eq}(\bar{\varepsilon}_{n+1})}{B_0}$$

$$\gamma = \frac{2\mu_{n+1}}{\frac{2}{3}\sigma^{2}_{eq}(\bar{\varepsilon}_{n+1})}\left[\frac{1}{1+\frac{1}{3\mu_{n+1}}\frac{d\sigma_{eq}(\bar{\varepsilon}_{n+1})}{d\bar{\varepsilon}_{n+1}}} + \alpha - 1\right]$$

$$\mathbf{I}_{ijkl} = \frac{1}{2}[\,\delta_{ik}\delta_{jl} + \delta_{il}\delta_{jk}\,]$$

$$(\mathbf{I}\otimes\mathbf{I})_{ijkl} = \delta_{ij}\delta_{kl}$$

The operator $\otimes$ denotes the tensor product. For a second order of tensor $\mathbf{q}$, $(\mathbf{q}\otimes\mathbf{q})$ is a fourth order tensor with its component $(\mathbf{q}\otimes\mathbf{q})_{ijkl} = \mathbf{q}_{ij}\mathbf{q}_{kl}$.

For the elastic deformation, $\alpha=1$ and $\gamma=0$.

The detail of computation of tangent modulus can be found in the paper of Simo and Taylor [1985].

- **Adaptations for the two-dimensional analysis**

For clarity, let us consider the incompressible liquid phase and a purely elastic solid phase with constant physical properties. Their behaviors present the two limit cases of our model, for which the tangent modulus then becomes simpler. Hereunder taking these two cases as examples, we show the adaptation to the different coordinates (from 3D to 2D), particularly for axisymmetric problems.

For simplicity, we use the Voigt notation, mapping the indices for the components of stress, strain and tangent modulus into convenient matrix form, as shown in Table C-1.

Tensor index	Matrix index					
	1	2	3	4	5	6
ab	11	22	33	12 21	23 32	31 13

Table C-1 Transformation of indices from tensor to matrix

With the Voigt notation one writes the deviatoric stress and the total deformation rate as follows:

$$\begin{aligned}\mathbf{s}&=\{\mathbf{s}_1,\mathbf{s}_2,\mathbf{s}_3,\mathbf{s}_4,\mathbf{s}_5,\mathbf{s}_6\}^T\\&=\{\mathbf{s}_{11},\mathbf{s}_{22},\mathbf{s}_{33},\ \mathbf{s}_{12},\mathbf{s}_{23},\mathbf{s}_{13}\}\end{aligned} \qquad \text{(C-3)}$$

and

$$\begin{aligned}\dot{\boldsymbol{\varepsilon}}&=\{\dot{\boldsymbol{\varepsilon}}_1,\dot{\boldsymbol{\varepsilon}}_2,\dot{\boldsymbol{\varepsilon}}_3,\dot{\boldsymbol{\varepsilon}}_4,\dot{\boldsymbol{\varepsilon}}_5,\dot{\boldsymbol{\varepsilon}}_6\}^T\\&=\{\dot{\boldsymbol{\varepsilon}}_{11},\dot{\boldsymbol{\varepsilon}}_{22},\dot{\boldsymbol{\varepsilon}}_{33},\dot{\boldsymbol{\varepsilon}}_{12},\dot{\boldsymbol{\varepsilon}}_{23},\dot{\boldsymbol{\varepsilon}}_{13}\}\end{aligned} \qquad \text{(C-4)}$$

Firstly, let us consider the incompressible ($Tr(\dot{\boldsymbol{\varepsilon}})=0$) Newtonian fluid model, the constitutive equation writes $\mathbf{s}=2\mu\dot{\boldsymbol{\varepsilon}}$, where μ is the dynamic viscosity. In three dimensions, using the Voigt notation we then have:

$$\{\mathbf{s}\}=\mu\begin{bmatrix}2&0&0&0&0&0\\0&2&0&0&0&0\\0&0&2&0&0&0\\0&0&0&1&0&0\\0&0&0&0&1&0\\0&0&0&0&0&1\end{bmatrix}\{\dot{\boldsymbol{\varepsilon}}\} \qquad \text{(C-5)}$$

Therefore, the tangent modulus for the incompressible Newtonian fluid can be expressed by:

$$C^d=\frac{\partial\mathbf{s}}{\partial\dot{\boldsymbol{\varepsilon}}}=\begin{bmatrix}C_{11}&C_{12}&C_{13}&C_{14}&C_{15}&C_{16}\\&C_{22}&C_{23}&C_{24}&C_{25}&C_{26}\\&&C_{33}&C_{34}&C_{35}&C_{36}\\&&&C_{44}&C_{45}&C_{46}\\&sym&&&C_{55}&C_{56}\\&&&&&C_{66}\end{bmatrix}=\mu\begin{bmatrix}2&0&0&0&0&0\\&2&0&0&0&0\\&&2&0&0&0\\&&&1&0&0\\&sym&&&1&0\\&&&&&1\end{bmatrix} \qquad \text{(C-6)}$$

In equation (C-6) , all the off-diagonal terms are zero. In plane strain, $\dot{\varepsilon}_{i3}=0$, *i.e.*, $\dot{\varepsilon}_{13}=\dot{\varepsilon}_{23}=\dot{\varepsilon}_{33}=0$, hence, for the plane strain problem with incompressible Newtonian behavior, only three components ($C_{11}=\frac{\partial \mathbf{s}_{11}}{\partial \dot{\boldsymbol{\varepsilon}}_{11}}=2\mu$, $C_{22}=\frac{\partial \mathbf{s}_{22}}{\partial \dot{\boldsymbol{\varepsilon}}_{22}}=2\mu$ and $C_{44}=\frac{\partial \mathbf{s}_{12}}{\partial \dot{\boldsymbol{\varepsilon}}_{12}}=\mu$) need to be considered. However, for the axisymmetric case, since $\dot{\varepsilon}_{33}=\dot{\varepsilon}_{\theta\theta}\neq 0$, an additional term $C_{33}=\frac{\partial \mathbf{s}_{33}}{\partial \dot{\boldsymbol{\varepsilon}}_{33}}=2\mu$ should be taken into account.

Secondly, we consider the purely elastic model, the deviatoric stress can be expressed by:

$$\dot{\mathbf{s}}=\mathbf{D}_{dev}\dot{\boldsymbol{\varepsilon}}=2\mu\, dev(\dot{\boldsymbol{\varepsilon}}) \tag{C-7}$$

where μ is the Lame coefficient, and $\mathbf{D}_{dev}$ is defined by:

$$\mathbf{D}_{dev}=\frac{\mu}{3}\begin{bmatrix} 4 & -2 & -2 & 0 & 0 & 0 \\ -2 & 4 & -2 & 0 & 0 & 0 \\ -2 & -2 & 4 & 0 & 0 & 0 \\ 0 & 0 & 0 & 3 & 0 & 0 \\ 0 & 0 & 0 & 0 & 3 & 0 \\ 0 & 0 & 0 & 0 & 0 & 3 \end{bmatrix} \tag{C-8}$$

This time, the tangent modulus may be expressed by:

$$C^{d}=\frac{\partial \mathbf{s}}{\partial \dot{\boldsymbol{\varepsilon}}}=\begin{bmatrix} C_{11} & C_{12} & C_{13} & C_{14} & C_{15} & C_{16} \\ & C_{22} & C_{23} & C_{24} & C_{25} & C_{26} \\ & & C_{33} & C_{34} & C_{35} & C_{36} \\ & & & C_{44} & C_{45} & C_{46} \\ & sym & & & C_{55} & C_{56} \\ & & & & & C_{66} \end{bmatrix}=\frac{\mu}{3}\begin{bmatrix} 4 & -2 & -2 & 0 & 0 & 0 \\ & 4 & -2 & 0 & 0 & 0 \\ & & 4 & 0 & 0 & 0 \\ & & & 3 & 0 & 0 \\ & sym & & & 3 & 0 \\ & & & & & 3 \end{bmatrix} \tag{C-9}$$

In contrast to the Newtonian liquid model, some non-zero components appear in the off-diagonal terms, seeing equation (6-36). In the plane strain case, the terms, $C_{11}=\frac{\partial \mathbf{s}_{11}}{\partial \dot{\boldsymbol{\varepsilon}}_{11}}$, $C_{22}=\frac{\partial \mathbf{s}_{22}}{\partial \dot{\boldsymbol{\varepsilon}}_{22}}$, $C_{12}=C_{21}=\frac{\partial \mathbf{s}_{11}}{\partial \dot{\boldsymbol{\varepsilon}}_{22}}$ and $C_{44}=\frac{\partial \mathbf{s}_{12}}{\partial \dot{\boldsymbol{\varepsilon}}_{12}}$ should be considered.

For the axisymmetric problems, besides the terms appearing in the plane case, the additional terms, $C_{33}=\frac{\partial \mathbf{s}_{33}}{\partial \dot{\boldsymbol{\varepsilon}}_{33}}$, $C_{13}=C_{31}=\frac{\partial \mathbf{s}_{33}}{\partial \dot{\boldsymbol{\varepsilon}}_{11}}$ and $C_{23}=C_{32}=\frac{\partial \mathbf{s}_{33}}{\partial \dot{\boldsymbol{\varepsilon}}_{22}}$, should be taken into account.

During the local resolution of constitutive equations, the tangent modulus C_{n+1}^{d} of the THEVP model are computed using equation (6-30). The components in the tensor C_{n+1}^{d} that need to be considered are similar as what we have discussed for the elastic model.

Résumé

Ce travail est consacré à la modélisation des macroségrégations et des distorsions se produisant lors de la solidification de pièces métalliques. Un modèle bidimensionnel d'éléments finis est développé pour l'analyse des écoulements de convection thermo-solutale à l'origine des macroségrégations. Dans ce modèle, l'ensemble des équations, moyennées spatialement, de conservation de l'énergie, de la quantité de mouvement, de la masse et des espèces chimiques est résolu en prenant pour modèle de microségrégation la règle des leviers. Plusieurs formulations permettent une résolution avec couplage faible ou fort des différentes résolutions ainsi qu'une approche en système ouvert ou fermé. Dans le but d'augmenter la précision des résultats, un algorithme de remaillage dynamique est également proposé, de façon à enrichir le maillage au voisinage du front de solidification. L'orientation et la norme du gradient de fraction liquide guident le remaillage dans la zone pâteuse, tandis que la distance à l'isotherme liquidus est utilisée dans le liquide.

L'approche numérique est validée grâce à un benchmark de macroségrégation tiré de la littérature et portant sur des alliages Pb-Sn. Les influences de la discrétisation spatiale et temporelle et des schémas de couplage sont discutées, notamment par rapport à la capacité de prédiction des canaux ségrégés. En outre, l'efficacité de l'adaptation de maillage est illustrée dans un cas de solidification dirigée, donnant lieu à l'apparition de « freckles », ainsi que pour la prédiction de bandes ségrégées de type A dans un gros lingot d'acier.

La dernière partie du document présente une modélisation thermo-mécanique visant à calculer le développement, pendant le procédé, des contraintes et distorsions dans les zones solidifiées, ainsi que le retrait et les mouvements de thermo-convection affectant les régions liquides. Le comportement de l'alliage est alors considéré comme newtonien à l'état liquide, comme celui d'un milieu continu viscoplastique à l'état pâteux, et comme élasto-visco-plastique à l'état solide. Cette simulation thermo-mécanique est utilisée pour calculer la formation des lames d'air, la génération des déformations, des contraintes et la formation des retassures primaires.

Mots-clefs: solidification, modélisation, macroségrégation, éléments finis, 2D, adaptation de maillage, thermomécanique, mécanique des fluides.

Abstract

This work is dedicated to the modeling of macrosegregation and deformation during solidification of castings. A two-dimensional finite element model to simulate macrosegregation due to thermal-solutal convection in the case of columnar dendritic solidification is presented. A set of volume-averaged conservation equations of energy, solute, momentum and mass is solved in conjunction with the use of the lever rule as a microsegregation model. Several formulations have been implemented, permitting a resolution with either weak or strong coupling, closed or open system. In order to improve the prediction accuracy, an algorithm for dynamic remeshing is proposed. The basic idea is to generate fine elements near the liquidus isotherm. The norm of the gradient of solid fraction is used for piloting the remeshing in the mushy zone; while the objective mesh size in the liquid is considered as a function of the distance to the liquidus isotherm.

The numerical approach has been validated with a benchmark test of macrosegregation in Pb-Sn alloys taken from the literature. The influences of mesh size, time step and coupling scheme have been investigated. Sufficient fine meshes, small time step and possibly coupling iterations should be applied in order to predict segregated channels. Moreover, the efficiency of mesh adaptation is demonstrated by predictions of freckles in a case of unidirectional solidification, and of 'A-type' segregation bands in a large industrial carbon steel ingot.

In the last part of this work, regarding fluid flow in the liquid induced by solidification shrinkage and thermo-convection and deformation in the solid, a thermal mechanical model has been implemented with a Eulerian-Lagrangian formulation. The alloy in the liquid state is Newtonian, and in the mushy state it is modeled by a viscoplastic continuum. Below a critical temperature the alloy is considered by a thermal elastic viscoplastic model. The thermo-mechanical simulation is used to predict the shrinkage pipe, air gap, strains and stresses.

Keywords: solidification, modeling, macrosegregation, 2D finite elements, mesh adaptation, thermomechanics, fluid mechanics